Dhar, Rakshita Pritamsingh (2023) *Optimization of the design of experimental (DoE) simulations of Ion-sensitive Field Effect Transistors.* PhD thesis.

http://theses.gla.ac.uk/83715/

Optimization of the design of experimental (DoE) simulations of Ion-sensitive Field Effect Transistors

RAKSHITA PRITAMSINGH DHAR

Submitted in partial fulfilment of the requirements for the
Degree of
DOCTOR OF PHILOSOPHY

College of Science and Engineering
University of Glasgow

March 2023

Declaration of Originality

University of Glasgow
College of Science and Engineering
Statement of Originality to Accompany Thesis Submission

Name: RAKSHITA PRITAMSINGH DHAR

Registration Number:

I certify that the thesis presented here for examination for [PhD] degree of the University of Glasgow is solely my own work other than where I have clearly indicated that it is the work of others (in which case the extent of any work carried out jointly by me and any other person is clearly identified in it) and that the thesis has not been edited by a third party beyond what is permitted by the University's PGR Code of Practice.

The copyright of this thesis rests with the author. No quotation from it is permitted without full acknowledgement. I declare that the thesis does not include work forming part of a thesis presented successfully for another degree.

I declare that this thesis has been produced in accordance with the University of Glasgow's Code of Good Practice in Research. I acknowledge that if any issues are raised regarding good research practices based on a review of the thesis, the examination may be postponed pending the outcome of any investigation of the issues.

26/06/2023
Rakshita Dhar
March 2023
Glasgow, UK

Abstract

To make personalised medicines for cancer treatment we need to detect a specific antigen with antibodies. Studies are being carried out for these antigen-antibody interactions. This can be done with the help of nano biosensors. Nano biosensors are nano-scaled biosensors used to detect specific biomolecules in the sample. The sample can be present in a solution. This thesis is a radical vision of imitating the electrochemical synthesis of peptide [1] receptors by a programmable in-situ protein (target molecules) detection with nano-functionalised FinFET sensors by simulations.

In order to do so, we have started first by simulation of an Ion-sensing field effect transistor (ISFET) where we detect the ions to determine the absolute pH of the solution. The ions/target molecules are protons in this case. The receptors are further modified to increase the surface complexity. This helps us understand better the solution/surface interactions which will help us in future to detect a specific protein.

This thesis aims to achieve a technological breakthrough of the first fully programmable ion screening simulation tool. This simulation tool will come as a faster, cheaper, and more efficient technology. The simulation of this is performed by using MATLAB and Synopsys Sentaurus TCAD software. A study of different types of models for the bio-interface along with an analysis of output characteristics obtained from simulation is presented in this report.

Acknowledgements

List of Acronyms

Acronyms	Definition
DNA	Deoxyribonucleic Acid
RNA	Ribonucleic Acid
ISFET	Ion-sensitive Field Effect Transistor
FinFET	Fin Field Effect Transistor
TCAD	Technology Computer Aided Design
MHC	Major Histocompatibility Complex
CMOS	Complimentary Metal-oxide semiconductor
ISFET	Ion-sensitive field effect transistor
BioFET	Biofield effect transistor
AA	Amino Acid
TCAD	Technology Computer Aided Design
ITC	Interface trap Charges
PMI	Physical Model Interface
SOI	Silicon On Insulator
IMFET	Immunologically modified field effect transistor
FET	Field Effect Transistor
JL-FET	Junctionless field effect transistor
ATGC	Adenine, Thymine, Guanine and Cytosine (ATGC)
APTES	(3-Aminopropyl)triethoxysilane
low-k	low dielectric constant
high-k	high dielectric constant
SEM	Scanning Electron Microscope
AA	Amino acid
R	Arginine
D	Aspartic acid
P	Proline
PEG	Polyethylene Glycol
C-Imm.	carboxylic immobilized
N-Imm.	Amine immobilized
DoE	Design of Experimental
ITC	Interface Trapped charges
PMI	Physical Model Interface

List of Symbols

Symbol	Definition
σ_0	Surface Charge
Ψ_{Var}	Potential variation throughout the electrolyte starting from oxide-electrolyte interface to the bulk
pH_B	Bulk pH
pH_S	Surface pH
Ψ_0	Surface potential
Ψ_ξ	Zeta Potential
α	Sensitivity factor
C_{ox}	Oxide Capacitance
W_D	Depletion width
I_{SD}	Drain Current
β_{int}	Intrinsic Buffer Capacity
C_{diff}	Differential capacitance
C_{eq}	Equivalent Capacitance
C_{ox}	Oxide Capacitance
C_{sc}	semi-conductor Capacitance
Q_g	Charge in metal gate
Q_{sc}	Charge in semi-conductor
n_s	Charge carriers in surface of MOSFET
n_i	Intrinsic concentration of carriers
k_B	Boltzman constant
T	Temperature
Φ_b	Work function of bulk (semiconductor region)
Φ_s	Work function of metal surface
e	Charge of an electron
ε_0	permittivity of free space
ε_r	relative permittivity
N_A	doping concentration
$I_{D,lin}$	Drain current of MOSFET in linear region
$I_{D,sat}$	Drain current of MOSFET in saturation region
μ_p	Mobility of majority charge carriers
W	Width of the device
L	Length of the device

V_{GS}	Gate Voltage
V_T	Thermal voltage
V_{th}	Threshold voltage
V_{DS}	Drain to source voltage
C_{DL}	Double Layer Capacitance
C_{dl}	Diffusive Layer Capacitance
Q_{DL}	Charge formed in electrolyte due to formation of double layer
Q_{bio}	Charge on surface of oxide
N_{avg}	Avogadro's constant
I_0	Ionic strength
V_{pinch}	Pinch-Off Voltage
σ_{0-SD}	surface charge density site dissociation model
$\sigma_{0-SD-APTES}$	Site dissociation surface charge density due to APTES
$\sigma_{0-SD-Total}$	Total site dissociation surface charge density
q	unit charge
N_s	Total number of sites per unit area (Silanol)
N_n	Total number of sites per unit area (APTES)
K_a	Dissociation constant for acid
K_b	Dissociation constant for base
$[H_s]$	Concentration of $[H^+]$ ions on surface
Θ^+	Total number of positive charges on oxide surface
Θ^-	Total number of negative charges on oxide surface
E	Electric Field
σ_{0-GC}	surface charge density Gouy Chapman model
σ_{0-GCS}	surface charge density Gouy Chapman Stern model
c_0	Ionic strength of electrolyte solution
c^+	concentration of positive ions in bulk
c^-	concentration of negative ions in bulk
pH_{pzc}	pH at point of zero charge
C_{stern}	Stern layer capacitance
Ψ_{Var}	Potential variation throughout the electrolyte
λ_D	Debye Length
p_b	Concentration of positive ions in the bulk
n_b	Concentration of negative ions in the bulk
t_{ox}	Oxide thickness
Ψ_s	Potential drop in semiconductor at Equilibrium condition
$p_{variations}$	Concentration of positive ions in the electrolyte
$n_{variations}$	Concentration of negative ions in the electrolyte
C_{ox}^1	Oxide Capacitance without any degradation
C_{ox}^2	Oxide Capacitance with degradation
V_{ox}	Potential drop in oxide at Equilibrium
σ	conductivity
A	cross-section area
L	length of Si channel
h	height of the Si channel
ρ	resistivity
x	length of degradation in oxide
β_{intTiO_2}	Intrinsic buffer capacity for TiO_2

σ_{gcsSiO_2}	Gouy Chapman Stern surface charge density due to SiO_2
σ_{gcsHfO_2}	Gouy Chapman Stern surface charge density due to HfO_2
σ_{gcsTiO_2}	Gouy Chapman Stern surface charge density due to TiO_2
$\Psi_{\xi SiO_2}$	Zeta Potential of SiO_2
$\Psi_{\xi HfO_2}$	Zeta Potential of HfO_2
$\Psi_{\xi TiO_2}$	Zeta Potential of TiO_2
Ψ_{0SiO_2}	Surface Potential of SiO_2
Ψ_{0HfO_2}	Surface Potential of HfO_2
Ψ_{0TiO_2}	Surface Potential of TiO_2
N_{sSiO_2}	Number of sites for SiO_2
N_{sHfO_2}	Number of sites for HfO_2
N_{sTiO_2}	Number of sites for TiO_2
K_{aSiO_2}	Acid Dissociation constant for SiO_2
K_{aHfO_2}	Acid Dissociation constant for HfO_2
K_{aTiO_2}	Acid Dissociation constant for TiO_2
K_{bSiO_2}	Basic Dissociation constant for SiO_2
K_{bHfO_2}	Basic Dissociation constant for HfO_2
K_{bTiO_2}	Basic Dissociation constant for TiO_2
α_{SiO_2}	sensitivity factor for SiO_2
α_{HfO_2}	sensitivity factor for HfO_2
α_{TiO_2}	sensitivity factor for TiO_2
N_c	Electron Density of State
N_v	Hole Density of State
E_f	Fermi Energy Level
E_c	Conduction Band
E_v	Valence Band
$C_{electrolyte}$	Electrolyte capacitance
I_{on}	ON current
I_{off}	OFF current
$t_{electrolyte}$	Thickness of electrolyte
$\varepsilon_{electrolyte}$	Permittivity of electrolyte
N_S^d	Interface Donor Traps
N_S^a	Interface Acceptor Traps
f^d	Occupation probabilities of donor traps
f^a	Occupation probabilities of acceptor traps
c_v^d	Electron capture rate
e_v^d	Electron emission rate
c_v^a	Hole capture rate
e_v^a	Hole emission rate
cH_S	Concentration of $[H^+]$ ions on oxide surface
n_s	concentration of negative charge carriers in semiconductor
p_s	concentration of positive charge carriers in semiconductor
$C_{i,st}$	Intrinsic Stern Layer capacitance
σ_T	Surface charge density of traps in semi-conductor
$C_{diffSiO_2}$	Differential Capacitance for SiO_2
$C_{diffHfO_2}$	Differential Capacitance for HfO_2
$C_{diffTiO_2}$	Differential Capacitance for TiO_2
β_{intSiO_2}	Intrinsic buffer capacity for SiO_2
β_{intHfO_2}	Intrinsic buffer capacity for HfO_2

Contents

List of Tables

List of Figures

Chapter 1

Introduction

In 1999, an article in "The Wall Street Journal" with the title "New Era of Personalised Medicine: Targeting Drugs for Each Unique Genetic Profile" introduced the term personalised medicine. This concept has changed our approach to therapies in the last two decades with the evidence that each one of us reacts differently to diseases due to the molecular heterogeneity amongst individuals, and thus therapies must be adapted. Personalised medicines started with the detailed de-codification of genetic profiles thanks to DNA sequencing and it has progressed with other molecules that have derived to the different -omics that refer to the study of the variability amongst individuals of the constituents of the molecules like proteins, or metabolites, or cells. This new paradigm of medicine requires however much more information from each patient.

Molecular microarrays or simply microarrays are libraries of molecules that enable increasing the number of experiments in an assay. The different types of microarrays include DNA/RNA microarrays, small molecule microarrays and protein microarrays depending on the molecules required to build them [2], [3], [4]. They are very useful since they are adaptable in the detection of proteomics, cellomics, genomics and glycomics [5], [6], [7], [8]. Most of the time microarrays are sensed by fluorescence to detect molecular interactions of target molecules with different molecules. It is also interesting to combine microarrays with biosensors or a sensing element, in this way they can increase their sensitivity to lower the limits of detection (detecting fewer molecules) or allow label-free sensing, that due to online detection is able to decipher the kinetics and provide information about the binding affinity between each of the spots in the microarray and the target molecules. The information of a microarray can be used to search for biomarkers with different specific molecules (antibodies) immobilised in each of the spots of the microarray [9]. They can also be used to screen the interactions of a single molecule towards different targets. Due to the variability in the chemistry of proteins, these applications of microarrays convert them into powerful tools in protein detection and analysis. Microarrays along with sensing elements can increase specificity to the recognition for the early detection and prediction of diseases like cancer, and enable the screening or the interactions of molecules, leading to new therapies.

Sensors that can be used for microarrays can be classified based on transduction techniques. The receptor-target molecule interaction transduces as electrical, mechanical or optical signals, hence making it detectable [9]. Some of the devices used in microarrays include - cantilevers, optical and FETs. In these, the receptor-target molecule interactions get transduced in a shift of the resonant vibration of the cantilever, fluorescence or plasmonic signal and electrical signal respectively. These transduction methods can also be used in label and label-free schemes. The labelling detection method includes labelling the target molecule so it can be detected. In the Label-free detection method, the transduction is sensitive to the target molecule, providing advantages like the simplicity of the assay, avoiding the interference of unwanted molecular interactions with the target, and providing access online access to the binding kinetics.

Of the different kinds of microarrays, DNA was the first one that was studied due to the progress of DNA sequencing thanks to the use of polymerase which can amplify the number of DNA molecules. However, there is not a polymerase-like molecule for proteins, thus, the study of protein interactions remains a challenge.

This thesis is framed in the European project *Electromed* (grant No 862539) financed by the European Commission under the H2020-FET OPEN program for the development of a new platform to screen proteins. The rationale behind this was to combine microarrays with Field Effect Sensors (FETs). FETs are compact and have the potential to be better integrated with microarray systems, which makes them suitable for large multiplexing. The *Electromed* project aims to combine the potential of FET sensors with *in-situ* electrochemical peptide synthesis to have a full electrochemical system with the potential of high multiplexing and enable fastly peptide microarrays where the peptide sequences from each spot can be programmed. This would allow the study of peptide/protein interactions, which in our project would be used for the development of vaccines with peptide sequences that could trigger the immune system, by finding the peptides that can be detected by the molecules of the major histocompatibility system (MHC molecules).

In the past few years, highly sensitive, label-free and specific detection of various antigen-antibody interactions have been demonstrated using silicon-based immunoFETs [10]. Mucin-1, prostate-specific antigen (PSA), PSA-1-antichymotripsin and carcinoembryonic antigen are all cancer biomarkers using FET nanowire sensors at femtomolar concentrations [11]. Silicon-based immunoFETs allow for label-free and real-time detection, ultra-high sensitivity, excellent selectivity, the possibility for multiplexing, support low sample volumes and CMOS compatibility [12]. Despite the apparent simplicity of the immunoFET, the commercialization of such technologies is yet to be demonstrated. The main hurdle for the realization of a product-based immunoFET is the solid/solution interface which is a multi-parameter system that introduces substantial complexity to the device. The key to the next advancement in immunoFET technology is to further develop an appropriate management strategy of the solid/solution interface [13].

There are new ways that need to be developed for designing biomarkers which cannot only

be derived from the experiment studying the inherent properties of how the molecules interact with the FET surface but also include computational methods. Rapid and simple examination are the advantages that these computational methods offer.

In this thesis, we have produced solid/solution interface models for a better understanding of the applications of FETs for the detection and characterization of biomolecules. The most time-efficient and cost-effective way to improve the sensor design is to perform modelling and simulations. The modelling allows us to design the sensor using simulations in which we can disentangle the effects of the inorganic components (FET architecture, material, doping and etc.) and organic interface (e.g. solvent, proteins and peptides), together with controlling the effects of all the fluctuations in the parameters linked to the device and the thermodynamic. Various simulation techniques and methods were implemented and also combined. In general, the simulations help researchers and companies to reduce the exploration space and focus the fabrication technology on the design most likely to deliver the desired sensor sensitivity and dynamic range for multiplexing. A simulation methodology has been developed and implemented, which allows us to execute numerical experiments along with analytical simulations to study the behaviour of a nano-biosensor. The simulation results are used to analyse the behaviour of nano-biosensors and predict the device performance so that it can be used as input information in the fabrication process in order to optimise nano-biosensor.

One of the main results of this thesis has been the characterisation of ISFETs using computational techniques. We strive to obtain the digital fingerprints of amino acids for protein detection by simulations. Towards the end, we have done characterisation of ISFETs combining both the homogeneous and heterogeneous surfaces of the sensor.

1.1 Outline of thesis

Chapter 2 gives a general explanation of the origin of different types of semiconductor devices and explains in detail an ISFET. The label-free detection of charged macromolecules along with types of sensing for label-free detection is described comprehensively. Also, the working principle of a BioFET is described for better comprehending the device's functioning along with the state of art.

Chapter 3 describes various analytical models for the charge on the oxide surface. The analytical simulation of these models is done in MATLAB and the results are obtained. Site-dissociation model is explained along with our work to imbibe the functionalisation in this model. Similarly, the Gouy-Chapman Model and Gouy-Chapman-Stern Model are explained along with the methodology used in MATLAB to implement these models. After obtaining the surface charge (σ_0) for the oxide surface, the potential distribution (Ψ_{Var}) throughout the electrolyte from the oxide surface to debye length and beyond that is derived. The effect of varying pH_B on Ψ_0, Ψ_ξ and α shown.

Chapter 4 shows the effect of different oxides (namely SiO_2 and HfO_2) and their application to an absolute pH sensor. A capacitance model has been made to analyse the effect of the degradation of different oxides due to electrolyte on the oxide capacitance (C_{ox}). The effect of oxide degradation has also been analysed on the depletion width (W_D) for a pH range from 2 to 12. Also, the effect of oxide degradation on drain current (I_{SD}) for ideal and non-ideal sensors.

Chapter 5 shows the effect of oxides on amino-acid sensing when three types of oxides are used- namely SiO_2, HfO_2 and TiO_2. The study of the effect of varying pH_B on Ψ_0, Ψ_ξ, α, β_{int} for SiO_2, HfO_2 and TiO_2 is done. Amino acid (AA) fingerprints for C-Immobalised and N-Immobalised Arginine, Aspartic acid and Proline are obtained for these three oxides. Also, the depletion width (W_D), and drain current (I_{SD}) for varying pH_B are analysed for these AAs.

Chapter 6 is TCAD: Projection of the implementation of the analytical model with a numerical model. This chapter contains the numerical simulations in Synopsys Senaturas. The device architecture is explained along with device physics. Transfer characteristics for 5nm SiO_2, 10nm SiO_2, 5nm HfO_2 and 10nm HfO_2 are plotted with and without electrolyte. Two methods for modelling the oxide/electrolyte interaction are executed here- namely the Interface Trapped Charges method (ITC) and the Physical model interface (PMI). Both these methods are executed by combining analytical and numerical simulations.

Chapter 2

From semiconductor devices to BioFETs

This chapter discusses the transformation of semiconductor device simulations from a simple PN junction diode to Field effect transistors (FETs) and their modifications to be used as biosensors. It describes, how semiconductor devices have been integrated with ion-sensing leading to ion-sensitive field-effect transistors (ISFETs). The working principle of ISFET/BioFETs is detailed along with the problems which occur in biosensing. Finally the biosensing problem this thesis will solve.

2.1 Metal oxide semiconductor FETs to Bio FETs

This section introduces the devices and developments that gave rise to the FET biosensors, starting from the first semiconductor heterojunctions.

The PN-junction diode is the fundamental building block of the transistors developed in the middle of the last century and was invented by Russel Ohl in 1940 in Bell Labs Holmdel Complex, Building complex in Holmdel, New Jersey [14]. A PN-junction diode is made up of a Silicon crystal having n-type donors (created by adding pentavalent impurities in Si crystal) and p-type ones (created by adding trivalent impurities in Si crystal) in the two different regions of the device. The n-type and p-type materials are combined by diffusion or ion-implantation techniques [15]. Its application in the field of technology includes rectifiers and inverters as shown in fig. 2.1 (a) [16]. Following the PN-diode, the first working model of the transistor was made also at Bell Labs, New Jersey by John Bardeen and Walter Brattain working under the supervision of William Shockley. They executed a point junction transistor with a triode-like semiconductor device. For this achievement, they shared a Nobel prize in 1956 [17]. This achievement opened the door to the development of many modern devices like transistor radios, switches in digital circuits and amplifiers (illustrated in fig. 2.1 (b)). The metal oxide semiconductor field effect transistor (MOSFET) was developed by Kahng and Atalla in 1960 and was highly influenced by the first practical metal-oxide-semiconductor (MOS) device fabricated by Ligenza and Spitzer in 1960 [18]. MOSFETs are based on modulating the current flowing through a source-drain channel with a metal gate capacitively coupled to this conductive channel. First MOSFETs were created by inducing a single carrier channel through a double heterojunction (PNP or NPN). Currently, with thin layers created by Silicon on insulator (SOI) materials, junctionless and Fin-FET MOSFETs can be created. The MOSFET is arguably the most important and widely used technology that is utilised in making power electronics converters and drives (illustrated in fig. 2.1 (c)).

The use of semiconductor devices was later realized not only in the strictly electrical engineering field but also in the chemical and biomedical fields. This was done by the modification of the MOSFET structure where instead of depositing metal on gate oxide, the electrolyte solution was placed on top of the gate oxide. Instead of providing the gate voltage on the metal, the gate voltage is actuated by a reference electrode immersed in an electrolyte, which can be used to compensate for the changes in the surface potential due to the biological effects. The first form of these sensors was the ion-sensitive field-effect transistor (ISFET) (illustrated in fig. 2.1) (d) [18] whose main applications included ion detection (and pH sensing) which was then extended to blood and urine analysis [19]. Almost after approximately two decades (in 1989), it was redesigned for biomedical applications for protein and DNA sensing. Different architectures using different receptor molecules were designed with the principle of using the charges of target molecules to change the surface potential. Amongst them, the ones targetting proteins are designed as immunologically modified field effect transistors (IMFETs) [19]. They were made

possible by the functionalisation of the oxide layer with selective molecules which act as receptors (typically with an antibody-like molecule) and would come in contact with target molecules (the proteins) as shown in fig. 2.1 (e).

Lorem ipsum dolor sit amet, consectetuer adipiscing elit. Etiam lobortis facilisis sem. Nullam nec mi et neque pharetra sollicitudin. Praesent imperdiet mi nec ante. Donec ullamcorper, felis non sodales commodo, lectus velit ultrices augue, a dignissim nibh lectus placerat pede. Vivamus nunc nunc, molestie ut, ultricies vel, semper in, velit. Ut porttitor. Praesent in sapien. Lorem ipsum dolor sit amet, consectetuer adipiscing elit. Duis fringilla tristique neque. Sed interdum libero ut metus. Pellentesque placerat. Nam rutrum augue a leo. Morbi sed elit sit amet ante lobortis sollicitudin. Praesent blandit blandit mauris. Praesent lectus tellus, aliquet aliquam, luctus a, egestas a, turpis. Mauris lacinia lorem sit amet ipsum. Nunc quis urna dictum turpis accumsan semper.

Lorem ipsum dolor sit amet, consectetuer adipiscing elit. Etiam lobortis facilisis sem. Nullam nec mi et neque pharetra sollicitudin. Praesent imperdiet mi nec ante. Donec ullamcorper, felis non sodales commodo, lectus velit ultrices augue, a dignissim nibh lectus placerat pede. Vivamus nunc nunc, molestie ut, ultricies vel, semper in, velit. Ut porttitor. Praesent in sapien. Lorem ipsum dolor sit amet, consectetuer adipiscing elit. Duis fringilla tristique neque. Sed interdum libero ut metus. Pellentesque placerat. Nam rutrum augue a leo. Morbi sed elit sit amet ante lobortis sollicitudin. Praesent blandit blandit mauris. Praesent lectus tellus, aliquet aliquam, luctus a, egestas a, turpis. Mauris lacinia lorem sit amet ipsum. Nunc quis urna dictum turpis accumsan semper.

Figure 2.1: Summary of the history of Semiconductor devices simulation and their applications as per the year of the invention of the devices. (a) In 1940 diode was invented leading to its application in rectifiers. (b) In 1947, a transistor was invented having applications in Radio/switches. (c) In the 1960s MOSFET was invented, and power electronics converters and drives were developed. (d) In 1970 ISFET device was made, and its application includes the biomedical field. (e) In 1989, IMFET came into existence which now is used as Biosensor.

2.1.1 MOSFET

We will now describe the working principles of a metal oxide semiconductor field effect transistor (MOSFET). The heart of the MOSFET is the MOS capacitor, where a thin insulating oxide layer is sandwiched between a metal and a semiconductor where doping is limited such as the capacitance potential can modulate the charge in the region close to the interface between the semiconductor and the metal. Since the structure has a dielectric between the metal and the semiconductor, no charge is transferred within the threshold of the breakdown voltage. Thus, the MOSFET structure is essentially a capacitor whose capacitance can be controlled by the gate voltage applied to the metal and hence control the drain current in the semiconductor device.

Capacitance Model

The equivalent capacitance (C_{eq}) of a MOSFET is the series combination of oxide capacitance (C_{ox}) and semiconductor capacitance (C_{sc}) as shown in equation 2.1.

$$\frac{1}{C_{eq}} = \frac{1}{C_{ox}} + \frac{1}{C_{sc}} \tag{2.1}$$

Conceptually, the easiest transistor may be the junctionless transistor in which there is only one type of carrier in the channel. In the accumulation mode, the equivalent capacitance is equal to the oxide capacitance as given by equation 2.2. As the semiconductor capacitance is much greater than oxide capacitance ($C_{sc} \gg C_{ox}$) and can be considered equal to infinity having no contribution in equivalent capacitance (C_{eq})

$$C_{eq} \approx C_{ox} \tag{2.2}$$

ISFET and BioFET architectures with junctionless transistors work in depletion mode where C_{sc} is neglected and the only capacitance formed is the one defined by the oxide dielectric between the charges of the metal side and the one in the semiconductor channel. Figure 2.2 (a) shows the charge balance and (b) shows the equivalent circuit diagram for the metal oxide semiconductor field effect transistor in depletion mode. The charge Q_g is equal to Q_{sc}.

$$Q_g = Q_{sc} \tag{2.3}$$

This configuration allows relating the current in the MOSFET to the surface potential acted by the metal, as the charging of the semiconductor channel in the depleted region decreases to the total cross-section of the conductive channel. This principle will be used by the ISFET to detect the charges accumulated in the sensor interface, as described in the next section.
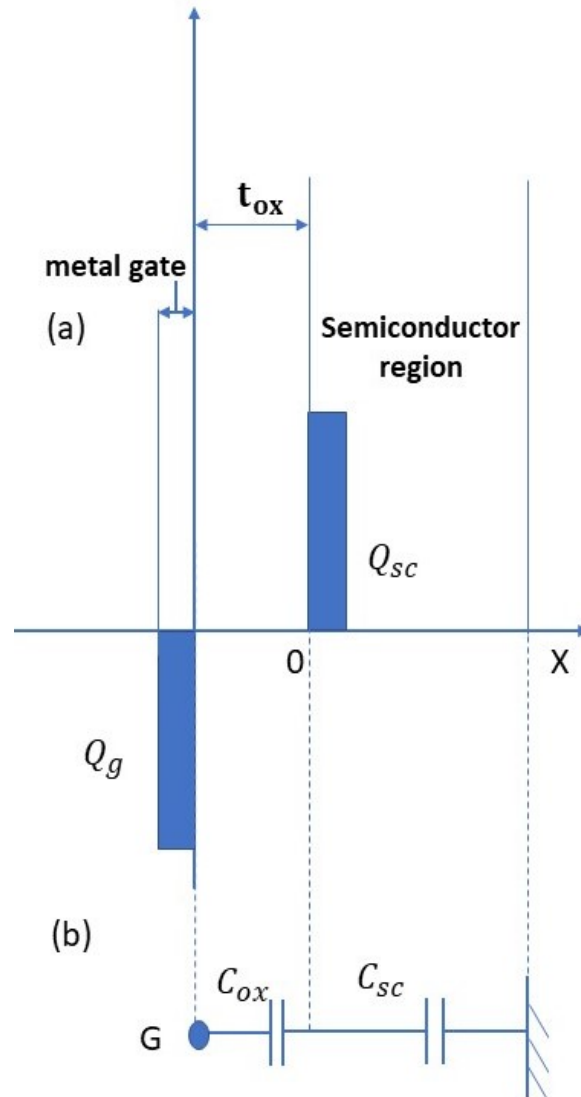
Figure 2.2: (a) Charge balance in metal oxide semiconductor where t_{ox} is the oxide thickness, metal gate thickness indicated and semiconductor region shown. Q_g is the charge in the metal gate. Q_{SC} is the charge in the p-channel of semiconductor material. These are equal $Q_{SC} = Q_g$. (b) Equivalent circuit diagrams for MOS capacitor in accumulation mode where C_{ox} is the oxide capacitance and C_{SC} is the semiconductor capacitance in series.

Calculation for depletion width (W_D) and drain current (I_{SD})

For a p-type MOSFET in inversion mode, the electron concentration at the surface (n_s) can be linked to the intrinsic concentration of carriers (n_i) by the equation

$$n_s = n_i exp[\frac{\Phi_s - \Phi_b}{k_B T}]$$

(2.4)

where

Φ_s = surface potential

Φ_b = bulk potential

k_B = Boltzmann constant

T = Temperature

$\Phi_s - \Phi_b$ is the measure of band bending at the surface due to applied potential. Φ_s also depends on acceptor concentration (N_A) and to the depletion width (W_D) by

$$\Phi_s = \frac{e^2 N_A W_D^2}{2\varepsilon_0\varepsilon_r}$$

(2.5)

where

e = charge of an electron

ε_0 = permittivity of free space

ε_r = relative permittivity By rearranging equation 2.5, we obtain equation 2.6 for finding the depletion width.

$$W_D = \sqrt{\frac{2\Phi_s\varepsilon_0\varepsilon_r}{e^2 N_A}}$$

(2.6)

So to find the depletion width (W_D) for an ideal MOS capacitor on p-type Si with $N_A = 10^{16}$ cm^{-3}, n_i as 1.5 x 10^{10} cm^{-3} and ϕ_s = 0.347 V. These values are substituted in equation 2.6 to obtain W_D as 0.301 μ m.

The drain current of a MOSFET in the linear region is given by

$$I_{D,lin} = \frac{\mu_p C_{ox}}{2}\frac{W}{L}[2(V_{GS} - V_{th})V_{DS} - V_{DS}^2]$$

(2.7)

where

μ_p = mobility of majority carriers

C_{ox} = oxide capacitance

W = width of the device

L = length of the device

V_{GS} = gate voltage
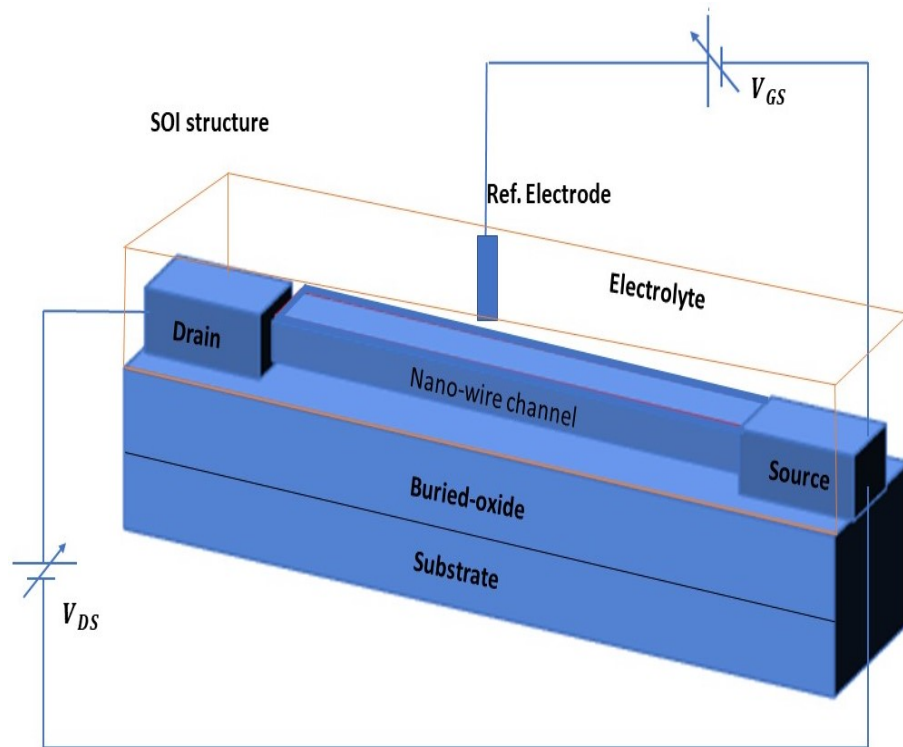
Figure 2.3: Nanowire ISFET (meaning Ion sensitive field effect transistor). Its structure consists of a Si substrate at the bottom. On top of it is the buried oxide (BOX). A nanowire on top of BOX has the source, channel and drain. The nanowire is immersed in electrolyte limited in our simulations to the space enclosed by the transparent orange line. Gate voltage V_{GS} is provided by the reference electrode and the drain to source voltage is given by V_{DS}.

V_{th} = threshold voltage

V_{DS} = drain to source voltage

The drain current of a MOSFET in the saturation region is given by

$$I_{D,sat} = \frac{\mu_p C_{ox}}{2} \frac{W}{L} [2(V_{GS} - V_{th}^2)] \tag{2.8}$$

To find the drain current I_{SD} for voltages V_D =1 V, V_G = 2 V, V_S = 4 V and V_{th} = -0.8 V having $\mu_p \, C_{ox}$ = 200 μA/V^2, W = 10 μm, L = 2μm substitute these values in equation 2.8. The drain current is -360 μA.

2.1.2 ISFETs

In 1970, Bergveld developed an ion-sensitive Field-Effect Transistor (ISFET) which is used for ion detection in a chemical environment [20]. Fig. 2.3 shows a schematic diagram of a JL-ISFET junctionless ion-sensitive field effect transistor, which is a FET immersed in the electrolyte and the gate voltage is provided by the reference electrode. Ion sensitive field effect transistor as the
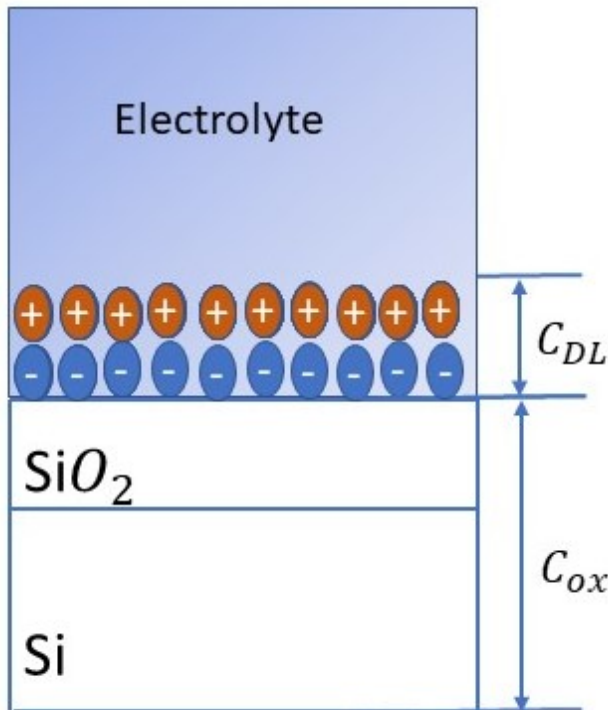
Figure 2.4: This figure shows the double layer formation in an ion-sensitive field effect transistor. The Silicon channel is at the bottom, with oxide SiO_2 on top of it. The negative ions having blue colour are due to the deprotonation of silanol. The orange positive ions are H^+ ions in electrolyte attracted to the deprotonated silanol groups. C_{DL} is the double layer capacitor. C_{ox} is the capacitance due to oxide is shown as it dominates over the semiconductor capacitance C_{SC}.

name suggests is sensitive to the ions present that can be adsorbed to the sensor liquid interface. Oxides were first used to sense the pH of the solution which is the concentration of protons in the solution or the $[H^+]$ ions. Depending on the $[H^+]$ ions in the electrolyte, there is a chemical equilibrium in the oxide surface that modulates the drain current in the ISFET.

Capacitance Model

The ions being adsorbed change the configuration of the charges in the electrolyte resulting in the formation of a double layer of charges in the liquid interface of the ISFET. The first layer consists of ions adsorbed onto the oxide surface due to chemical interactions like deprotonation. The second layer consists of ions attracted to the first layer for e.g. $[OH^-]$ ions. This double layer is shown in fig. 2.4.

The charge distribution is shown in fig. 2.5 (a). Q_{DL} is the charge formed in the electrolyte due to the formation of the double layer. Q_{bio} is the charge on the surface of the oxide. Q_{sc} is the charge due to the semiconductor. The total charge on the oxide surface Q_{bio} is given by equation 2.9.
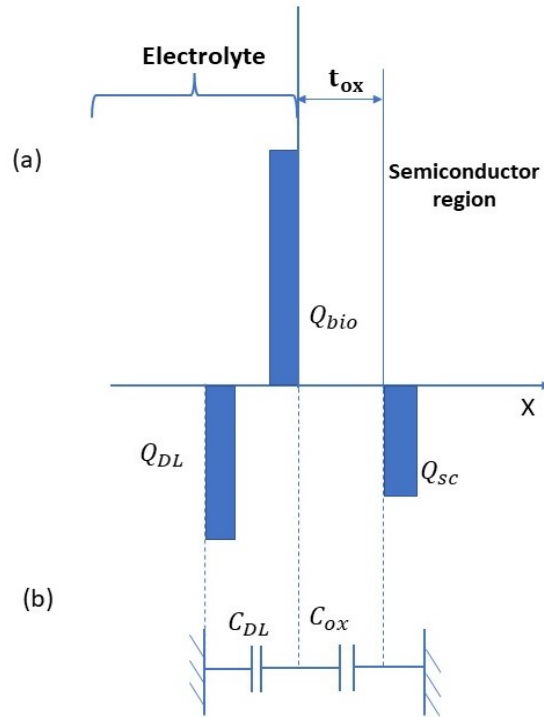
Figure 2.5: (a) Charge balance in ion sensing field effect transistor where t_{ox} is the oxide thickness, electrolyte region indicated and semiconductor region shown. Q_{DL} is the charge in the double layer. Q_{sc} is the charge in the p-channel of semiconductor material. (b) Equivalent circuit diagrams for ISFET capacitor where C_{ox} is the oxide capacitance and C_{DL} is the double layer capacitance in series.

$$Q_{bio} = Q_{DL} + Q_{sc} \tag{2.9}$$

where Q_{DL} is the charge due to double layer and Q_{sc} is the charge due to semiconductor. Fig. 2.5 (b) shows the equivalent capacitance for the ISFET. The C_{ox} will be due to oxide capacitance only hence represented by C_{ox}. The equivalent capacitance (C_{eq}) is given by oxide capacitance (C_{ox}) in series with double layer capacitance (C_{DL}) as shown in equation 2.10.

$$\frac{1}{C_{eq}} = \frac{1}{C_{ox}} + \frac{1}{C_{DL}} \tag{2.10}$$

The charge Q_{bio} on the oxide surface leads to the formation of surface potential (Ψ_0). Hence, we need to determine the surface potential (Ψ_0) as it affects the drain current. Equation 2.9 can be written as shown below:

$$Q_{bio} = Q_0 exp(\frac{-zq\Psi_0}{2kT}) + C_{ox}\Psi_0 \tag{2.11}$$

where
Ψ_0 = surface potential

z = number of valencies

q = charge of an electron

k = Boltzmann constant

T = temperature

In order to determine the surface potential Ψ_0, equation 2.11 can be rearranged to obtain equation 2.12.

$$\Psi_0 = \frac{2kT}{zq} ln \frac{Q_{bio}}{Q_0} \tag{2.12}$$

and $Q_0 = \sqrt{(2kT\varepsilon_0\varepsilon_r N_{avg} I_0)}$ where

ε_0 = permittivity of free space

ε_r = relative permittivity

N_{avg} = Avogadro's constant

I_0 = Ionic strength

In order to determine the surface potential Ψ_0 from equation 2.12, Q_{bio} and I_0 must be known.

2.2 BioFETs

A BioFET structure is the same as that of an ISFET but with functionalised layer (receptors) on top of the gate oxide and having the target molecules in solution. These chemically function-alised layers (receptors) can detect biomolecules(targets) in an aqueous solution (electrolyte) selectively so as to covalently bond the receptor-target or protein-peptide interaction as shown in figure 2.6. The V_{GS} is given through the reference electrode immersed in an electrolyte.

2.2.1 Four elements in BioFETs

BioFET has four main elements as described below:

(i) Media: The media is the electrolyte. It represents the media in which the target molecules need to be detected. In our case, the electrolyte is water and salt (NaCl).

(ii)Bio-interface: This is the electrolyte oxide interface referred to here.

(iii) Transducer: Transducer is the p-type channel where the charges present in the electrolyte bring about the change in drain current. Hence we can note down the number of charges present in the electrolyte.

(iv) Data Collector: A data collector is a computer used to store the data for the changes in drain current with respect to the varying pH of the electrolyte.
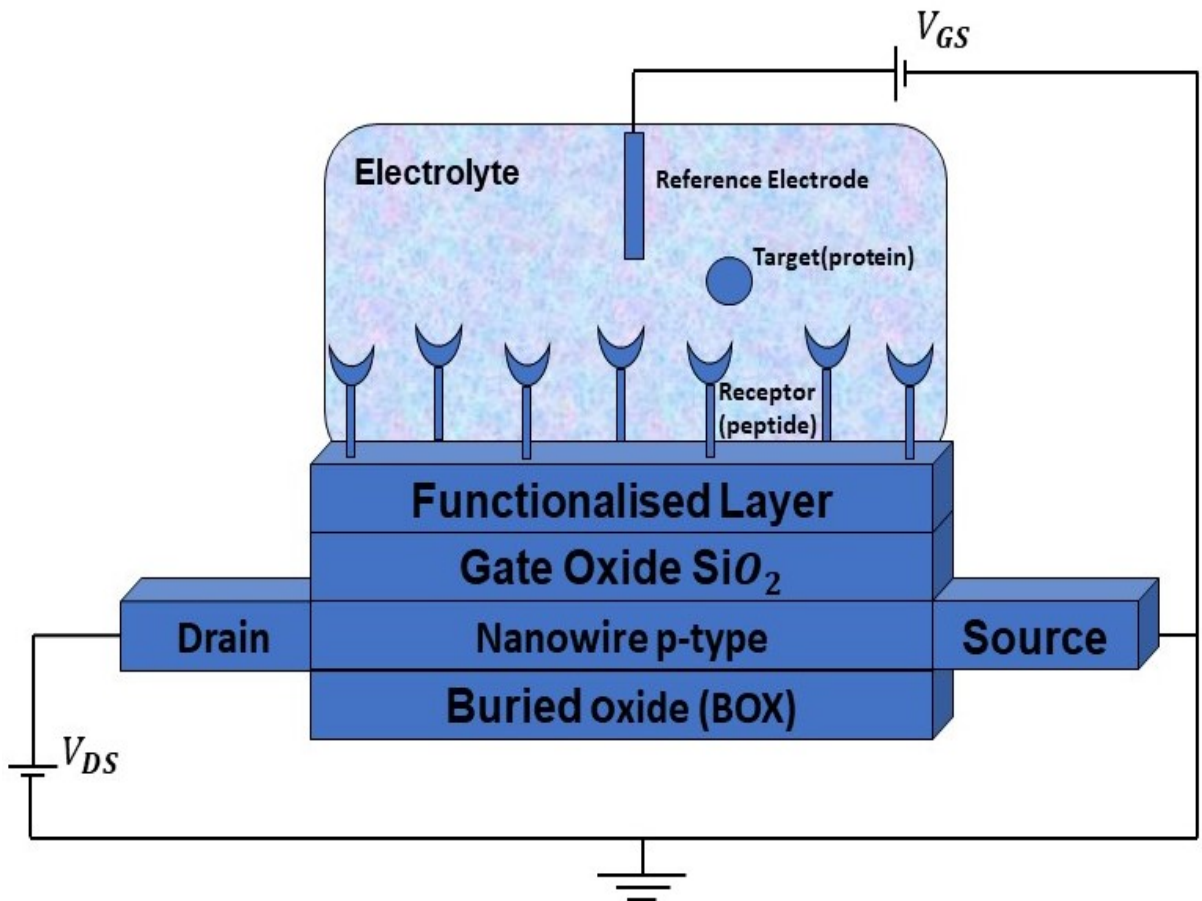
Figure 2.6: BioFET structure consists of an additional functionalised layer on top of the gate oxide. In our case, the functionalized layer can be 3-Amino propyl triethoxysilane (APTES)/Amino acid and the gate oxide is SiO_2. The APTES/Amino acid linkage at SiO_2 /electrolyte interface brings about changes from the Silanol group to the amine group that can now accept or release protons. The target molecule is the biomolecule to be detected by the Biosensor. This whole structure along with receptor and target molecules is a Biosensor.

2.2.2   Label-free detection of charged macromolecules

There are two ways to detect the target molecules shown in fig. 2.6:

(i)Label sensing

The target molecules are captured by the receptors on the nano-biosensors. Instead of the target molecule moving alone an extra probe molecule or label molecule like an optical tag is attached. This is referred to as label sensing [21]. The receptors could be a DNA molecule. The target molecule could also be another segment of the DNA molecule. Receptor and target molecules attach to each other because of Adenine, Thymine, Guanine and Cytosine (ATGC) these are the four nitrogenous bases that comprise the DNA (Deoxyribonucleic Acid), as A goes with T and G goes with C. This tag is inactive when the target molecule is moving on its own but becomes active when it attaches itself. When light is shined on it, it will be lit up to tell that something is captured [9, 10]. In this method, a secondary marker is used to indicate this configuration. This method does not rely on intrinsic properties of the biomolecule (or the targets) [21, 22]. The drawback of label sensing is that it requires DNA labelling [21]. Major limitations of labelled sensing include problems such as: (i) time-consuming preparation steps; (ii) non-native signal interference; (iii) unsuitability for in-situ observation; (iv) necessity of sophisticated, high-cost equipment; and (v) need for specialized technicians and motivated researchers to keep improving or combining principles in detection methods [18].

(ii)Label-free sensing [16]. Hence a label-free detection technique using nano-transistors is preferred. Its basic detection scheme is based on the intrinsic characteristics (for example charge distribution, electron affinity and mass of the biomolecule) of DNA such that an electronic nano-biosensor can detect it [17]. Label-free sensing provides more reliable dynamic constant parameters that involve molecular interactions. From another perspective, detection methods that require no labelling are easily reproducible. Thus, these methods hold great potential to be further developed into a unique class of microarray analytical techniques [18].

2.2.3   Working principle

This section aims to describe the operation of a bioFET. Since the bioFET is a junctionless field effect transistor, there is current (I_{SD}) flowing in the device even when $V_{GS} = 0V$ as a channel already exists or the channel formation is already there. As the positive gate voltage is increased the drain current I_{SD} (holes) becomes less [23]. This is due to the fact that the depletion width (W_D) increases leaving less area for the drain current to flow. From this, we can draw a conclusion that when the depletion width increases, the drain current decreases as shown in fig. 2.7 (a) and fig. 2.7 (b).

The semiconductor material is p-type Silicon that gets depleted on the application of the electric field which can be gate voltage (V_{GS}), accumulated charges due to changes in the pH of the electrolyte and surface functionalization. The important terminology related to the working
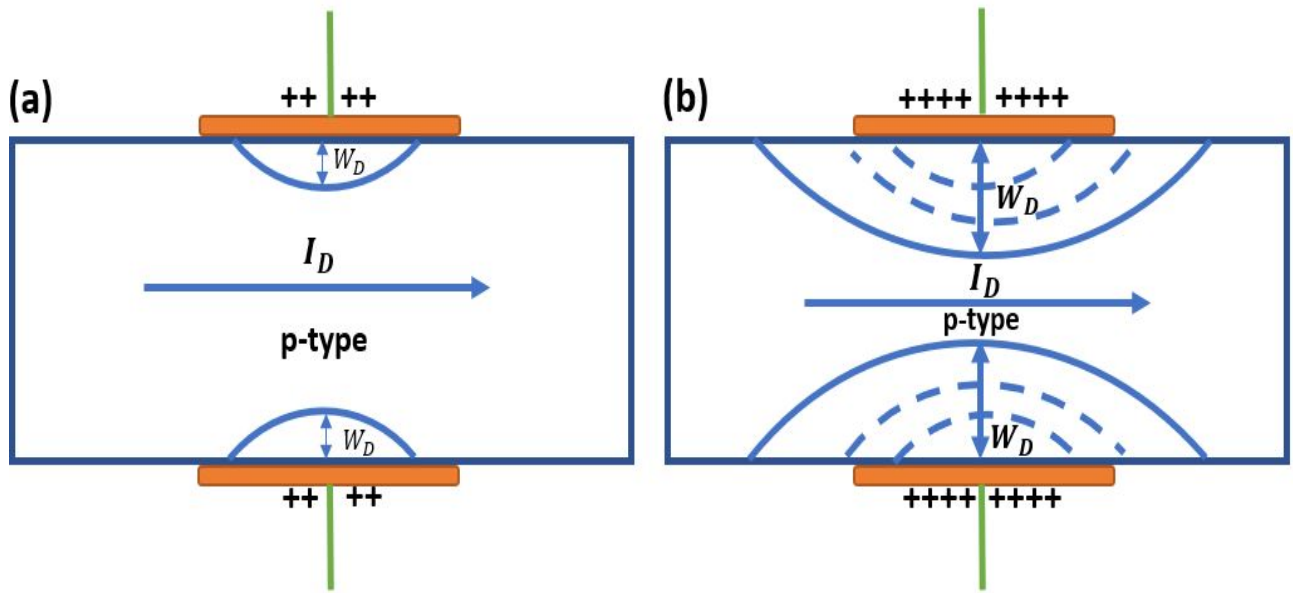
Figure 2.7: Schematic diagram explaining the effect of positive gate charges on the depletion width W_D (a) shows the drain current when the device is close to flat band condition meaning full device channel contributes to hole conduction (b) shows partial depletion which has now less area for the hole conduction and is closer to full depletion mode

of BioFETs is given below: (i) Threshold Voltage: The threshold voltage V_{th} is defined as the gate voltage V_{GS} required to be applied which will cause the depletion widths (W_D) on both sides to collide and there will be no drain current (I_{SD}) [24]. Hence turning the device off. (ii)Pinch-off voltage: The Pinch-off voltage (V_{pinch}) is the gate voltage applied (V_{GS}) at which the drain current (I_{SD}) saturates (meaning becomes constant irrespective of the gate voltage applied).To obtain full depletion in the device, better gating mechanisms are advised such as double gated, tri-gate and gate all around nanowire JLFET.

2.2.4 Mass transport

This section discusses the mass transport of analytes in electrolytes. This mass transport of analytes is analyzed for the different structures of biosensors. The analytes include the proton (having high diffusion constants) and DNA, protein (having lower diffusion constants). The different structures considered for biosensors are - planar, nanowire, nanoarray and FinFET as shown in figure 2.8.

As the pH is varied from higher pH to lower pH, the protons get adsorbed into the oxide sensing surface creating a surface gradient. The time required for analytes (protons in this case) to give a stable electrical signal is the settling time. The efficiency of a sensor depends on the settling time. Initially, FET biosensors were fabricated as large planar architectures. They permitted only one-dimensional diffusion of the analytes towards the sensor's surface. In a planar sensor, the mass transport occurs in 1D while in an NW happens in the two directions (hemi-
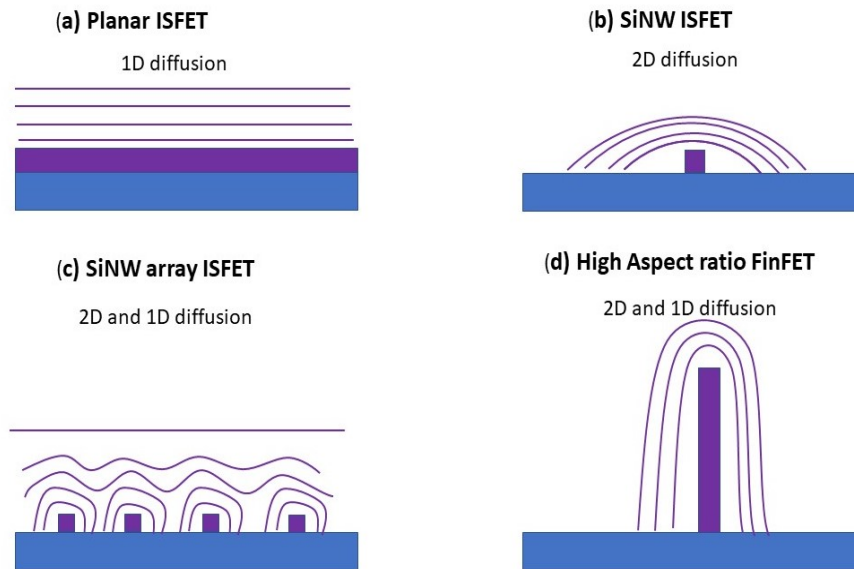
Figure 2.8: Schematic diagram representing 1D and 2D diffusion for different structures (a) shows traditional planar ISFET having parallel lines to sensor surface as a gradient. Diffusion occurs in 1D perpendicular to the surface (b) shows Si nanowire ISFET having parallel lines to the axis of the sensor as a gradient. Diffusion occurs in 2D perpendicular to the surface. (c) shows the nanowire array showing mixed behaviour of both (a) and (b). As it behaves as 2D diffusion for higher concentration and 1D diffusion for lower concentration (d) shows a high aspect ratio ISFET where diffusion goes from 1D to 2D as opposed to 2D to 1D in (c)

cylindrical) perpendicular to the NW, providing several orders of magnitude better detection limits than traditional planar FETs. Figure 2.8(b) has a much shorter settling time as compared to figure 2.8(a). For the nanowire array shown in figure 2.8 (c), since at higher concentrations the diffusion occurs from close to the surface the settling time is less compared to a lower concentration where diffusion occurs from far off. This decreases the overall efficiency of nanowire arrays. The settling time is small in high and low concentrations since the analytes are protons having fast diffusion. In the case of analytes such as DNA or protein having slow diffusion or low diffusion constants, we need another structure as shown in figure 2.8 (d). For initial higher concentrations, it will diffuse from near to the surface behaving as 1D diffusion. And for the lower concentrations, since the diffusion takes place from further away, 2D diffusion is possible by high aspect ratio FinFET. Thus the last structure provides an advantage of measuring slow diffusing analytes at low concentrations.

2.3   Biosensing challenges currently faced by the BioFET

The challenge is to miniaturise the original protein sensing so that it can deal with very low concentrations of the target molecules in biological conditions. In the absence of the possibility to amplify the target molecules, sensors must be reliable. The superior sensitivity of NWs is due

to a more effective 3D gating and the diffusion mechanism of low concentrations.

However, despite their superior sensitivity, NWs have not reached clinical applications because of their unreliability [25]. This unreliability comes as a result of the difficulty in transferring the BioFET from laboratory to industry. The issues faced are a lower signal-to-noise ratio, diffusion and difficulty to implement the functionalization [26] [27]. Also, the efficiency of the BioFET to detect the target molecules at their physiological condition along with the hurdles developed due to defects in the fabrication and functionalization process.

The challenges faced by BioFET as summarized below in bullet points:

- Develop an understanding of the charges developed at the oxide/Electrolyte interface (Or Solid/Solution interface)

- Functionalization of BioFET with receptors such as APTES or linkers like PEG is difficult

- Low signal-to-noise ratio

- Detection of target molecules(for e.g. proteins) in physiological conditions

This thesis aims to create a digital twin of the BioFET wherein these issues can be substantially addressed as it would consider the optimization of the whole biosensing process. Our focus will be on the third element of the BioFET which is a bio-interface, this is further integrated with the whole device structure. We address the reliability issue with a new label-free FET architecture based on high height-to-width aspect-ratio FET [25]. This geometry improves the signal, minimising the footprint while optimising the design for mass transport towards the sensor. These FinFETs have the potential to solve the issues of noise faced by nanosensors. The ISFET device considered for this project has a high aspect ratio meaning the height-to-width ratio is high (approx. H: W = 10) as this will allow high adsorption of analytes as the surface area increases from one dimension to two dimensions [25]. Large aspect ratio FinFETs allowed an increase in the total surface area thereby improving the reliability of biofunctionalization and the sensitivity of the sensor [25].

First, we start with analytical simulations which simulate the solid/solution bio-interface. The different models we use to understand this solid/solution interface are the Site dissociation model, the Gouy-Chapman model and the Gouy-Chapman-stern layer model. The simulated interface is then integrated with the FET device for biosensor simulations.

In order to improve the device design based on ISFET technology, we have performed device simulations based on Synopsys Technology Computer-Aided Design (TCAD) and MATLAB. Our models consider ISFET at various pH values. Also, simulations based on the combination of analytical simulations and numerical simulations have been successfully done.

Chapter 3

Analytical Models

Analytical simulations can be used to model the material properties and the behaviour of electronic devices. In this chapter, we will first go over the creation and implementation of analytical models that predict the performance of ISFETs with increasing interface complexity. And how these models have been modified to meet the demand of simulating increasing interface complexity. Our analytical models are implemented in a MATLAB simulation environment. A methodology has been developed in MATLAB to solve these models and its detailed explanation is mentioned.

This chapter is based on the publication by Dhar, R., Kumar, N., Garcia, C.P. and Georgiev, V., 2022. Assessing the effect of Scaling High-Aspect-Ratio ISFET with Physical Model Interface for Nano-Biosensing Application. Solid-State Electronics, p.108374. I did MATLAB programming for section 3.3 and 3.3.1. Also, plotted the graphs and did the writing.

3.1 Site-Dissociation Model

The development of the analytical models in this work starts with the Site-Dissociation Model [28]. This model incorporates the influence of the chemical affinity of the atoms at the sensor interface with the ions contained in the solution to describe the charging of the sensor surface. To illustrate the model, we will work mostly with sensors with oxide surfaces that have affinities mainly for the hydrogen ions (protons) in the electrolyte. Depending on the concentration of hydrogen ions in the electrolyte, the interactions of such ions with the oxide surface vary resulting in different surface charges. As a result of these interactions, we will calculate a pH or acidity response of the sensor in terms of variations of the surface potential at the dielectric/electrolyte interface, which can be transduced by the direct output of the sensor (output current) or by the transconductance. The model can be then extended by analogy to other chemical interfaces, for example, amino groups that also have an affinity for protons, or other groups with a special affinity with other ions in the electrolyte.

The surface charge density in the sensor interface σ_{0-SD} is derived by the difference between the fraction of positive and negative charges (Θ^+ and Θ^-, respectively), multiplied by the total number of sites per unit area (cm^{-2}) (N_s) and the unitary charge (q):

$$\sigma_{0-SD} = qN_s(\Theta^+ - \Theta^-) \tag{3.1}$$

Considering an oxide represented by MO_x (where M can be a semiconductor or a metal such as Si, Hf or Ta, and x is the conjugation state of the compound) is in contact with the electrolyte (containing water, salt and possible other analytes) there is a chemical equilibrium between the concentration of the hydrogen ions present in the electrolyte and the protonation or deprotonation of such oxide groups at the sensor interface. Using SiO_2 as an example, when it comes in contact with the electrolyte, Silanol groups (SiOH) are formed which undergo deprotonation and protonation as shown below:

De-protonation:
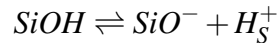
$$SiOH \rightleftharpoons SiO^- + H_S^+$$

$$\frac{\left[SiO^-\right]\left[H_S^+\right]}{\left[SiOH\right]} = K_b \tag{3.2}$$

Protonation:
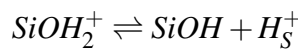
$$SiOH_2^+ \rightleftharpoons SiOH + H_S^+$$

$$\frac{\left[SiOH\right]\left[H_S^+\right]}{\left[SiOH_2^+\right]} = K_a \tag{3.3}$$

where $[H_S^+]$ is the concentration of hydrogen ions close to the sensor surface and $[SiOH]$, $[SiO^-]$ and $[SiOH_2^+]$ are the neutral, deprotonated and protonated surface concentration groups at the sensor interface, respectively. K_a, and K_b are the chemical affinities of the material for protons, which in many cases can be known beforehand and hence represent a parameter that can be later adjusted phenomenologically. The net surface charge density from equation 3.1 can be re-written as:

$$\sigma_{0-SD} = qN_s \left(\left[SiOH_2^+ \right] - \left[SiO^- \right] \right)$$

Equations 3.2 and 3.3 can be used to clear $[SiO^-]$ and $[SiOH_2^+]$:

$$\left[SiO^- \right] = K_b \frac{\left[SiOH \right]}{\left[H_S^+ \right]}$$

$$\left[SiOH_2^+ \right] = \frac{\left[SiOH \right] \left[H_S^+ \right]}{K_a}$$

The net surface charge density obtained by the Site-Dissociation model can then be written as follows:

$$\sigma_{0-SD} = qN_s \left(\left[SiOH_2^+ \right] - \left[SiO^- \right] \right)$$

$$\sigma_{0-SD} = qN_s \left(\frac{\left[SiOH \right] \left[H_S^+ \right]}{K_a} - K_b \frac{\left[SiOH \right]}{\left[H_S^+ \right]} \right)$$

$$\sigma_{0-SD} = q \left[SiOH \right] N_s \left(\frac{\left[H_S^+ \right]}{K_a} - \frac{K_b}{\left[H_S^+ \right]} \right) \tag{3.4}$$

The chemical affinities K_a and K_b, like pH, can be written in the logarithmic form to express their chemical activity as shown below:

$$pK_a = -log(K_a)$$

$$pK_b = -log(K_b)$$

where the values of K_a and K_b are obtained from experiments or 1st principles.
$[SiO^-]$, $[SiOH]$ and $[SiOH_2^+]$ together sum to 1 as shown below

$$\left[SiO^- \right] + \left[SiOH \right] + \left[SiOH_2^+ \right] = 1$$

$$\frac{K_b \left[SiOH \right]}{\left[H_S^+ \right]} + \left[SiOH \right] + \frac{\left[SiOH \right] \left[H_S^+ \right]}{K_a} = 1$$

$$\left[SiOH\right]\left(\frac{K_b}{\left[H_S^+\right]} + 1 + \frac{[H_S^+]}{K_a}\right) = 1$$

$$\left[SiOH\right] = \frac{1}{\left(1 + \frac{\left[H_S^+\right]}{K_a} + \frac{K_b}{\left[H_S^+\right]}\right)} \tag{3.5}$$

Substitute $\left[SiOH\right]$ from above equation 3.5 in equation 3.4 to obtain the equation below:

$$\sigma_{0-SD} = qN_s \frac{\left(\frac{\left[H_S^+\right]^2 - K_a K_b}{K_a\left[H_S^+\right]}\right)}{\left(\frac{K_a\left[H_S^+\right] + \left[H_S^+\right]^2 + K_a K_b}{K_a\left[H_S^+\right]}\right)}$$

Or the above equation can also be written as

$$\sigma_{0-SD} = qN_s \frac{H_s^2 - K_a K_b}{H_s^2 + K_a H_s + K_a K_b} \tag{3.6}$$

where H_s = concentration of H^+ ions on the surface

The surface charge density (σ_{0-SD}) depends thus on the total number of sites (N_S), the chemical affinity (K_a, K_b) for protons of the dielectric layer and the concentration of H^+ ions on the dielectric surface (H_S). Different dielectrics can be used for ISFET device fabrication. For example, the dielectric can be SiO_2, HfO_2, Al_2O_3 or Ta_2O_5. A metal M of the dielectric (in this case Si, Hf, Al, Ta) would now form MOH. Also, the proton affinity can be replaced by other interactions with other solvated ions using the proper equilibrium equations.

The oxide layer can be functionalized with different layers above it. Different materials can be functionalization layers that can be engineered depending on their affinity to the ions or analytes in the electrolyte to be detected. In our case, we can exemplify the effect of a functionalisation layer, using APTES (3-Aminopropyl)triethoxysilane layer leading the formation of a surface charge density to be represented by $\sigma_{0-SD-APTES}$.

The surface charge density σ_{0-SD} can be derived for different materials functionalized on the oxide surface.

APTES has a structure as shown in fig. 3.1 that consists of Si in the center bonded by -OCH_2CH_3 for three valence electrons and another branch consisting of -$(CH_2)_3NH_2$ bonded to the fourth valence electron. It is important to understand how the device structure looks for APTES deposition on top of gate oxide (SiO_2). In reality, deposition of APTES leaves many gaps in silanol groups originating in the SiO_2, but also on the APTES, as often some of the branches of APTES do not react with silanol groups. Hence an idealisation is used for the system calculation where the number of silanol and APTES groups are adjusted phenomenologically. This is shown in fig. 3.2 [29]. The linkage of APTES at SiO_2 causes only protonation as there
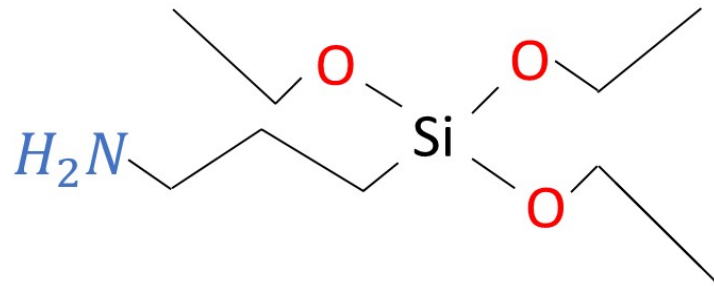
Figure 3.1: Schematic diagram showing APTES structure having chemical formula $C_9H_{23}NO_3Si$. This structure consists of Si in the centre covalently bonded by $-[OC_2H_5]$ for three of its valence electrons and the fourth valence electron is bonded by $-[C_3H_6NH_2]$
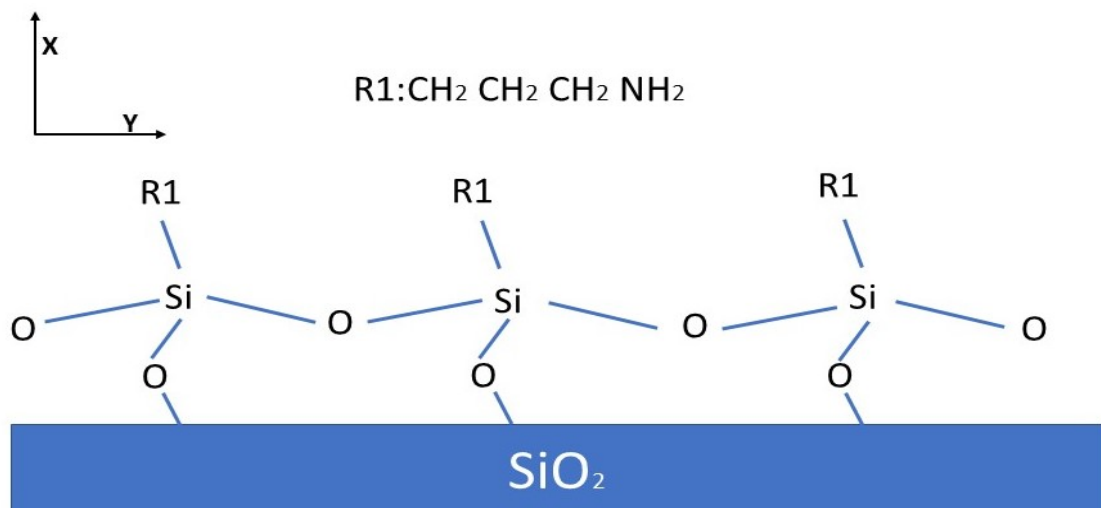
Figure 3.2: Schematic diagram is shown for deposition of APTES over gate oxide SiO_2. It can be seen that the two valence electrons of APTES are bonded with the neighbouring valence electrons of APTES. One valence electron is bonded with gate oxide. The fourth valence electron bonded with the amine group undergoes protonation.

are only amine groups (-NH_2) that are free to react. Hence only the side branch denoted by R1 in fig. 3.2 is discussed as the interaction with the electrolyte/solvent is happening in only that part.

Protonation:
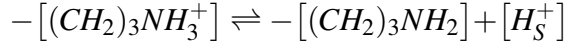
$$-\left[(CH_2)_3NH_3^+\right] \rightleftharpoons -\left[(CH_2)_3NH_2\right]+\left[H_S^+\right]$$

Basic dissociation constant $K_{b-APTES}$ is given by

$$K_{b-APTES} = \frac{-\left[(CH_2)_3NH_2\right]\left[H_S^+\right]}{-\left[(CH_2)_3NH_3^+\right]}$$

after rearranging

$$-\left[(CH_2)_3NH_3^+\right] = \frac{-\left[(CH_2)_3NH_2\right]\left[H_S^+\right]}{K_{b-APTES}}$$

The net surface charge density for APTES as per the site-binding model is given below:

$$\sigma_{0-SD-APTES} = qN_n(\Theta^+ - \Theta^-)$$

where N_n is the total number of sites for APTES

$$\sigma_{0-SD-APTES} = qN_n(-\left[(CH_2)_3NH_3^+\right] - 0)$$

$\Theta^- = 0$ as there is no deprotonation. Therefore,

$$\sigma_{0-SD-APTES} = qN_n\left(\frac{-\left[(CH_2)_3NH_2\right]\left[H_S^+\right]}{K_{b-APTES}}\right) \tag{3.7}$$

As APTES has only $K_{b-APTES}$ value, $pK_{b-APTES}$ is given by $pK_{b-APTES} = -log(K_{b-APTES})$ = 3.63 [30] and it is very different from SiO_2 material described previously [28]. Again, the sum of protonated amine groups and the APTES as shown below:

$$-\left[(CH_2)_3NH_3^+\right] + -\left[(CH_2)_3NH_2\right] = 1$$

$$\frac{-\left[(CH_2)_3NH_2\right]\left[H_S^+\right]}{K_{b-APTES}} + -\left[(CH_2)_3NH_2\right] = 1$$

$$-\left[(CH_2)_3NH_2\right]\left(\frac{[H_S^+]}{K_{b-APTES}} + 1\right) = 1$$

$$-\left[(CH_2)_3NH_2\right] = \frac{1}{\left(\frac{[H_S^+]}{K_{b-APTES}} + 1\right)} = \frac{K_{b-APTES}}{[H_S^+] + K_{b-APTES}}$$

$$-\left[(CH_2)_3NH_2\right] = \frac{K_{b-APTES}}{[H_S^+] + K_{b-APTES}} \tag{3.8}$$

Substitute equation 3.8 in the equation 3.7 to obtain surface charge density for APTES given by Site-Dissociation model $\sigma_{0-SD-APTES}$, given by equation 3.9 as follows:

$$\sigma_{0-SD-APTES} = qN_n \left(\frac{[H_s^+]}{[H_s^+] + K_{b-APTES}} \right) \tag{3.9}$$

$\sigma_{0-SD-APTES}$ represents the surface charge density for the area covered with APTES on the sensor surface. In reality, there is a possibility of the area not being covered completely with APTES due to fabrication defects. In that case, equation 3.10 is used to describe the sensor surface. When a certain percentage of SiO_2 and a certain percentage of APTES are considered in direct contact with electrolyte or when APTES is not considered in 100% contact with electrolyte $\sigma_{0-SD-Total}$ is the surface charge density.

$$\sigma_{0-SD-Total} = \sigma_{0-SD} + \sigma_{0-SD-APTES}$$

$$\sigma_{0-SD-Total} = q(N_s - N_n) \frac{H_s^2 - K_a K_b}{H_s^2 + K_b H_s + K_a K_b} + qN_n \frac{H_s}{H_s + K_{a-APTES}} \tag{3.10}$$

From equation 3.10, it can be seen that the surface charge density for the device with functionalized layers depends on N_n and K_a of the additional chemical groups. In the surface charge density's of σ_{0-SD}, $\sigma_{0-SD-APTES}$ and $\sigma_{0-SD-Total}$, assumption of homogenous distribution of charges is made. Homogenous means the deposited layer has the same type of uniformly distributed material throughout the sensor surface above the oxide layer. There are limits to this assumption in the analytical model which includes that the model can determine only the Ψ_0 and Ψ_ξ. But not the potential between them. The MATLAB code for the Site-Dissociation model is mentioned in Appendix D.6.

Our aim is to find the pH. This depends on the logarithm of the inverse of hydrogen ion concentration [31]. The concentration of hydrogen ions can be found from equations 3.6,3.9 and 3.10. But the surface charge density's (σ_{0-SD}, $\sigma_{0-SD-APTES}$ and $\sigma_{0-SD-Total}$) needs to be known beforehand in order to find $[H_s^+]$ or the pH. In order to do this, first the oxide surface potential (Ψ_0) needs to be measured experimentally. The experimentally measurable quantity (Ψ_0) needs to be related to the surface charge density ($\sigma_{0-SD-Total}$). This can be done using Maxwell's equations as shown below:

We know that the electric field (E) in any medium is given as

$$E = -\nabla . \Psi_0$$

Taking the gradient of electric field (E), we can obtain equation 3.11 which is Maxwell's equation:

$$\nabla . E = \frac{\sigma_{0-SD-Total}}{\varepsilon} \tag{3.11}$$

where $\varepsilon = \varepsilon_0.\varepsilon_r$. Then Poisson's equation 3.12 is given below as:

$$\nabla.E = -\nabla^2\Psi_0 = -\frac{\partial^2\Psi_0}{\partial x^2} = \frac{\sigma_{0-SD-Total}}{\varepsilon} \tag{3.12}$$

Generally, Poisson's equation is given in three dimensions. But in our case, as seen in equation 3.12 only the x-direction is considered. It can be seen from fig. 3.2, the direction of the X axis. This model has been applied in one direction only in this thesis. This is because the electric field (E) is developed from the charges on the oxide surface towards the bulk of the electrolyte considering the uniform charge distribution with a negligible variation in the high-dielectric constant of the electrolyte. That is the x-direction. In the YZ plane, there would be some type of charges which doesn't lead to the formation of the electric field. From equation 3.12, the surface charge density $\sigma_{0-SD-Total}$ is determined from the experimentally measured value of Ψ_0. The experimentally measured surface potential Ψ_0 substituted in equation 3.12 gives σ_{0-SD}. This surface charge density's (σ_{0-SD}, $\sigma_{0-SD-APTES}$ and $\sigma_{0-SD-Total}$) substituted in equations 3.6,3.9 and 3.10 gives $[H_s^+]$. The problem is that the Site-Dissociation model does not define how $[H_s^+]$ is related to determining the pH in the bulk of electrolytes. The spatial dependence needed to have a surface potential that is not zero comes with the next model. Hence, we move on to the next model which is the Gouy- Chapman model.

3.2 Gouy-Chapman Model

The electrolyte on the gate oxide SiO_2 leads to protonation and deprotonation of Silanol SiOH groups depending on the pH of the electrolyte. This develops an oxide surface potential (Ψ_0). The concentration of hydrogen ions fades away from the oxide surface due to the charge repulsion. This concentration is given by the Boltzmann equation, which is expressed in equation 3.13, showing the relation between the concentration of ions in the surface $[H_s]$ and in the bulk $[H_B]$, that depends on the surface potential (Ψ_0) built:

$$[H_s] = [H_B]e^{\frac{-q\Psi_0}{k_B T}} \tag{3.13}$$

The Boltzmann equation 3.13 can also be written as

$$pH_S = pH_B + \frac{q\Psi_0}{2.3k_B T} \tag{3.14}$$

The surface charge density will vary for every pH of the electrolyte (pH_B) [28]. Connecting equation 3.13 with equation 3.10 gives the pH of the electrolyte bulk. The capability of any material to buffer the pH at the surface resulting in the charging of the surface can be defined as the intrinsic buffer capacity:

$$\frac{\delta\sigma_{0-GC}}{\delta pH_S} = -q\beta_{int} \qquad (3.15)$$

where

σ_{0-GC} = surface charge density obtained by Gouy-Chapman model

β_{int} = Intrinsic buffer capacity

Due to charge neutrality, an equal and opposite charge will be built up in the electrolyte side given by σ_{DL}. The charge neutrality occurs due to the free movement of ions in the solvent/electrolyte. The ability of the electrolyte to adjust the amount of stored charge as a result of a small change in electrostatic surface potential is the differential capacitance, C_{diff}

$$\frac{\delta\sigma_{DL}}{\delta\Psi_0} = -C_{diff} = -\frac{\delta\sigma_{0-GC}}{\delta\Psi_0} \qquad (3.16)$$

The intrinsic buffer capacity equation 3.15 divided by differential capacitance equation 3.16 gives:

$$\frac{\delta\Psi_0}{\delta pH_S} = \frac{-q\beta_{int}}{C_{diff}} \qquad (3.17)$$

Using the Boltzmann relation in equation 3.14 we can provide the Nerst relation that states the varying of the surface potential with the pH:

$$\frac{\delta\Psi_0}{\delta pH_B} = -2.3\frac{k_BT}{q}\alpha \qquad (3.18)$$

where pH_B is the pH of the bulk, α is the sensitivity factor which is a dimensionless quantity that employs the relation of the buffering and differential capacitances expressing the change of surface potential with the concentration of ions at the surface:

$$\alpha = \frac{1}{1+2.303\frac{k_BTC_{diff}}{q^2\beta_{int}}} \qquad (3.19)$$

The surface charge density (σ_{DL}) for the Gouy-Chapman model will be derived by the combination of the Boltzmann equation 3.13 and Poisson equation. It can be noticed in equation 3.19 that the values of alpha will range between 0 and 1.

Equation 3.13 shows how the concentration of H^+ ions varies from the oxide surface to the bulk. Since we are considering a 1:1 electrolyte the number of positive ions and negative ions are the same, we can write $n_+ = n_- = $ n.

For positive ions,

$$c_+ = c_0\exp\left\{\frac{-nq\Psi_0}{k_BT}\right\}.$$

For negative ions,

$$c_- = c_0\exp\left\{\frac{+nq\Psi_0}{k_BT}\right\}.$$

where c_0 is the concentration of ions in bulk. From Poisson's equation, we have

$$\frac{d^2\Psi_0}{dx^2} = -\frac{\sigma_{0-GC}}{\varepsilon} = \frac{-nF(c_+ - c_-)}{\varepsilon} \tag{3.20}$$

$$\frac{d^2\Psi_0}{dx^2} = \frac{-nFc_0(\exp\left\{\frac{nq\Psi_0}{k_BT}\right\} - \exp\left\{\frac{-nq\Psi_0}{k_BT}\right\})}{\varepsilon}$$

$$\frac{d^2\Psi_0}{dx^2} = \frac{2nFc_0}{\varepsilon}.sinh(\frac{nq\Psi_0}{k_BT}) \tag{3.21}$$

where $F = qN_A$ is the Faraday constant.

Using the form for the derivate of a square function, we can rewrite equation 3.21 as

$$\frac{d}{dx}(\frac{d\Psi_0}{dx})^2 = 2 * \frac{d\Psi_0}{dx}\frac{2nqN_Ac_0}{\varepsilon}sinh(\frac{nq\Psi_0}{k_BT}) \tag{3.22}$$

Integrating equation 3.22 between the surface and the potential at the bulk electrolyte, we can obtain a form for the surface potential given below

$$\int_0^\infty \frac{d}{dx}(\frac{d\Psi_0}{dx})^2 dx = \int_{\Psi_0}^0 2 * \frac{d\Psi_0}{dx}\frac{2nqN_Ac_0}{\varepsilon}sinh(\frac{nq\Psi_0}{k_BT})d\Psi_0$$

we will obtain

$$\frac{d\Psi_0}{dx_{atx=0}} = \sqrt{\frac{8c_0N_Ak_BT}{\varepsilon}}.sinh(\frac{nq\Psi_0}{2k_BT}) \tag{3.23}$$

Again the electric field (E) is given below as

$$E = \frac{Q_{DL}}{\varepsilon} = \frac{d\Psi_0}{dx_{atx=0}}$$

Rearranging we obtain

$$\sigma_{DL} = \varepsilon * \frac{d\Psi_0}{dx_{atx=0}} \tag{3.24}$$

To obtain σ_{DL} from the Gouy-Chapman model substitute equation 3.23 in equation 3.24. Then the surface charge density developed at the electrolyte side given by the Gouy-Chapman model is shown in equation 3.25 below:

$$\sigma_{DL} = \sqrt{8k_BT\varepsilon_r\varepsilon_0c_0}sinh(\frac{nq\Psi_0}{2k_BT}) \tag{3.25}$$

where

ε_0 = is the permittivity of vacuum, which is 8.854 e^{-12} F/m ,

ε_r = relative permittivity of the electrolyte,

c_0 = concentration of ions in solution,

k_B = Boltzmann constant,

T = the room temperature in Kelvin,

Ψ_0 = Surface potential developed

The surface charge density σ_{DL} developed on the electrolyte side depends on the square root of ion concentration c_0 and sine hyperbolic of surface potential Ψ_0. In order to find σ_{DL}, we need to obtain Ψ_0. Equation 3.18 can be integrated to obtain Ψ_0 for pH_B with varying C_{diff} and β_{int} values. But in order to do this we need to determine the value of α. And α depends on C_{diff} and β_{int}.

The C_{diff} can be found out by substituting the value of σ_{DL} from equation 3.25 in equation 3.16 as shown below:

$$C_{diff} = \sqrt{\frac{2q^2\varepsilon\varepsilon_0 c_0}{k_B T}} cosh(\frac{q\Psi_0}{2k_B T}) \tag{3.26}$$

The β_{int} is obtained by differentiating σ_0 in equation 3.6 with respect to pH_S and expanding.

$$\beta_{int} = 2.303 N_s H_S \frac{K_b H_S^2 + 4K_a K_b H_S + K_a K_b^2}{(K_a K_b + K_b H_S + H_S^2)^2} \tag{3.27}$$

The N_s, K_a, and K_b values are dependent on the gate oxide. The equation 3.27 can be expressed in terms of the pH_B of electrolyte and surface potential as given below:

$$\beta_{diff} = 2.303 N_s 10^{-pH_B} e^{-q\Psi_0/k_B T} \frac{K_b(10^{-pH_B}e^{-q\Psi_0/k_B T})^2 + 4K_a K_b 10^{-pH_B}e^{-q\Psi_0/k_B T} + K_a K_b^2}{(K_a K_b + K_b 10^{-pH_B}e^{-q\Psi_0/k_B T} + (10^{-pH_B}e^{-q\Psi_0/k_B T})^2)^2} \tag{3.28}$$

The changing value of pH causes different types of surface potentials (+'ve, -'ve or zero). Protonation leads to positive surface potential. Deprotonation leads to negative surface potential. The pH at which an equal amount of protonation and deprotonation occurs leads to surface potential being zero. And the pH at which this happens is denoted as a point of zero charge (pH_{pzc}). It means that the potential developed at the surface of the electrolyte-oxide interface is zero $\Psi_0 = 0$. For SiO_2, the point of zero charge is 2 [32]. The point of zero charge is different for various oxides.

The main aim here is to find the value of the surface potential Ψ_0 for each value of pH_B. Equation 3.18 can be integrated to obtain the value of Ψ_0 if α is constant. But α is varying. From equation 3.19, it can be seen that α depends on C_{diff} and β_{int}. Equations 3.26 and 3.27 show that C_{diff} and β_{int} depend on Ψ_0. Thus the conclusion can be made that in order to find Ψ_0, it is necessary to find α. The value of α depends on β_{diff} and C_{diff}. Again β_{diff} and C_{diff} depend on Ψ_0. This forms a self consistence dependence illustrated in Fig.3.4. It means the unknown variables which we are trying to find by solving equations depend on other unknown variables which in turn depend on the previous unknowns.

We need to solve the three equations simultaneously with three unknown variables forming

Figure 3.3: Self-consisting loop for finding Ψ_0. It means the unknown variables Ψ_0 which we are trying to find by solving equations depend on other unknown variables (β_{diff} and C_{diff}) which in turn depend on the previously unknown (Ψ_0).

a self-consistent loop. To solve this, our method is implemented in MATLAB and it is based on the bisection method. The following steps are described to solve this:

STEP 1:

Assume a range of the pH (in this case from 0-14) having 5000 points. The point of zero charge needs to be found out by bisection method. In MATLAB, a function called charden() is created that needs to pass two arguments pH and potential. The pH range is assumed to be from -10 to 30 for the bisection. pH_{low} = -10 and pH_{high} = 30. charden() function consists of equations to find the surface charge density $\sigma - SD$ and $\sigma - GC$. Both of which depend on pH and potential respectively. We start by finding the mid of pH_{low} and pH_{high} and pass these arguments in charden() function. The potential we pass is zero since we are trying to find pH_{pzc}. We keep on repeating this until the error = (pH_{high}- pH_{low}) pH_{high} is less than 10^{-50}.

STEP 2:

After finding the pH_{pzc} in the above step. We need to find the surface potential for each bulk pH. Check whether the surface potential (ψ_0) to be found out is for

(i) pH < pH_{pzc}

(ii) pH = pH_{pzc}

(iii) pH > pH_{pzc} by comparing the pH_{pzc} obtained in STEP 1 for a particular oxide with all the 5000 points in the pH range.

STEP 3:

If pH_B< pH_{pzc},assuming ψ_{low} (0V) and ψ_{high} (0.33 V) values. This range has been assumed because we already know for SiO_2, the surface potential will be positive for pH < pH_{pzc}. Hence we assume a range from 0 to a value greater than zero. Substitute ψ_{high} in the surface charden() function having equation 3.6 and equation 3.25.

STEP 4:

In a for loop from 1 to 100;

Check if $\sigma_{0-GC(high)}$ - $\sigma_{0-SD(high)} > 0$, if yes then find ψ_{mid} by adding these values of ψ_{low} and ψ_{high} then divide by 2. Substitute this ψ_{mid} in the surface charge density equation 3.6 and equation 3.25.

STEP 5:

Check if $\sigma_{0-GC(mid)}$ - $\sigma_{0-SD(mid)} > 0$. If yes then $\psi_{high} = \psi_{mid}$. And again find the bisection of these two which will be the new midpoint for surface potential. If $\sigma_{0-GC(mid)}$ - $\sigma_{0-SD(mid)} < 0$ then $\psi_{low} = \psi_{mid}$. And again find the bisection of these two which will be the new midpoint for surface potential.

STEP 6:

Check the error(ψ_{high} - ψ_{low})/ψ_{high}. If error < tolerance (1e-50) then we break the for loop implemented in STEP 4. We obtain the value of $\psi_0 = \psi_{low}$ or ψ_{high}.

STEP 7:

If error > tolerance (1e-50), keep on repeating STEP 4, STEP 5 and STEP 6.

STEP 8:

If $pH_B = pH_{pzc}$ then $\psi_0 = 0$.

STEP 9:

If $pH_B > pH_{pzc}$, assuming ψ_{low} (0V) and ψ_{high} (-0.28 V) values. These values are assumed as we know for pH greater than pH_{pzc}, the surface potential is negative for SiO_2.

STEP 10:

In a for loop;

Repeat STEP 4, STEP 5 and STEP 6 but in the opposite way. Meaning shift the high-potential or low-potential for $\sigma_{0-GC(high)}$ - $\sigma_{0-SD(high)} < 0$ and $\sigma_{0-GC(mid)}$ - $\sigma_{0-SD(mid)} > 0$.

STEP 11:

Then $\psi_0 = \psi_{low}$. Substitute ψ_0 in equation 3.25 to get the value of σ_{0-GC} or σ_{DL} .

The MATLAB code for the Gouy-Chapman model is mentioned in Appendix D.7. However, this Gouy-Chapman model doesn't represent this very well the reality. In reality, there is the formation of the stern layer. The assumption of the charges/ions approaching the surface arbitrarily causes a high charge on the surface. This cannot be realistic and the model needs modification. The section below describes the formation and inclusion of the Stern layer into the Gouy-Chapman method. Hence known as the Gouy-Chapman-Stern model.

3.3   Gouy-Chapman-Stern Model

The Gouy-Chapman-Stern layer model combines the Gouy-Chapman model and the Stern layer [33]. The Gouy-Chapman explains well the development of the double-layer capacitance, you just need free charges, and it develops. The Stern layer accounts for the immobile counter-cations attached to the immobile anions belonging to the solid phase material interface (also known as the interface charged layer). The Stern layer accounts for the increased short-range

interface between the solid phase material ions and the ions and the electrolyte, which results in fixed charges. Fig.3.5 accounts for a FET sensor with the Stern Layer. It has a transducer layer, its Si in our case. There is gate oxide on top of the transducer layer, it's SiO_2 in our case. The electrolyte added on top of it causes Silanol groups $SiOH$ to deprotonate $Si-O^-$ or protonate $Si-OH_2^+$ depending on the pH. The negative charge (immobile anions) on the oxide surface is formed due to deprotonation of $SiOH$. Due to this, $[H^+]$ ions are attracted towards the surface of the gate oxide. The $[H^+]$ ions forming a layer is called a Stern layer.

The stern layer capacitance C_{stern} develops as a competition of the short-range Coulomb interaction of the ions, the ionic strength and the temperature. As a result of this, some ions get trapped, and the C_{stern} will be formed, leaving the rest of the ions to form the rest of C_{diff}.

The top plane of the stern layer is called the plane of shear. The potential developed at the plane of shear is called Zeta potential ψ_ξ. Above the shear plane is the diffuse layer of electrolyte. It consists of mobile ions. Above the diffuse layer is the electrolyte bulk. The difference between the diffuse layer and the bulk of the electrolyte is the concentrations of ions in the solutions are different. To distinguish both layers in the electrolyte and new parameter is introduced which is called a Debye length λ. The Debye length is the length of charge screening, which in this model coincides with the diffuse layer. Or Debye length is the length of the diffuse layer in this model.

In the described approach here, the Ψ_0 must include also the Ψ_ξ. Since, we have included the stern layer, another equation 3.29 comes into consideration as given below

$$\Psi_0 = \frac{\sigma_{0-GCS}}{C_{stern}} + \Psi_\xi \tag{3.29}$$

The surface potential Ψ_0 depends on the zeta potential Ψ_ξ and the potential developed in the stern layer being given by $\frac{\sigma_{0-GCS}}{C_{stern}}$. C_{stern} is the stern layer capacitance whose value can be predetermined either experimentally or by 1st principles. In this model, the value of C_{stern} has been taken from experiments mentioned in the literature [28].

$$\sigma_{0-GCS} = \sqrt{8k_B T \varepsilon_r \varepsilon_0 c_0} sinh(\frac{nq\Psi_\xi}{2k_B T}) \tag{3.30}$$

The surface charge density σ_{0-GCS} developed on the electrolyte side depends on the square root of ion concentration c_0 and sine hyperbolic of zeta potential Ψ_ξ.

The main aim here is to find the value of the surface potential Ψ_0 and zeta potential Ψ_ξ for each value of pH_B. Equations 3.18 can be integrated to obtain the value of Ψ_0 if α is constant. But α is varying. From equation 3.19, it can be seen that α depends on C_{diff} and β_{int}. Equations 3.26 and 3.27 show that C_{diff} and β_{int} depend on Ψ_0. Thus the conclusion can be made that in order to find Ψ_0, it is necessary to find α. The value of α depends on β_{diff} and C_{diff}. Again β_{diff} and C_{diff} depend on Ψ_0. This forms a self consistence dependence illustrated in Fig.3.4. It means the unknown variables which we are trying to find by solving equations depend on other
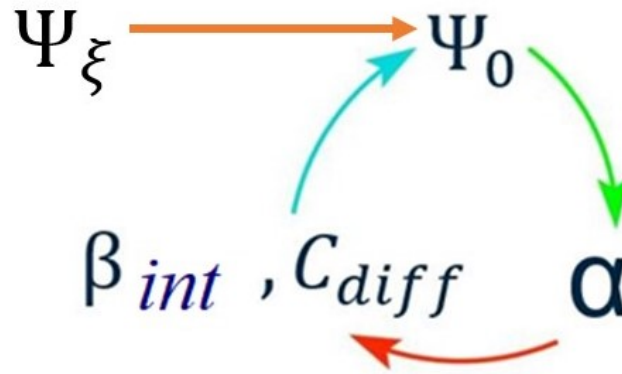
Figure 3.4: Self-consisting loop for finding Ψ_ξ. It means the unknown variable Ψ_ξ which we are trying to find by solving equations depend on another unknown variable (Ψ_0). Ψ_0 depends on α. $\aleph$ depends on β_{diff} and C_{diff} which in turn depends on the previous unknown(Ψ_0).

unknown variables which in turn depend on the previous unknowns.

We need to solve at the same time three equations with three unknown variables forming a self-consistent loop. To solve this, our method is implemented in MATLAB and it is based on the bisection method. The following steps are described to solve this:

STEP 1:

Assume a range of the pH (in this case from 0-14) having 5000 points. The point of zero charge needs to be found out by bisection method. In MATLAB, a function called charden() is created that needs to pass two arguments pH and potential. The pH range is assumed to be from -10 to 30 for the bisection. pH_{low} = -10 and pH_{high} = 30. charden() function consists of equations to find the surface charge density $\sigma - SD$ and $\sigma - GC$. Both of which depend on pH and potential respectively. We start by finding the mid of pH_{low} and pH_{high} and pass these arguments in charden() function. The potential we pass is zero since we are trying to find pH_{pzc}. We keep on repeating this until the error = (pH_{high}- pH_{low}) pH_{high} is less than 10^{-50}.

STEP 2:

After finding the pH_{pzc} in the above step. We need to find the surface potential for each bulk pH. Check whether the zeta potential (ψ_ξ) is to be found out for

(i) pH < pH_{pzc}

(ii) pH = pH_{pzc}

(iii) pH > pH_{pzc} by comparing the pH_{pzc} for a particular oxide with all the 5000 points in the pH range.

STEP 3:

If pH_B< pH_{pzc},assuming ψ_{low} (0V) and ψ_{high} (0.33 V) values. This range has been assumed because we already know for SiO_2, the surface potential will be positive for pH < pH_{pzc}. Hence we assume a range from 0 to a value greater than zero. Substitute ψ_{high} in the surface charge

density equation 3.6 and 3.25.

STEP 4:

In a for loop from 1 to 100;

Check if $\sigma_{0-GCS(high)}$ - $\sigma_{0-SD(high)} > 0$, if yes then find ψ_{mid} by adding these values of ψ_{low} and ψ_{high} then divide by 2. Substitute this ψ_{mid} in the surface charge density equation 3.6 and 3.25.

STEP 5:

Check if $\sigma_{0-GCS(mid)}$ - $\sigma_{0-SD(mid)} > 0$. If yes then $\psi_{high} = \psi_{mid}$. And again find the bisection of these two which will be the new midpoint for surface potential. If $\sigma_{0-GCS(mid)}$ - $\sigma_{0-SD(mid)} < 0$ then $\psi_{low} = \psi_{mid}$. And again find the bisection of these two which will be the new midpoint for surface potential.

STEP 6:

Check the error(ψ_{high} - ψ_{low})/ψ_{high}. If error < tolerance (1e-50) then we break the for loop implemented in STEP 4. We obtain the value of $\psi_{\xi} = \psi_{low}$ or ψ_{high}.

STEP 7:

If error > tolerance (1e-50), keep on repeating STEP 4, STEP 5 and STEP 6.

STEP 8:

If $pH_B = pH_{pzc}$ then $\psi_{\xi} = 0$.

STEP 9:

If $pH_B > pH_{pzc}$, assuming ψ_{low} (0V) and ψ_{high} (-0.28 V) values. These values are assumed as we know for pH greater than pH_{pzc}, the surface potential is negative for SiO_2.

STEP 10:

In a for loop;

Repeat STEP 4, STEP 5 and STEP 6 but in the opposite way. Meaning shift the high-potential or low-potential for $\sigma_{0-GCS(high)}$ - $\sigma_{0-SD(high)} < 0$ and $\sigma_{0-GCS(mid)}$ - $\sigma_{0-SD(mid)} > 0$.

STEP 11:

Then $\psi_{\xi} = \psi_{low}$. Substitute ψ_{ξ} in equation 3.30 to get the value of ψ_0.

Once the Ψ_{ξ} is obtained, surface potential Ψ_0 is also obtained. The MATLAB code for the Gouy-Chapman-Stern model is mentioned in Appendix D.7.

3.3.1 Gouy-Chapman-Stern Model extension in the electrolyte to a direction perpendicular to oxide surface

Along with surface potential, surface charge density, and double-layer capacitance, it is essential to know the potential distribution away from the oxide-electrolyte interface to capture the effect of surface charges within the bulk electrolyte. Thus, this section gives the potential variation occurring in the electrolyte in a direction perpendicular to the oxide surface taking the zeta potential (Ψ_{ξ}) from the Gouy-Chapman-Stern Model into consideration. The potential variation throughout the electrolyte is denoted by ψ_{Var}. The potential variation (ψ_{Var}) throughout the
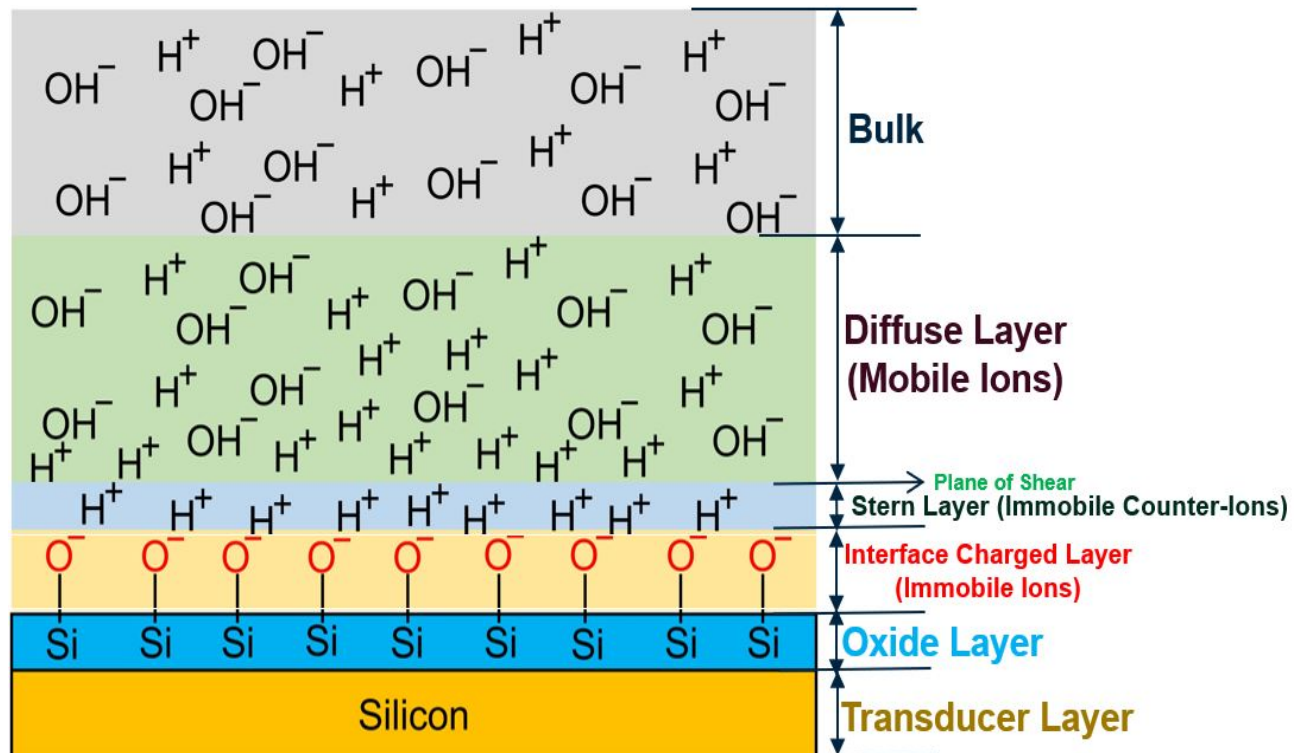
Figure 3.5: Gouy-Chapman-Stern layer model diagram in detail. The bottommost part is the Silicon semiconductor where the drain current flows. On top of it is SiO_2 which forms the oxide layer. $[SiO^-]$ forms the next layer which is of negatively charges immobile ions. On top of this, we have a layer of immobile counter ions. It is known as the stern layer. The potential at the plane of shear is Ψ_ξ. Then comes the mobile ions layer also known as the diffuse layer as the ions are moving. On the top is the bulk of the electrolyte.

electrolyte starting from the distance (x_d) near the oxide surface and moving far away from the oxide surface has been derived here [34]. In order to accomplish this, we need to integrate equation 3.21 twice. It would be difficult to solve having two integrals hence we need to introduce dimensionless variables Ψ^*, x^* in place of Ψ, x making equation 3.21 a single integration as shown in the below equations from 3.31 to 3.38:

$$\Psi^* = \frac{ze\Psi_0}{k_B T}$$

$$x^* = \frac{x}{\lambda_D}$$

Now we can rewrite equation 3.21 as follows

$$\left(\frac{ne}{k_B T}\right)^{-1} \frac{1}{(\lambda_D)^2} \frac{d^2\Psi^*}{dx^{*2}} = \frac{2neN_A c_0}{\varepsilon} sinh(\Psi^*) \tag{3.31}$$

$$\frac{1}{(\lambda_D)^2} \frac{d^2\Psi^*}{dx^{*2}} = \frac{2(ne)^2 N_A c_0}{\varepsilon k_B T} sinh(\Psi^*) \tag{3.32}$$

$$\frac{d^2\Psi^*}{dx^{*2}} = sinh(\Psi^*) \tag{3.33}$$

Multiply by $\frac{d\Psi^*}{dx^*}$ on both the sides

$$\frac{d^2\Psi^*}{dx^{*2}} \frac{d\Psi^*}{dx^*} = sinh(\Psi^*) \frac{d\Psi^*}{dx^*} \tag{3.34}$$

$$\frac{1}{2} \frac{d(\frac{d\Psi^*}{dx^*})^2}{dx^*} = \frac{d}{dx^*} cosh(\Psi^*) \tag{3.35}$$

Integrating both sides;

$$\left(\frac{d\Psi^*}{dx^*}\right)^2 = 2cosh(\Psi^*) + c_1 \tag{3.36}$$

when $x^* \to \infty$, $\Psi_0 \to 0$ and $\frac{d\Psi^*}{dx^*} \to 0 \Rightarrow c_1 = -2$

It means that when the distance x is far far away from the surface of the oxide. The potential reduces to its minimum, hence taken as tending to zero. It's an approximation to find the value of c_1 and $\frac{d\Psi^*}{dx^*}$.

$$\left(\frac{d\Psi^*}{dx^*}\right)^2 = 2cosh(\Psi^*) - 2 = 2(cosh(\Psi^*) - 1) = 4\left(sinh\left(\frac{\Psi^*}{2}\right)\right)^2 \tag{3.37}$$

$$\left(\frac{d\Psi^*}{dx^*}\right) = -2sinh\left(\frac{\Psi^*}{2}\right) \tag{3.38}$$

Rearrange and single integrate Ψ^* equation 3.38 as shown below:

$$\int_{\frac{ne\Psi_\xi}{kT}}^{\Psi^*} \frac{1}{2sinh(\frac{\Psi^*}{2})} d\Psi^* = -\int_0^{x^*} dx^*$$

$$\log\left(tan(\frac{\Psi^*}{4})\right) = -x^*$$

$$\log\left(tan(\frac{\Psi^*}{4})\right) - \log\left(tan(\frac{ne\Psi_\xi}{4k_BT})\right) = -x^*$$

$$\frac{\log\left(tan(\frac{\Psi^*}{4})\right)}{\log\left(tan(\frac{ne\Psi_\xi}{4k_BT})\right)} = -x^*$$

$$e^{-x^*} = \frac{tanh(\frac{\Psi^*}{4})}{tanh(\frac{ne\Psi_\xi}{4k_BT})}$$

$$e^{-x^*}.tanh(\frac{ne\Psi_\xi}{4kT}) = tanh(\frac{\Psi^*}{4})$$

$$\frac{\Psi^*}{4} = tanh^{-1}[e^{-x^*}.tanh(\frac{ne\Psi_\xi}{4k_BT})]$$

$$\Psi^* = 4tanh^{-1}[e^{-x^*}.tanh(\frac{ne\Psi_\xi}{4k_BT})]$$

replace Ψ^* with

$$\Psi^* = \frac{ne\Psi_{Var}}{k_BT}$$

and replace x^* with

$$x^* = \frac{x_d}{\lambda_D}$$

$$\Psi^* = 4tanh^{-1}[e^{-x^*}.tanh(\frac{ne\Psi_\xi}{4k_BT})]$$

$$\frac{ne\Psi_{Var}}{k_BT} = 4tanh^{-1}[e^{-\frac{x_d}{\lambda_D}}.tanh(\frac{ne\Psi_\xi}{4k_BT})]$$

$$\Psi_{Var} = \frac{4k_BT}{ne}tanh^{-1}[e^{-\frac{x_d}{\lambda_D}}.tanh(\frac{ne\Psi_\xi}{4k_BT})] \tag{3.39}$$

where

n = number of positive/negative ions

x_d = distance from oxide/electrolyte interface

λ_D = debye length

Ψ_ξ = zeta potential

k_B = Boltzmann constant

e = electron charge

Hence the above equation 3.39 is derived for this thesis. It is an equation for potential variations across the electrolyte. The potential at a particular point in electrolyte depends on debye length (λ_D), its distance from the oxide/electrolyte interface (x_d) and the zeta potential (Ψ_ξ)

To find out the distribution of concentration of $[H^+]$ ions and $[OH^-]$ ions in the electrolyte as a function of distance from the oxide/electrolyte interface we use Boltzmann distribution using the information from potential

$$p_{variation} = p_b \exp\left\{\frac{-\Psi_{var}}{V_T}\right\} \qquad (3.40)$$

$$n_{variation} = n_b \exp\left\{\frac{\Psi_{var}}{V_T}\right\} \qquad (3.41)$$

where

$p_{variation}$ = Conc. of the H^+ ions in electrolyte

$n_{variation}$ = Conc. of the OH^- ions in electrolyte

p_b and n_b are the concentration of $[H^+]$ and $[OH^-]$ ions in the bulk respectively.

V_T is the thermal voltage.

The MATLAB code for determining the potential variation (Ψ_{Var}), n variation ($n_{variation}$) and p variation ($p_{variation}$) are given in the Appendix D.8.

The length from the oxide/electrolyte interface to the centroid of the diffusive layer is the debye length [35]. The debye length is derived as follows:

Equation 3.13 is the Boltzmann equation or the Boltzmann distribution.

Since $\Psi(x=0) = \Psi_\xi$ (zeta potential), $\Psi(x \to \infty) = 0$ V and

$$\frac{ne\Psi_\xi}{kT} << 1$$

$$\Rightarrow \Psi_\xi << \frac{kT}{ne}.$$

$$\Rightarrow \Psi_\xi << \frac{V_T}{n}.$$

When the zeta potential is much lesser than thermal voltage, it is considered as Debye Huckel approx.

Continuing from eq. 3.21 again we have

$$\frac{d^2\Psi}{dx^2} = \frac{c_0 nF}{\varepsilon} \cdot \frac{2ne\Psi}{kT} = \frac{2(ne)^2 N_A c_0}{\varepsilon kT}\Psi = \frac{\Psi}{\lambda_D^2} \qquad (3.42)$$

where

$$F = eN_A$$

And now λ_D can be written as

$$\lambda_D = \sqrt{\frac{\varepsilon kT}{2(ne)^2 c_0 N_A}} \tag{3.43}$$

$$\lambda_D = \sqrt{\frac{\varepsilon_r \varepsilon_0 kT}{2(ne)^2 c_0 N_A}} \tag{3.44}$$

where ε_{elec} = permittivity of electrolyte (water + NaCl in our case) = $\varepsilon_r \varepsilon_0$

ε_r = relative permittivity,

ε_0 = permittivity of free space

k = Boltzmann constant

T = temperature

q = charge of an electron

N_A = Avogadro's number

c_0 = ionic strength of the electrolyte solution (in per m^{-3}).

It can be seen from the equation 3.44 derived for debye length λ_D that the debye length depends only on the ionic strength c_0 of the electrolyte. If the ionic strength c_0 is more then the debye length λ_D will be less and vice-versa.

The below equation is valid only with debye-huckel approx

$$\Psi = \Psi_\xi \exp\left\{\frac{-x}{\lambda_D}\right\} \tag{3.45}$$

The Debye length (λ_D) is calculated from the equation 3.43 and its value is approx. 1nm for $c_0 = 0.1$ M = 0.1 mol/L. In order to use the c_0 in the equation 3.44 we need to convert it in m^{-3}.

$$c_0 = \frac{0.1 mol}{0.001 m^3}$$

$$c_0 = \frac{0.1 * 6.023 * 10^{23}}{0.001} m^{-3}$$

$$c_0 = 0.6023 * 10^{26} m^{-3}$$

Using the above value of c_0 in equation 3.44, we obtain

$$\lambda_D = \sqrt{\frac{(78.5)(8.85x10^{-12}\frac{s^4 A^2}{kg.m^2.m})(1.38x10^{-23}\frac{m^2 kg}{s^2 K})(298K)}{(2)(1^2)(1.6x10^{-19})^2 C^2 (0.6023 * 10^{26}) m^{-3}}}$$

$$\lambda_D = 0.96 nm$$

$$\lambda_D \approx 1nm$$

To check how the debye length λ_D varies with concentration c_0. We consider an example of having c_0 = 1M

$$c_0 = 1M = 6.023 * 10^{26} m^{-3}$$

$$\lambda_D = 0.3043nm$$

This shows that as the concentration of ions in the electrolyte increases, the debye length decreases. Or the distance for screening the charges on the surface of oxides decreases with an increase in concentration. For e.g., if the length of the amino acid is less than the debye length λ_D then we can detect it. But if the length of amino acid is more than debye length λ_D then it's not possible for the FET device to detect its presence.

3.3.2 Results and Discusions

Our results reveal a correlation between the variations of surface potential (Ψ_0), H^+ ions and OH^- ions with respect to distance from the electrolyte/oxide interface. Fig.3.6 shows for lower values of pH, close to pH = 0, the potential decreases (see the dark green region) when the distance from the oxide/electrolyte interface increases. The figure 3.6 has been plotted based on the equation 3.39. This is consistent with the data from the experiments since lower pH means a higher concentration of H^+ ions leading to decreasing potential far away from the oxide/electrolyte interface. Ψ_{Var} = 0 represents the pH at the point of zero charge. In our case, it's 2 for SiO_2. For higher values of pH, close to pH = 14, the potential increases (see the light green region) as we move away from the oxide/electrolyte interface. This is again consistent with the experiments since higher pH means a higher concentration of OH^- ions leading to positive potential away from the interface.

Moreover, the potential increases for higher pH and decreases for lower pH values after crossing the Debye length (1nm) due to repulsion from the charges present at the interface compared to the bulk that balances the potential to reach a minimum value (approx. 0V).

Fig. 3.7 shows the distribution of concentration of H^+ and OH^- ions in the electrolyte. This graph is plotted from the equation 3.40 and equation 3.41. The distribution is shown normally away from the oxide/electrolyte interface as we move from left to right on the x-axis. For lower values of pH, the concentration of H^+ ions increases and for higher values of pH the concentration of H^+ ions decreases as we move away from the interface. This is justified due to the positive/negative potential at the interface at lower/higher pH values respectively.

Also, the proton concentration $[H^+]$ is inversely proportional to the $[OH^-]$ concentration and equation 3.41 describes such a relationship which again is using the information of the surface potential (Ψ_0) obtained as an initial value from equation 3.39. The OH^- ions concentration increases for higher pH value after crossing the Debye length away from the interface due to
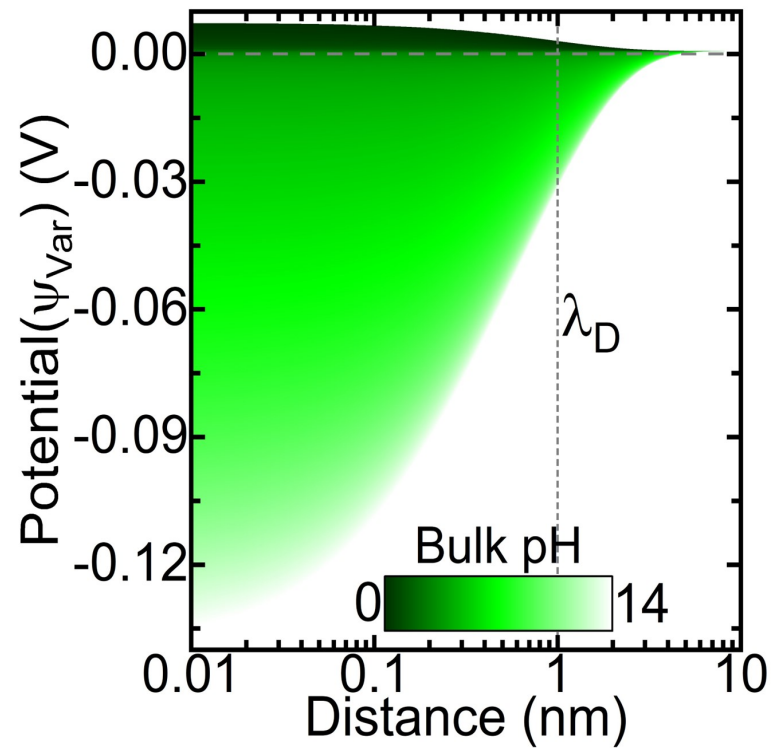
Figure 3.6: Potential distribution throughout the electrolyte in a direction normal to the oxide electrolyte interface. Potential (Ψ_{var}) as a function of the distance away from the oxide/electrolyte interface calculated from the analytical model consisting of Gouy-Chapman-Stern theory and Site-Binding theory.
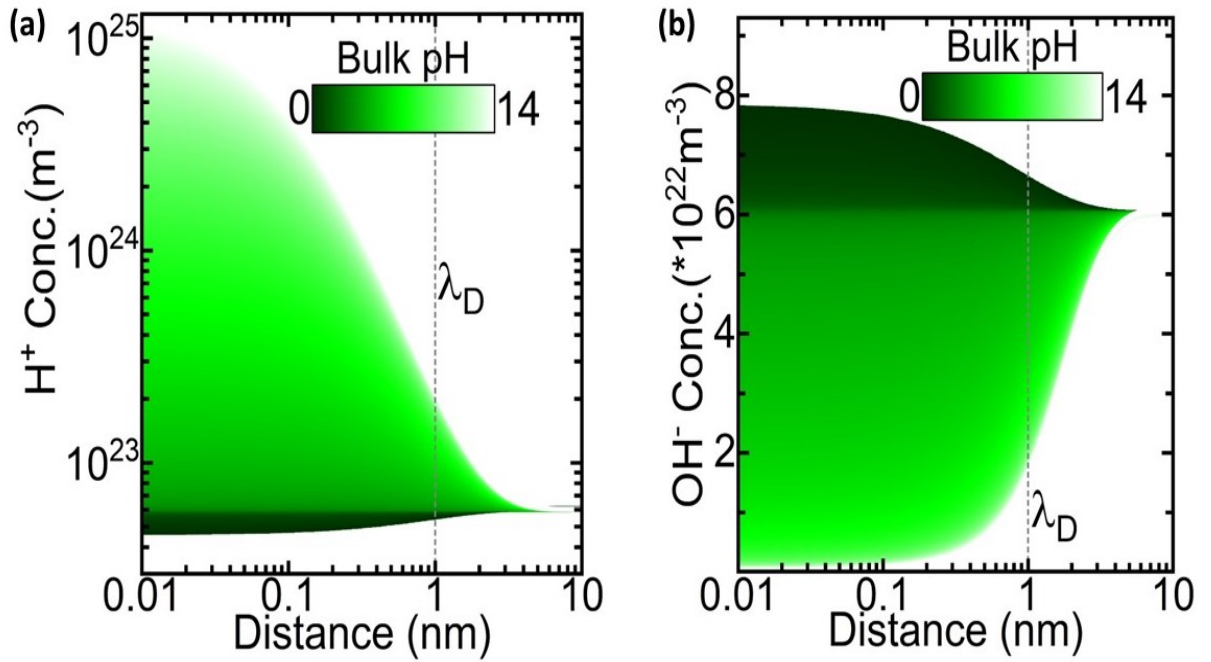
Figure 3.7: H^+ and OH^- ions distributed throughout the electrolyte in a direction normal to the oxide electrolyte interface. (a) The concentration of H+ ions (b) Concentration of OH- ions as a function of the distance away from the oxide/electrolyte interface calculated from the analytical model consisting of Gouy-Chapman-Stern theory and Site-Binding theory.

repulsion from the negative charges present at the interface and OH^- concentration gradient as compared to the bulk.

From the simulation results, we have obtained surface potential (Ψ_0), zeta-potential (Ψ_ξ) and sensitivity factor (α). Surface potential (Ψ_0) is defined as the potential developed at the interface between oxide and electrolyte. Zeta potential (Ψ_ξ) is the average potential developed at the plane of shear [28]. The sensitivity factor (α) is a dimensionless quantity ($0 < \alpha < 1$), that defines the response of the sensor based on the pH of the interacting electrolyte. The results are very different if the dielectric material is changed.

Fig. 3.8 shows the variations in sensitivity parameter (α), zeta potential (Ψ_ξ) and surface potential (Ψ_0) with respect to the bulk pH for dielectric material SiO_2. The value of α is non-linear for low values of bulk pH and almost constant for higher values of bulk pH. Also, the α value is close to one (ideal state) for higher bulk pH. From equation 3.29, it is noted that Ψ_0 will have a higher negative value compared to Ψ_ξ.

As pH increases from 1 to 14, the surface potential Ψ_0 will become more negative as the concentration of OH^- ions in the electrolyte increases. A similar effect will be observed on zeta potential Ψ_ξ but it would be less negative compared to surface potential Ψ_0. At pH = 2, the surface potential will be zero for SiO_2 as the dielectric material. Another observation to be made is that for lower values of pH, the surface potential has a value close to zero (Ψ_0) and for higher values of pH, the surface potential Ψ_0 has a linear dependence on pH. This behaviour of the
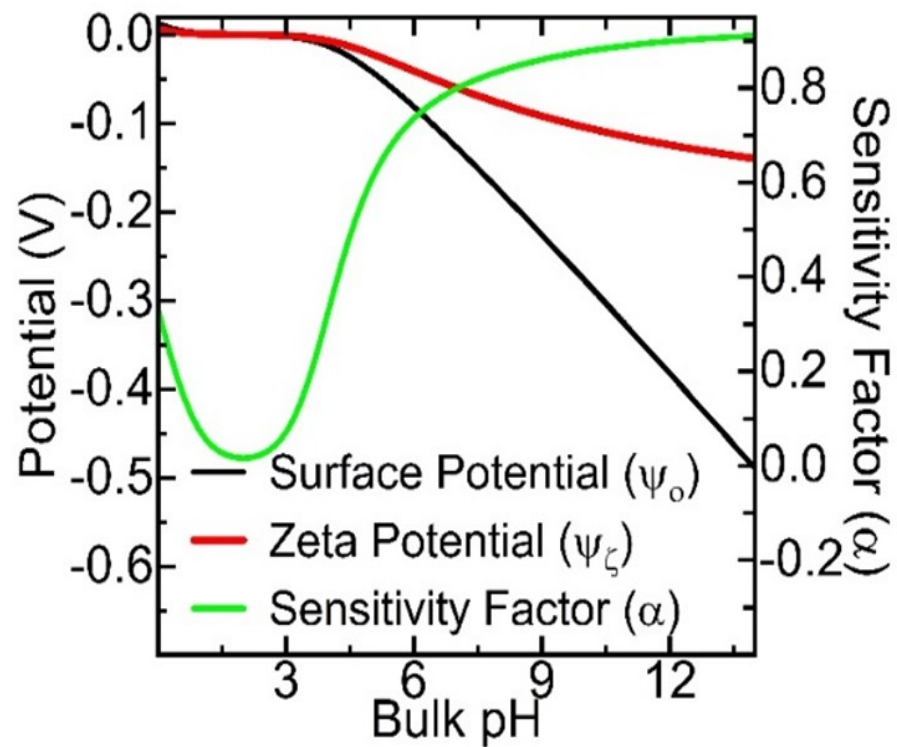
Figure 3.8: Effect of pH variation on surface potential (Ψ_0), zeta potential (Ψ_ξ) and sensitivity factor α. Surface potential (black line), Zeta potential (red line) and sensitivity factor (green line) as a function of Bulk pH are shown which is calculated from the analytical model in MATLAB of the Gouy-Chapman Stern layer theory.

surface potential Ψ_0 leads to the conclusion that there will be more change in surface potential Ψ_0 for higher pH values making it easier to detect the target molecules.

Chapter 4

Effect of oxides and its application to an absolute pH sensor

In the previous chapter we have seen the analytical models. This chapter shows the application of the Gouy-Chapman-Stern model described in section 3.3 of chapter 3 to both SiO_2 and HfO_2 along with addressing the issue of drift. ISFETs have triggered a serious limitation known to anyone using them that they require continuous re-calibration. ISFETs show unreliability that can be manifested in the drift of the threshold voltage (V_{th}) or the output current (I_{SD}) used to transduce the acidity/basicity [36–38]. This limits the applications that require accurate monitoring of the pH during periods lasting hours as well as the miniaturisation of highly multiplexed devices. Due to drift, ISFETs require compensation strategies based on calculations or using reference devices that require extra resources.

Our work aims to address a critical scientific issue such as the impact of oxide degradation (sensing interface deterioration) on the sensor's performance. The methods described here are based on analytical equations derived and implemented in MATLAB code. We propose a method to determine the absolute pH using a dual capacitance system, which can be mapped to determine the acidity. We compare the impact of degradation in two materials: SiO_2 and HfO_2, having low-k and high-k dielectric respectively.

This chapter is based on a publication by Cristina Medina-Bailon, Naveen Kumar, Rakshita Dhar, Ilina Todorova, Vihar Georgiev and Cesar Pascual García, 2021. Comprehensive analytical modelling of an absolute pH sensor. Sensors, 21(15), p.5190. I did MATLAB programming and graphs for section 4.1.

4.1 Oxide Capacitance methodology

There is an irreversible chemical degradation of the dielectric barrier responsible for the change in capacitance at the origin of the drift. The migration of charges into the oxide materials [39–42] decreases the dielectric constant of the affected region [43]. The re-calibrations are achieved using external reference buffers with known acidity. More sophisticated systems make use of an internal generation of acid that performs a titration curve [44, 45]. Finally, there are models that propose to predict the degradation of the capacitance [41, 43, 46, 47]. However, all of the above methods require experimental interruptions or can be sensitive to drastic changes in ambient conditions. Most of the ongoing work focuses on the reliability and material properties of different oxides to enhance the ISFET performance but the operation of a FET device may get affected due to several process parameters that may make the results less reliable. Here, we present a detailed methodology to enhance the sensor reliability by aiming to get accurate values irrespective of FET operation.

The migration of ions from the electrolyte into the dielectric is observed experimentally as a decrease of the capacitance resulting from the irreversible chemical transformation of a layer of the original material. The ions diffuse down to an effective depth that in some cases can be calculated for given experimental conditions [43, 48]. The degraded material experiences a decrease of the dielectric constant which in some materials like Al_2O_3 reaches values of 20% of the original one [43]. The typical penetration depths of ions account for several nanometers in the span of hours depending on experimental conditions that include the pH of the electrolyte, the ionic strength and the temperature. In steady-state conditions, the degradation often leads to a fast transition and a complete failure of the device when leakage currents appear between the electrolyte and the semiconductor channel.

To simulate the degradation, both the effective dielectric constant and penetration depth can be adjusted phenomenologically to match the capacitance with several combinations that can provide a successful description of the sensor behaviour before the avalanche of leakage currents makes the device fail. In our model, we have modelled the degradation with a reduction to an arbitrary dielectric constant with a value of 20% of the original one. The degraded region is associated with a corresponding effective penetration depth of the ions of x that is used to parameterize the degradation. To determine the absolute pH, we consider two ISFET devices with different thicknesses t_{ox1} and t_{ox2} of the dielectric barrier, subjected to the same experimental conditions and thus, with the same penetration of the effective degradation x on both of devices.

Figure 4.1(a) shows schematically sections of the interface between the electrolyte and the silicon channel using our model for two cases corresponding to devices of SiO_2 and HfO_2, respectively. The dielectric barrier in each device can be considered to be made of two materials in a series. The first material in contact with the electrolyte accounts for the degraded region with the adopted effective dielectric constant 20% of the original material and the total effective thickness x corresponding to the penetration of the degradation. The second material has the

dielectric properties of the original material (SiO_2 or HfO_2) with a total thickness of ($t_{ox1} - x$) or ($t_{ox2} - x$) for the first and the second device respectively that will be used to determine the pH. Underlying the non-degraded dielectric in each device, there is the silicon channel as shown in grey in the schemes of figure 4.1(a). Each sensor of absolute pH could consist of more than two of these devices which would be redundant but could help in improving the precision. However, for simplicity in this work, we have considered only the use of two devices to determine the absolute pH. We also consider that all the devices with SiO_2 or HfO_2 dielectric barriers will have the same configurations (silicon dimensions, doping, length, etc.) except for the oxide thickness (t_{ox1}=5nm and t_{ox2}=10nm). For practical reasons, in the simulations of this work, we have considered a maximum penetration of ions degrading the oxide of 3nm. We have also considered in our configuration a common reference electrode for both devices.

For each device, the total oxide capacitance (C_{ox}) is calculated as two capacitances in series including a capacitance without any degradation (C_{ox}^1) and another one with the degradation (C_{ox}^2):

$$\frac{1}{C_{ox}} = \frac{1}{C_{ox}^1} + \frac{1}{C_{ox}^2} = \frac{t_{ox} - x}{\varepsilon_r^1 \varepsilon_0} + \frac{x}{\varepsilon_r^2 \varepsilon_0} \tag{4.1}$$

where ε_r^1 is the relative dielectric constant of the original material, ε_r^2 is the relative dielectric constant of the degraded region material and ε_0 is the vacuum dielectric constant.

Accordingly, the total oxide capacitance for each sensor has been calculated from Equation 4.1:

$$C_{ox_i} = \frac{\varepsilon_r^1 \varepsilon_r^2 \varepsilon_0}{\varepsilon_r^1 x + \varepsilon_r^2 (t_{ox,i} - x)} \tag{4.2}$$

where the index i has been added to the total capacitance to determine ox_1 or ox_2 referring to the devices with the original dielectric of 5nm or 10nm, respectively.

Figure 4.1(b) shows the oxide capacitance calculated using Equation 4.2 as a function of the degraded region x, for the sensor interfaces with both thicknesses and materials. The observed behaviour corresponds to the decrease of the capacitance with increasing degradation depth x, which is equivalent to what is observed in other works [48]. Regarding the total change in the oxide capacitance in the degradation range studied, it is much more pronounced for HfO_2 than for SiO_2. This is due to the higher dielectric constant ε_r of HfO_2 in comparison to the one of SiO_2 (23.4 and 3.9, respectively [49]). Comparing the devices within the same material, as expected, the total variation of the capacitance is more pronounced for the configurations with 5nm oxide thickness with respect to the thicker oxides of 10nm, as the degraded region represents a larger part of the total dielectric thickness. Overall, it can be concluded that the HfO_2 capacitance shows larger susceptibility to the degradation and the variations in the thickness due to the diffusion process when it is compared to the SiO_2.

4.2 Impact of the degradation of the dielectric on the depletion width on different materials

To calculate the effect of the adsorbed charges on the device's current, the energy band diagram in the direction perpendicular to the surface of the oxide is considered as shown in figure 4.1(c). The model does not take into account the possible differences in the chemical potential between the semiconductor and the electrolyte, charges accumulated on the interface between the silicon and the dielectric barrier or phenomenon like the degradation of the reference electrode. When the semiconductor and the electrolyte are connected through a reference electrode and a gate voltage is applied between the two, it is possible to set the relation between the different potentials:

$$\Psi_0 = V_{ox} - V_G + \Psi_S \tag{4.3}$$

where Ψ_0 is the oxide-electrolyte interface potential, Ψ_S is the oxide-silicon interface potential, V_{ox} is the potential drop across the oxide and V_G is the external bias at the backgate. To understand it better, it can be re-written as
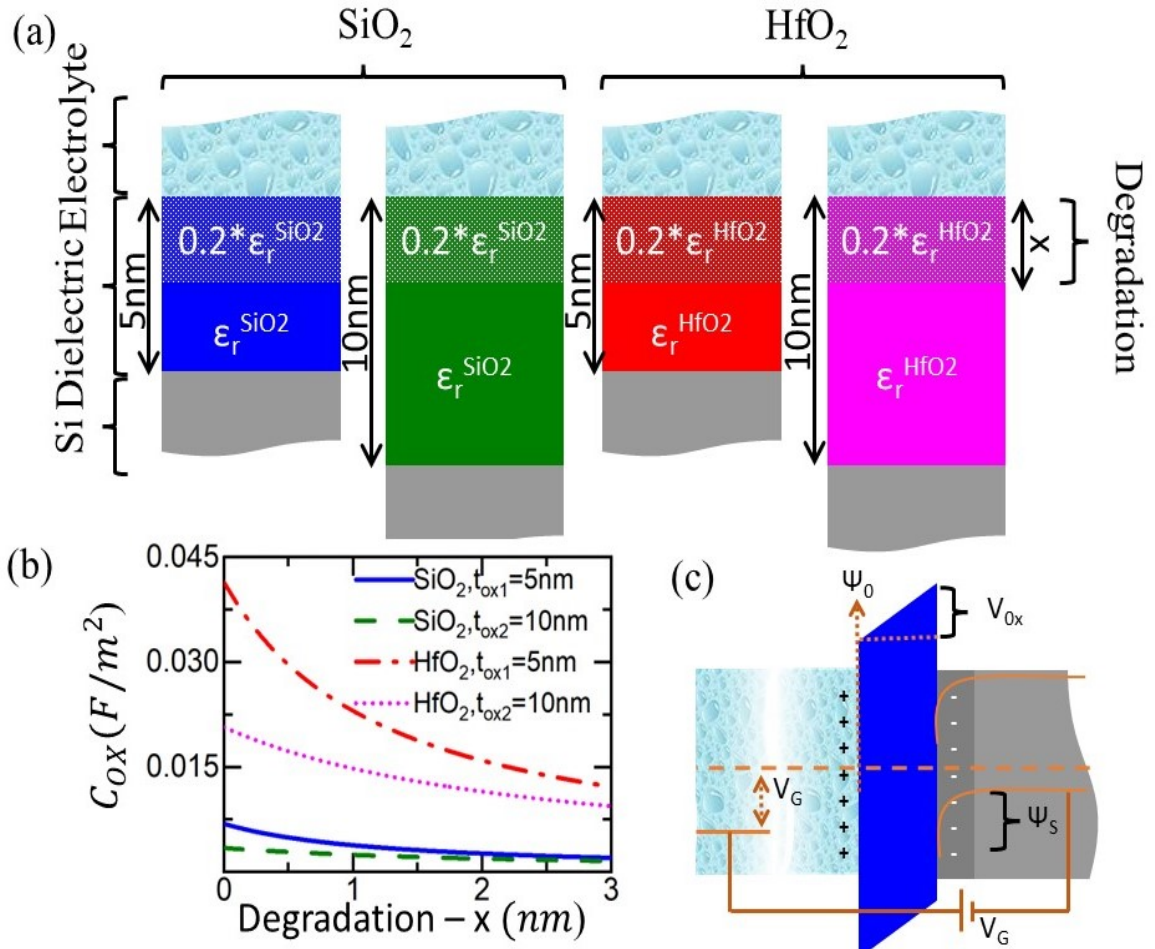
Figure 4.1: (a) Schematic representation that shows how the oxide capacitance is modelled considering a degraded region. Two different couple of devices is described in the diagrams including the combinations of two different oxide materials in the dielectric region. For each device couple, we have considered two oxide thicknesses: (blue) $t_{ox,1}$ = 5 nm and SiO_2, (green) $t_{ox,2}$ = 10 nm and SiO_2, (red) $t_{ox,1}$ = 5nm and HfO_2, and (magenta) $t_{ox,2}$ = 10nm and HfO_2. This colour notation to identify each device has been kept the same throughout the whole paper. (b) Total capacitance vs. degradation using the penetration depth of the degrading charges as a parameter of the degradation. (c) Schematic of the energy band alignment along one interface in a generic ISFET sensor.

$$\Psi_0 - \Psi_S = V_{ox} - V_G \tag{4.4}$$

The term V_{ox} in Equation 4.3 accounts for the energy accumulated across the dielectric barrier. It can be expressed using the charge on the semiconductor side and considering a planar condenser:

$$V_{ox} = \frac{qN_AW_D}{C_{ox}} \tag{4.5}$$

where C_{ox} is the area capacitance of the dielectric barrier (typically a metal oxide) described in Section 4.1, q is the elementary charge, N_A is the density of dopants in the semiconductor and W_D is the region in the semiconductor channel depleted from carriers shown in figure 4.1 (c) in darker grey colour . W_D can be derived solving the Poisson equation for Ψ_S with a planar configuration:

$$\frac{\partial^2 \Psi_S}{\partial x^2} = \frac{-qN_A}{\varepsilon_s \varepsilon_0} \Big|_{x=0}^{x=W_D} \longrightarrow \Psi_S = \frac{qN_AW_D^2}{2\varepsilon_s\varepsilon_0} \tag{4.6}$$

where ε_s is relative dielectric constant of the semiconductor. We have replaced $\varepsilon_s\varepsilon_0=\varepsilon_{Si}$ as p-type doped Silicon is used as a semiconductor channel for this work. Note that W_D changes the region populated with carriers and thus can modulate the conductivity of the FET channel. Combining Equations 4.3, 4.5, and 4.6, we have the following dependence:

$$\Psi_0 + V_G = \frac{qN_AW_D}{C_{ox}} + \frac{qN_AW_D^2}{2\varepsilon_{Si}} \tag{4.7}$$

In Equation 4.7, W_D changes with respect to the pH through the dependence of Ψ_0 with the acidity expressed in Equation 3.18 and so it is possible to get a final expression for W_D as a function of the pH:

$$W_D = -\frac{\varepsilon_{Si}}{C_{ox}} + \sqrt{\left(\frac{\varepsilon_{Si}}{C_{ox}}\right)^2 + 2\left(\frac{\varepsilon_{Si}}{qN_A}\right)(\Psi_0 + V_G)} \tag{4.8}$$

A drift in the current will be observed due to the dependence of W_D with the degradation of the different parameters. In particular, the parameters from Equation 4.8 which are responsible for the drift are *(i)* the changes in the dielectric material and thus in C_{ox} due to the possible penetration of ions or modifications of the dielectric (Section 4.1); and *(ii)* the changes in the sensitivity (α) of the material, mainly due to the modifications in β_{diff} because of the degradation of the surface with absorbed molecules that change the number of sites (N_S) for the binding of protons. In this work, the sensitivity has been calculated assuming the ideal sensor (in order to equally compare the oxides) and making use of an iterative method with respect to Ψ_0 to consider the real sensor. Accordingly, we have focused on studying the impact of different penetration of ions in C_{ox}.

Based on the analytical model described in the Gouy-Chapman model of section 3.2 in chapter 3, we have simulated the four devices detailed in section 4.1 grouped in couples having two thicknesses (5nm and 10nm) for each material (SiO_2 or HfO_2). The effect of the degradation in W_D as a function of the pH is calculated. As a first step, to simplify the study of the drift from other effects like the combination of the chemical affinity with the changes in the electrolyte, we have considered the case with ideal sensitivity ($\alpha = 1$).

We used equation 4.8 to calculate the parameters of the semiconductor channel, considering a desirable dynamic range from 2 to 12. Thus, considering a p-doped semiconductor channel that is going to be depleted in acidic conditions, we calculated a bias external voltage V_G necessary to have full conductivity ($W_D = 0nm$) at pH=12, and calculated the value for both oxide materials. N_A was chosen to have a depletion region of $W_D = 100nm$ at pH=pH_{pzc} considering the devices with t_{ox1}= 5nm.

Figure 4.2 shows W_D vs. pH for the interfaces described in figure 4.1 using the designated colour codes. A tone scale convention from darker to a lighter colour for increasing x has been added and will be maintained hereafter. As expected, W_D decreases with pH in all the devices as a result of the effect of the adsorbed protons. Comparing SiO_2 figure 4.2(a)(b) and HfO_2 figure 4.2(c)(d), the latter has a larger variation across the pH dynamic range due to the lower dielectric constant. The impact of the drift caused by the degradation on the pH determination by each of the devices is clearly observed in these graphics, as for a single depletion width, there are a broad number of possible pH values corresponding to different states of degradation in the material. For instance, if the constant W_D=60nm is considered (solid orange line in Figure 4.2), the pH uncertainty between the cases of no degradation (x=0nm) and the maximum degradation considered (x=3nm) are ΔpH=3.15 and ΔpH=3.30 for the SiO_2 dielectric with t_{ox1}=5nm and t_{ox2}=10nm, respectively; whereas the uncertainty is dramatically reduced to ΔpH=0.30 and ΔpH=0.31 for the HfO_2 dielectric with t_{ox1}=5nm and t_{ox2}=10nm, respectively. In both cases, ΔpH is slightly higher for the device with t_{ox1}=10nm.

On the other side, queerly as considering Figure 4.2(c) and (d), HfO_2 devices can offer a better pH resolution as the current range of pH values possible relative to the total current variation in the dynamic range, is much more restricted than for SiO_2. In addition, even if it is not taken into account by these simulations, the chemical stability of HfO_2 largely exceeds the one of SiO_2 and thus is less prone to ion penetration which makes the degradation occurs in longer time periods. Elseways, SiO_2 has proportionally a larger variation of W_D as the degradation increases. In order to resolve the absolute pH, we intend to determine the degradation considering the current from a dual device composed of the two sensors with one of the two materials that we had calculated. In this sense, SiO_2 may have the advantage to determine an absolute pH as it provides proportionally larger current contrasts within a given pH range.
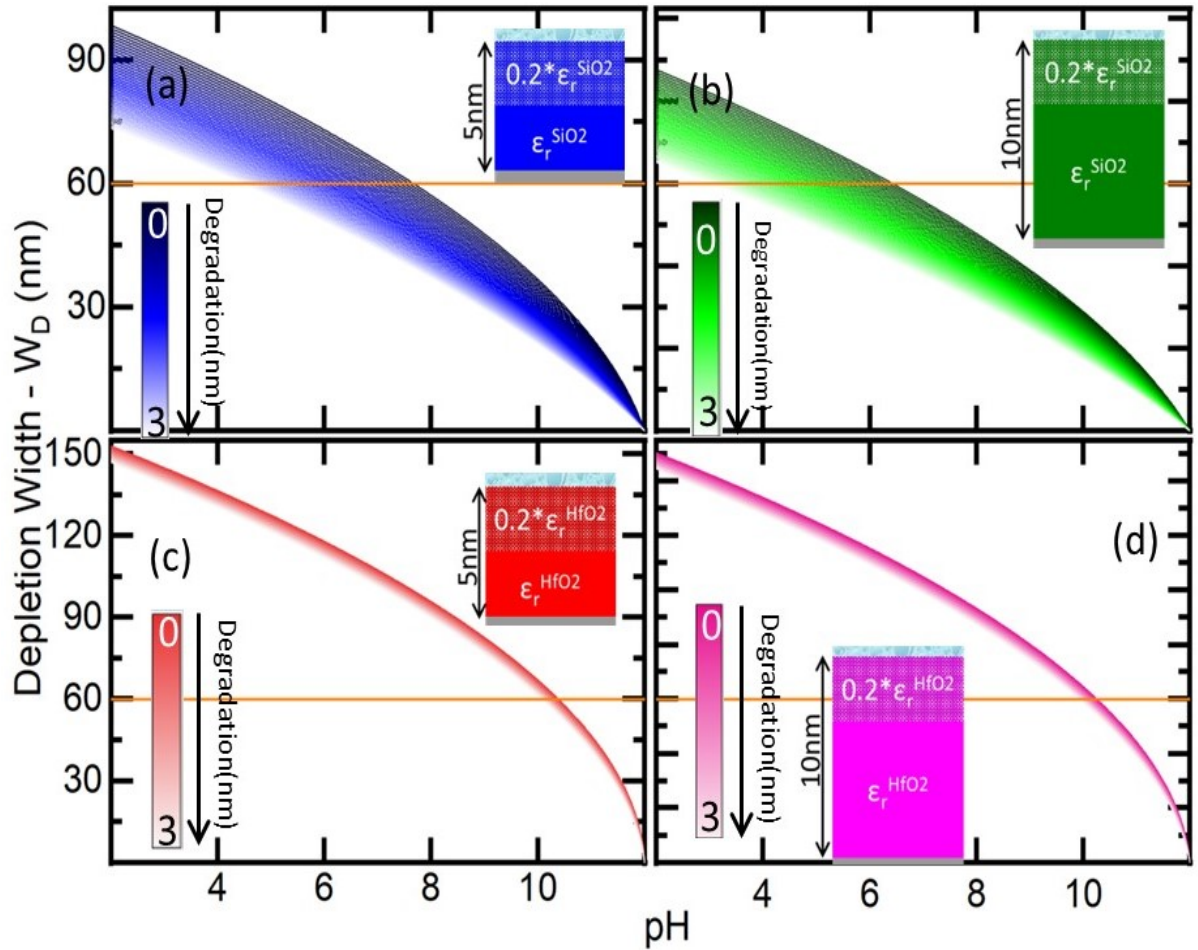
Figure 4.2: Depletion Width (W_D) as a function of the pH considering the different degraded regions in the oxide (x) from x = 0nm (non-degraded oxide) to x = 3nm for the two different oxides ((a)/(b) SiO_2 and (c)/(d)HfO_2) and two different ideal biosensors (a = 1) which main difference is the oxide thickness ((a)/(c)t_{ox1} = 5nm and (b)/(d)t_{ox2} = 10nm). The solid orange line represents the example of the variation of the pH range for a constant W_D = 60nm.

4.3 Determination of absolute pH from the current acquisition in FET sensors

To illustrate the determination of pH in a case scenario, we used our model to calculate the response of a pair of sensors with the geometry of a high aspect ratio FinFET shown in figure 4.3 (a). This ISFET geometry has been recently proposed by us as a robust and advanced design for a biosensor [50]. Similarly to a single Silicon-Nanowire (SiNW), this geometry offers a three-dimensional direct gating advantage with respect to typical planar devices or extended gates. With respect to the nanowires (NWs), the high aspect ratio FinFETs can also improve *(i)* the reproducibility of the sensitivity for ion sensing (pH), *(ii)* the total signal, and *(iii)* the linearity of the current response. Moreover, high aspect ratio FinFETs have better linearity and a smaller footprint if compared to NW arrays. Due to the planar configuration of the conduction channel, the influence of small defects in pH sensing is localised and negligible for the sensor signal if compared to their influence in nanoscale SiNWs. For our work, we have chosen the device dimensions similar to the one shown in figure 4.3(a), where the width W was 200nm, the height h was 2μm and the length L was 10μm.

For a given FinFET, W_D can be related to the measured current depending on the geometry of the sensor considering that the size of the channel is diminished across the cross-sectional area by W_D in all the directions perpendicular to the surfaces in contact with the electrolyte, and then the total current (I_{SD}) can be calculated as:

$$I_{SD} = \sigma \frac{A}{L} V_{SD} \tag{4.9}$$

where σ, A, and L are the conductivity (a material property), the cross-section, and the length of the silicon channel , respectively. At the point of zero charge, A coincides with the geometrical dimensions of the FinFET channel ($A = W \times h$) as pH increases [$A = (W - 2W_D) \times (h - W_D)$]. In this way, W_D is connected to the experimental data using the original geometrical cross-section and the actual resistance of the channel ($\rho = 1/\sigma$). Given the large aspect ratio, we have considered $h >> W_D$ and thus we have approximated as $A = (W - 2W_D) \times (h)$. This possibility to neglect the depletion width in one direction, is indeed the origin of the higher linearity of the high aspect ratio FinFET with respect to NWs described in our works [50, 51]. Figure 4.3 (a) shows two SEM pictures from different perspectives of a typical high aspect ratio FinFETs in which we have included schematics showing the electrical connections and the geometrical parameters W, h and L.

Figure 4.3 (b) shows I_{SD} vs. pH for the pair of devices with silica dielectric at three different degradation points (x=0.5nm, x=1.5nm and x=2.5nm shown in darker to lighter colours and using solid blue lines for the thinner sensor and green dashed lines for the thicker sensor). We illustrate that at an arbitrary pH, the acidity can be unequivocally determined using the current values that intersect for example the orange lines in figures 4.3(b), (c) and (d) that mark constant pH for values 3 and 10. For each of these pH values and for each state of degradation (x), figure 4.3(b) provides a pair of current values that will be observed on the pair of sensors at the intersection with the indicated orange lines with each of the curves respective to each degradation x. For each sensor alone, there are several combinations of pH vs degradation x that provide such currents values, but only at one point, a pair of currents converge with the same pH and degradation x. Figure 4.3(d) shows the equivalent situation for pH 10.

Both figures 4.2 and 4.3 show that at more basic pH values, the differences in signal between devices of the same material become smaller, and thus discriminating the value of the currents for each state of degradation becomes more difficult depending on the values of the noise signal. By this effect, also the determination of pH is also more affected by the noise signal at a more basic pH as the acidity has not acted on the surface potential that builds the depletion width W_D. This becomes also apparent comparing the range of pH variation for a given current in figures 4.3(c) and (d). The range of pH in the degradation span of our studies for each current is nearly three times larger for the pair of current values acquired at pH 3 (figure 4.3(c)) than for the ones at pH 10 (figure 4.3(d)), showing that the degradation can depend less in the measuring error in the first case. It is to be noted, that the current map calculations shown in figure 4.3 using our simultaneous of current vs. pH, is equivalent to an experimental mapping in a pair of devices with the same fabrication parameters except for oxide thickness, and where the simultaneous current response would be mapped during the degradation of the oxide. In such a case, we would bet a current map equivalent to figure 4.3(b). Given the broader response of SiO_2 to the degradation, it would require less precision on the determination of the current to obtain a match in the current response to a single pH compared to materials with less change with degradation, as for example the case of HfO_2. However, the lifetime and the variability of the sensor over time would still be beneficial for the material with higher chemical stability and dielectric constant.

4.4 Implementation of the proton affinity on the sensor response for non-linear sensitivities

Figure 3.8 in section 3.3.2 of Chapter 3 shows the relationship between α, Ψ_0 and pH. The model is able to reproduce the saturation of the surface potential observed in our previous experiments [50–52]. At pH=2, which is the point of zero charge for SiO_2, α has its minimum value. The origin of the surface potential Ψ_0 is also set equal to 0 at pH 2. Figure 3.8 shows that with
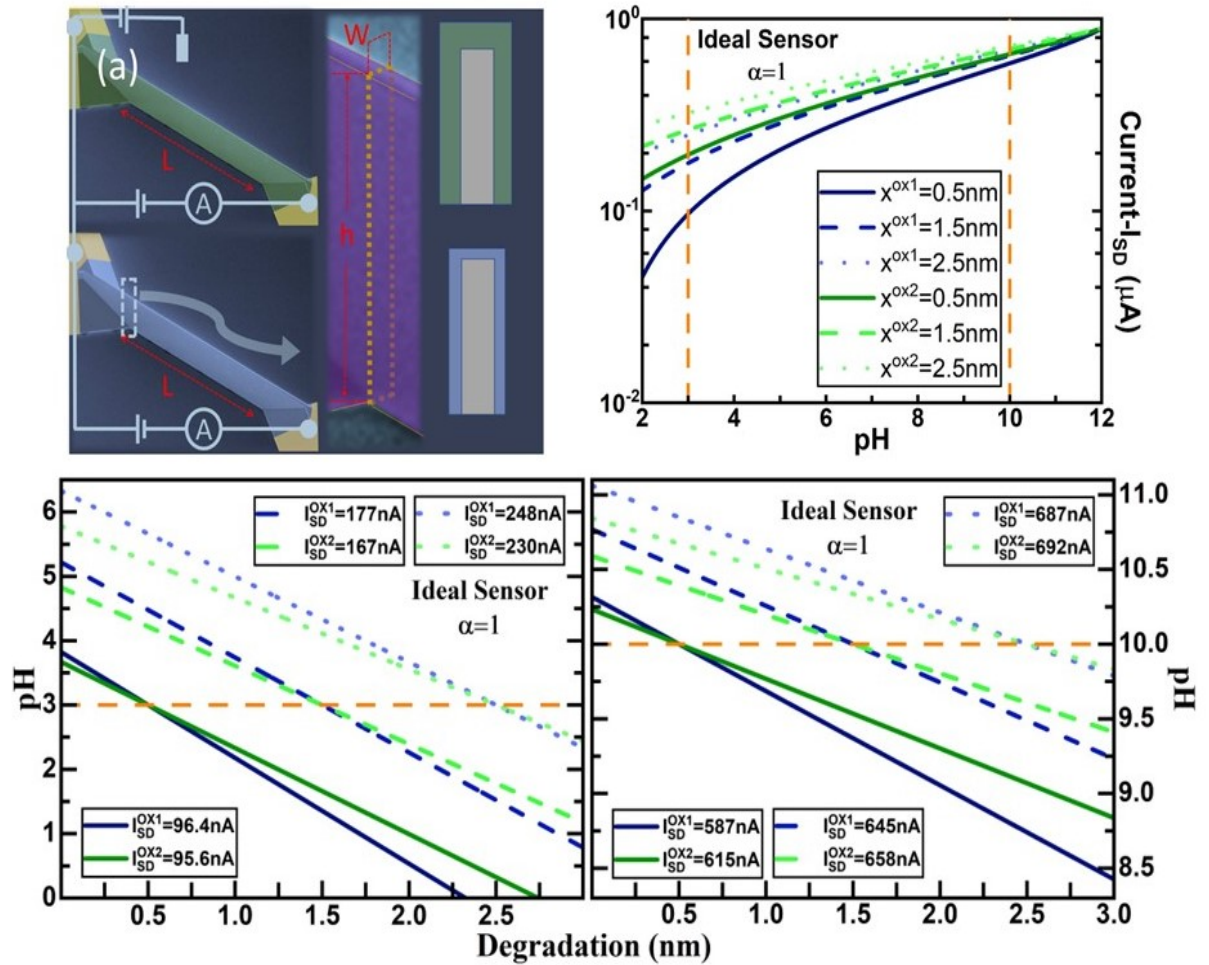
Figure 4.3: (a) SEM pictures from a typical FinFET device fabricated in LIST, schematically showing the electrical connections and the dimensions. In our work W, h and L have been chosen from 200nm, 2 mm and 10 mm, respectively. (b) Current (I_{SD}) as a function of the pH considering three degraded regions in the oxide (x=0.5nm, x=1.5nm, and x=2.5nm) for SiO_2 and two different ideal biosensors (a=1) having main difference is the oxide thickness (t_{ox1}=5nm and t_{ox2}=10nm). (c-d) Calculated pH as a function of the degradation (x) for SiO_2 and two different ideal biosensors (a=1) having the main difference is the oxide thickness (tox1=5nm and tox2=10nm). The pH has been calculated considering the W_D given by Equation 9 with three degraded regions in the oxide (x=0.5nm, x=1.5nm, and x=2.5nm) and an initial (c) pH=3 and (d) pH=10. The solid orange line represents the constant initial pH. Drain bias equals 50mV and calculated gate bias equals 0.5914V are used for the simulation.

increasing of the pH, the value of α becomes close to 1.0 (α must have a value between 0 and 1) and the surface potential Ψ_0 increases to a higher negative value. As the acidity is increased, the decrease in α results in the saturation of change in Ψ_0. It is also to be noted, that contrary to what is assumed in most cases, the behaviour of Ψ_0 is not linear through the pH range, and that has singularities due to the interplay of proton affinities with the double-layer capacitance.

Figure 4.4 shows I_{SD} vs. pH for a device couple of SiO_2 with corrected α. As in the case of the ideal sensitivity, the current values in both devices converge to the maximum at basic conditions due to the vanishing W_D. Contrary, when the pH is very acidic (pH = 2 or 3), there is a larger drift of the current values with x. The effect of the drift is even larger for the device with t_{ox1} in comparison to the t_{ox2}. This is expected due to the larger proportion of degraded material in the device with an oxide thickness equal to 5nm. Another interesting point is that both devices have an almost identical current profile for all pH values at maximum degradation of 3nm (I_{SD} vs pH curves with lighter colours). Hence, it seems that once the degraded region of the oxide dominates the contribution of the capacitance. The effects of the saturation of the sensitivity α are also observed in the acidic range for both currents simulated in figure 4.4 as the variation of I_{SD} vs pH decreases as the pH becomes more acidic. This loss of sensitivity affects also the determination of pH, as for a given noise signal, more pH values will fall within the range of error. However, this is a property of the material observed in the saturation of the surface potential in figure 3.8 which can not be resolved with a different operation mode.

The lines of constant I_{SD} at 20% of the total conductance ($I_{SD} = 0.2\mu A$) are indicated as horizontal orange lines in figure 4.4. It can be noticed, that the pH uncertainty associated with that measurement is much greater for the device with thinner oxide.

4.5 Optimisation of pH determination using a I_{SD} follower in one of the sensors

The current response obtained in figure 4.4 (a) and (b) can be used to reproduce the plan of action described at the end of section 4.3 to obtain the absolute pH. However, using a constant gate voltage is detrimental to the accuracy at more basic pH values due to the similar values between currents at different x because of the small values of W_D. The traditional method to measure the acidity follows the surface potential Ψ_0 by compensating with a voltage bias applied between the channel and the reference electrode to maintain a constant current, usually closed to one obtained with the threshold voltage of the transistor (maximum W_D), but not too low as to increase the signal to noise ratio.

Figures 4.5 (a) and (b) show the calculation of the gate voltage correction to maintain a current of 0.2 μA (equivalent to a W_D of 80 % of the width of the sensor) as a function of pH and for all the states of degradation within the range of our study for the devices with thinner and thicker dielectrics, respectively. The different curves of V_G vs pH for each state of degra-
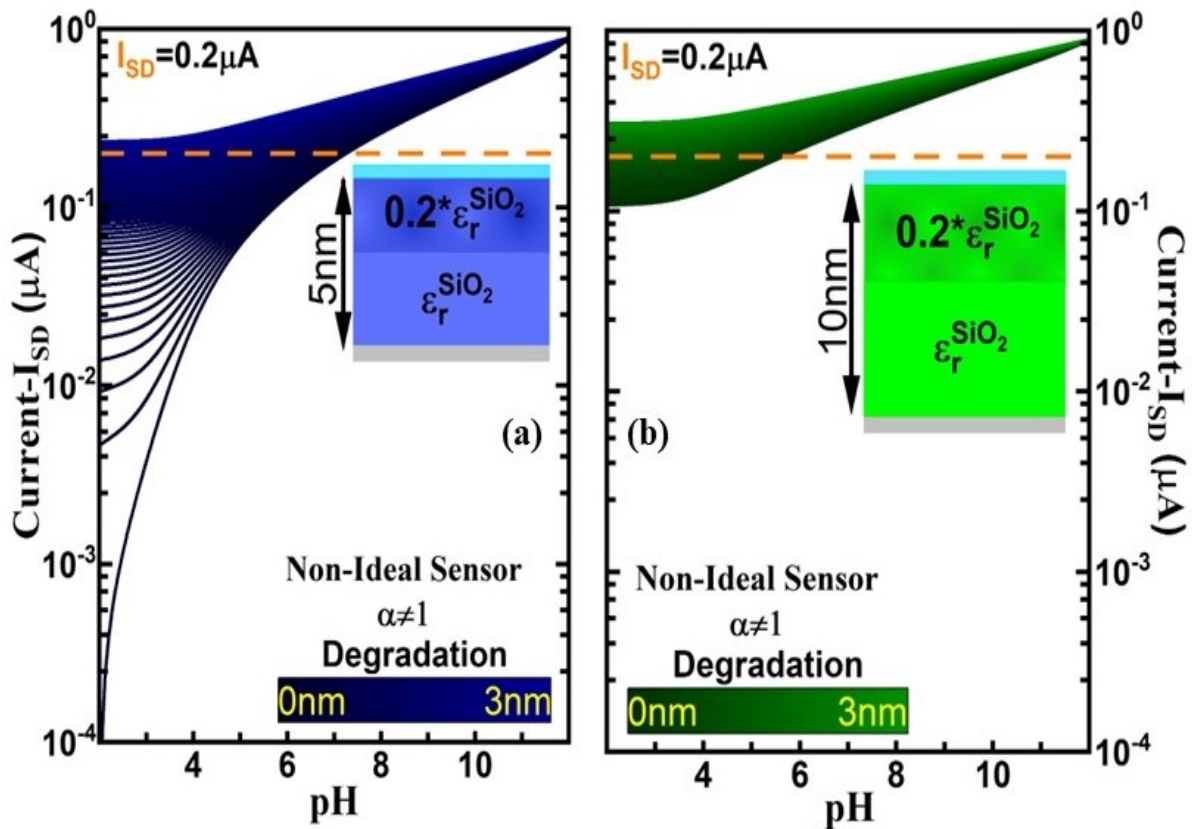
Figure 4.4: Current (I_{SD}) as a function of the pH considering different degraded regions in the oxide(x) from x=0nm (non-degraded oxide) to x=3nm for SiO_2 and two different non-ideal biosensors(α is self-consistently computed using the iterative method as shown in Chapter 3) which main difference is the oxide thickness ((a) t_{ox1}=5nm and (b) t_{ox2}=10nm). The solid orange line represents the example of the variation of the pH range for a constant I_{SD} =0.2mA. Drain bias equals 50mV and calculated gate bias equals 0.3825V are used for the simulation

dation are parallel to each other, showing an opposite behaviour to Ψ_0 (shown in figure 3.8) to compensate the charge accumulated due to the pH.

In order to use figure 4.5(a) and 4.5(b) as a map of values to determine the pH, we have to take into consideration that there is only a common reference electrode in the system. Consequently, only one of the devices can be kept at constant current I_{DS}. Here, we have arbitrarily chosen to maintain constant the device with the smaller oxide thickness, and use the map in figure 4.5(a) corresponding to a particular pH and state of degradation, while using the obtained values of V_G and parameter of degradation x to calculate the current that corresponds in the second device. Figure 4.5(c) and 4.5(d) show the possible values of pH vs. degradation that could be obtained at the values mapped for pH 3 and 10 respectively for both sensors shown in blue and green for the 5nm and 10nm sensors, respectively. We have extracted the values of V_G and the current of the second sensor obtained at the levels of degradation of 0.5nm, 1.5nm and 2.5nm. It can be observed that equally to the method of the current, for each pair of devices, there is a single point that determines the pH and the parameter of degradation. Comparing the slopes obtained in the pH determination using the current output figures 4.3(c) and 4.3(d) with the ones obtained with the mapping of V_G and the current of the second sensor in figure 4.5(c) and 4.5(d), we can notice that the later have a steeper slope. This signals also better determination as determined the range of degradation corresponds to a shorter range of pH with the best precision acquired in figure 4.5(c) of the determination only with the current. Thus, using current as the mapping parameter for an unknown variable "oxide degradation" and a controlled variable "operating bias", we were able to accurately determine the pH value with the help of two similar devices with different oxide thicknesses.

In conclusion, in this chapter, we have implemented the effect of the degradation at the dielectric barrier that induces the current drift. The derived model used a capacitance representing the degraded region which is adjusted with a phenomenological effective dielectric constant and depth connected in series with the capacitance of the rest of the non-degraded material with the original properties. We calculated the response of the degradation of the capacitance for two materials, SiO_2 and HfO_2 as examples of low and high dielectric constants, respectively. The relative effect of the degradation is higher for materials with lower dielectric strength. Also, without any correction, the materials with a higher dielectric constant have less uncertainty of the measured pH.

Using the modification of the capacitance with degradation, we propose a method to determine the absolute pH using a mapping of dual sensor response. We have used a mapping with calculations equivalent to a mapping that would be produced experimentally with reproducible devices. To simulate the effects of the chemical response of the materials, we have implemented the site-binding model interacting with stern and double-layer capacitances. This model does not take into account the modification of binding sites at the interface of the dielectric and the electrolyte. We have shown that using a common reference electrode at constant voltage, the
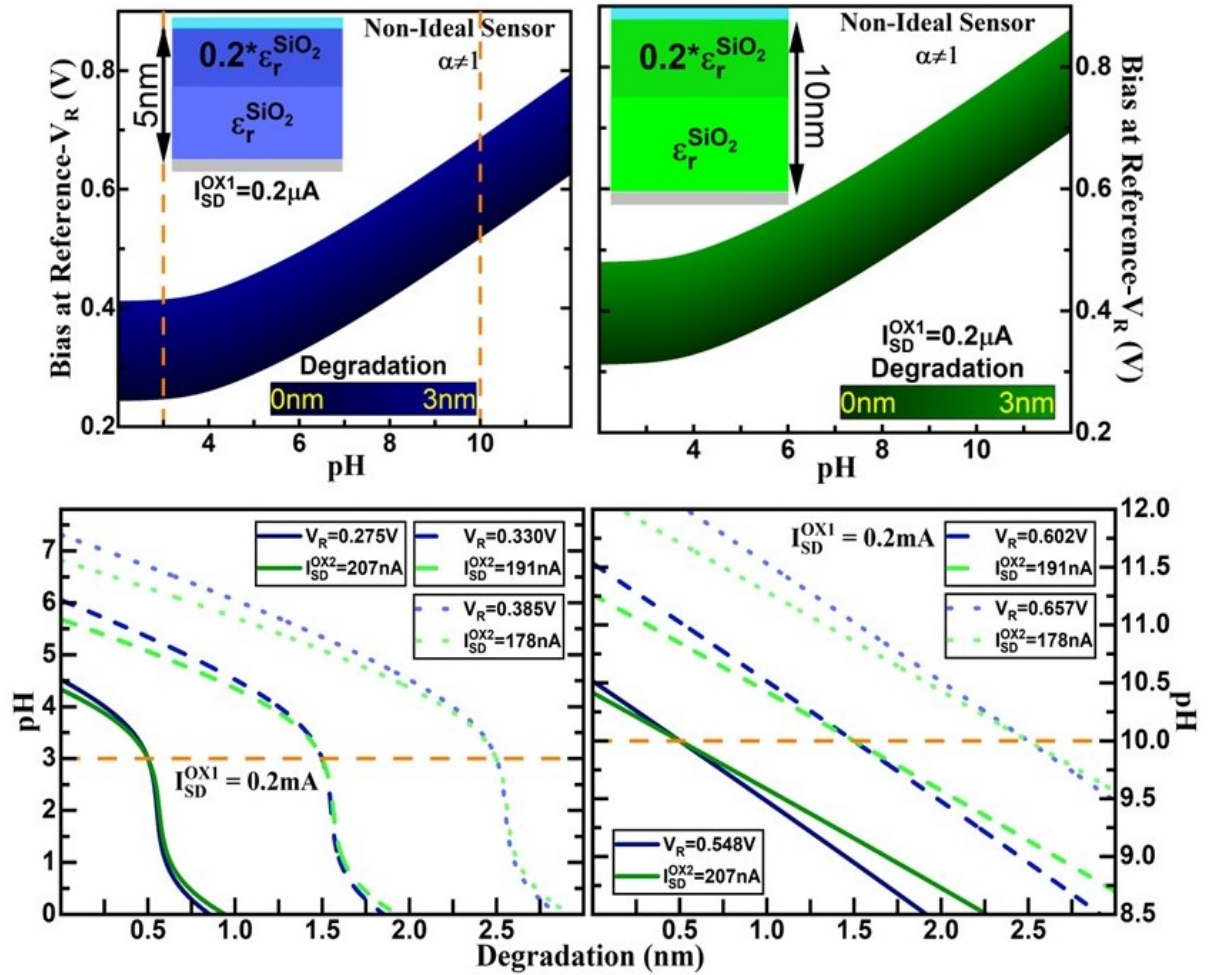
Figure 4.5: (a-b) External bias at the back gate (V_G) as a function of the pH calculated using Equation 3 for a constant I_{SD}=0.2mA considering different degraded regions in the oxide (x) from x=0nm (non-degraded oxide) to x=3nm for SiO_2 and two different non-ideal biosensors whose main difference is the oxide thickness ((a)t_{ox1}=5nm and (b)t_{ox2}=10nm). (c-d) Calcu-lated external bias at the back gate (V_G) as a function of the degradation (x) for SiO_2 and two different non-ideal biosensors whose main difference is the oxide thickness (tox1=5nm and tox2=10nm). The V_G has been calculated using Equation 3 considering the W_D given by Equa-tion 9 with three degraded regions in the oxide (x=0.5nm, x=1.5nm, and x=2.5nm) and an ini-tial (c) pH=3 and (d) pH=10. The solid orange line represents the constant V_G in which the curves for both devices cross. In all the figures (a-d), a is self-consistently computed using the iterative method as shown in Chapter 3

current values are less accurate to determine the pH at basic pH where there is less action of the acid and less depleted region in the semiconductor. This effect can be partially corrected using the voltage of the reference electrode as a current follower for one of the devices. However, in the case of materials like SiO_2, the effect of site-binding saturation at acidic pH also causes a decrease in the sensitivity, which affects also the possibility to determine the absolute pH.

Chapter 5

Effect of different oxides on Amino acid (AA) sensing

This chapter explores the effect of low-k, high-k and very high-k oxides for amino acid sensing. For this purpose, three types of oxides are considered -SiO_2, HfO_2 and TiO_2 having increasing k values respectively. We are interested in simulating amino acid (AA) because eventually, it will lead to protein sensing.

Amino acids are the basic building blocks for protein. Amino acids (AA) consist of an alpha-Carbon C_α or a tetrahedral carbon. This alpha-Carbon C_α or a tetrahedral carbon has one amine, tetrahedral nitrogen attached to the carbon. The other is carboxylic acid where carbon is double-bonded to oxygen and also attached to a hydroxyl OH. Also, a side chain -R is shown in figure 5.1 below.

This chapter shows the application of the Gouy-Chapman-Stern model described in section 3.3 of chapter 3 to amino acids (AA) on top of the oxides -SiO_2, HfO_2 and TiO_2. Or we can say extended to increasing surface complexity. This is an analytical model implemented in the MATLAB program and it is used for sensing different types of amino acids (AAs) such as Arginine (R), Aspartic acid (D), and Proline (P). We are increasing the surface complexity from a
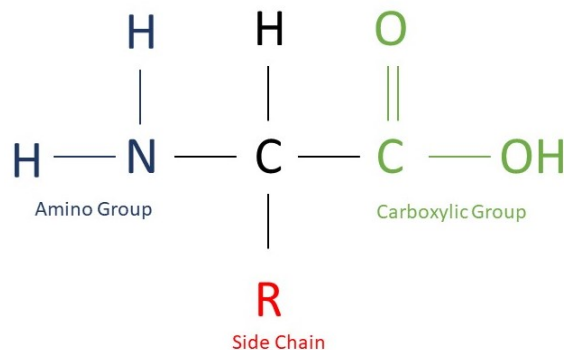
Figure 5.1: Structure of Amino acid showing the tetrahedral carbon having amine, carboxylic and R side chain.

simple oxide layer to the addition of AA. Moreover, in order to represent as close as possible the experimental environment in our model we have considered linker groups which provide the connections between the AA and gate oxides. The dielectric constant of the gate oxide has a significant impact on tuning the device's primary characteristics such as surface potential (Ψ_0) and intrinsic buffer capacity (β) which are used to evaluate the sensor's reliability and sensitivity. In order to show the capability of our model, in this chapter we have reported the simulation experiment with three amino acids (AAs) with different side chains. The three amino acids chosen are such that depending on the electrolyte and pH value of the solvent they can exist in basic (R), acidic (D) and neutral (P) forms in the solution. The main conclusion from our simulation is that our work shows each AA has a unique signature or fingerprint that can be used to distinguish and identify each AA [53].

This chapter is based on the publication by Dhar, R., Kumar, N., Garcia, C.P. and Georgiev, V., 2023. Deriving a novel methodology for nano-BioFETs and analysing the effect of high-k oxides on the amino-acids sensing application. Solid-State Electronics, 200, p.108525. I did MATLAB programming, made diagrams and did the writing for this Chapter.
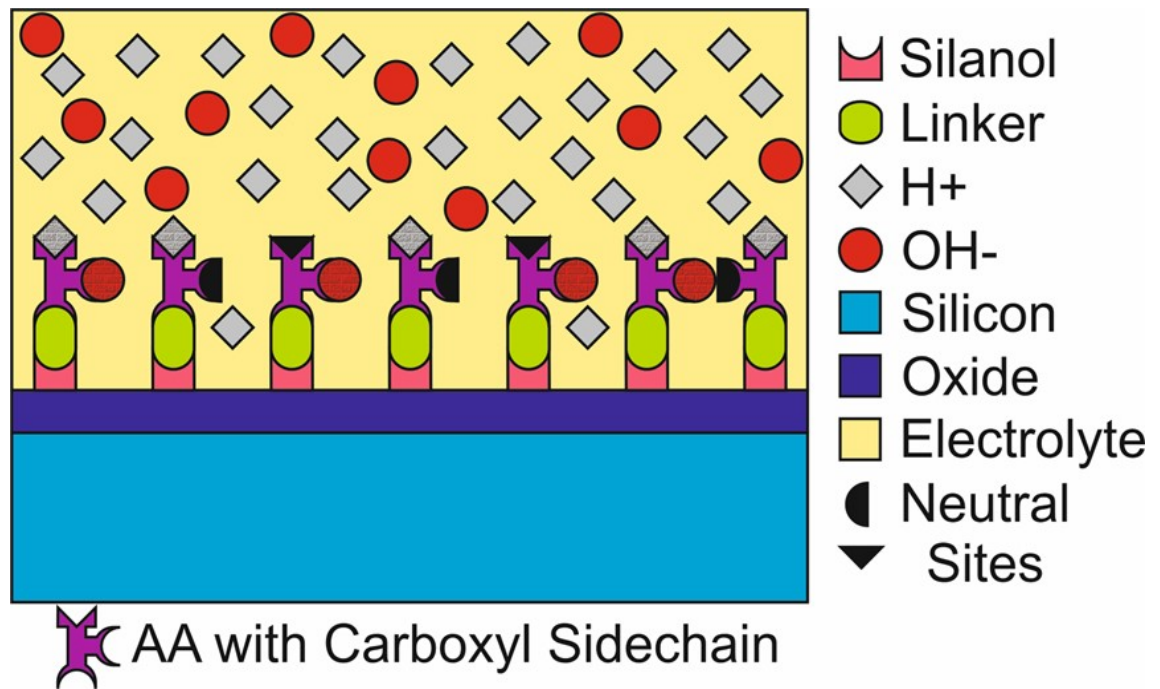
Figure 5.2: Schematic diagram of the BioFET sensor with immobilised amino acids over the oxide. AA denotes the amino acid with carboxyl sidechains (example-Aspartic Acid). At the very bottom, the light blue colour is the Silicon nanowire channel. Immediately on top of it, as seen in dark blue colour, is the oxide that can be TiO_2, HfO_2 or SiO_2. The Silanol groups (SiOH) are represented directly above SiO_2 in this case having pink colour. The top of a silanol group is covered with light green colour which is the linker also known as a polyethene glycol (PEG) layer. PEG is covalently bonded to the amino acids on one side and to silanol on the other as seen in purple colour. The AA has the possibility to be protonated/ deprotonated or to have active

5.1   Structure of FET with immobilized amino acids (AA)

Fig. 5.2 shows a schematic diagram of the ISFET sensor with immobilized amino acids over the gate oxide. AA is shown with carboxyl side chains (for example - aspartic acid as seen in the fig. 5.2). The light blue colour is the Silicon channel. Above that, as seen in dark blue is the oxide, silicon dioxide, in this case, SiO_2. Then comes the electrolyte shown in light yellow colour. The electrolyte is NaCl + H_2O (Salt and water). When the electrolyte comes in contact with the gate oxide, Silanol groups (SiOH) are formed as shown by the light pink colour having a crown shape. Various symbols are shown addressing the different chemical species in the solution, e.g. protons (H^+)and hydroxide anion (OH^-). The linker as seen in light green colour having an elliptical shape is used in experiments [54] and for simulation purposes as well here. The linker is a (3-Aminopropyl)trithoxysilane molecule or APTES for shorter. Biosensors use a linker for providing stability and affinity towards target molecules [55]. Linker connects the silanol group to AA by covalent bonds which are chemically very stable and more over the links passivates the silanol group on the oxide surface. Immediately above the linker in purple colour is AA with

a carboxyl sidechain having active sites, neutral sites, sites occupied with H^+ or sites occupied with OH^-. The active AA sites are shown by an inverted triangle with black colour. Next are the neutral sites meaning it is not possible for anything to attach to them. They are shown in a semi-circle in black colour. Sites occupied by H^+ ions are shown in a grey colour diamond shape. Sites occupied by OH^- are shown by a red colour circle. From Fig. 5.2 it is clear that the system under investigation is very complex with many chemical and biological species which must be considered if we want to describe accurately the sensing process in nano-biosensors. We want to emphasise that our simulation considers the equilibrium conditions of the solvent and our analytical model represents a static picture (snapshots).

The subsequent sections will explain how important parameters, Figures of Merit (FoM), like- zeta potential (Ψ_ξ), surface potential (Ψ_0), sensitivity, intrinsic buffer capacity (β), total capacitance (C_T), drain current (I_D) and depletion width (W_D) depend on the bulk value of the pH. More importantly, all of these FoM can be used as unique fingerprints for the identification of AAs and polypeptides.

5.2 Calculations of the Zeta Potential for oxides

The methodology used to calculate the zeta potential (Ψ_ξ) is as described in the previous chapter 3 section 3.3 of the Gouy-Chapman-Stern theory. Follow steps 1-3 and the value of zeta potential (Ψ_ξ) for all oxides- silicon dioxide SiO_2, hafnium oxide HfO_2 and titanium dioxide TiO_2 is obtained. The relative permittivity (ε_{SiO_2}, ε_{HfO_2} and ε_{TiO_2}) used are different for different oxides. The Eq. 3.30 is then modified as follows for each gate oxide.

$$\sigma_{gcsSiO_2} = \sqrt{8k_BT\varepsilon_{SiO_2}\varepsilon_0 c_0}sinh(\frac{q\Psi_{\xi SiO_2}}{2k_BT}) \tag{5.1}$$

where ε_{SiO_2} = 3.7 [56]

$$\sigma_{gcsHfO_2} = \sqrt{8k_BT\varepsilon_{HfO_2}\varepsilon_0 c_0}sinh(\frac{q\Psi_{\xi HfO_2}}{2k_BT}) \tag{5.2}$$

where ε_{HfO_2} = 25 [57]

$$\sigma_{gcsTiO_2} = \sqrt{8k_BT\varepsilon_{TiO_2}\varepsilon_0 c_0}sinh(\frac{q\Psi_{\xi TiO_2}}{2k_BT}) \tag{5.3}$$

where ε_{TiO_2} = 80 [57] The concentration c_0 = 0.1 M as mentioned previously which is a low concentration solution [25] [58].Rest remaining terms in the Eq.'s 5.1, 5.2, 5.3 are constants.

The surface charge density (σ_0) is then again calculated by the site-dissociation model/site-binding model as per Eq.3.6 for three different oxides SiO_2,HfO_2 and TiO_2.

$$\sigma_{0SiO_2} = qN_{sSiO_2}\frac{cH_s^2 - K_{aSiO_2}K_{bSiO_2}}{cH_s^2 + K_{bSiO_2}cH_s + K_{aSiO_2}K_{bSiO_2}} \tag{5.4}$$

where

N_{sSiO_2} = Number of sites for SiO_2 (in per cm^2)

K_{aSiO_2} = Acidic dissociation constant for SiO_2

K_{bSiO_2} = Basic dissociation constant for SiO_2

$$\sigma_{0HfO_2} = qN_{sHfO_2}\frac{cH_s^2 - K_{aHfO_2}K_{bHfO_2}}{cH_s^2 + K_{bHfO_2}cH_s + K_{aHfO_2}K_{bHfO_2}} \tag{5.5}$$

where

N_{sHfO_2} = Number of sites for HfO_2 (in per cm^2)

K_{aHfO_2} = Acidic dissociation constant for HfO_2

K_{bHfO_2} = Basic dissociation constant for HfO_2

$$\sigma_{0TiO_2} = qN_{sTiO_2}\frac{cH_s^2 - K_{aTiO_2}K_{bTiO_2}}{cH_s^2 + K_{bTiO_2}cH_s + K_{aTiO_2}K_{bTiO_2}} \tag{5.6}$$

where

N_{sTiO_2} = Number of sites for TiO_2 (in per cm^2)

K_{aTiO_2} = Acidic dissociation constant for TiO_2

K_{bTiO_2} = Basic dissociation constant for TiO_2

Ideally, the values obtained from equation 5.1 and equation 5.4 should be equal for SiO_2. And similarly, the values for equation 5.2 and equation 5.5 should be equal for HfO_2. Along with the values for equation 5.3 and equation 5.6 for TiO_2 should be equal.

However in this case they aren't when the values are drawn by the six equations, equation 5.1 to 5.6 mentioned above. This is so because we still need to find the "correct" value of zeta potential Ψ_ξ in order to solve the surface charge density. To solve this problem we have initialised the potential and we have solved the equations self-consistently. Hence, now we compare surface charge density obtained by Site-binding with that of the Gouy-Chapman Stern layer model. Checking which value is greater and deciding whether the higher potential or lower potential needs to be shifted for the bi-section method as described in the chapter above. We need to continue this comparison until the error in the surface charge density is < less than the tolerance (1e-50).

Figure 5.3 (a) has been obtained which shows the variation in zeta potential (Ψ_ξ) with respect to pH for three different oxides namely SiO_2, HfO_2 and TiO_2. As can be seen from the figure 5.3(a), the pH_{pzc} for SiO_2,HfO_2 and TiO_2 can be easily recognized from the simulated graphs. Ψ_ξ is the potential on the shear plane [59], which is most negative for the SiO_2 due to its higher affinity for losing protons and Ψ_ξ is most positive for HfO_2 because of its higher pK value of protonated sites. For SiO_2, the pH_{pzc} is in agreement with the experimental value [60]. In the case of HfO_2 and TiO_2, the pH_{pzc} simulation value differs from the data available in the literature [28], [61], [62]. This may be attributed to the ways in which oxides are grown and impurities present on the surface of oxides [63], [60].

Figure 5.3 (b) is the graph of the sensitivity factor (α) as a function of the bulk pH. $\alpha = 1$ is the ideal case meaning the device is highly sensitive. This has been called the ideal case as a small change in pH does not cause a change in sensitivity. When $\alpha < 1$, it is a non-ideal case and the device is less sensitive. Since during this region, a small change in pH causes a large change in sensitivity. During the higher values of pH, α has a value nearer to 1 and constant. It means there is no change in sensitivity to the change in pH. For lower values of pH, α has a non-linear trend and values are less than 1. It means that there is a huge change in sensitivity to the change in pH. It can be noted from fig. 5.3 (b) that α has lowest values (almost near to zero) for SiO_2, HfO_2 and TiO_2 when pH = pH_{pzc}. As the Ψ_ξ becomes negative or positive, the α increases on both sides due to an increase in Ψ_ξ away from the pH_{pzc}. Also the equation 3.19 has C_{diff} and β_{diff} terms. From equation 3.26, it is noted that it has a cosine hyperbolic term. The increase in the α on both sides of pH_{pzc} can also be attributed to this. Equation 5.7 - equation 5.9 shows the values for α of different types of oxides:

$$\alpha_{SiO_2} = \frac{1}{1 + 2.303\frac{k_B T C_{diffSiO_2}}{q^2 \beta_{diffSiO_2}}} \tag{5.7}$$

$$\alpha_{HfO_2} = \frac{1}{1 + 2.303\frac{k_B T C_{diffHfO_2}}{q^2 \beta_{diffHfO_2}}} \tag{5.8}$$

$$\alpha_{TiO_2} = \frac{1}{1 + 2.303\frac{k_B T C_{diffTiO_2}}{q^2 \beta_{diffTiO_2}}} \tag{5.9}$$

Where equation 5.10 - equation 5.12 shows the values of $C_{diffSiO_2}$, $C_{diffHfO_2}$ and $C_{diffTiO_2}$ respectively.

$$C_{diffSiO_2} = \sqrt{\frac{2q^2 \varepsilon \varepsilon_0 c_0}{K_B T}} cosh(\frac{q\Psi_{0SiO2}}{2K_B T}) \tag{5.10}$$

$$C_{diffHfO_2} = \sqrt{\frac{2q^2 \varepsilon \varepsilon_0 c_0}{K_B T}} cosh(\frac{q\Psi_{0HfO2}}{2K_B T}) \tag{5.11}$$

$$C_{diffTiO_2} = \sqrt{\frac{2q^2 \varepsilon \varepsilon_0 c_0}{K_B T}} cosh(\frac{q\Psi_{0TiO2}}{2K_B T}) \tag{5.12}$$

where equation 5.13 - equation 5.15 shows values of Ψ_{0SiO_2}, Ψ_{0HfO_2} and Ψ_{0TiO_2}

$$\Psi_{0SiO_2} = \frac{\sqrt{8k_B T \varepsilon \varepsilon_0 c_0} sinh(\frac{q\Psi_{\xi SiO_2}}{2k_B T})}{C_{stern}} + \Psi_{\xi SiO_2} \tag{5.13}$$

$$\Psi_{0HfO_2} = \frac{\sqrt{8k_B T \varepsilon \varepsilon_0 c_0} sinh(\frac{q\Psi_{\xi HfO_2}}{2k_B T})}{C_{stern}} + \Psi_{\xi HfO_2} \tag{5.14}$$

$$\Psi_{0TiO_2} = \frac{\sqrt{8k_BT\varepsilon\varepsilon_0c_0}sinh(\frac{q\Psi_{\xi TiO_2}}{2k_BT})}{C_{stern}} + \Psi_{\xi TiO_2} \tag{5.15}$$

And equation 5.16 - equation 5.18 shows the values of β_{intSiO_2}, β_{intHfO_2} and β_{intTiO_2} respectively.

$$\beta_{intSiO_2} = 2.303N_{sSiO_2}H_{surf}\frac{K_{bSiO_2}H_{surf}^2 + 4K_{aSiO_2}K_{bSiO_2}H_{surf} + K_{aSiO_2}K_{bSiO_2}^2}{(K_{aSiO_2}K_{bSiO_2} + K_{bSiO_2}H_{surf} + H_{surf}^2)^2} \tag{5.16}$$

$$\beta_{intHfO_2} = 2.303N_{sHfO_2}H_{surf}\frac{K_{bHfO_2}H_{surf}^2 + 4K_{aHfO_2}K_{bHfO_2}H_{surf} + K_{aHfO_2}K_{bHfO_2}^2}{(K_{aHfO_2}K_{bHfO_2} + K_{bHfO_2}H_{surf} + H_{surf}^2)^2} \tag{5.17}$$

$$\beta_{intTiO_2} = 2.303N_{sTiO_2}H_{surf}\frac{K_{bTiO_2}H_{surf}^2 + 4K_{aTiO_2}K_{bTiO_2}H_{surf} + K_{aTiO_2}K_{bTiO_2}^2}{(K_{aTiO_2}K_{bTiO_2} + K_{bTiO_2}H_{surf} + H_{surf}^2)^2} \tag{5.18}$$

Figure 5.3 (c) shows β has a similar trend with respect to pH_B as that of α. It is so because β denotes the change in surface charge density (σ_0) with respect to surface pH (pH_S) as shown in equation 5.19 [28]. The ability of the surface to store charge on the surface after changes in the H^+ ions concentration on the surface is called the intrinsic buffer capacity. Hence it can be observed that for all the pH_{pzc} of SiO_2, HfO_2 and TiO_2 the value of β is the lowest. It means there is no change in the surface charge at pH_{pzc} or it is zero.

$$\frac{\delta\sigma_0}{\delta pH_S} = -q\beta_{int} \tag{5.19}$$

5.3   Calculations of Surface potential for oxides

In the analytical simulation methodology as described in chapter 3, the zeta potential (Ψ_ξ) is obtained first. From equation 5.13 - equation 5.15 then we can obtain the surface potentials Ψ_0 for SiO_2, HfO_2 and TiO_2. Figure 5.4 (a) shows the variation of surface potential with respect to bulk pH for different types of oxides SiO_2, HfO_2 and TiO_2. The trend is similar to that of Ψ_ξ clearly showing the pH_{pzc}'s for all oxides including the addition of stern layer potential (Ψ_{stern}). Non-linearity of Ψ_0 for TiO_2 and SiO_2 is due to the large difference between the affinity constants [61].

Figure 5.4 (b) shows the 2nd order derivative of Ψ_0 with respect to bulk pH. It shows the transition of reactive sites over the oxide from protonation to deprotonation clarifying the pH_{pzc} value for all three oxides - SiO_2, HfO_2 and TiO_2. All curves cross the zero value of the 2nd
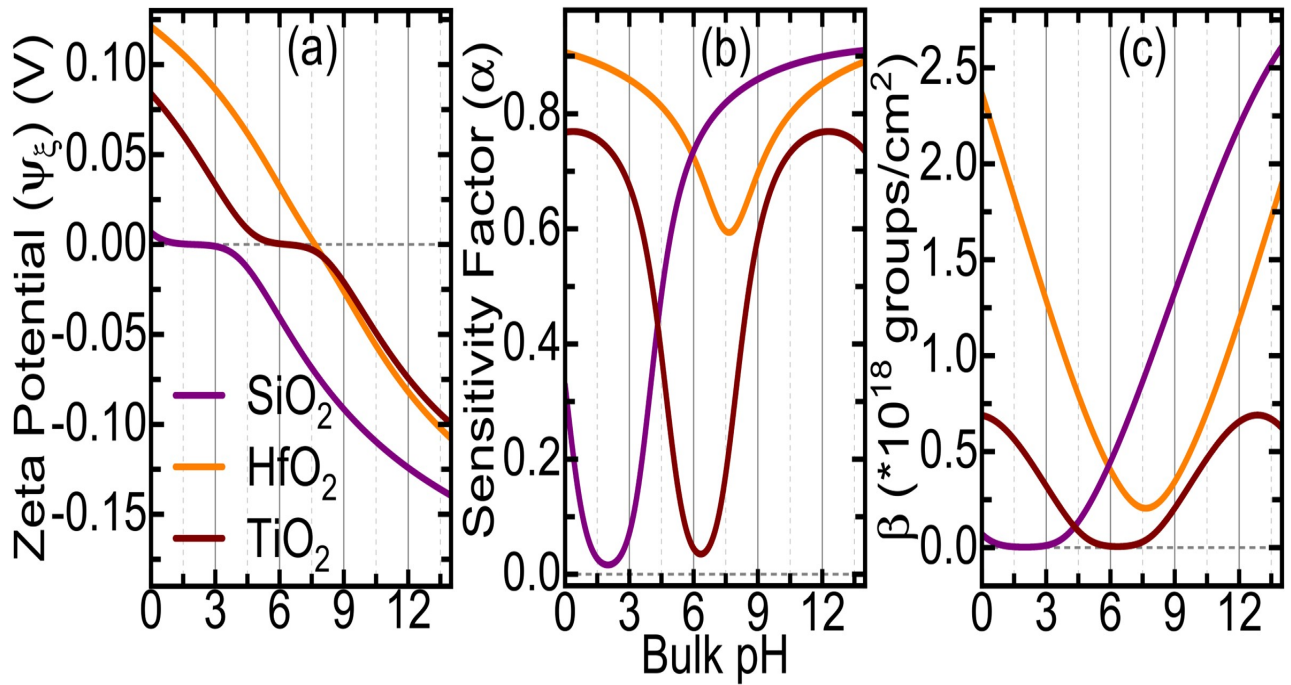
Figure 5.3: (a) Zeta potential (Ψ_ξ),(b) Sensitivity factor (α), (c) Intrinsic buffer capacity (β) variation in relation to pH for three different gate oxide materials

order derivative of Ψ_0 at a pH value which corresponds to the point of zero charge. Indeed, this is consistent with the experimental observation and the simulation methodology.

Figure 5.4 (c) shows the total capacitance or equivalent capacitance for all the three oxides considered in this case. Total capacitance (C_T) is calculated by considering the following capacitance in series:

(i) C_{ox} (Oxide capacitance - SiO_2, HfO_2 or TiO_2)

(ii) C_{stern} (Stern layer capacitance depending on the oxide)

(iii) C_{dl} (Diffusive layer capacitance depending on the oxide)

As all these capacitance (i)-(iii) are connected in series, their total capacitance can be calculated as shown in the equation 5.20 below [28]:

$$\frac{1}{C_T} = \frac{1}{C_{ox}} + \frac{1}{C_{stern}} + \frac{1}{C_{dl}} \tag{5.20}$$

The total capacitance for TiO_2 is the highest because the TiO_2 permittivity is higher compared to HfO_2 which is next and SiO_2 which has the least permittivity of all.

5.4 Amino Acids (AA) fingerprints

In Fig. 5.2 the AAs are immobilized by the carboxylic terminal leaving the AA with lower affinity sites. As an example, aspartic acid (D) is immobilized over the linker with a carboxylic terminal which eliminates the affinity corresponding to the C- terminal is shown.
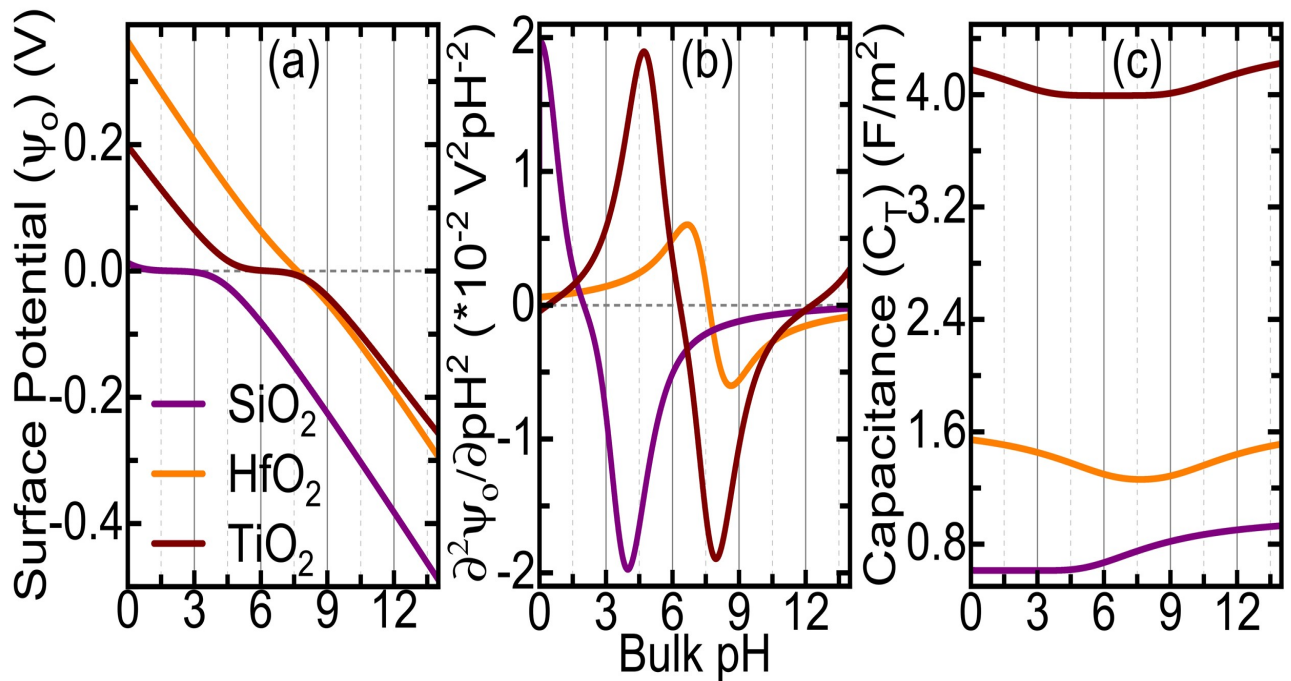
Figure 5.4: (a) Surface potential (Ψ_0), (b) 2nd order derivative of Ψ_0, (c) total capacitance (C_T) Vs pH. Graphs are shown for three different types of gate oxide materials

C-Imm. R on PEG

C-Imm. R on PEG
protonated once
$pK_b^2 = 9.04$

C-Imm. R on PEG
protonated once
$pK_x^3 = 12.48$

C-Imm. R on PEG
protonated twice
$pK_b^2 = 9.04$
$pK_x^3 = 12.48$
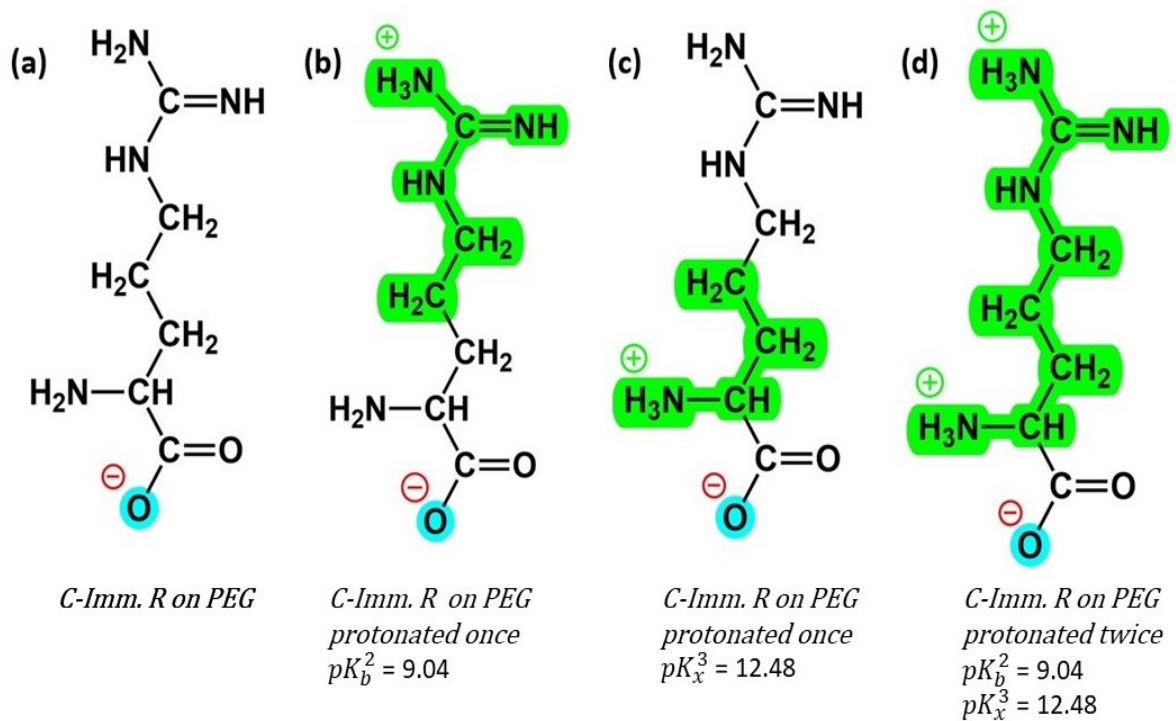
Figure 5.5: (a) shows the structure of C-immobilized Arginine(R) amino acids (AA) over PEG, the blue highlight means that it is attached to PEG forming a covalent bond (b) shows the protonation in 1st amine side chain, highlighted in green (c) shows protonation in 2nd amine, highlighted in green (d) shows protonation in both the amine
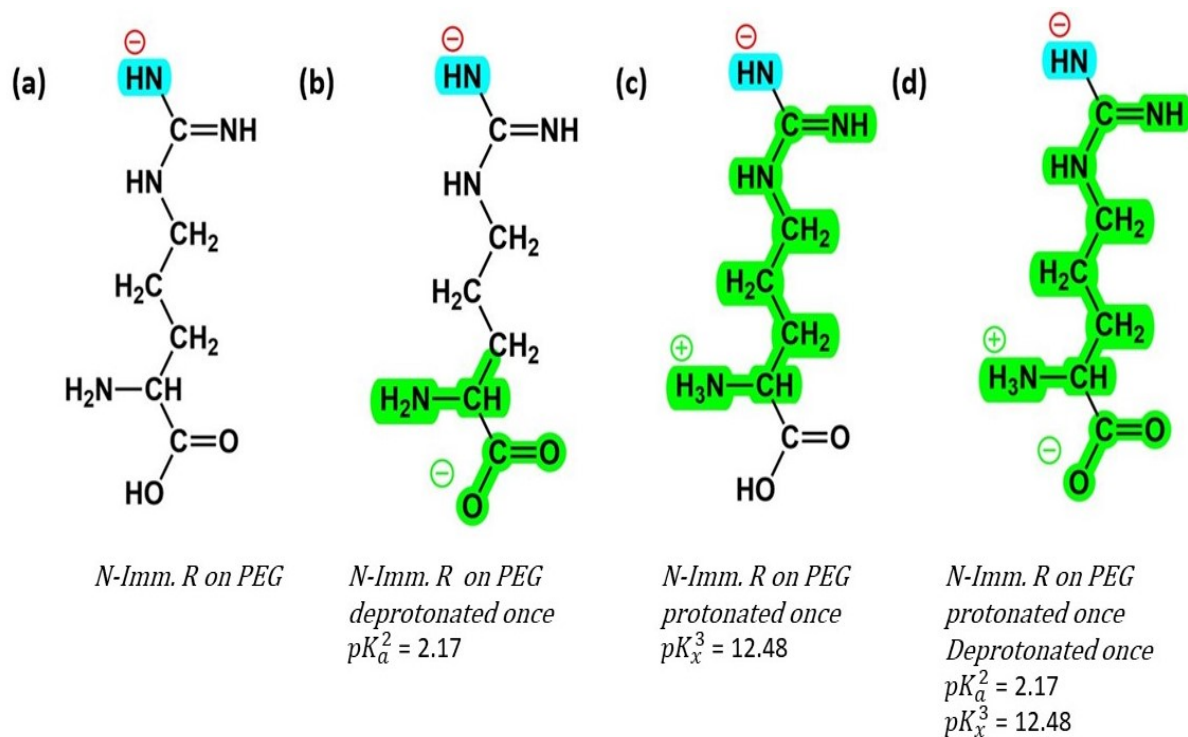
Figure 5.6: (a) shows the structure of N-immobilized Arginine(R) amino acids (AA) over PEG, the blue highlight means that it is attached to PEG forming a covalent bond (b) shows the deprotonation in carboxylic, highlighted in green (c) shows protonation in amine, highlighted in green (d) shows both- protonation in the amine and deprotonation in carboxylic
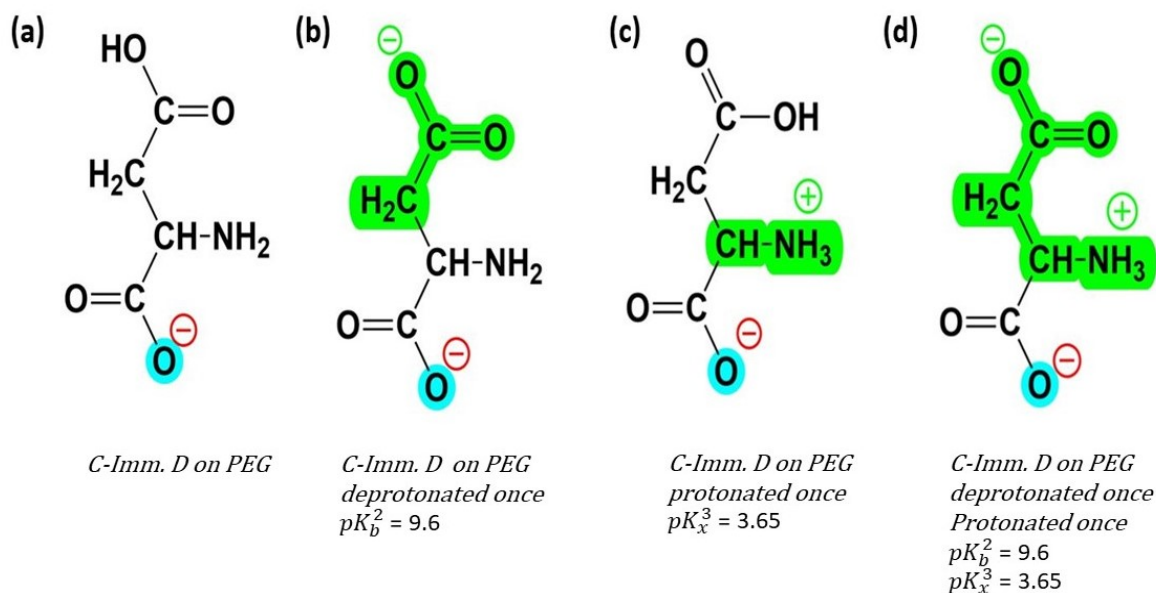
Figure 5.7: (a) shows the structure of C-immobilized Aspartic(D) amino acids (AA) over PEG, the blue highlight means that it is attached to PEG forming a covalent bond (b) shows the deprotonation in the carboxylic, highlighted in green (c) shows protonation in amine, highlighted in green (d) shows both- protonation in the amine and deprotonation in carboxylic

(a)	(b)	(c)	(d)
N-Imm. D on PEG	N-Imm. D on PEG deprotonated once $pK_a^2 = 1.88$	N-Imm. D on PEG deprotonated once $pK_x^3 = 3.65$	N-Imm. D on PEG deprotonated twice $pK_a^2 = 1.88$ $pK_x^3 = 3.65$
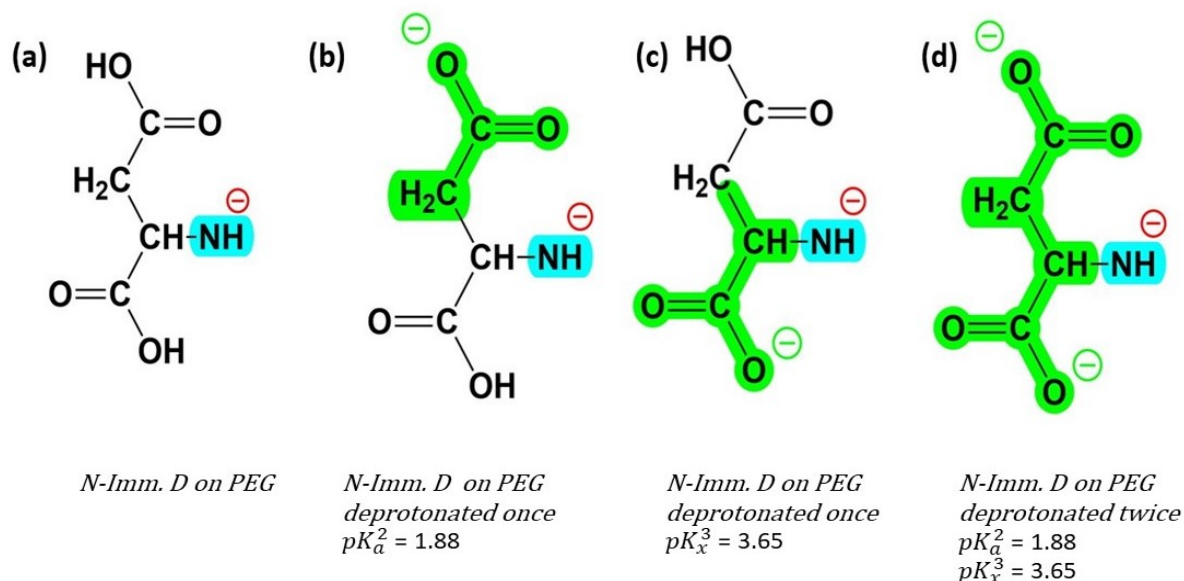
Figure 5.8: (a) shows the structure of N-immobilized Aspartic(D) amino acids (AA) over PEG, the blue highlight means that it is attached to PEG forming a covalent bond (b) shows the deprotonation in 1st carboxylic, highlighted in green (c) shows deprotonation in 2nd carboxylic, highlighted in green (d) shows deprotonation in both carboxylic

(a)	(b)	(c)	(d)
C-Imm. P on PEG	C-Imm. P on PEG protonated $pK_a^1 = 1.99$	N-Imm. P on PEG	N-Imm. P on PEG deprotonated $pK_b^2 = 10.66$
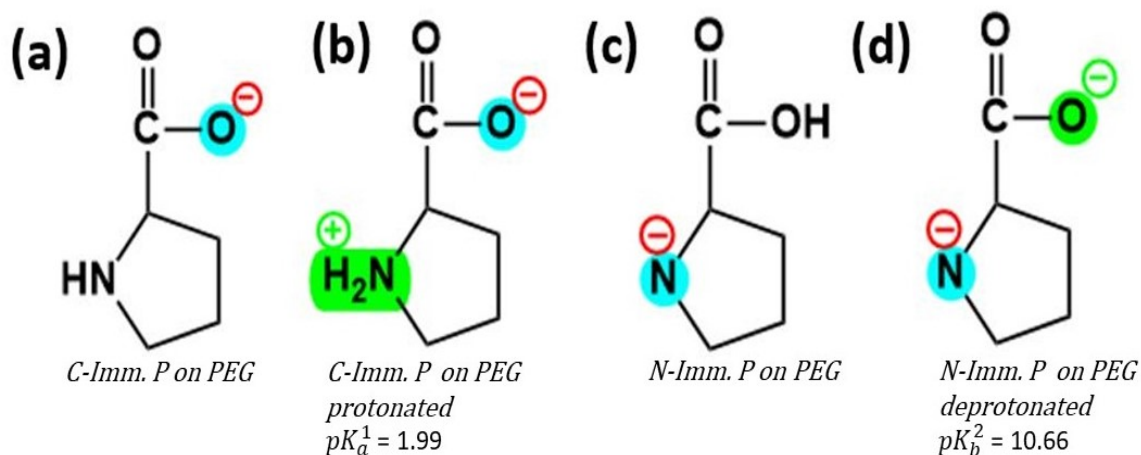
Figure 5.9: (a) shows the structure of C-immobilized Proline amino acids (AA) over PEG, the blue highlight means that it is attached to PEG forming a covalent bond (b) shows protonation of the amine (c) shows the structure of N-immobilized Proline amino acids (AA) over APTES, the blue highlight means that it is attached to PEG forming a covalent bond (d) shows deprotonation of carboxylic
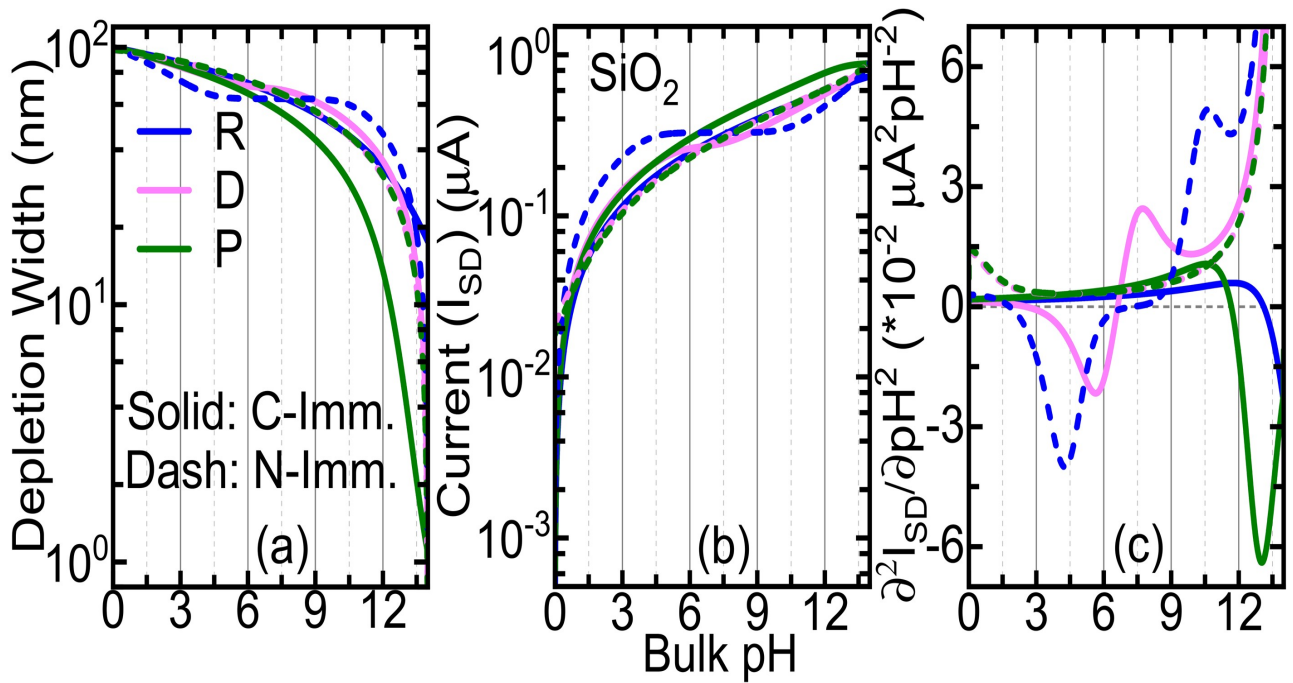
Figure 5.10: (a) Depletion width (W_D) (b) drain current (I_{SD}) and (c) 2nd order derivative of I_{SD} (Graphs shown are for Arginine (R), Aspartic Acid (D) and Proline (P) amino acids considering SiO_2 as a gate oxide with carboxyl group immobilised (solid line: C-Imm) and amine group immobilised (dash line: N-Imm).

Fig. 5.5 (a) shows C-immobilised Arginine (R) amino acids (AA). Fig. 5.5 (b),(c),(d) shows all its possibilities when it interacts with electrolytes of varying pH.

Fig. 5.6 (a) shows N-immobilised Arginine (R) amino acids (AA). Fig. 5.6 (b),(c),(d) shows all its possibilities when it interacts with electrolytes of varying pH.

Fig. 5.7 (a) shows C-immobilised Aspartic (R) amino acids (AA). Fig. 5.7 (b),(c),(d) shows all its possibilities when it interacts with electrolytes of varying pH.

Fig. 5.8 (a) shows N-immobilised Aspartic (R) amino acids (AA). Fig. 5.8 (b),(c),(d) shows all its possibilities when it interacts with electrolytes of varying pH.

Fig. 5.9 (a) shows C-immobilised Proline (P) amino acids (AA). Fig. 5.9 (b) shows all its possibilities when it interacts with electrolytes of varying pH. Similarly, fig. 5.9 (c) shows C-immobilised Proline (P) amino acids (AA). Fig. 5.9 (d) shows all its possibilities when it interacts with electrolytes of varying pH.

As the last step, we consider SiO_2, HfO_2 and TiO_2 as an oxide surface for the immobilization of the three different AAs (R, D and P). Two variants of each AA are considered C-Imm. and N-Imm. (carboxylic or amine terminal is immobilized respectively). The full surface coverage (no active silanol active groups on the surface) by the AA is considered for simulation. In this thesis, the FET surfaces considered were completely covered with linker and amino acids.

Fig.5.10(a), fig.5.11 (a) and fig.5.12 (a) show the depletion width (W_D) variation with respect to pH_B for different AAs (R,D,P) immobilised (C-Imm. or N-Imm.) over the SiO_2, HfO_2 and
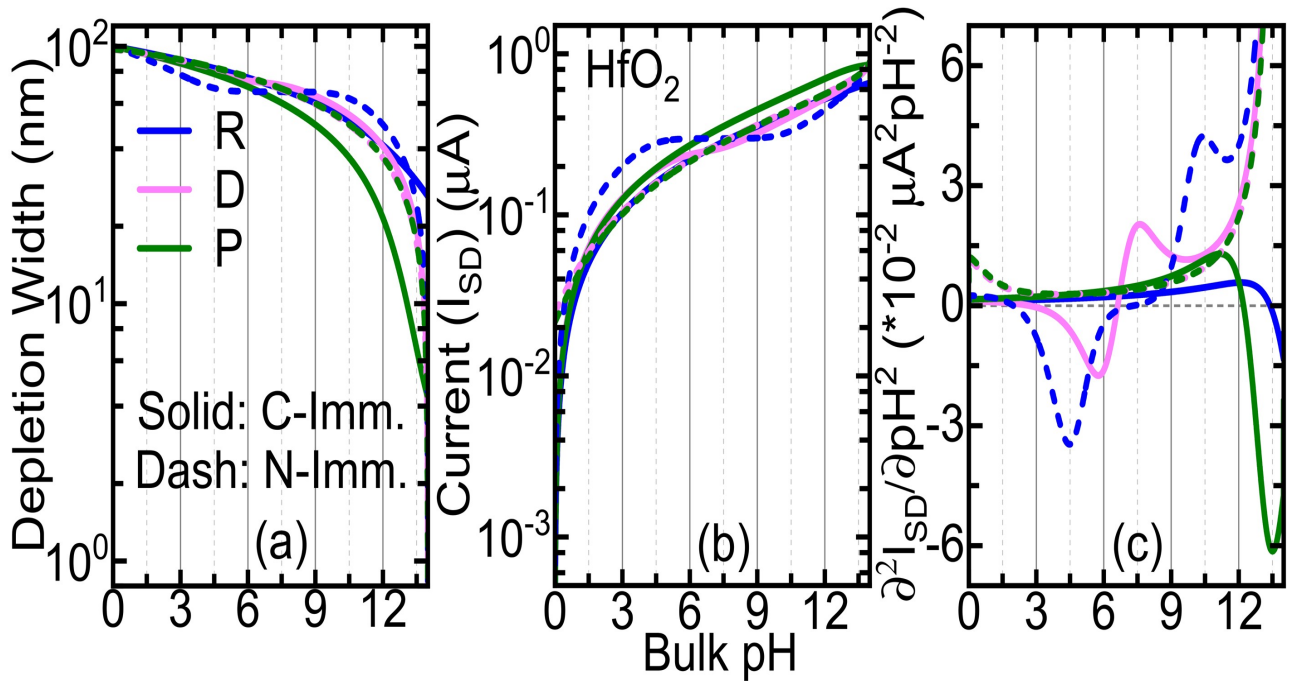
Figure 5.11: (a) Depletion width (W_D) (b) drain current (I_{SD}) and (c) 2nd order derivative of I_{SD} (Graphs shown are for Arginine (R), Aspartic Acid (D) and Proline (P) amino acids considering HfO_2 as a gate oxide with carboxyl group immobilised (solid line: C-Imm) and amine group immobilised (dash line: N-Imm).
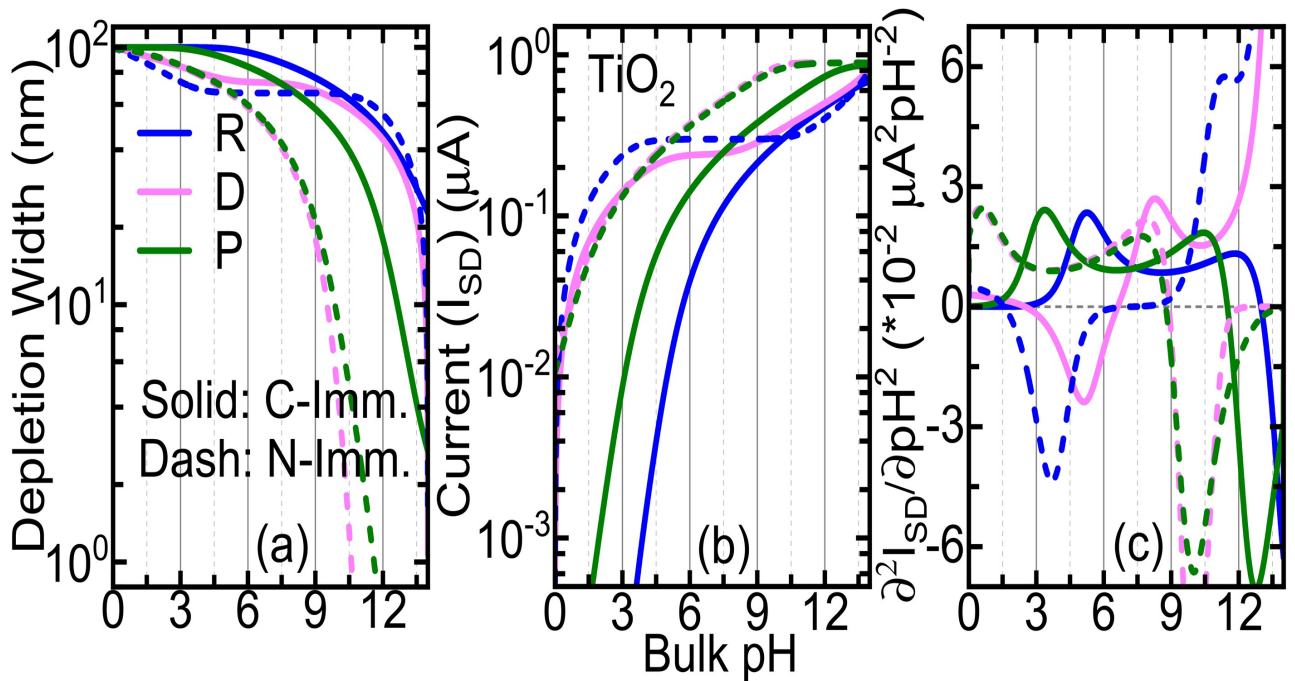
Figure 5.12: (a) Depletion width (W_D) (b) drain current (I_{SD}) and (c) 2nd order derivative of I_{SD} (Graphs shown are for Arginine (R), Aspartic Acid (D) and Proline (P) amino acids considering TiO_2 as a gate oxide with carboxyl group immobilised (solid line: C-Imm) and amine group immobilised (dash line: N-Imm).

TiO$_2$ as gate oxide respectively. The depletion width (W_D) is given in [23] and by equation 5.21 below.

$$W_D = -\frac{\varepsilon_{Si}}{C_{ox}} + \sqrt{(\frac{\varepsilon_{Si}}{C_{ox}})^2 - 2(\frac{\varepsilon_{Si}}{qN_A})(\Psi_0 + V_G)} \tag{5.21}$$

where

$\varepsilon_{Si} = \varepsilon_r.\varepsilon_0$ (relative permittivity of Si)

C_{ox} = Oxide capacitance

Ψ_0 = Surface potential

V_G = Gate Voltage

N_A = The density of dopants in the semiconductor

Considering the ISFET to be completely depleted at the lowest pH, a shift in surface potential towards negative decrease the depletion width as seen from Fig.5.10(a), fig.5.11 (a) and fig.5.12 (a). With the same depletion width at the lowest pH, the higher permittivity of *TiO$_2$* amplified the effect of Ψ_0 to further decrease the depletion width as compared to the *SiO$_2$* and *HfO$_2$*.

From Fig.5.10(a), fig.5.11 (a) and fig.5.12 (a), it can be seen that N-Imm. R and C-Imm. D have same wave kind of trend as compared to rest AA's. This can be understood from fig. 5.6 and fig. 5.7, they have deprotonated carboxylic side chains in lower pH values which reduces the depletion width. As the pH increases, it causes protonation of the amine side chains as seen in 5.6 (c) and fig. 5.7 (c). This leads to the depletion width decreasing for lower pH and increasing for higher pH.

Fig.5.10(b), fig.5.11(b) and fig.5.12(b) represent the drain current (I_{SD}) variation with respect to the *pH$_B$* for *SiO$_2$*, *HfO$_2$* and *TiO$_2$* as gate oxide respectively.The drain is current I_{SD} is given in [23] by equation 5.22 below:

$$I_{SD} = \sigma \frac{A}{L} V_{SD} \tag{5.22}$$

where

σ = conductivity

A = cross-section area

L = length of Si channel

V_{SD} = Drain to source voltage As the depletion width (W_D) increases in a pMOS, the I_{SD} decreases and vice versa as per the theory explained in section 2.7 of chapter 2. The same can be seen when we compare fig.5.10(a), fig.5.11 (a) and fig.5.12 (a) with fig.5.10(b), fig.5.11(b) and fig.5.12(b) respectively. The N-Imm. D and N-Imm. P is closer to each other as compared with C-Imm. D and C-Imm. P as seen in fig. 5.12(b). This behaviour can be understood from fig.5.8 (b),(c),(d) and fig. 5.9 (d). From these, it is observed that there is deprotonation taking place at all pH values as there are no amine groups and it becomes very difficult to identify them. Fig. 5.9 (a) and fig. 5.5 (a) undergoes protonation only as compared to fig. 5.7 (a) which undergoes

protonation and deprotonation both. Hence, making it easier to distinguish.

Fig.5.10(c), fig.5.11(c) and fig.5.12(c) show the immobilized AAs ISFET behaviour in terms of $\frac{\partial^2 I_{SD}}{\partial pH^2}$ for SiO_2, HfO_2 and TiO_2 respectively. C-Imm. R and P exhibit positive charges on the oxide surface across the pH range due to the presence of only amine sites. Also, the positive charge acquired by C-Imm. R is more than C-Imm. P due to an extra amine side chain. C-Imm. D is more balanced due to the presence of one C-terminal side chain and one N-terminal with an isoelectric point at pH = 6.625.

N-Imm. D and N-Imm. P result in negative charges over the surface across the pH range due to the presence of only carboxylic sites. N-Imm. D has an extra carboxylic compared to N-Imm. P. N-Imm. R is balanced with an isoelectric point at pH = 7.325 similar to the C-Imm. D.

Different site-binding relations are used to calculate the Ψ_0 and the affinity of remaining amine/carboxyl sites is responsible for the distinct fingerprints of the AAs in I_{SD} and $\frac{\partial^2 I_{SD}}{\partial pH^2}$. TiO_2 helped in generating more distinct fingerprints in terms of inflection points while maintaining the same zero-crossover points as compared to the SiO_2 and HfO_2.This can be attributed to the high dielectric constant of TiO_2.

Chapter 6

TCAD Simulation Results

To explore different structures and geometries, this PhD project will perform numerical simulations. The numerical simulations are carried out in Synopsys Sentaurus TCAD software. As seen in chapter 4 that SiO_2 is the best-suited oxide for our application. We are going to use SiO_2 as a gate oxide for our holistic simulations in this chapter. This chapter introduces the device in the simulations in addition to the analytical models of chapter 3. This will give us a holistic view of how the ISFET behaves. This includes the heterogenous surface along with the homogenous surface. In order to do this, the results of analytical simulations mentioned in section 3.3 can be used as input parameters to numerical simulations that may include other factors such as the device heterogeneity or the spatial distribution of charges, as it is described in this chapter. The combination of analytical modelling and numerical simulations allows additional flexibility, which will help us explore the operation of the ISFET responses and the design of FET-based biosensors.

This chapter is based on the publication by Dhar, R.P.S., Kumar, N., Medina-Bailon, C., García, C.P. and Georgiev, V.P., 2021, September. TCAD Simulations of High-Aspect-Ratio Nano-biosensor for Label-Free Sensing Application, In 2021 Joint International EUROSOI Workshop and also
International Conference on Ultimate Integration on Silicon (EuroSOI-ULIS) (pp. 1-4). IEEE and Dhar, R., Kumar, N., Garcia, C.P. and Georgiev, V., 2022. Assessing the effect of Scaling High-Aspect-Ratio ISFET with Physical Model Interface for Nano-Biosensing Application. Solid-State Electronics, p.108374. This complete chapter is done by Rakshita Dhar and the review/guidance was done by other authors.
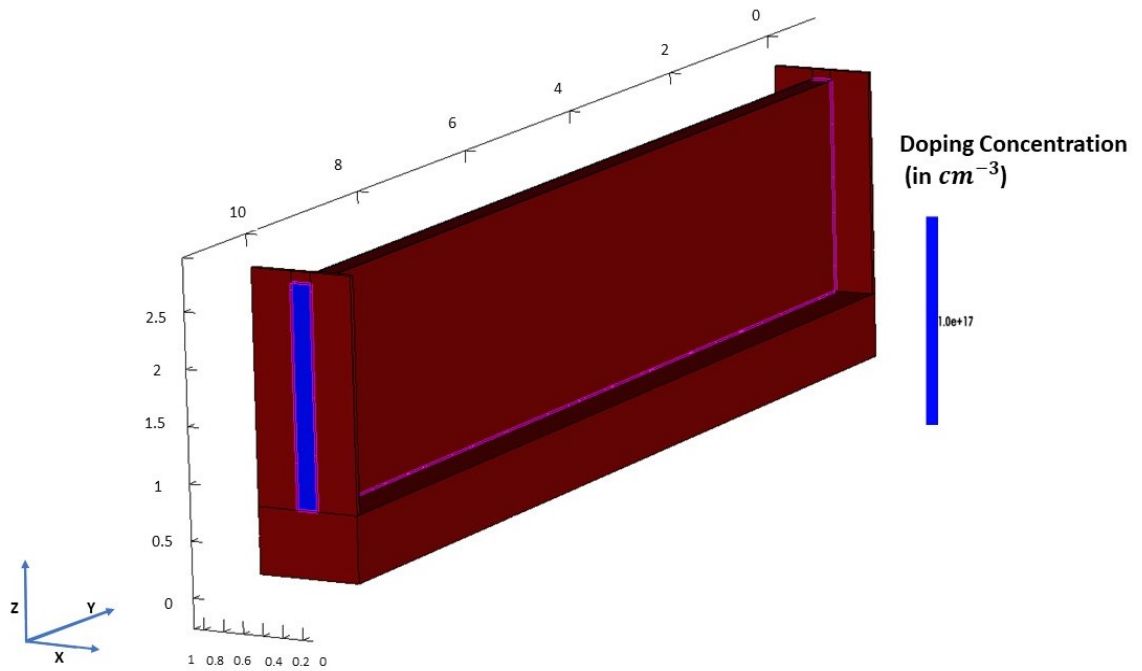
Figure 6.1: p-type Silicon nanowire 3D view in TCAD having a high aspect ratio (H: W $\approx$ 10) to scale. The length is along Y-axis, the width is along X-axis and the height is along Z-axis. The doping concentration of the semiconductor material is shown in the colour bar. Since only one type of doping is present it shows only one colour as it is a junctionless field effect transistor (JL-FET)

6.1   Device Architecture

In this work, we have performed a numerical design-of-experimental (DoE) study to improve the device design based on junctionless ion-sensitive field-effect transistor (JL-ISFET) based on FinFET technology. The device dimensions are taken from experiments [25]. The ISFET device is considered to have a high aspect ratio meaning the height-to-width ratio is high (H: W $\approx$ 10). This will allow high adsorption of analytes as the surface area increases from one dimension to two dimensions [25]. The 3D structure in Sentaurus TCAD is shown in figure 6.1. This structure is without the electrolyte. The blue region is the p-type Si nanowire channel. The brown region is SiO_2 oxide. The pink borders around the blue region show the source and drain contacts. Similarly, the pink border on the brown region shows the 3D gate contact. The structure has the device dimensions in micrometres (μm). The dimension of the full device is 10.1 X 0.2 X 2 μm (length X width X height) respectively. Detailed dimensions are shown in table 6.1. Further, the details of doping concentrations are shown in table 6.2.

Figure 6.2 shows the 3D structure as seen in Sentaurus TCAD with electrolyte. The red region is the electrolyte which is water and salt (H_2O + NaCl). The electrolyte is modelled by creating a new semi-conductor material in Sentaurus having doping $6.023 X 10^{19}$ cm^{-3} [64]. The blue region is the Si fin and the brown region is SiO_2. The doping concentration colour bar can also be taken as a reference to check the doping in each region. The gate voltage V_G is the

Parameter	Source(μm)	Channel(μm)	Drain(μm)
Length	10	10	10
Width	0.2	0.2	0.2
Height	2	2	2

Table 6.1: p-type Si nanowire dimensions of length, width, the height of the device for source, channel and drain regions. All the dimensions are mentioned in μm. It can be seen that the dimensions are uniform throughout the nanowire consisting of source, channel and drain

Parameter	Source	Channel	Drain
Material	Silicon	Silicon	Silicon
Doping	p-type Boron	p-type Boron	p-type Boron
Doping level(per cubic cm)	1e17	1e17	1e17

Table 6.2: p-type Silicon nanowire doping level, type of doping and material used for the source, channel and drain. It can be seen that the doping is uniform throughout the nanowire consisting of source, channel and drain

pink border which surrounds the electrolyte. The device dimensions and doping are the same as mentioned in table 6.1 and 6.2.

To obtain a better understanding of the 3D structure, the device cross-sectional view is shown in Fig. 6.3. Figure 6.3 (a) shows a 3D cut along the X-axis. It's the YZ plane showing the length of the device as 10.1 μm. Figure 6.3(b) shows a 3D cut along the Y-axis. It shows the device in the XZ plane having a width of $1\mu m$. Figure 6.3 (c) is a zoom of the upper part of figure 6.3 (b). It shows the oxide thickness to be 5nm which can be varied.

6.2 Device Physics

This section describes the physics of the devices taken into consideration in TCAD simulation for figure 6.1 and figure 6.2.

6.2.1 Drift-Diffusion

The drift-diffusion model is the carrier transport model used in these simulations [65]. For semiconductor devices, two different approaches are employed to solve the coupled set of equations that comprises the Drift-Diffusion model (it is also possible to combine the two methods for the same problem when needed):

(i)The Newton iteration (or fully coupled method) and

(ii)The Gummel iteration (or de-coupled method)

In these simulations, the Gummel iteration is used because convergence was not met by the newton iteration. But after further research, the mesh was improved and the implementation of fully
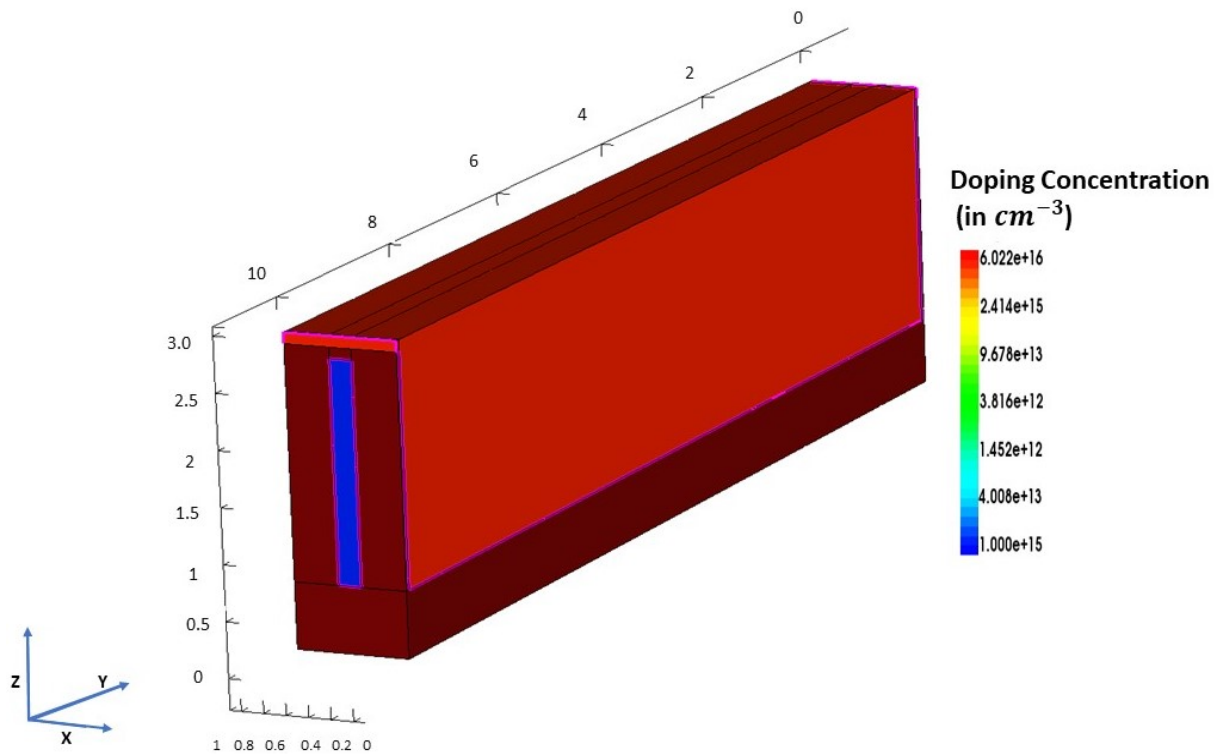
Figure 6.2: p-type Silicon nanowire 3D view in TCAD having a high aspect ratio (H: W ≈ 10) with Electrolyte to scale. The length is along Y-axis, the width is along X-axis and the height is along Z-axis. The doping concentration of the semiconductor material is shown in the colour bar. Since only one type of doping is present it shows only one colour as it is a junctionless field effect transistor (JL-FET)
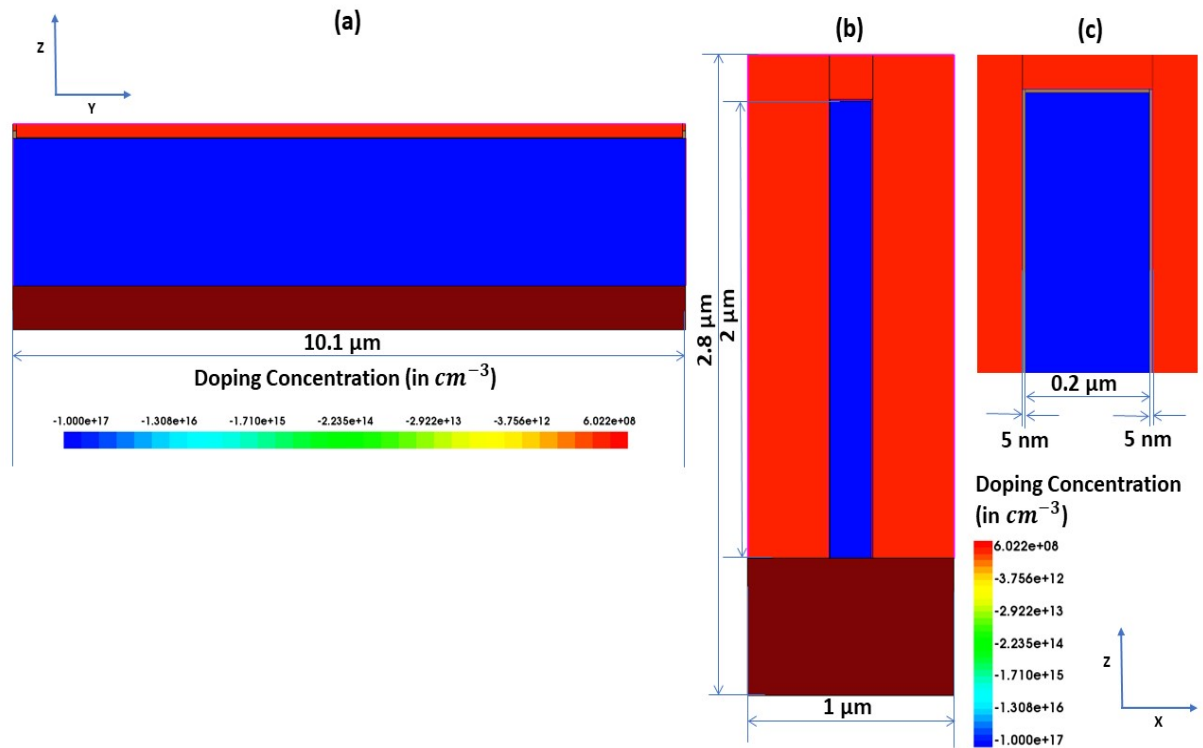
Figure 6.3: shows the 2D structure of the device (a) shows the YZ plane or the side view to scale along with doping concentration colour bar (b) shows the XZ plane or the front view (c) shows the zoom of the upper part of (b) where SiO_2 has 5nm thickness

coupled Newton iterations was achieved. To obtain convergence, the invariance of the solution with respect to variations of the numerical mesh was checked. That means, once a mesh has been created to assure convergence in a reasonable time, try to further reduce the mesh spacing and see if the solutions do not change. If the solution does not change mesh is good [66]. A mesh of 0.1 μm for non-interface regions and 0.01 μm for interface regions was established in this process for 3D device simulations. In general, in an iterative solution method, we start with a guess for the solution and then we successively renew this guess, getting closer to the solution at each stage. The iterations continue until the solution converges to the desired accuracy $x_i - x_{(i-1)} <$ e, where x is the solution vector, that is the vector of the values of the problem unknowns, (i) is the index counting the iteration number, and e is the vector which defines the needed accuracy [65].

6.2.2   Doping Dependent Masetti Mobility Model

The constant mobility model is used for undoped materials. For doped materials, the carriers scatter with the impurities. This leads to a degradation of mobility. Doping-dependent mobility degradation models are used henceforth in these simulations [65]. The default doping-dependent model for predefined materials (e.g., Si) is the Masetti model. In places where new materials are created (in this project the Electrolyte and stern layer), the Masetti model needs to be defined

explicitly in the Physics section.

6.3 Device simulations without Electrolyte

This section describes the transfer characteristics obtained by implementing the Drift-diffusion and the mobility models in Sentaurus TCAD for different oxide materials and thicknesses.

6.3.1 Transfer characteristics for four types of oxide material and thickness

In the beginning for a simplistic simulation of the JL-ISFET device, 3D simulations are carried out in TCAD without electrolyte material having two different types of oxides each having different thicknesses. The below four cases of oxide materials and thicknesses were simulated:

(i) 5nm SiO_2

(ii) 10nm SiO_2

(iii) 5nm HfO_2

(iv) 10nm HfO_2

The transfer characteristics for all the above four devices are seen in figure 6.4. These graphs are plotted both in linear and logarithmic scales. The results can be explained as follows. According to metal oxide semi-conductor (MOS) equation 6.1, drain current (I_D) is given by [67].

$$I_{D,lin} = \frac{\mu_p C_{ox}}{2} \frac{W}{L} [2(V_G - V_{th})V_{DS} - V_{DS}^2] \tag{6.1}$$

where

μ_p = mobility of majority carriers

C_{ox} = oxide capacitance

W = width of the device

L = length of the device

V_G = gate voltage

V_{th} = threshold voltage

V_{DS} = drain to source voltage

The permittivity for SiO_2 is given by ε_{SiO_2} = 3.9 and that of HfO_2 is given by ε_{HfO_2} = 25 [32]. The drain current $I_{D,lin}$ as per equation 6.1 is directly proportional to oxide capacitance and inversely proportional to oxide thickness $C_{ox} \propto \frac{\varepsilon}{t_{ox}}$. This means that $I_{D,lin}$ should be more for HfO_2 than SiO_2. It is the case in simulations as seen in figure 6.4. There is a channel at V_G = 0 because it's a junctionless transistor. Hence there would be current flowing at V_G = 0 which leads to less hole current in the channel compared to the negative voltages V_G.
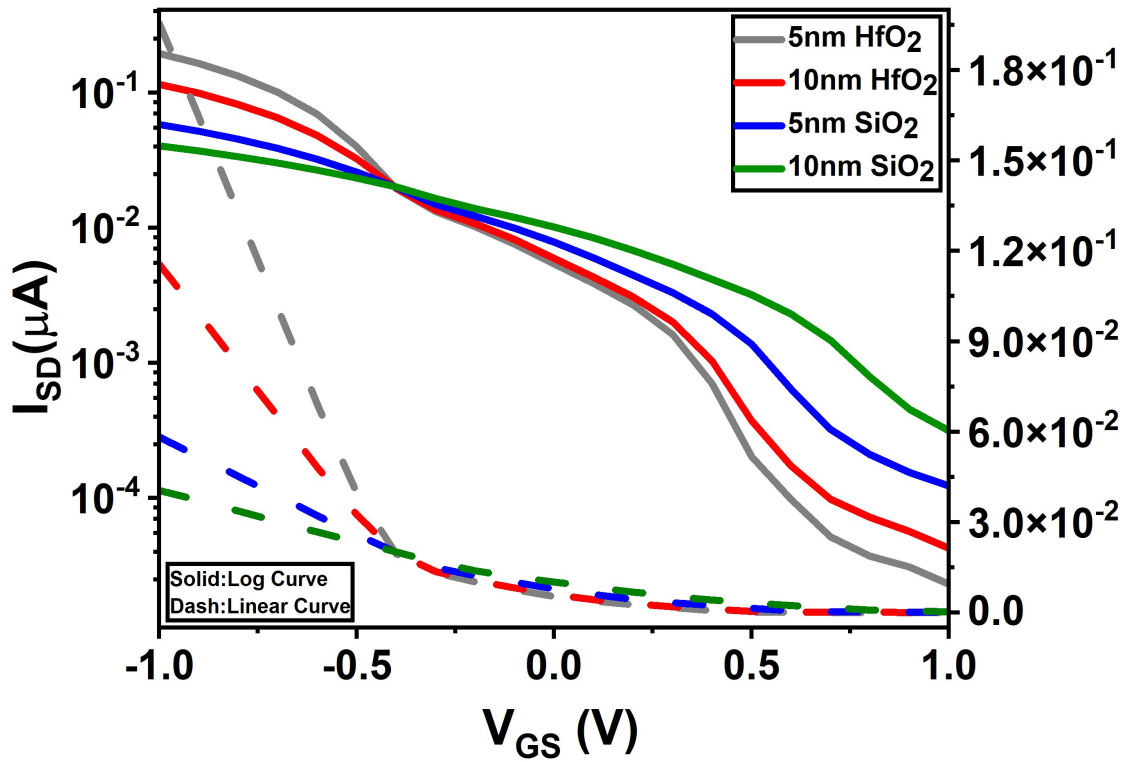
Figure 6.4: Current-Voltage(I_{SD}-V_{GS}) characteristics of four different MOSFET devices (without electrolyte in the gate). The device dimensions are the same except for the thickness and the type of gate oxide.

For $V_G > 0$V, the depletion is more, and it will affect the most on a 5nm HfO_2 device, leading to the lowest drain current as per the equation 6.2 below for positive gate voltages [67].

$$I_{D,sat} = \frac{\mu_p C_{ox}}{2} \frac{W}{L} (V_G - V_{th})^2 \tag{6.2}$$

6.4 Device simulations with Electrolyte

This section describes the transfer characteristics obtained by implementing the Drift-diffusion and the mobility models in Sentaurus TCAD for different oxide materials and thicknesses with electrolytes.

6.4.1 Modelling the Electrolyte in Sentaurus TCAD

The electrolyte is modelled as stated in [68]. The electrolyte which is an ionic solution (H_2O + NaCl) is modelled as an intrinsic semiconductor material having a dielectric constant that of water $78\varepsilon_0$. The electrolyte's charge distribution is represented by the Poisson-Boltzmann equation which is very close to the semiconductor equation [69]. By changing the mobility of holes and electrons of the intrinsic semiconductor, the salt concentration in the solution has been

simulated. Mobility of electrons has a value set to Cl^- ions in water $6.88 * 10^{-4}$ cm^2 V^{-1} S^{-1} and the mobility of holes is set to value of Na^+ ions in water $4.98 * 10^{-4}$ cm^2 V^{-1} S^{-1}.

Calculation of Electrolyte parameters

At 25^0 C, pure water has $[H^+] = [OH^-] = 1e^{-7}$ mol/L [68] [70]. The Avogadro constant N_A = 6.022 x 10^{23} mol^{-1} is converted to 1 mol/L = 6.022 x 10^{23}/L = 6.022 x 10^{20} cm^{-3}. Now for electrolyte having pH = 7, the concentration of $[H^+]$ ions = 10^{-7} mol/L which corresponds to p = N_A x $[H^+]$ = 10^{-7} x 6.022 x 10^{20} cm^{-3} = 6.022 x 10^{13} cm^{-3}. The equation 6.3 is the Boltzmann equation for semi-conductors which gives the majority carrier concentration as given below:

$$p = N_v e^{\frac{E_v - E_f}{k_B T}} \tag{6.3}$$

where

N_v is the hole density of states

E_v is the valence band

E_f is the Fermi energy level

k_B is boltzmann constant

T is temperature

N_V value is calculated as 2.33 x 10^{26} cm^{-3} from equation 6.3. (E_c - E_v) is E_g i.e. the energy band gap for electrolyte material. The energy band gap E_g is considered as 1.5eV [68]. The same calculation can be done for N_c which is the electron density of states by using equation 6.4 below:

$$n = N_c e^{\frac{E_f - E_c}{k_B T}} \tag{6.4}$$

where

N_c is the electron density of states

Below is a table 6.3 which shows the calculation of electron and hole concentration for different pH values.

6.4.2 Transfer characteristics for four types of oxide material and thickness

This section explains the device characteristics when the electrolyte is added to a high aspect ratio ISFET. The transfer characteristics are shown in figure 6.5. The ON current (I_{on}) depends on the equivalent oxide capacitance (C_{eq}). The C_{eq} is equal to two capacitances in series. The capacitance of oxide and capacitance of electrolyte. It can be given by the formula of two capacitances in series as shown in equation 6.5:

pH	p([H+] in solution) (cm^{-3})	Nv(cm^{-3})	n([OH-]in solution)(cm^{-3})	Nc(cm^{-3})
1	6.022×10^{19}	2.33×10^{20}	6.022×10^{7}	2.33×10^{32}
2	6.022×10^{18}	2.33×10^{21}	6.022×10^{8}	2.33×10^{31}
3	6.022×10^{17}	2.33×10^{22}	6.022×10^{9}	2.33×10^{30}
4	6.022×10^{16}	2.33×10^{23}	6.022×10^{10}	2.33×10^{29}
5	6.022×10^{15}	2.33×10^{24}	6.022×10^{11}	2.33×10^{28}
6	6.022×10^{14}	2.33×10^{25}	6.022×10^{12}	2.33×10^{27}
7	6.022×10^{13}	2.33×10^{26}	6.022×10^{13}	2.33×10^{26}
8	6.022×10^{12}	2.33×10^{27}	6.022×10^{14}	2.33×10^{25}
9	6.022×10^{11}	2.33×10^{28}	6.022×10^{15}	2.33×10^{24}
10	6.022×10^{10}	2.33×10^{29}	6.022×10^{16}	2.33×10^{23}
11	6.022×10^{9}	2.33×10^{30}	6.022×10^{17}	2.33×10^{22}
12	6.022×10^{8}	2.33×10^{31}	6.022×10^{18}	2.33×10^{21}
13	6.022×10^{7}	2.33×10^{32}	6.022×10^{19}	2.33×10^{20}
14	6.022×10^{6}	2.33×10^{33}	6.022×10^{20}	2.33×10^{19}

Table 6.3: This table shows the values of hole and electron concentration in the electrolyte solution for pH values from 1 to 14 of a p-type Silicon nanowire

$$\frac{1}{C_{eq}} = \frac{1}{C_{ox}} + \frac{1}{C_{electrolyte}} \tag{6.5}$$

Equation 6.6 and equation 6.7 show values for oxide capacitance and electrolyte capacitance respectively.

$$C_{ox} \propto \frac{\varepsilon_o x}{t_{ox}} = \frac{25}{10} = 2.5 \mu F/m^2 \tag{6.6}$$

$$C_{electrolyte} \propto \frac{\varepsilon_{electrolyte}}{t_{electrolyte}} = \frac{80}{400} = 0.2 \mu F/m^2 \tag{6.7}$$

The equivalent capacitance C_{eq} is found to be ≈ 0.0925. It's going to be the same small value for any other types of oxides or their varying thicknesses. This is because the impact of $C_{electrolyte}$ is more collectively due to its small value. Also, the addition of electrolyte decreases the impact of V_G on the device hence the I_D decreases. At $V_G = 1$V, the I_D depletes more. The OFF-current is also as expected due to the fact that the HfO_2 provides better electrostatic control over the channel due to its higher dielectric constant compared to SiO_2.

This figure 6.5 is for the equilibrium state(isoelectric point). Now we further need to move on towards varying the pH of the electrolyte.

6.5   Interface Trapped Charges (ITC) Method

The interface trap charges (ITC) method has been introduced to represent the charges developed on the oxide surface. This has been done by introducing a novel simulation methodology to rep-
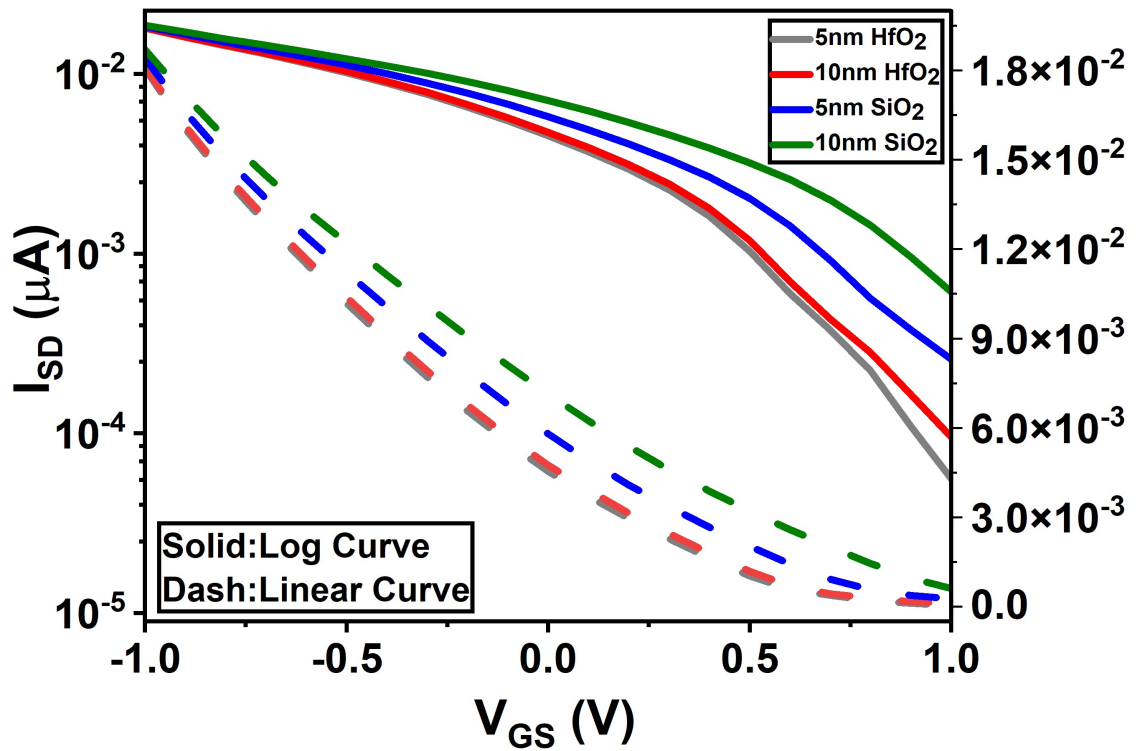
Figure 6.5: Current-Voltage (I_{SD}-V_{GS}) characteristics of the different 3D structure devices with an electrolyte above the gate oxide. The device dimensions are the same except for the thickness and the type of gate oxide.

resent the potential developed on the surface of oxide or the oxide/electrolyte interaction. This method involves a combination of the analytical simulations carried out previously in chapter 3 and the numerical simulations in Synopsys Sentaurus TCAD.

The I_D - V_G curve simulated in previous sections was in the 3D domain. Now we move from 3D to 2D. This is done to save computational time. Moving to the 2D devices is also justified due to the high aspect ratio of the devices. The device can be described as a transistor with gates on all three sides. The top gate can be ignored due to the significantly smaller surface area in comparison to the area of both side gates. A 2D schematic of the device simulated is shown in figure 6.6 along with their dimensions.

The interface trap charges from the section 3.2 of chapter 3 are shown by the red line in figure 6.6. Once the ψ_0 is obtained, the surface charge density (σ_{0-GC}) is obtained. σ_{0-GC} is the bulk charges values as the surface charge density is in per cm^{-3}. These bulk charge values are converted to interface trap charges as our device structure is in 2D. This conversion can be done by converting the σ_{0-GC} from cm^{-3} to cm^{-2}. These values are shown in the table 6.4 below.

The drawback of the above method of representing trapped charges is that the higher values of pH e.g. 14 cannot be simulated since the maximum number of interface trapped charges taken by the simulator is around 10^{17}. We got this limit by simulating this value of trapped charges. Further explanation of this limit from a physics perspective is as follows.In crystalline Silicon,
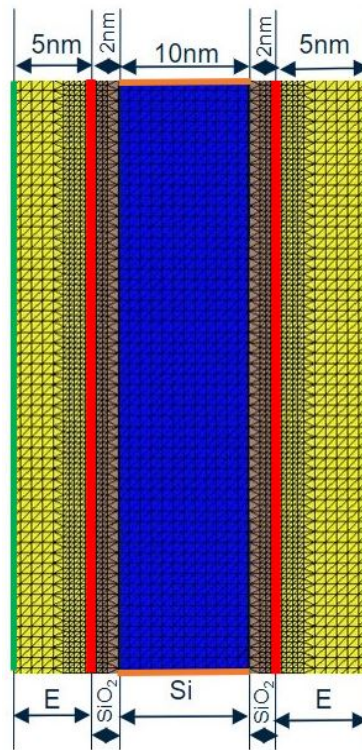
Figure 6.6: 2D schematic of the device where the blue region is Si (10nm wide), the brown region is SiO_2 (2nm wide) and the yellow region (5nm wide) is an electrolyte. The red line between oxide and electrolyte represents interface trap charges ITC. The green lines on the side represent gate voltages. The orange lines on the top and bottom of SiO_2 represent drain and source voltage V_{DS}

Sr.No.	pH	Interface Trapped Charges ITC (cm^{-2})	Bulk charges (cm^{-3})
1	12	-1.98 x 10^{16}	-1.98 x 10^{14}
2	11	-6.92 x 10^{15}	-6.92 x 10^{13}
3	10	-2.45 x 10^{15}	-2.45 x 10^{13}
4	9	-8.87 x 10^{14}	-8.87 x 10^{12}
5	8	-3.33 x 10^{14}	-3.33 x 10^{12}
6	7	-1.32 x 10^{14}	-1.32 x 10^{12}
7	6	-5.57 x 10^{13}	-1.32 x 10^{11}
8	5	-2.33 x 10^{13}	-2.33 x 10^{11}
9	4	-7.56 x 10^{12}	-7.56 x 10^{10}
10	3	-1.29 x 10^{12}	-1.29 x 10^{10}
11	2	-2.2 x 10^{10}	-2.2 x 10^{8}
12	1	1.27 x 10^{12}	1.27 x 10^{10}

Table 6.4: Values of interface trapped charges calculated from the analytical model in MAT-LAB code. The values obtained were in per cm^{-3}. Since we use a 2D model, the σ_{0-GC} is converted to per cm^{-2}.

there are $5x10^{22}$ atoms/ cm^{-3}. Doping concentration for Si is between 10^{13} to 10^{17} atoms/ cm^{-3}. Beyond this range, the semiconductor becomes degenerate at room temperature or can also start behaving like a normal metal. The same limit is applicable for the Si/SiO_2 interfaces that we are simulating.

The ITC values calculated from the analytical model as in table 6.4 is plotted Vs pH as seen from fig. 6.7. The point of zero charge for SiO_2 is at pH =2 [32] and hence the number of trapped charges will be less at that pH compared to the rest as expected and seen. When pH increases the modulus of a number of trapped charges will also increase as the surface potential becomes more negative. Based on fig. 6.7, the device characteristics were obtained as shown in fig. 6.8. A very important concept which is the essence of everything is that at pH =1. $[H^+]$ = 10^{-1}. It means that the $[H^+]$ ions in the electrolyte are less. When pH = 14, $[H^+]$ = 10^{-14} and it means the number of $[H^+]$ ions in the electrolyte are more. As seen from the diagram at a particular gate voltage when the pH increases, the drain current also increases since the number of positive ions in the solution increases. This will lead to highly negative surface potential and more hole current in the p-type device. This explanation also justifies why the I_D - V_G curve moves towards the right as the pH increases. Also, if we look at individual pH curves, the I_D decreases as the V_G varies from negative to positive since it's a p-type device.

Table 6.4 shows the value of surface charge density for different pH values. As can be seen when the pH increases, the interface trapped charges increase which cannot be simulated in Sentaurus TCAD. Values beyond 1e17 cm^{-2} cannot be simulated. Hence, to improvise further on the methodology used in simulation, we adopted a different method as discussed in section 5.7 of chapter 5. The improvement includes simulating all values of pH including the stern layer so its more close to the experiments. Also, the simulation time is more in the interface trapped
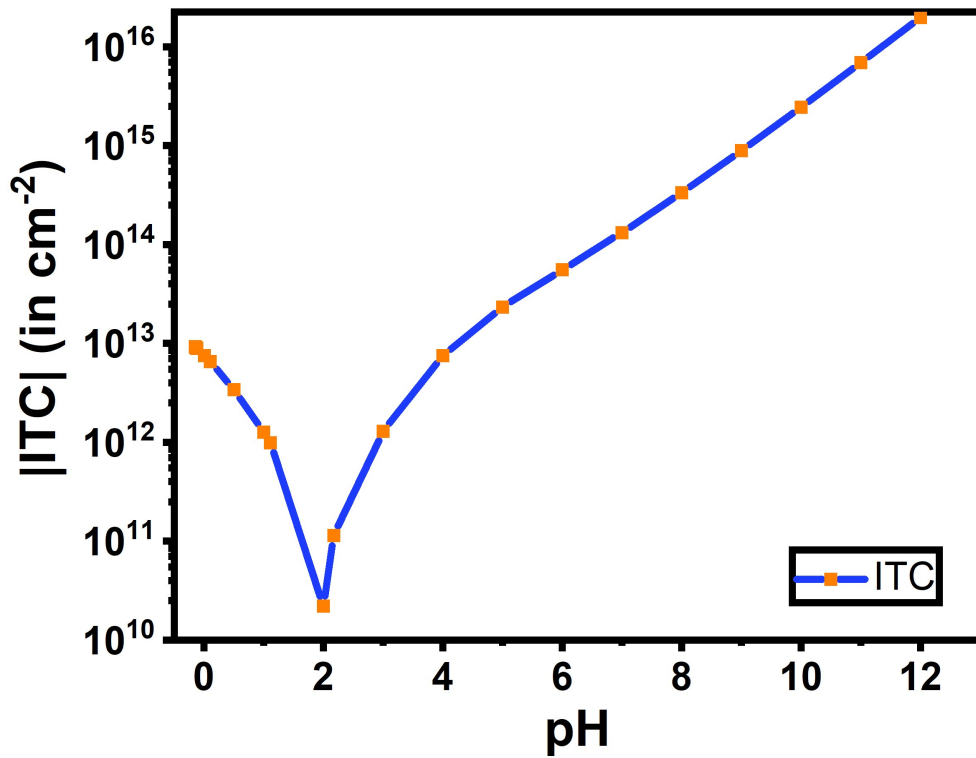
Figure 6.7: I_{SD}-V_{GS} curve of the device with an electrolyte having varying pH from 5 to 11 represented by blue and yellow colour respectively implementing the interface trap charges (ITC) concept at oxide-electrolyte interface
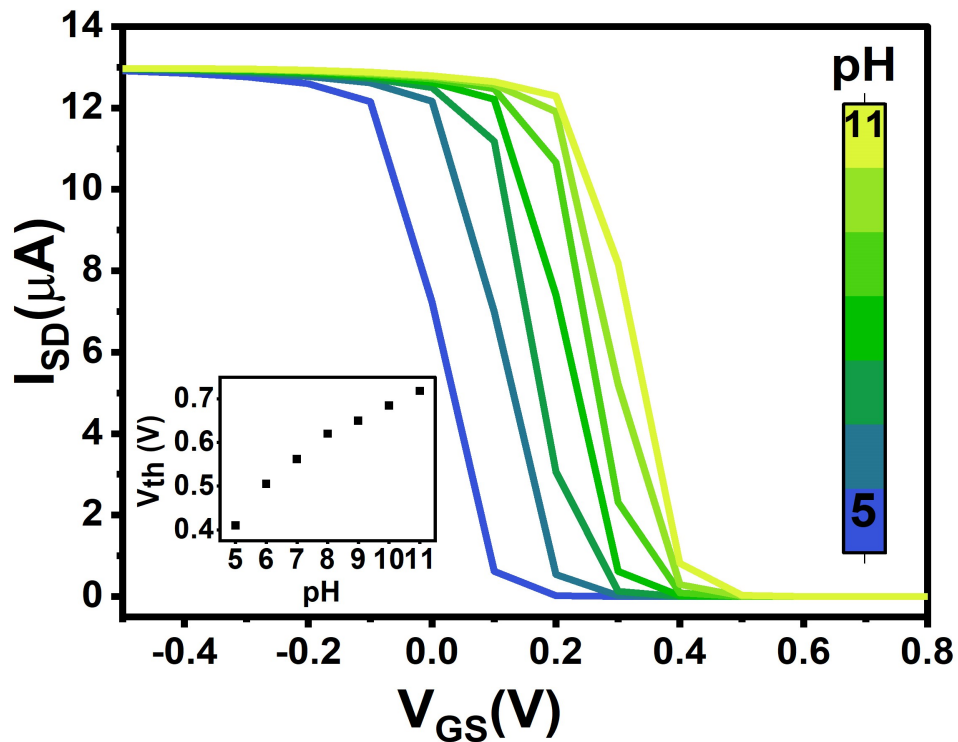
Figure 6.8: Current -Voltage characteristics (I_{SD}-V_{GS}) as a function of pH for a 2D ISFET device obtained with interface trapped charges (ITC) methodology. The pH varies from 5 to 11 which is represented by a blue and yellow line on the graph correspondingly.

charges (ITC) method compared to the physical model interface (PMI) method described in section 5.7 of chapter 5. Hence a new method to simulate the ISFET in TCAD is found which includes both the analytical MATLAB equations and Sentaurus TCAD. The new method is described in the section below, it's called as the implementation of the physical model interface (PMI) when the addition of electrolyte is included.

6.6 Physical Model Interface Method

In this section compared to the method described in the previous section we are using stern layer in the simulations. Also overcoming the shortcomings of the interface trapped charges method (ITC). Implementation of this in TCAD requires the values from Gouy-Chapman-Stern layer analytical model values to be put in the Sentaurus TCAD. The addition of electrolyte on top of oxide with the help of an automated physical model interface (PMI) is implemented and results are obtained.

pH	Hole		Electron	
	Capture	Emission	Capture	Emission
1	1×10^{-4}	8.34	0.0069	8.33
2	1×10^{-4}	0.9344	8.72×10^{-5}	0.9344
3	1×10^{-4}	0.1055	1.502×10^{-6}	0.1056
4	1×10^{-4}	0.0149	2.232×10^{-8}	0.015
5	1×10^{-4}	0.0047	2.236×10^{-9}	0.0048
6	1×10^{-4}	0.0023	5.23×10^{-10}	0.0024
7	1×10^{-4}	0.0013	1.819×10^{-10}	0.0014
8	1×10^{-4}	8.6×10^{-4}	7.4×10^{-11}	9.6×10^{-4}
9	1×10^{-4}	6.05×10^{-4}	3.663×10^{-11}	7.05×10^{-4}
10	1×10^{-4}	4.45×10^{-4}	1.98×10^{-11}	5.45×10^{-4}
11	1×10^{-4}	3.319×10^{-4}	1.1×10^{-11}	4.31×10^{-4}
12	1×10^{-4}	2.585×10^{-4}	6.686×10^{-12}	3.585×10^{-4}
13	1×10^{-4}	2.049×10^{-4}	4.19×10^{-12}	3.04×10^{-4}
14	1×10^{-4}	1.64×10^{-4}	2.69×10^{-12}	2.64×10^{-4}

Table 6.5: The values obtained from the analytical model are the Electron-Hole emission and capture. These values are used as input in the PMI model of TCAD.

These values obtained from the analytical model which is implemented in MATLAB are used as input parameters in the physical model interface (PMI) used in Synopsys Sentaurus TCAD simulation tool. From surface potential Ψ_0 obtained from equation 3.29, the value of H^+ ions from eq. 3.13 can be obtained which is used to find the values of capture and emission rates of electron and hole density as shown in table 6.5.

The PMI is implemented between the oxide layer and the stern layer. A 2D diagram of the device simulated along with the dimensions is mentioned in fig. 6.9.A simple table was prepared
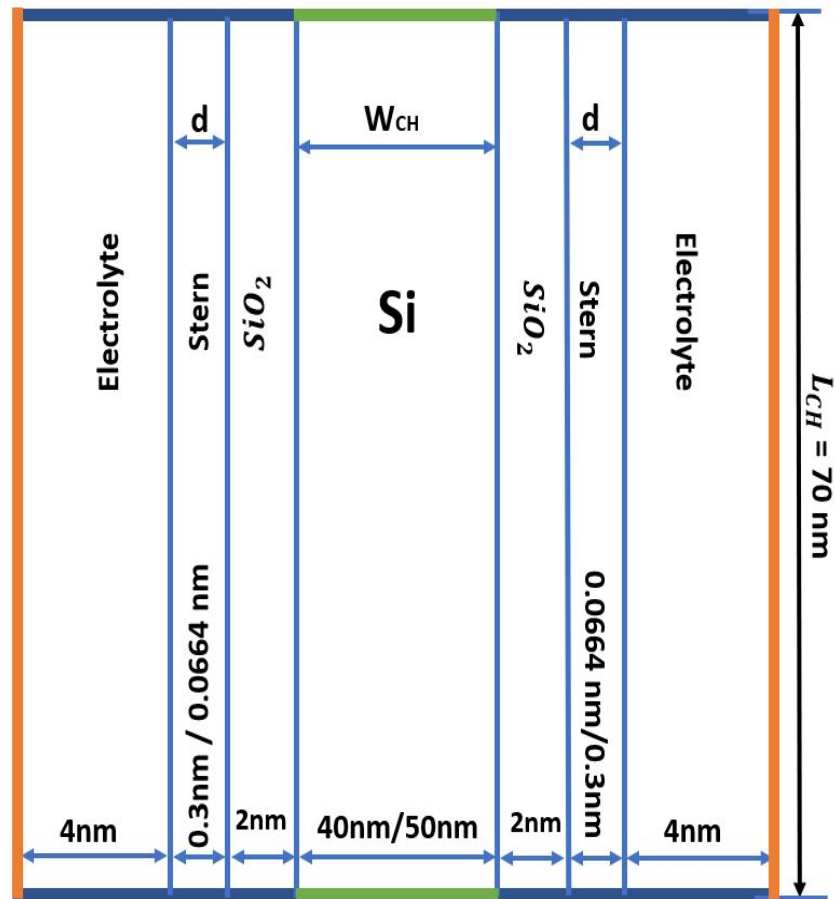
Figure 6.9: 2D schematic of the device where Si channel width is 40nm/50nm, SiO_2 is 2nm wide, the stern layer is 0.3 nm/0.0664 nm wide and electrolyte width is 4nm. The length of the device or the Si channel length is 70nm. The orange lines on the side represent gate voltages. The green lines on the top and bottom of Si represent drain and source voltage V_{DS}

to select what parameters should be varied for implementing the PMI. For the implementation of the surface charge density σ_0 as shown in equation 3.6 in the analytical simulations chapter 3. This σ_0 in the electrochemistry needs to be related to the surface charge density of traps(σ_T) in the semiconductor device simulation software of TCAD which corresponds to interface donor (N_s^d) and interface acceptor traps (N_s^a) as in [71] given by

$$\sigma_T = qN_s(f^d - f^a) \tag{6.8}$$

where f^a and f^d are the occupation probabilities of acceptor and donor traps respectively as in equation 6.8. These equations 3.6 and equation 6.8 need to be equated in order to obtain the electron and hole capture and emission rates. By doing this we obtain

$$\sigma_0 = \sigma_T = qN_s(f^d - f^a) = qN_s[\frac{c_v^d}{c_v^d + e_v^d} - \frac{c_c^a}{c_c^a + e_c^a}] \tag{6.9}$$

where

c_v^d = electron capture rate

e_v^d = electron emission rate

c_c^a = hole capture rate

e_c^a = hole emission rate

The stern layer in the electrolyte is up to the point where the H^+ ions are immobile. The distance after which it becomes mobile is the diffuse layer. In order to solve the drawbacks of the interface trap charges (ITC) method, a new method called the physical model interface (PMI) was introduced. PMI would depict the interaction between the electrolyte and oxide interface. The electrolyte is modelled as a semiconductor material in TCAD simulations.In this case,pK_a = 6 and pK_b = -2 is considered. The values for emission and capture rates for electrons and holes are given by the following equations as in [71]:

$$c_v^d = cH_S^2 \tag{6.10}$$

$$e_v^d = K_aK_b + K_bcH_S \tag{6.11}$$

$$c_c^a = K_aK_b \tag{6.12}$$

$$e_c^a = K_bcH_S + cH_S^2 \tag{6.13}$$

The cH_S is the concentration of H^+ ions on the surface. cH_S is the same as described in the site-dissociation model in chapter 3.
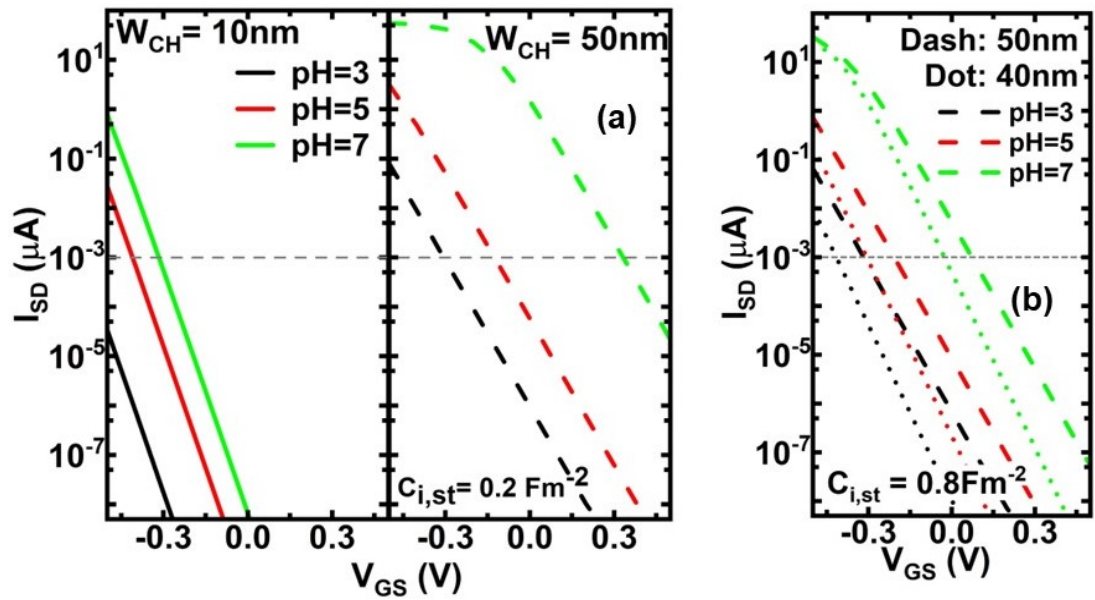
Figure 6.10: I_{SD} -V_{GS} curve of the 2D ISFET device with different channel width (W_{CH}) (a) 10 nm and 50 nm and $C_{i,st}$ = 0.2 F/m^2 (b) 40 nm and 50 nm and $C_{i,st}$ = 0.8 F/m^2; Note: Graph scale is same for (a) and (b) for proper comparison with I_{SD} = 1nA as the reference for graphs represented with dashed grey line

Table 6.6 shows different parameters which could be varied when $N_cN_v = n_sp_s$. It shows four cases. Each case has very low pH = 1 and very high pH =14. Close examination of these four cases reveals that case IV is near to the experimental values because of the considerable distance between the $I_{SD} - V_{GS}$ curve for pH1 and pH14 at V_{GS} = 0. Hence in the subsequent sections, case IV is implemented.

6.6.1 Si channel width = 10nm/40nm/50nm, SiO_2 = 2nm

Here in order to observe the effect of an increase in Si channel width, these simulations are carried out. Figure 6.10(a) and (b)shows I_D- V_G curve for the same. As pH increases from 3 to 7, for the same V_G, the I_D increases. This trend is seen in 10nm, 40nm and 50nm widths. The simulations are done for varying intrinsic stern layer capacitances $C_{i,st}$. The parameter which can be observed from these I_D- V_G graphs is sensitivity.

The observation made from fig. 6.10 (a) is that the slope of I_{SD} - V_{GS} curve decreases as the Si channel width increases. Hence, the sensitivity ($\frac{\Delta I_D}{\Delta pH}$) of the device decreases as the Si device width increases. Another interesting finding from these PMI simulations is that for the same Si channel width of 50nm and different intrinsic capacitance, the slope of the device remains the same! It means the sensitivity is the same. But from fig. 6.10 (a) and (b) for the same W_{CH} of 50 nm, the ISFET is more dominated by the surface potential as the I_D is higher (saturated) even with lower stern capacitance for all pH values. The width of the stern layer is found from the intrinsic stern layer capacitance value taken from literature [28].

Interface = SiO_2 / Stern layer ($N_v N_c = p_s n_s$)								
pH	Case I (direct formula/ electrolyte doping changing w.r.t. pH)		Case II (direct formula/ electrolyte doping not changing w.r.t. pH)		Case III (direct values/ electrolyte doping changing w.r.t. pH)		Case IV (direct values/ electrolyte doping not changing w.r.t. pH)	
	$V_g (in\,V)$	I_d(in µA)	$V_g (in\,V)$	I_d(in µA)	$V_g (in\,V)$	I_d(in µA)	$V_g (in\,V)$	I_d(in µA)
1	0	$1.16e^{-2}$	0	$5.57e^{-2}$	0	$1.04e^{-2}$	0	$4.534e^{-13}$
	-1	0.1302	-1	0.1283	-1	0.1302	-1	0.1282
14	0	$3.57e^{-8}$	0	$3.56e^{-8}$	0	0.1281	0	0.1281
	-1	0.1298	-1	0.1298	-1	C.E.	-1	C.E.

Table 6.6: This table shows the different cases explored to reach a conclusion of which would be the best way to simulate our device for $N_c N_v = n_s p_s$ when we consider the stern layer.

6.6.2 Calculation of the width of stern layer capacitance

This section shows the calculation of stern layer width d. The stern layer capacitance C considered for TCAD simulations is given by equation 6.14.

$$C = \frac{\varepsilon_r}{d} \tag{6.14}$$

$$C = \frac{\varepsilon_0 * k}{d} \tag{6.15}$$

$$C = \frac{8.854x10^{-12} * 6}{d}$$

when C = 0.8 F/m^2

$$d = \frac{8.854x10^{-12} * 6}{0.8}$$

$$d = 0.0664nm$$

when C = 0.2 F/m^2

$$d = \frac{8.854x10^{-12} * 6}{0.2}$$

$$d = 0.2656nm \approx 0.3nm = 3Angstrom$$

6.6.3 Depletion Width as seen in TCAD results

Fig. 6.11, fig. 6.12 and fig. 6.13 show precisely the depletion width in the junctionless field effect transistors when V_G = -0.1 V, V_G = 0V and V_G = 0.1 V respectively. The gate voltages applied are negative (-0.1 V), zero (0 V) and positive (0.5 V). When V_G = -0.1 V, there is more hole current in the device and the depletion width reduces allowing more space in the bulk for holes to carry the drain current. As the gate voltage becomes more positive, it is observed that the depletion width of the device increases and the hole density in the bulk decreases. As the gate voltage becomes more positive, the depletion width increases $W_{D1} < W_{D2} < W_{D3}$, leading to less hole density and hence less I_D.
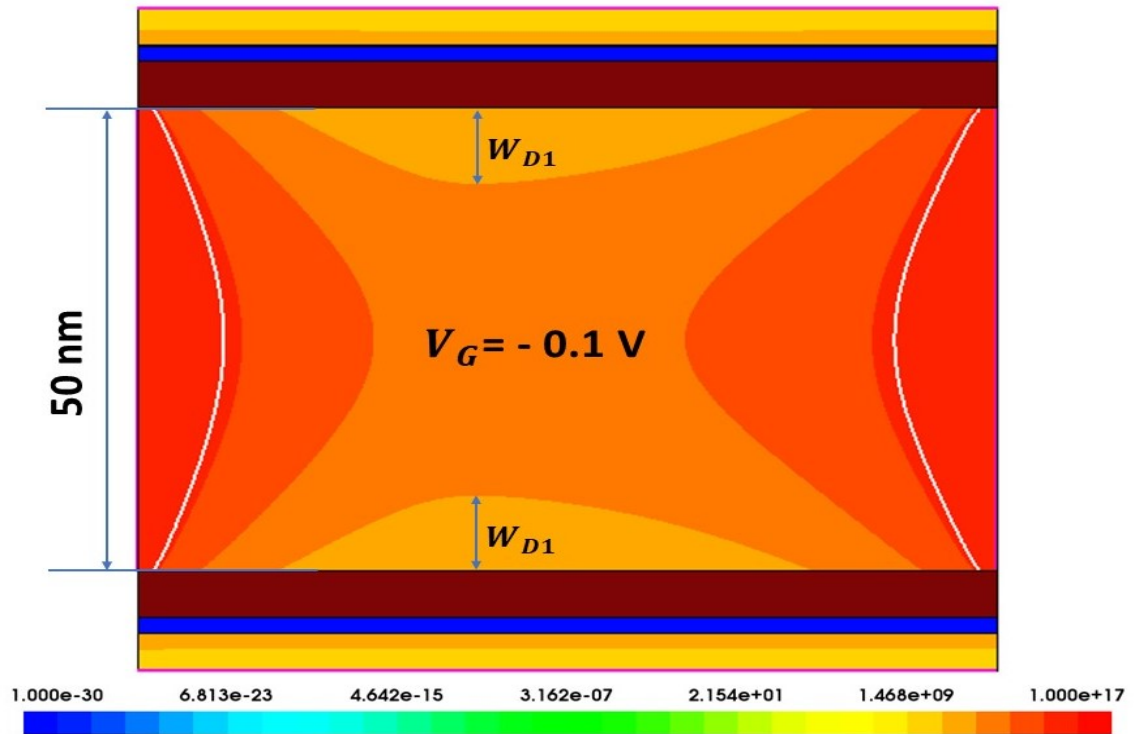
Figure 6.11: This figure shows the depletion width W_{D1} for our 2D device when the gate voltage V_G = -0.1 V for a 50nm Si channel width with the hole density colour bar. Red is the maximum hole density and blue is the minimum.
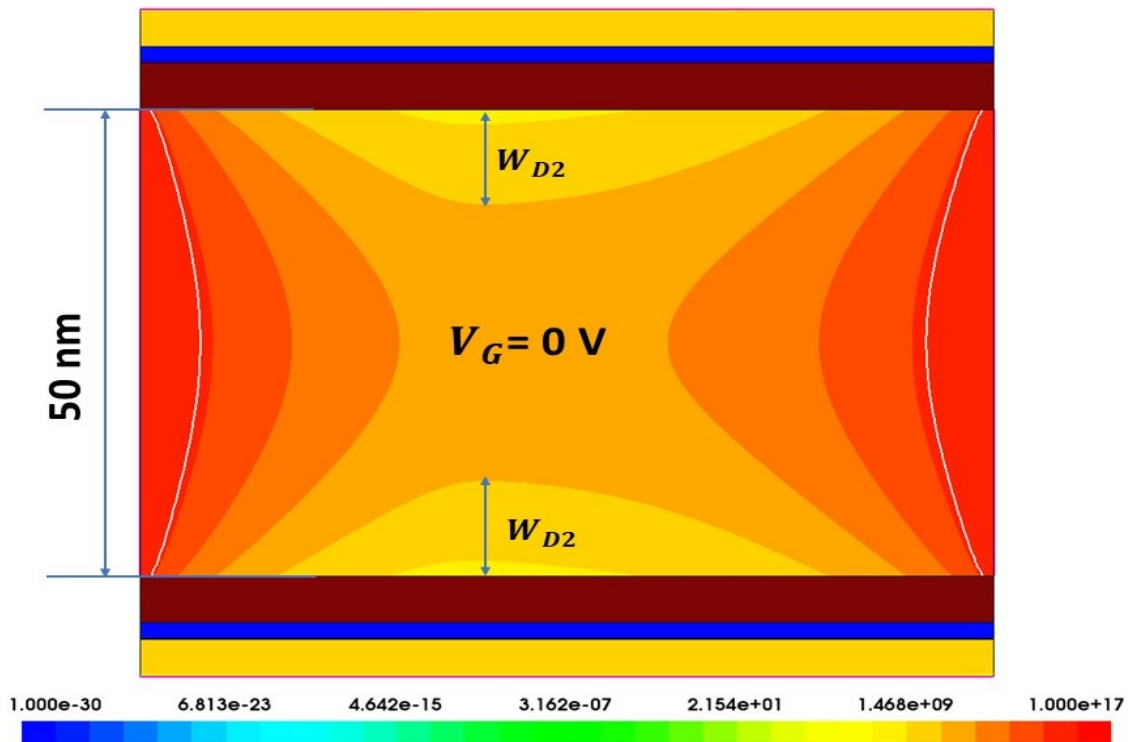
Figure 6.12: This figure shows the depletion width W_{D2} for our 2D device when the gate voltage V_G = 0 V for a 50nm Si channel width with the hole density colour bar. Red is the maximum hole density and blue is the minimum.
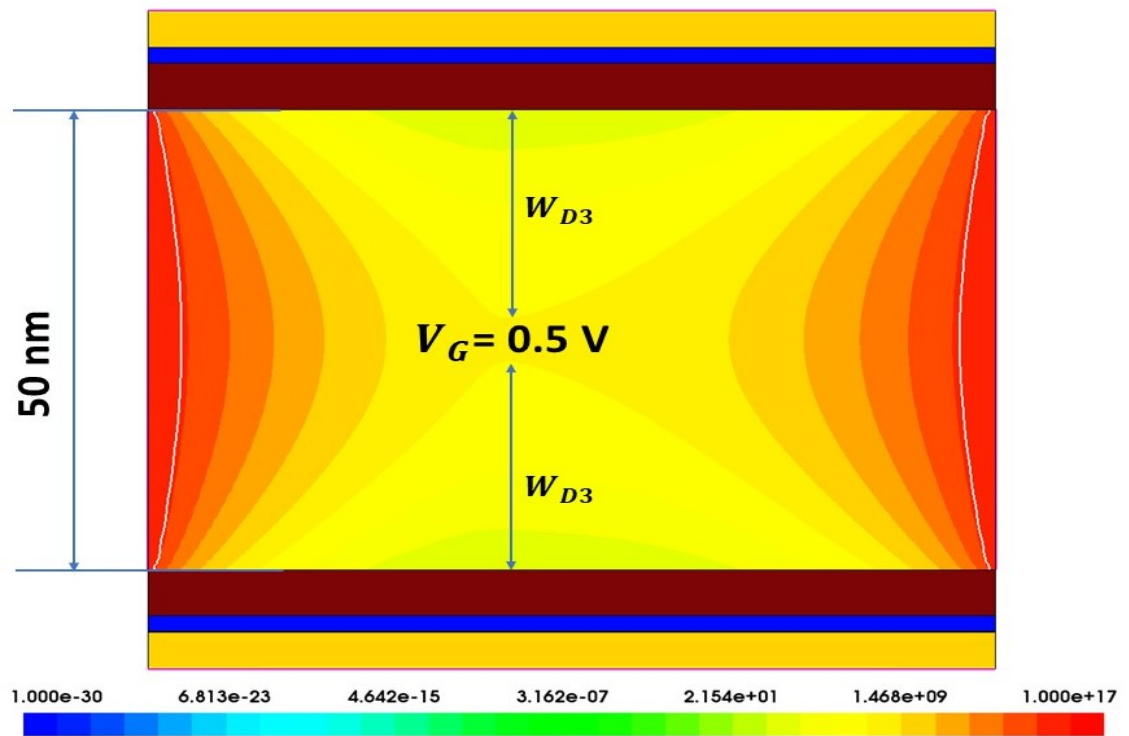
Figure 6.13: This figure shows the depletion width W_{D3} for our 2D device when the gate voltage $V_G = 0.1$ V for a 50nm Si channel width with the hole density colour bar. Red is the maximum hole density and blue is the minimum.

Chapter 7

Conclusion and Future work

In this thesis, we have developed a simulation methodology for the Ion-sensing field effect transistor (ISFET) that combines both analytical and numerical simulations.

We developed an analytical simulation methodology in the 1st part for different types of models for the bio-interface like the Site Dissociation Model, Gouy-Chapman Model and Gouy-Chapman-Stern layer Model in MATLAB. These models were simulated one by one in the order of their increasing complexity at the interface. By developing these models we can understand better and faster the potential developed at the oxide surface. And if other layers like APTES (or something else) are present we can easily incalculate them in this simulation method. Also, we have derived an equation for finding the potential at any point in the electrolyte which is an extension of the Gouy-Chapman-Stern layer model into the electrolyte.

We have shown the influence of using different dielectric materials (SiO_2 and HfO_2) in ISFET. We found out that SiO_2 is best suited for ISFET as it provides proportionally larger current contrasts within a given pH range. The device with different oxide thicknesses and degradation were simulated for the case study.

Fingerprints for different Amino acids such as C and N-Imm. Arginine (R), Aspartic (D) and Proline (P) have been established by extending the analytical simulation model's application to amino acids having different dielectric materials (SiO_2, HfO_2 and TiO_2). For fingerprints of different AA, TiO_2 is the best-suited oxide as we can distinguish very starkly the different fingerprints for R, D, and P amino acids

In the 2nd part, these analytical models were further integrated with numerical simulations to obtain a holistic view or a digital twin where we obtain the transfer characteristics. Modelling of electrolyte was done in TCAD for different pH values. Transfer characteristics for different pH values using the interface trap charges (ITC) method were carried out. Further implementing a new model called a physical model interface (PMI).

This work can further be extended to different types of functionalizations for e.g. APTES (3-

Aminopropyl)triethoxysilane on the oxide surface. The target molecules can be introduced as trapped charges to see their effect on the drain current. Also, gold nanoparticles can be included in TCAD simulations to increase the debye length of the ISFET device.

Appendix A

Experimental Setup and measurements at LIST

This appendix represents the work which was carried out by me as a visiting scientist at the Luxembourg Institute of Science and Technology, Luxembourg (LIST). I was awarded a mobility scholarship in 2022 from the College of Science and Engineering, University of Glasgow. We decided to pursue my further PhD work for two weeks from 28th July 2022 to 10th August 2022 at the Luxembourg Institute of Science and Technology. LIST is also the institute which performs the experimental work for ISFET in the ELECTROMED project from which my thesis work is part. The main motivation for the visit to LIST was to gather knowledge about the experimental work and to gather the data which can be used to validate the described above methodology.

The experimental setup consists of a few major parts such as electrolyte, sample (fabricated device having FETs on it), experimental setup and microfluidics flow control.

A.1 Electrolyte

The process of electrolyte formation along with the steps to vary pH is described here. As per the recipe of Dr Wouter Olthuis from University of Twente [54], the electrolyte would have three components - KNO_3 (acidic buffer), KH_2PO_4 + citric acid + boric acid (or main solution) and KOH (basic buffer). A buffer is a solution which is able to resist small changes in pH when acid or base is added. This is very important for pH sensing where specific and stable pH values are required. Buffer is able to neutralise small amounts of acid/base added hence aiding in stabilising the pH causing small changes in pH [72]. KNO_3 and the main solution are mixed in a 1:1 ratio forming the mother solution. These two (acidic buffer and main solution) when added in a 1:1 ratio gives a pH of 2.48. In these experiments, we want to have a pH range of 2 to pH 12 during the measurements as the device (nanowire) goes from fully conductive (no depletion) to almost fully depleted in this pH range [25]. The buffer KNO_3 and main solution both have a strength of 0.1M. The electrolyte is made by calculating the weight of the chemical compounds. Fig. A.1 shows a summary of the electrolyte formation process. The mass (in g) of KNO_3, KH_2PO_4 + citric acid + boric acid and KOH can be calculated as follows

$$n = \frac{m}{M} \tag{A.1}$$

where n is the number of moles, m is mass and M is the molar strength.

Similarly, another formula for the number of moles is given below:

$$n = C.V \tag{A.2}$$

where C is the concentration in Molar and V is the volume in litres. We can now equate these two equations A.1 and A.2 hence we can write

$n = \frac{m}{M} = C.V$

Finding the mass of KOH

$m = C.V * M = (0.1)(0.25) * 56$

$m = 1.4$ g

Therefore in 1 litre, the mass would be

$m = (0.1)(1)(56)$

$m = 5.6$ g in 1 litre

Hence, the KOH solution was prepared by first weighing it and adding it to 1 litre of water. Similarly, the other two solutions of KNO_3 and KH_2PO_4 + citric acid + boric acid were prepared. The mass (in grams) for the above-mentioned chemicals for a 1-litre solution is given as follows. KH_2PO_4 = 4.6 g

citric acid = 7 g

boric acid = 2.06 g

KNO_3 = 10.11 g
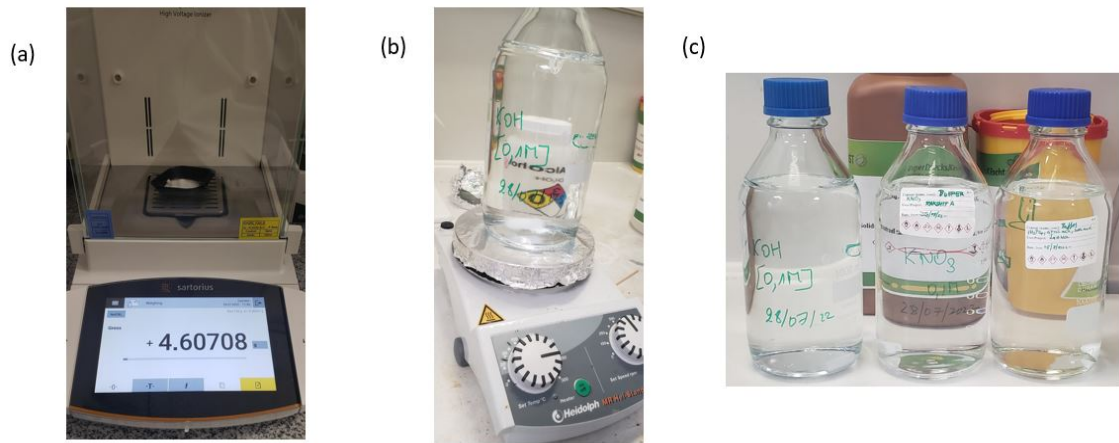
Figure A.1: Experimental process of preparation of electrolyte (a)Weigh the chemical compound as per calculation on a weighing machine (shown for KH_2PO_4) (b) Mixing the chemical compound in deionized water using a magnetic stirrer (shown for KOH) till the chemicals completely dissolve in it (c) Solutions are prepared and stored in a 1-litre bottle for future use (KOH,KNO_3 and mother solution respectively of 1 litre)

The pH is measured with a pH meter with having glass electrode as the working electrode. The pH was measured using a pH meter as shown in figure A.2 after the mother solution was prepared in a 250ml beaker. pH calibration needs to be done when the pH meter doesn't give the required value. The pH value of the electrolyte is changed by titration with KOH and to cover the full range of pH from 2 to 12, 22.5 ml of KOH will be needed to be added [73]. This titration process keeps the ionic strength constant. As KNO_3 and KH_2PO_4 are both basic buffers addition of KOH does not change the ionic strength. Buffer neutralises the small amount of base added thus maintaining the ionic strength constant.

A.2   Sample

The sample consists of the fabricated device (12 FETs) and contact pads. The sample was tested and characterized. The reference electrode and fabricated device (12 FETs) are mounted on the PCB chip as seen in fig. A.3 (a).

A.2.1   Fabricated device

The fabricated device has three microfluidic channels with dimensions 250nm, 150nm and 100nm through which the electrolyte flows above the FET sensors. In each channel, there are four FET devices as we want the 12 FETs to be equally distributed in three microfluidic channels. 12 FETs have different dimensions. In total, there are 12 FETs on the fabricated device having a high aspect ratio (L x W x H = 10 μ m x 250 nm x 5 μ m). At present, the reference

Figure A.2: The pH meter used for the experimental setup is shown in the above diagram and it had to be calibrated before we started using it for experiments. The calibration was done for pH = 4, pH = 7 and pH = 10 and the meter was set.

electrode is not on the fabricated device and hence the PCB is required to provide a reference voltage to the FET. As can be seen in fig. A.3 (a) there are 12 drain contacts marked from D1 to D12. Each drain contact is linked to a FET device so that we can provide a specific drain voltage (V_{DS})to each individual FET. LabView program is used to control the voltages on each drain and gate contact in order to turn ON and turn OFF the twelve FETs on the chip.

Isolation of the golden bonds was carried out on the PCB shown in fig. A.3. This process involves applying PDMS (Polydimethylsiloxane) and cross-linking agent (acts as a catalyst to stick the polymer on the PCB) to the part of the PCB which needs to be protected from the immersion of the PCB in the electrolyte. After this, the PCB is kept on the hotplate as seen in fig. A.4 and the temperature set to 80°C for 15 -20 minutes until it hardens. The isolation process is used to avoid leakage current in the ISFET.

A.3 Experimental setup for characterization

The experiment is carried out in a Faraday cage to avoid noise (or to provide shielding from electromagnetic radiation as the measurements are in nano/micro scales and it's vulnerable to this radiation).

The experimental setup consists of a source meter, multiplexer and faraday cage consisting of the FETs-based sensor as seen in fig. A.5. The source meter provides the voltage sources (V_{DS}) to each drain pad of the FETs, by using the multiplexer. At every specific moment, only one FET will be connected to the source meter. The experimental setup allows us to take measurements
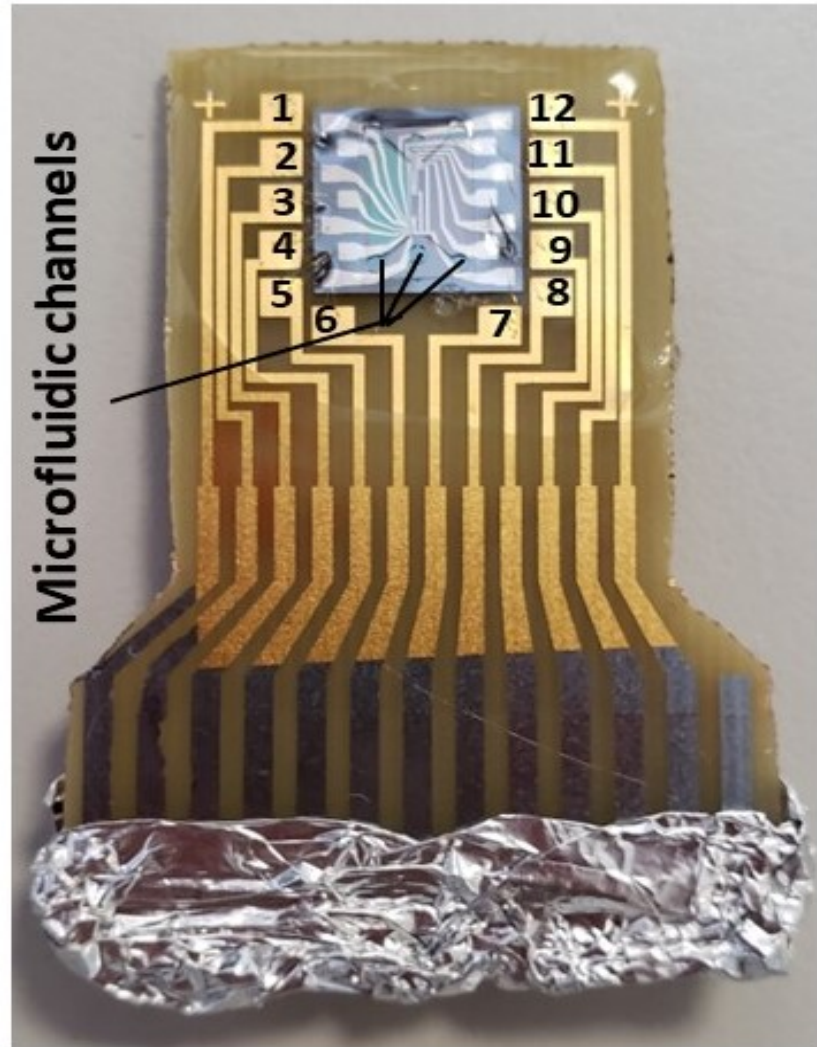
Figure A.3: Sample characterized at LIST: Final sample having 12 drain and three microfluidic channels. Each microfluidic channels have 4 FETs. Sample showing the fabricated device, PCB and the part where all legs are shorted by foil will hold connections to the connector used to change the drain voltage (V_{DS})
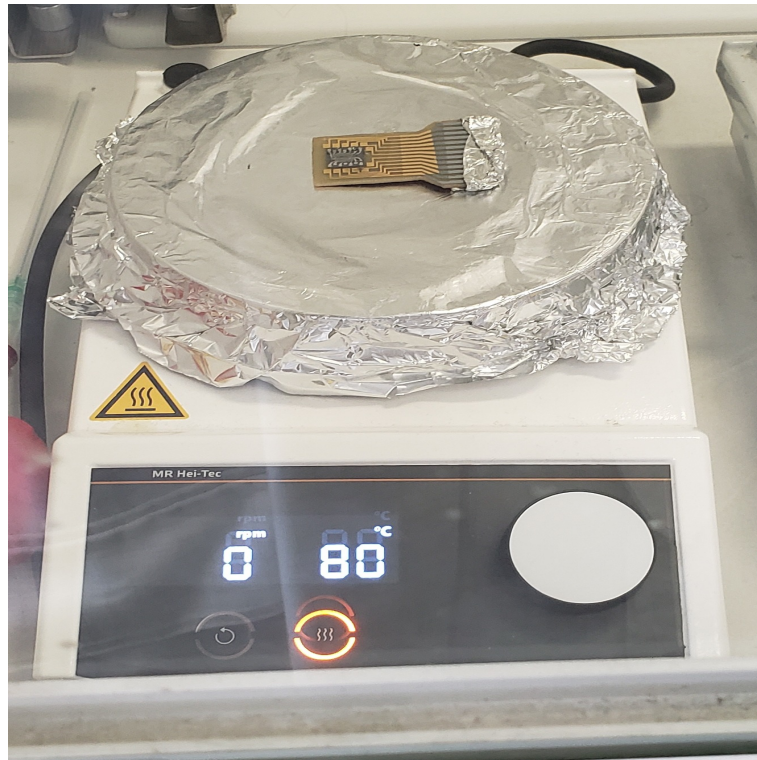
Figure A.4: This photo shows the hotplate kept at 80°C for hardening the PDMS and the cross-linking agent applied on the sample for isolation from the golden bonds. It had taken about 10 minutes for this process.

of I_{DS} for all 12 FETs by applying the same V_{GS} step by step or complete one cycle of varying V_{GS} values for one FET device.

The multiplexer is a PCB designed to provide voltages (V_{DS} drain-source voltage, V_{WE} working electrode voltage, V_{RE} reference electrode voltage, V_{CE} counter electrode voltage) to the FETs and also switch the voltages between different FETs on the input side. On the output, the PCB has different connectors which would go to the fabricated device and the source meter. Apart from that, another function of the multiplexer is to ground all of the 12 FETs before we apply any V_{DS}. The main reason to ground the device before the measurement is to discharge the FET from any previous electrostatic charge. The presence of the electrostatic charge can create a hard breakdown through the gate oxide and hence damage the FET device.

The Faraday cage is a metal container, generally Copper or Aluminium. Inside the faraday cage, the beaker containing electrolyte was placed. Faraday cage is used to avoid noise or shield from electromagnetic radiation in the nano/micro scale measurements. The beaker, containing the electrolyte, the pH meter, the sample and the electrode immersed in it is seen in fig. A.6. Care is taken so that they don't touch each other and are separated at a distance at all times. This is crucial for the correct readings to be obtained from the setup, if the electrode touches the fabricated device there are chances of wrong readings and also the fabricated devices being damaged.
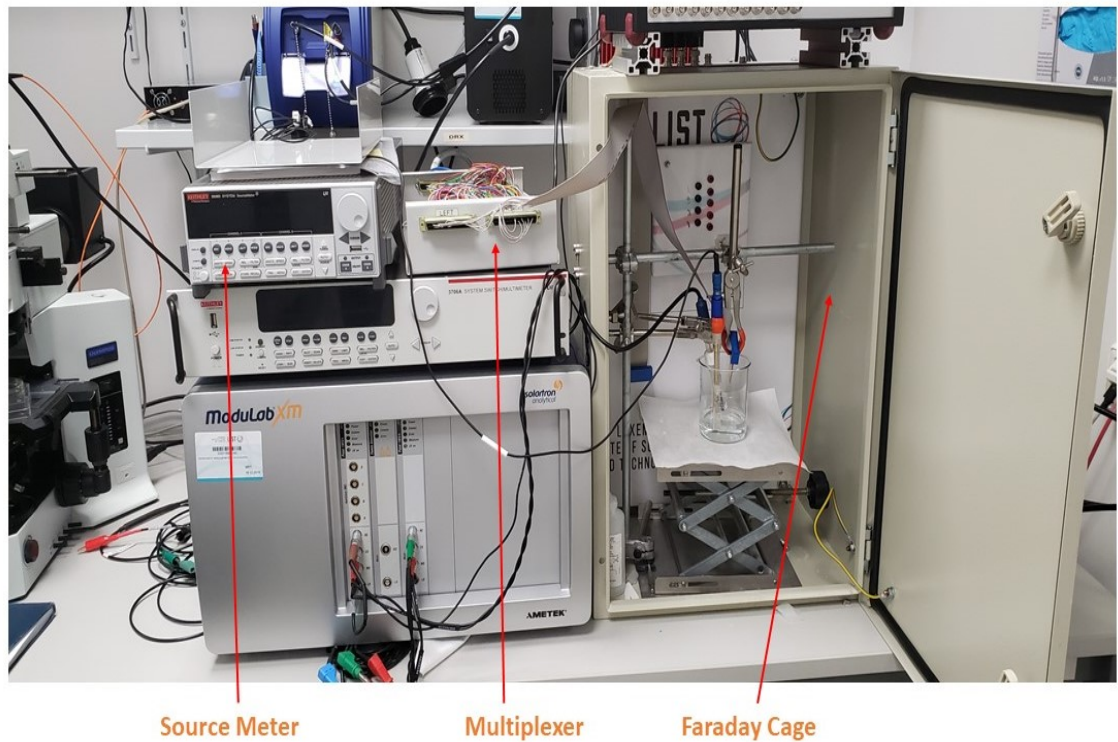
Figure A.5: Experimental setup implemented for characterization of a sample. The experimental setup consists of the source meter, multiplexer and the faraday cage as seen above. The source meter is connected to the input of the multiplexer. The output of the multiplexer is connected to the sample.
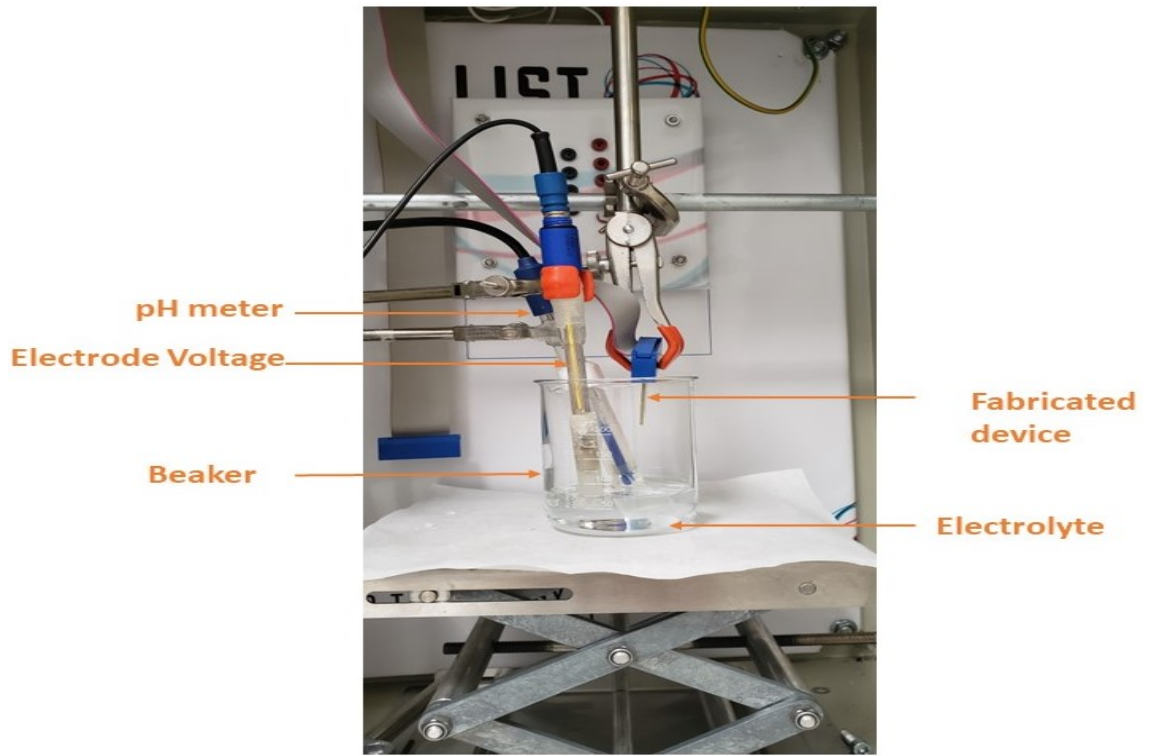
Figure A.6: Inside the faraday cage: The faraday cage consists of electrolyte in a 250ml beaker, the pH meter, electrode voltage (i.e. reference voltage) and sample (consisting of the fabricated device)

A.4 Microfluidics flow control

The microfluidic channels are used to guide the electrolyte flowing in those channels. This flow of electrolyte is done with the help of the setup as seen in fig. A.7 provided by Elvesys which is one of the partners in the ELECTROMED project. As seen in fig. A.7 (a), it shows the complete mechanical structure which will be utilised for the flow of electrolyte. The structure is circular having two inlets and two outlets outside the circular metal. The electrolyte will flow in the microfluidic channels from the inlets and out through the outlets. There are three microfluidic channels inside the circular metal. And each channel has an input point and an output point. This concludes that there are three inlets labelled 1-3 and three outlets labelled 4-6 in fig. A.7 (a). Apart from this, there are wires on the top which will be used for supplying V_{DS}, V_G, V_{CE}, V_{WE} and V_{RE} to the fabricated device. Fig. A.7 (b) shows the chip stencil and the PDMS inside of the mechanical structure. PDMS is put on top of the chip stencil on which the testing was carried out to avoid the overflow of electrolytes in parts other than the microfluidic channel. Fig. A.7 (c) shows the structure after unscrewing it to the measurement platform.
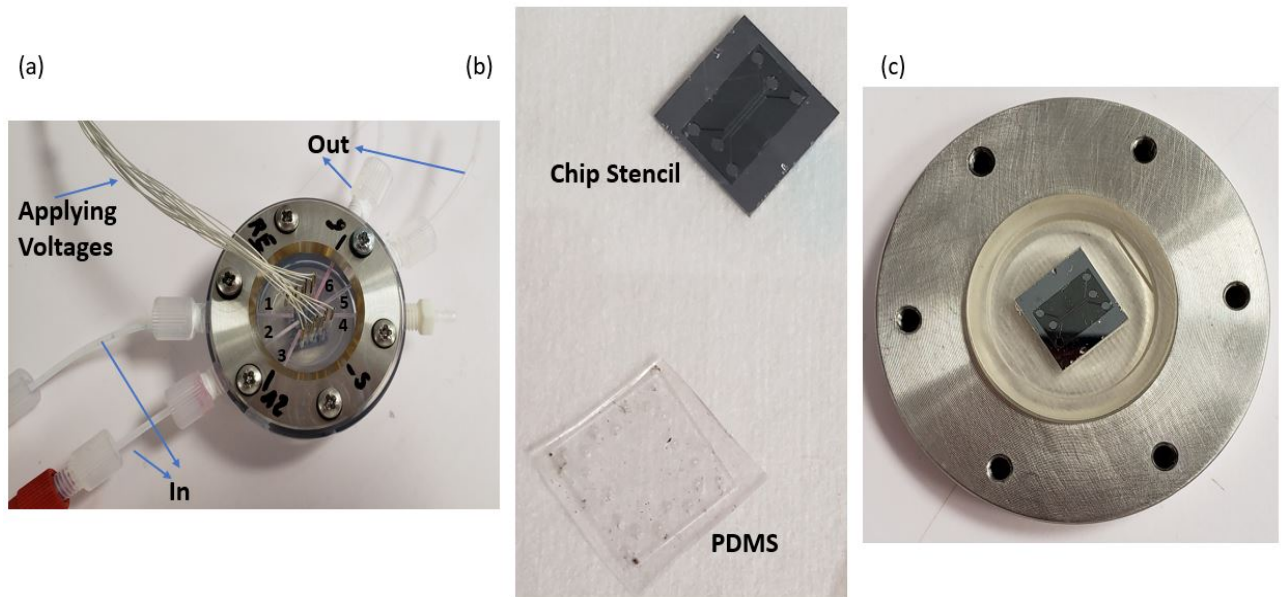
Figure A.7: Microfluidic flow control system provided by Elvesys (a) shows the two IN channels and two OUT channels (b) shows the stencil of the chip used for demonstration purpose (c) shows the system which is inside when the (a) is unscrewed

A.5 Experimental Measurement setup for testing the fabricated FETs

The device has been fabricated in LIST and tested with the help of a 2-point probe measurement setup. The fabricated device is shown in fig. A.8. It shows the fabricated device has 20 FETs each having a common ground and common reference along with the source, the working electrode and the counter electrode. All the twenty FETs on the chip have varied dimensions. There are 10 devices on the right (odd numbers) and 10 devices on the left (even numbers). A voltage V_{DS} is applied between the source and common ground of each device, working electrode is the voltage applied in the liquid gate (or electrolyte). Here we can classify the system as a three-electrode system. This system is used for the ISFETs.

A.5.1 Two electrode system

A two-electrode system has a working electrode and reference electrode to measure potential across a complete electrochemical cell as shown in fig. A.9(a). The potential of one electrode is sensitive to the concentration of the analyte and is called the working electrode and is denoted by WE in figure A.9(a). The second electrode which is the reference electrode serves to complete the electric circuit and provide a reference potential against which the working electrode's potential is measured. It is denoted by RE (reference electrode). Ideally, the reference electrode potential remains constant so that any change in the overall cell potential is attributed to the working electrode. The passage of the cell changes the concentration of species in the electro-
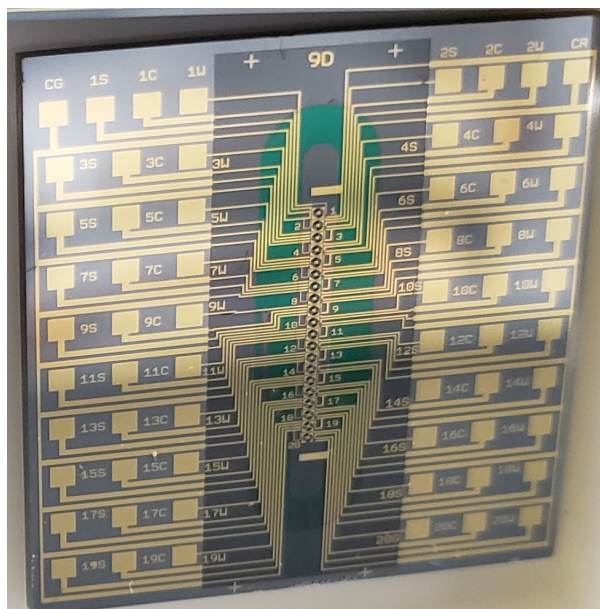
Figure A.8: The device fabricated in LIST has twenty FETs of high aspect ratio. There are 10 devices on the left and 10 devices on the right. Apart from the devices in the centre, padding is provided to give voltages. Each device has a common ground, common reference, source, working and counter electrode i.e.5. In total 5*20 = 100 padding is provided on the PCB.

chemical cell. Thus the potential is not in equilibrium which leads to the polarization of the electrode. In a two-electrode system current flows through the reference electrode. This results in polarization of the electrode. Due to polarization, the potential of the reference electrode may change over time. But reference electrode should not change the standard potential in order to measure the exact potential of the working electrode. Due to a change in the standard electrode potential of the reference electrode, it can no longer act as a reliable reference electrode.

Now, in order to make it work an additional potential should be applied which is called overpotential. Thus, over potential is that potential which should be added to drive the reaction at the reference electrode that should ideally occur.

Overpotential = $E_{applied}$ - $E_{equilibrium}$

The overpotential may be positive or negative. Positive potential indicates an anodic reaction (i.e. oxidation) and negative overpotential indicate a cathodic reaction (i.e. reduction) to enable this three-electrode system to be implemented.

A.5.2 Three electrode system

It is the electrode system which includes the working electrode, the reference electrode and the counter electrode to measure the potential across the complete cells as shown in fig. A.9(b). In a two-electrode system due to the flow of current through the reference electrode, overpotential arises which results in the deviation from expected results. Thus, this requires another electrode called a counter electrode which is added to the electrochemical system to carry the current be-
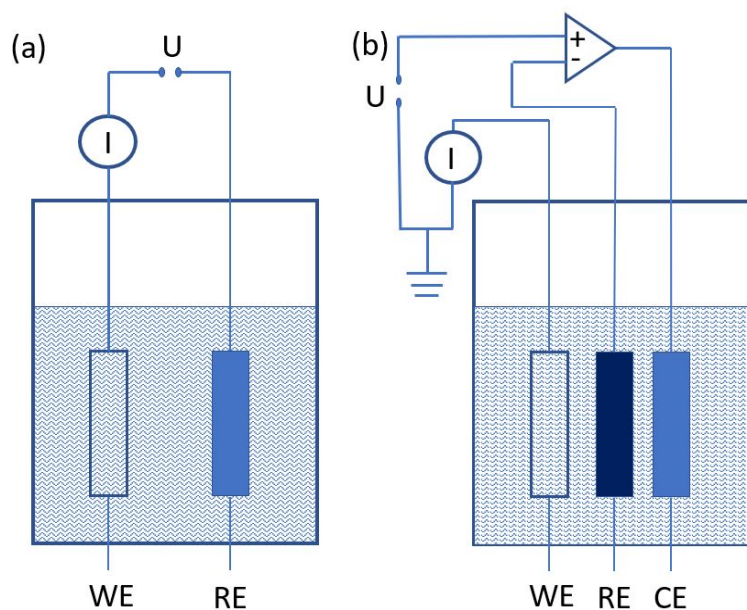
Figure A.9: Diagrams explaining the (a) two-point electrode system - it consists of the working electrode denoted by WE and reference electrode denoted by RE (b) three-point electrode system - it consists of the working electrode (WE), reference electrode (RE) and counter electrode (CE).

tween the working electrode and the counter electrode. The potential of the working electrode is measured with respect to the reference electrode. This potential is given by Ohm's law, $E = IR$, i.e. when the current (I) flows through an electric circuit with resistance(R), voltage (E) is developed.

Since the current now flows via the counter electrode, there is no current flow to the reference electrode and thus the change in reference potential due to the flow of current through it is accounted for by the counter electrode. Hence, the measurement of potential produced on the working electrode due to electrochemical change by the flow of current can be measured with the help of a reference electrode i.e. reference electrode becomes effective. The commonly used material as working electrodes is Pt, Au, pyrrolic graphite, liquid Hg, etc. Here, an extra electrode called a counter electrode is used to measure the exact potential. The working electrode should be polarizable so that we can remove the overpotential with the help of CE. The electrochemical properties of the counter electrode should not affect the behaviour of the electrode of interest (i.e. working electrode).

The properties of the counter electrode are that it is usually chosen to be an electrode that does not produce substances by electrolysis that will reach the working electrode surface and cause interfering reactions there. Frequently, it is placed in a compartment separated from the working electrode by the sintered glass disk or another separator. Properties of working electrodes include good electrical conductivity, inertness and wide potential window, low background current, geometric reproducibility, solvent compatibility and catalytic properties.

This is the exact system which is fabricated as shown in fig. A.8 [74].

Dev. no.	Dev.dim.W (nm)	V_{ds}(mV)	I_d(pA)	R (MΩ)	Voltage Offset (mV)
1	550	49.8	10	4980	0
3	540	49.8	595	83.6	0
6	276	50	222	225.2	18
5	187	50	139	359.7	0
8	165	50	248	201.6	21

Table A.1: The measured values obtained by using the two-point probe method measurements for constant slope observed in Labber software

Measurement taken using the two-probe method

A two-point probe method as described in Appendix C was implemented on the chip shown in fig.A.8 and the measurement results were obtained. The chip has 20 FETs but only FETs having device numbers 1-6 were measured as these were fabricated as required as seen in the SEM images (Scanning electron microscope used to capture high-resolution images). Other devices were not noted down as this is a problem of lab fabrication of FinFETs, which actually would not have any problem in an optimised industrial process. However, the lab processes allow better prototyping. This is the trade-off of fabrication: More reliability, less flexibility and more flexibility, and less reliability. Since the slope of the I_D - V_{DS} is constant, I have noted down a single reading of I_D and V_{DS} in table A.1 to find out the slope and eventually the ohmic resistance. The V_{DS} voltage was swept from 0V to -50mV, -50mV to 50mV and again back to 0V from 50mV.

We are using Ohmic contact in the ISFET as Schottky contact would give a rectifying effect and we are not looking to do this. We just want the signal to pass through the ISFET as it is and ohmic contact does this the best. We can easily determine the contact conductivity type- ohmic or Schottky by performing the two-probe measurement method and checking the slope. This has been performed on the fabricated device as mentioned in Appendix C. About the reason why the variability in contact resistance, the answer is that yes, there is variability in the fabrication process. But with our two-wire method, and even in the conditions we had we can't say much about the contacts other than they are Ohmic. Voltage offset is very small, and it has to be due to some material heterojunction in the circuit. There may be some charge trapping in the ohmic junctions. The problem is that there may be variability in the contact resistance.

Appendix B

Clean room at LIST

On 2nd August 2022, I visited the clean room at Luxembourg Institute of Science and Technology along with a Scientist for the first time in my life. It was a great experience to see all the machines and know their functionality. In this appendix, I would describe the various machines I saw and their functionality.

1. Mask Less Aligner (MLA): This machine does photo-lithography without a mask in four simple steps - set up system, substrate loading, alignment and exposure. It's flexible, fast and straight forward and outstandingly easy to use.

2. Atomic layer deposition/chemical layer deposition (ALD/CLD): It is a commonly used machinery in the semiconductor industry for high-k dielectric films in CMOS processing, sensors and MEMS devices. It is used to deposit a thin film deposition from the vapour phase of the oxide layer for e.g. SiO_2, Al_2O_3. Also called physical vapour deposition.

3. Electron beam evaporator: For deposition of some special materials e.g. gold a separate machine is there. The metal evaporates and the new material is deposited.

4. Wire Bonding machine: This machine is used to make the bonds between PCB and fabricated devices. It has a thin golden wire which is put in a tube having a conical end. When a connection needs to be made between the PCB and the pads fabricated, the thin golden wire is melted and put on the top of each pad to make a connection. This machine was used in the making of the sample.

5. FIB-SEM (Focused ion beam-scanning electron microscope): This machine is for taking the pics of the chip/fabricated device and the lithography can also be done upto the nm range. It is an enhanced technology developed from SEM machine that produces high-resolution images. The two techniques are identical apart from the fact that a beam of electrons is replaced with a focused beam of ions

6. Ellipsometer: Another machine that is used to determine the thickness and other optical constant parameters like doping concentration, roughness, crystallinity and other material properties associated with optical response. Through this machine, we come to know whether the deposition of certain materials is done properly or not.
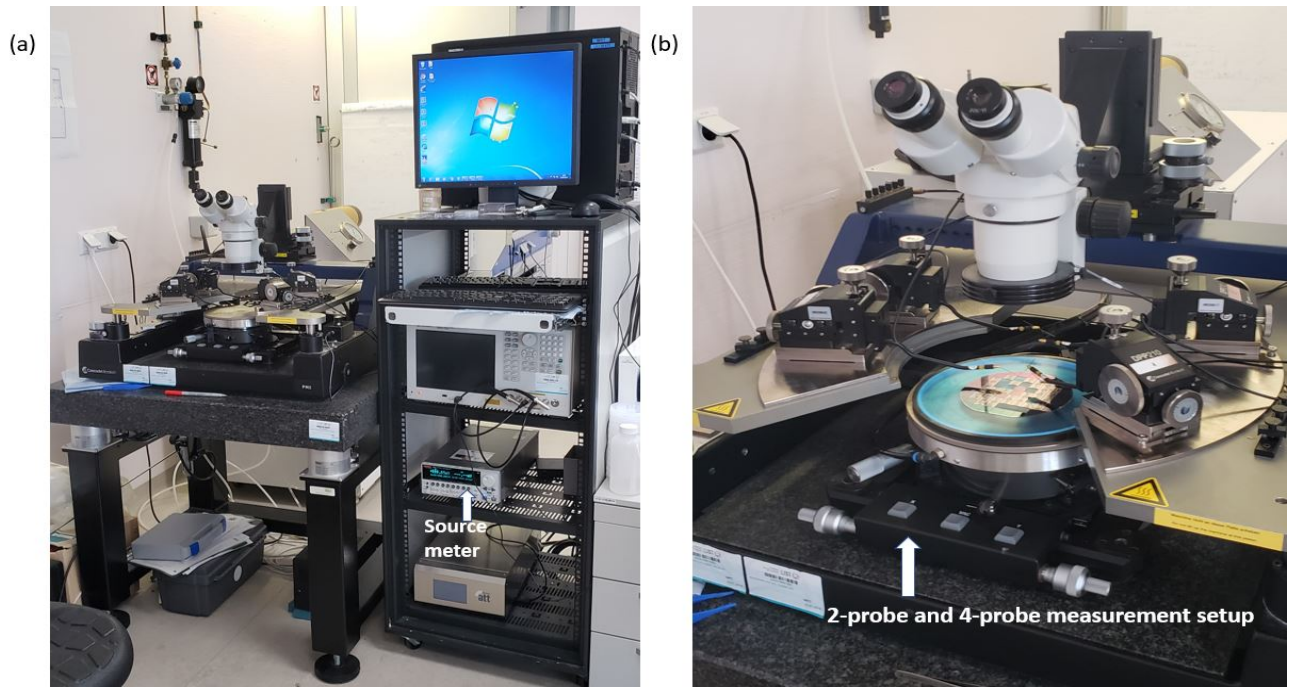
Figure B.1: 2-point probe and 4-point probe measurement setup at a laboratory in LIST. (a) It consists of the source meter, measurement setup and a PC used to read values from the device. (b) shows the close-up of the measurement setup having a 2-probe and 4-probe measurement setup.

7. Water contact angle measurement: For PCB's having biomolecules, the machine is used to determine whether the chip is hydrophobic or hydrophilic.

8. Reactive Ion Etching: It uses chemically reactive plasma to etch materials that are uniform and inductively coupled plasma (ICP) as well for directional etching e.g. nanowire. It is an etching technology used in microfabrication. It is dry etching which has different characteristics than wet etching.

9. Two-probe and four-probe measurements: A machine used to measure the resistivity of the fabricated device. Resistivity is a very important factor for semiconductor devices as it contributes to many device parameters like series resistance, capacitance, threshold voltage (V_{th}), hot carrier degradation of MOS,latch-up of CMOS circuits and other parameters. Resistivity depends on the carrier density and carrier mobility. These parameters are generally not known hence we need other device measurement techniques, a two-point probe and four-point probe measurement setup as shown in fig.B.1. In a 2-probe measurement setup, the current is passed through the device using the same probes which are used to measure voltage. This adds up the wire resistance, probe resistance, and contact resistance to the resistance of the device under test (DUT). In a 4-point probe measurement setup, the 2 probes used to pass the current through the device are different and the two probes used to measure the voltage are different. This makes the resistance of the DUT dominant as the current passed is less and we can ignore the values of probe resistance (R_p), contact resistance (R_c) and wire resistance (R_w). Whereas in the 2-

probe measurement setup, it adds up to the DUT and we are unable to distinguish between the resistance of the device under test and the other resistance such as R_p, R_c and R_w.

B.1   Fabrication process

Nanowires are the most promising structures for scaling of field effect transistor [75].Hence, they are the best candidate for making of a nanobiosensor. It has the simplest of fabrication process since it doesn't involve any heterojunctions.

Step 1: Start with an SOI wafer of p-type Silicon layer on top.

Step 2: Ion implantation is performed to achieve uniform doping through out the source/drain and channel with appropriate dopant for e.g. boron in this case of a p-type having 1^{17} per cm^3.

Step 3: Once the uniform doping is done,the active channel is defined using E-beam lithography followed by wet etching.

Step 4: Width of the channel is defined next followed by width of source /drain which in our case is the same.

Step5: Contact pads are then defined using photolithography or e-beam lithography

Step6: Gate oxide of SiO_2 is then deposited using atomic layer deposition.

Step 7: A gate metal layer is then deposited for the gate electrode.

Appendix C

Derivation of Boltzmann equation

The equation derieved here is the boltzmann equation. Also called as the boltzmann distribution

At T = 0 K, there is no thermal motion which represents the Brownian motion. Brownian motion is the random motion of a particle as a result of collisions with the surrounding gaseous molecules. For symmetric binary electrolyte (Na Cl), (Na^+) is positive charge species and (Cl^-) is negative charge species. Z+ = Z (valency of positively charged species) Z- = Z (valency of negatively charged species)

For symmetric binary electrolyte

$$\Rightarrow \frac{\partial C}{\partial t} + \nabla.(uC) + \nabla.(\mu CE) = \nabla.(D\nabla C) \tag{C.1}$$

where D = $\frac{\mu kT}{ze}$ by Nerst-Einstein equation for charged particle.For a stationary electrolyte media,

$$\frac{\partial C}{\partial t} = 0, u = 0 \Rightarrow \nabla.(uC) = 0$$
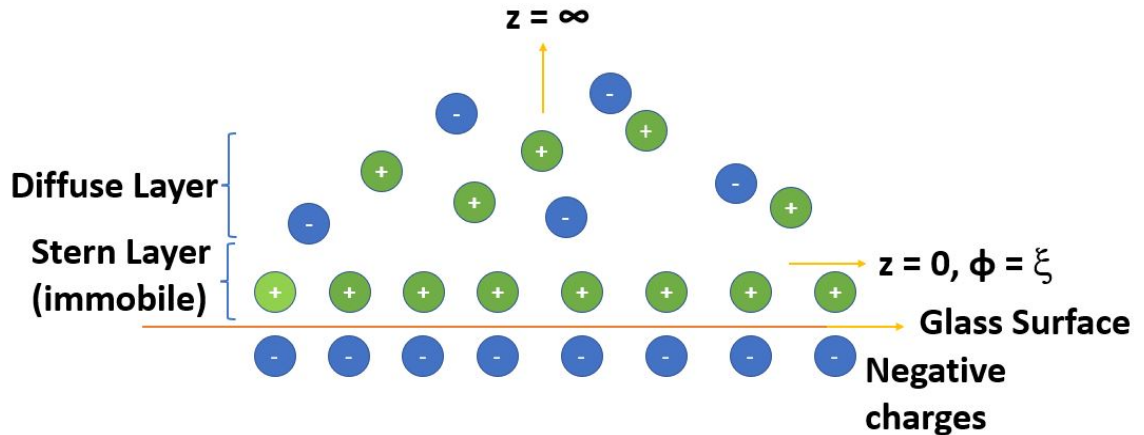
Figure C.1: Glass surface with electrolyte

Simplified,

$$\nabla(\mu CE - D\nabla C) = 0 \tag{C.2}$$

As concentration varies only in the z-direction and concentration variation in x and y directions are not affected. Assumed.

$$\frac{d(-\mu C\frac{d\Psi}{dz} - D\frac{dC}{dz})}{dz} = 0$$

Integrating;

$$\Rightarrow -\mu C\frac{d\Psi}{dz} - D\frac{dC}{dz}z = 0$$

Now substitute the value of D and rearrange

$$D = \frac{\mu kT}{ze}$$

$$\Rightarrow \frac{ze}{kT}C\frac{d\Psi}{dz} + \frac{dC}{dz} = 0$$

As $z \to \infty$, $\frac{d\Psi}{dz} \to 0$ and $\frac{dC}{dz} \to 0$

$$\Rightarrow \frac{ze}{kT}\frac{d\Psi}{dz} + \frac{dC}{dz}\frac{1}{C} = 0$$

$$\Rightarrow \frac{ze}{kT}\frac{d\Psi}{dz} + \frac{d}{dz}\ln C = 0$$

As $z \to \infty$, C = c_0 (bulk concentration) and $\phi = 0$

$$\Rightarrow \frac{ze}{kT}\frac{d\Psi}{dz} = -\frac{d}{dz}\ln C$$

Integrating,

$$-\frac{ze\Psi}{kT} = -\ln c_0 + \ln c$$

$$-\frac{ze\Psi}{kT} = \ln\frac{c}{c_0}$$

$$\Rightarrow c = c_0 \exp\left\{\frac{-ze\Psi}{kT}\right\} \tag{C.3}$$

Appendix D

MATLAB Code

Appendix A contains the MATLAB Code's main function and other functions for analytical simulations.

D.1   Main Function

```matlab
run global_inp.m

clc
clear;
close all;

global Ids pH_pzc K1 K2 K3 K4 K5 K6 N_mat1_active parent_folder project_dir
mol_per1 mol_length1 mol_per2 mol_length2 formula zDistance material1 material2
N_mat2_active numpHsteps;

project_dir = "/home/rakshita/Documents/MATLAB/ULIS2022_MATLAB_code/READ_XLS/";
parent_folder = "N-imm";

%3-aminoproplyethoxysilane
%material = ["alanine", "arginine", "asparagine", "aspartic_acid", "cysteine",
"glutamic_acid", "glutamine", "glycine", "histidine", "hydroxyproline",
"isoleucine", "leucine", "lysine", "methionine", "phenylalanine", "proline",
"pyroglutamatic", "serine", "threonine", "tryptophan", "tyrosine", "valine"];
%material = ["C-imm-alanine", "C-imm-arginine", "C-imm-asparagine", "C-imm-
aspartic_acid", "C-imm-cysteine", "C-imm-glutamic_acid", "C-imm-glutamine", "C-imm-
glycine", "C-imm-histidine", "C-imm-hydroxyproline", "C-imm-isoleucine", "C-imm-
leucine", "C-imm-lysine", "C-imm-methionine", "C-imm-phenylalanine", "C-imm-
proline", "C-imm-pyroglutamatic", "C-imm-serine", "C-imm-threonine", "C-imm-
tryptophan", "C-imm-tyrosine", "C-imm-valine"];
%material = ["N-imm-alanine", "N-imm-arginine", "N-imm-asparagine", "N-imm-
aspartic_acid", "N-imm-cysteine", "N-imm-glutamic_acid", "N-imm-glutamine", "N-imm-
glycine", "N-imm-histidine", "N-imm-hydroxyproline", "N-imm-isoleucine", "N-imm-
leucine", "N-imm-lysine", "N-imm-methionine", "N-imm-phenylalanine", "N-imm-
proline", "N-imm-pyroglutamatic", "N-imm-serine", "N-imm-threonine", "N-imm-
tryptophan", "N-imm-tyrosine", "N-imm-valine"];

material = ["3-aminoproplyethoxysilane"];
%material = ["silicon_dioxide"];

for j = 1:numel(material)
    material1 = material(j);

material2 = "silicon_dioxide";
total_surface_states = 5e18;
material1_percentage = 100;
material1_efficiency = 100;
material2_efficiency = 100;

[N_mat1_active, N_mat2_active] = population(total_surface_states,
material1_percentage, material1_efficiency, material2_efficiency);
[K1, K2, K3, mol_per1, mol_length1] = sitebinding(material1);
[K4, K5, K6, mol_per2, mol_length2] = sitebinding(material2);
```

```
pH_b = linspace(0, 14, numpHsteps);

[pot_zeta, pot_surface] = pot_cal(pH_b);

[char_Den_GCS, char_Den_GC] = char_den(pH_b, pot_zeta);

[H_bulk, H_surf, pHS, beta, diffuseLayerCap, diffLayerCap, alpha, totalCap,
debyeLength, potVariation, nVariation, pVariation] = parameters(pH_b, pot_zeta,
pot_surface);


width = 0.2e-6;
height = 2e-6;
length_channel = 10e-6;
resistivity = 2.24e-3;
depletion_width = 1e-7;
voltage_DS = 50e-3;
oxide = "silicon_dioxide";
oxide_thickness = 5e-9;
degradation = 0;
degradedOxideThickness = 2e-9;

pot_surface_max = pot_surface(numpHsteps);

[depletionWidth, current] = device(pot_surface, pot_surface_max, oxide,
oxide_thickness, degradedOxideThickness, degradation, width, height,
length_channel, resistivity, depletion_width, voltage_DS);

run generate.m


end
```

D.2   Global Input

```matlab
global material1 material2 parent_folder project_dir;

projectdir = project_dir;
parentFolder = parent_folder;
folderName = material1;

folderPath = fullfile(projectdir, parentFolder, folderName);

mkdir( folderPath );

Alpha = transpose(alpha);
Beta = transpose(beta);
Charge_Density_GC = transpose(char_Den_GC);
Charge_Density_GCS = transpose(char_Den_GCS);
Current = transpose(current);
Depletion_Width = transpose(depletionWidth);
Difference_Layer_Cap = transpose(diffLayerCap);
Diffuse_Layer_Cap = transpose(diffuseLayerCap);
H_Bulk = transpose(H_bulk);
H_Surf = transpose(H_surf);
N_Variation = (nVariation);
PH_Bulk = transpose(pH_b);
PH_Surf = transpose(pHS);
Pot_Surface = transpose(pot_surface);
Pot_Zeta = transpose(pot_zeta);
Pot_Variation = (potVariation);
P_Variation = (pVariation);
Total_Cap = transpose(totalCap);
Z_Distance = (zDistance);

DPOTZETA_DPH = gradient(Pot_Zeta, PH_Bulk);
D2POTZETA_DPH2 = gradient(DPOTZETA_DPH);

DPOTSURFACE_DPH = gradient(Pot_Surface, PH_Bulk);
D2POTSURFACE_DPH2 = gradient(DPOTSURFACE_DPH);

writematrix(Alpha, fullfile(folderPath, 'Alpha.csv'));
writematrix(Beta, fullfile(folderPath, 'Beta.csv'));
writematrix(Charge_Density_GC, fullfile(folderPath, 'Charge_Density_GC.csv'));
writematrix(Charge_Density_GCS, fullfile(folderPath, 'Charge_Density_GCS.csv'));
writematrix(Current, fullfile(folderPath, 'Current.csv'));
writematrix(Depletion_Width, fullfile(folderPath, 'Depletion_Width.csv'));
writematrix(Difference_Layer_Cap, fullfile(folderPath,
'Difference_Layer_Cap.csv'));
writematrix(Diffuse_Layer_Cap, fullfile(folderPath, 'Diffuse_Layer_Cap.csv'));
writematrix(H_Bulk, fullfile(folderPath, 'H_Bulk.csv'));
writematrix(H_Surf, fullfile(folderPath, 'H_Surf.csv'));
writematrix(N_Variation, fullfile(folderPath, 'N_Variation.csv'));
```

```matlab
writematrix(PH_Bulk, fullfile(folderPath, 'PH_Bulk.csv'));
writematrix(PH_Surf, fullfile(folderPath, 'PH_Surf.csv'));
writematrix(Pot_Surface, fullfile(folderPath, 'Pot_Surface.csv'));
writematrix(Pot_Zeta, fullfile(folderPath, 'Pot_Zeta.csv'));
writematrix(Pot_Variation, fullfile(folderPath, 'Pot_Variation.csv'));
writematrix(P_Variation, fullfile(folderPath, 'P_Variation.csv'));
writematrix(Total_Cap, fullfile(folderPath, 'Total_Cap.csv'));
writematrix(Z_Distance, fullfile(folderPath, 'Z_Distance.csv'));

writematrix(DPOTZETA_DPH, fullfile(folderPath, 'DPOTZETA_DPH.csv'));
writematrix(D2POTZETA_DPH2, fullfile(folderPath, 'D2POTZETA_DPH2.csv'));
writematrix(DPOTSURFACE_DPH, fullfile(folderPath, 'DPOTSURFACE_DPH.csv'));
writematrix(D2POTSURFACE_DPH2, fullfile(folderPath, 'D2POTSURFACE_DPH2.csv'));
```

Published with MATLAB® R2020a

D.3   Amino Acid Parameters

D.4   Population function

```matlab
function [nmat1active, nmat2active] = population(total, mat1_per, effi_mat1, effi_mat2)

N_T = total;
N_mat1 = (total*mat1_per)/100;
N_mat2 = N_T - N_mat1;
nmat1active = (N_mat1*effi_mat1)/100;
nmat2active = (N_mat2*effi_mat2)/100;

end
```

Published with MATLAB® R2020a

D.5 Determing pK values

```matlab
function [K1, K2, K3, mol_per, mol_length] = sitebinding(input_material)

global Eo;

input = input_material;

database = readtable('amino.xlsx', 'ReadVariableNames', true);
check = strcmp(database.material, input);
rowNum = find(check==1);

avalue = table2array(database(rowNum, 'pK1')); % dissociation cont.
bvalue = table2array(database(rowNum, 'pK2')); % dissociation cont.
cvalue = table2array(database(rowNum, 'pK3')); % dissociation cont.
permittivity = table2array(database(rowNum, 'permittivity'));
length = table2array(database(rowNum, 'length_A'));

mol_per = Eo*permittivity;
mol_length = length*1e-10;

combine_pK = [avalue bvalue cvalue];
combine_pK = sort(combine_pK);

if bvalue == 0 && cvalue == 0
    pK1 = avalue;
    pK2 = bvalue;
    pK3 = cvalue;
end
if bvalue ~= 0 && cvalue == 0
    pK1 = min(avalue, bvalue);
    pK2 = max(avalue, bvalue);
    pK3 = cvalue;
end
if bvalue ~= 0 && cvalue ~= 0
    pK1 = combine_pK(1);
    pK2 = combine_pK(2);
    pK3 = combine_pK(3);

end

if pK1 == 0
    K1 = 0;
else
    K1 = power(10,-pK1);
end
if pK2 == 0
    K2 = 0;
else
    K2 = power(10,-pK2);
```

```
    end
if pK3 == 0
    K3 = 0;
else
    K3 = power(10,-pK3);
end


end
```

D.6 Site Binding Model

This function calculates the surface charge density by the Site binding model.

```matlab
function [char_den_gcs, char_den_gc] = char_den(pH, pot_int_gc)

global q B Qo N_mat1_active N_mat2_active formula K1 K2 K3 K4 K5 K6 cstern;

display (pot_int_gc);

H_bulk = 10.^(-pH);

char_den_gc = Qo.*sinh(pot_int_gc./(2.*B));

pot_int_gcs = ((char_den_gc./cstern) + pot_int_gc);

H_surf = H_bulk.*exp(-pot_int_gcs./B);

if K1 == 0
    pK1 = 0;
else
    pK1 = -log10(K1);
end
if K2 == 0
    pK2 = 0;
else
    pK2 = -log10(K2);
end
if K3 == 0
    pK3 = 0;
else
    pK3 = -log10(K3);
end
if K4 == 0
    pK4 = 0;
else
    pK4 = -log10(K4);
end
if K5 == 0
    pK5 = 0;
else
    pK5 = -log10(K5);
end
if K6 == 0
    pK6 = 0;
else
    pK6 = -log10(K6);
end

if (pK1 < 5.99 && pK3 ~= 0) && (pK4 < 5.99 && pK6 ~= 0)
    if (pK2 < 5.99) && (pK5 < 5.99)
        formula = 'formula1';
```

```matlab
        char_den_gcs = ((q.*N_mat1_active).*((H_surf.^3 - H_surf.*K1.*K2 -
K1.*K2.*K3)./(H_surf.^3 + H_surf.^2.*K1 + H_surf.*K1.*K2 +
K1.*K2.*K3)))+((q.*N_mat2_active).*((H_surf.^3 - H_surf.*K4.*K5 -
K4.*K5.*K6)./(H_surf.^3 + H_surf.^2.*K4 + H_surf.*K4.*K5 + K4.*K5.*K6)));
    end
    if (pK2 > 5.99) && (pK5 > 5.99)
        formula = 'formula2';
        char_den_gcs = ((q.*N_mat1_active).*((H_surf.^3 + H_surf.^2.*K1 -
K1.*K2.*K3)./(H_surf.^3 + H_surf.^2.*K1 + H_surf.*K1.*K2 +
K1.*K2.*K3)))+((q.*N_mat2_active).*((H_surf.^3 + H_surf.^2.*K4 -
K4.*K5.*K6)./(H_surf.^3 + H_surf.^2.*K4 + H_surf.*K4.*K5 + K4.*K5.*K6)));
    end
    if (pK2 < 5.99) && (pK5 > 5.99)
        formula = 'formula3';
        char_den_gcs = ((q.*N_mat1_active).*((H_surf.^3 - H_surf.*K1.*K2 -
K1.*K2.*K3)./(H_surf.^3 + H_surf.^2.*K1 + H_surf.*K1.*K2 +
K1.*K2.*K3)))+((q.*N_mat2_active).*((H_surf.^3 + H_surf.^2.*K4 -
K4.*K5.*K6)./(H_surf.^3 + H_surf.^2.*K4 + H_surf.*K4.*K5 + K4.*K5.*K6)));
    end
    if (pK2 > 5.99) && (pK5 < 5.99)
        formula = 'formula4';
        char_den_gcs = ((q.*N_mat1_active).*((H_surf.^3 + H_surf.^2.*K1 -
K1.*K2.*K3)./(H_surf.^3 + H_surf.^2.*K1 + H_surf.*K1.*K2 +
K1.*K2.*K3)))+((q.*N_mat2_active).*((H_surf.^3 - H_surf.*K4.*K5 -
K4.*K5.*K6)./(H_surf.^3 + H_surf.^2.*K4 + H_surf.*K4.*K5 + K4.*K5.*K6)));
    end
end
char_den_gc = Qo.*sinh(pot_int_gc./(2.*B));
if (pK1 < 5.99 && pK3 == 0) && (pK4 < 5.99 && pK6 ~= 0)
    if (pK2 > 5.99) && (pK5 < 5.99)
        formula = 'formula5';
        char_den_gcs = ((q.*N_mat1_active).*((H_surf.^2 - K1.*K2)./(H_surf.^2 +
H_surf.*K1 + K1.*K2)))+((q.*N_mat2_active).*((H_surf.^3 - H_surf.*K4.*K5 -
K4.*K5.*K6)./(H_surf.^3 + H_surf.^2.*K4 + H_surf.*K4.*K5 + K4.*K5.*K6)));
    end
    if (pK2 > 5.99) && (pK5 > 5.99)
        formula = 'formula6';
        char_den_gcs = ((q.*N_mat1_active).*((H_surf.^2 - K1.*K2)./(H_surf.^2 +
H_surf.*K1 + K1.*K2)))+((q.*N_mat2_active).*((H_surf.^3 + H_surf^2.*K4 -
K4.*K5.*K6)./(H_surf.^3 + H_surf.^2.*K4 + H_surf.*K4.*K5 + K4.*K5.*K6)));
    end
    if (pK2 < 5.99) && (pK5 > 5.99)
        formula = 'formula7';
        char_den_gcs = ((q.*N_mat1_active).*((- H_surf.*K1 - K1.*K2)./(H_surf.^2 +
H_surf.*K1 + K1.*K2)))+((q.*N_mat2_active).*((H_surf.^3 + H_surf^2.*K4 -
K4.*K5.*K6)./(H_surf.^3 + H_surf.^2.*K4 + H_surf.*K4.*K5 + K4.*K5.*K6)));
    end
    if (pK2 < 5.99) && (pK5 < 5.99)
        formula = 'formula8';
```

```matlab
        char_den_gcs = ((q.*N_mat1_active).*((- H_surf.*K1 - K1.*K2)./(H_surf.^2 +
H_surf.*K1 + K1.*K2)))+((q.*N_mat2_active).*((H_surf.^3 - H_surf.*K4.*K5 -
K4.*K5.*K6)./(H_surf.^3 + H_surf.^2.*K4 + H_surf.*K4.*K5 + K4.*K5.*K6)));
    end
end

if (pK1 < 5.99 && pK3 ~= 0) && (pK4 < 5.99 && pK6 == 0)
    if (pK2 < 5.99) && (pK5 < 5.99)
        formula = 'formula9';
        char_den_gcs = ((q.*N_mat1_active).*((H_surf.^3 - H_surf.*K1.*K2 -
K1.*K2.*K3)./(H_surf.^3 + H_surf.^2.*K1 + H_surf.*K1.*K2 +
K1.*K2.*K3)))+((q.*N_mat2_active).*((- H_surf.*K4 - K4.*K5)./(H_surf.^2 +
H_surf.*K4 + K4.*K5)));
    end
    if (pK2 > 5.99) && (pK5 > 5.99)
        formula = 'formula10';
        char_den_gcs = ((q.*N_mat1_active).*((H_surf.^3 + H_surf.^2.*K1 -
K1.*K2.*K3)./(H_surf.^3 + H_surf.^2.*K1 + H_surf.*K1.*K2 +
K1.*K2.*K3)))+((q.*N_mat2_active).*((H_surf.^2 - K4.*K5)./(H_surf.^2 + H_surf.*K4 +
K4.*K5)));
    end
    if (pK2 < 5.99) && (pK5 > 5.99)
        formula = 'formula11';
        char_den_gcs = ((q.*N_mat1_active).*((H_surf.^3 - H_surf.*K1.*K2 -
K1.*K2.*K3)./(H_surf.^3 + H_surf^.2.*K1 + H_surf.*K1.*K2 +
K1.*K2.*K3)))+((q.*N_mat2_active).*((H_surf.^2 - K4.*K5)./(H_surf.^2 + H_surf.*K4 +
K4.*K5)));
    end
    if (pK2 > 5.99) && (pK5 < 5.99)
        formula = 'formula12';
        char_den_gcs = ((q.*N_mat1_active).*((H_surf.^3 + H_surf.^2.*K1 -
K1.*K2.*K3)./(H_surf.^3 + H_surf.^2.*K1 + H_surf.*K1.*K2 +
K1.*K2.*K3)))+((q.*N_mat2_active).*((- H_surf.*K4 - K4.*K5)./(H_surf.^2 +
H_surf.*K4 + K4.*K5)));
    end
end

if (pK1 > 5.99 && pK3 == 0) && (pK4 < 5.99 && pK6 ~= 0)
    if (pK2 > 5.99) && (pK5 < 5.99)
        formula = 'formula13';
        char_den_gcs = ((q.*N_mat1_active).*((H_surf.^2 + H_surf.*K1)./(H_surf.^2 +
H_surf.*K1 + K1.*K2)))+((q.*N_mat2_active).*((H_surf.^3 - H_surf.*K4.*K5 -
K4.*K5.*K6)./(H_surf.^3 + H_surf.^2.*K4 + H_surf.*K4.*K5 + K4.*K5.*K6)));
    end
    if (pK2 > 5.99) && (pK5 > 5.99)
        formula = 'formula14';
        char_den_gcs = ((q.*N_mat1_active).*((H_surf.^2 + H_surf.*K1)./(H_surf.^2 +
H_surf.*K1 + K1.*K2)))+((q.*N_mat2_active).*((H_surf.^3 + H_surf.^2.*K4 -
K4.*K5.*K6)./(H_surf.^3 + H_surf.^2.*K4 + H_surf.*K4.*K5 + K4.*K5.*K6)));
```

```matlab
        end
end


if (pK1 < 5.99 && pK3 ~= 0) && (pK4 > 5.99 && pK6 == 0)
    if (pK2 < 5.99) && (pK5 > 5.99)
        formula = 'formula15';
        char_den_gcs = ((q.*N_mat1_active).*((H_surf.^3 - H_surf.*K1.*K2 -
K1.*K2.*K3)./(H_surf.^3 + H_surf.^2.*K1 + H_surf.*K1.*K2 +
K1.*K2.*K3)))+((q.*N_mat2_active).*((H_surf.^2 + H_surf.*K4)./(H_surf.^2 +
H_surf.*K4 + K4.*K5)));
    end
    if (pK2 > 5.99) && (pK5 > 5.99)
        formula = 'formula16';
        char_den_gcs = ((q.*N_mat1_active).*((H_surf.^3 + H_surf.^2.*K1 -
K1.*K2.*K3)./(H_surf.^3 + H_surf.^2.*K1 + H_surf.*K1.*K2 +
K1.*K2.*K3)))+((q.*N_mat2_active).*((H_surf.^2 + H_surf.*K4)./(H_surf.^2 +
H_surf.*K4 + K4.*K5)));
    end
end


if (pK2 == 0 && pK3 == 0) && (pK4 < 5.99 && pK6 ~= 0)
    if (pK1 < 5.99) && (pK5 < 5.99)
        formula = 'formula17';
        char_den_gcs = ((q.*N_mat1_active).*((-K1)./(H_surf +
K1)))+((q.*N_mat2_active).*((H_surf.^3 - H_surf.*K4.*K5 - K4.*K5.*K6)./(H_surf.^3 +
H_surf.^2.*K4 + H_surf.*K4.*K5 + K4.*K5.*K6)));
    end
    if (pK1 < 5.99) && (pK5 > 5.99)
        formula = 'formula18';
        char_den_gcs = ((q.*N_mat1_active).*((-K1)./(H_surf +
K1)))+((q.*N_mat2_active).*((H_surf.^3 + H_surf.^2.*K4 - K4.*K5.*K6)./(H_surf.^3 +
H_surf.^2.*K4 + H_surf.*K4.*K5 + K4.*K5.*K6)));
    end
    if (pK1 > 5.99) && (pK5 < 5.99)
        formula = 'formula19';
        char_den_gcs = ((q.*N_mat1_active).*((H_surf)./(H_surf +
K1)))+((q.*N_mat2_active).*((H_surf.^3 - H_surf.*K4.*K5 - K4.*K5.*K6)./(H_surf.^3 +
H_surf.^2.*K4 + H_surf.*K4.*K5 + K4.*K5.*K6)));
    end
    if (pK1 > 5.99) && (pK5 > 5.99)
        formula = 'formula20';
        char_den_gcs = ((q.*N_mat1_active).*((H_surf)./(H_surf +
K1)))+((q.*N_mat2_active).*((H_surf.^3 + H_surf.^2.*K4 - K4.*K5.*K6)./(H_surf.^3 +
H_surf.^2.*K4 + H_surf.*K4.*K5 + K4.*K5.*K6)));
    end
end


if (pK1 < 5.99 && pK3 ~= 0) && (pK5 == 0 && pK6 == 0)
    if (pK2 < 5.99) && (pK4 < 5.99)
```

```matlab
        formula = 'formula21';
        char_den_gcs = ((q.*N_mat1_active).*((H_surf.^3 - H_surf.*K1.*K2 -
K1.*K2.*K3)./(H_surf.^3 + H_surf.^2.*K1 + H_surf.*K1.*K2 +
K1.*K2.*K3)))+((q.*N_mat2_active).*((-K4)./(H_surf + K4)));
    end
    if (pK2 > 5.99) && (pK4 < 5.99)
        formula = 'formula22';
        char_den_gcs = ((q.*N_mat1_active).*((H_surf.^3 + H_surf.^2.*K1 -
K1.*K2.*K3)./(H_surf.^3 + H_surf.^2.*K1 + H_surf.*K1.*K2 +
K1.*K2.*K3)))+((q.*N_mat2_active).*((-K4)./(H_surf + K4)));
    end
    if (pK2 < 5.99) && (pK4 > 5.99)
        formula = 'formula23';
        char_den_gcs = ((q.*N_mat1_active).*((H_surf.^3 - H_surf.*K1.*K2 -
K1.*K2.*K3)./(H_surf.^3 + H_surf.^2.*K1 + H_surf.*K1.*K2 +
K1.*K2.*K3)))+((q.*N_mat2_active).*((H_surf)./(H_surf + K4)));
    end
    if (pK2 > 5.99) && (pK4 > 5.99)
        formula = 'formula24';
        char_den_gcs = ((q.*N_mat1_active).*((H_surf.^3 + H_surf.^2.*K1 -
K1.*K2.*K3)./(H_surf.^3 + H_surf.^2.*K1 + H_surf.*K1.*K2 +
K1.*K2.*K3)))+((q.*N_mat2_active).*((H_surf)./(H_surf + K4)));
    end
end

if (pK3 == 0) && (pK6 == 0)
    if (pK2 ~= 0) && (pK5 ~= 0)
        if (pK1 > 5.99 && pK2 > 5.99) && (pK4 > 5.99 && pK5 > 5.99)
            formula = 'formula25';
            char_den_gcs = ((q.*N_mat1_active).*((H_surf.^2 +
H_surf.*K1)./(H_surf.^2 + H_surf.*K1 + K1.*K2)))+((q.*N_mat2_active).*((H_surf.^2 +
H_surf.*K4)./(H_surf.^2 + H_surf.*K4 + K4.*K5)));
        end
        if (pK1 > 5.99 && pK2 > 5.99) && (pK4 < 5.99 && pK5 > 5.99)
            formula = 'formula26';
            char_den_gcs = ((q.*N_mat1_active).*((H_surf.^2 +
H_surf.*K1)./(H_surf.^2 + H_surf.*K1 + K1.*K2)))+((q.*N_mat2_active).*((H_surf.^2 -
K4.*K5)./(H_surf.^2 + H_surf.*K4 + K4.*K5)));
        end
        if (pK1 > 5.99 && pK2 > 5.99) && (pK4 < 5.99 && pK5 < 5.99)
            formula = 'formula27';
            char_den_gcs = ((q.*N_mat1_active).*((H_surf.^2 +
H_surf.*K1)./(H_surf.^2 + H_surf.*K1 + K1.*K2)))+((q.*N_mat2_active).*((-
H_surf.*K4 - K4.*K5)./(H_surf.^2 + H_surf.*K4 + K4.*K5)));
        end
        if (pK1 < 5.99 && pK2 < 5.99) && (pK4 > 5.99 && pK5 > 5.99)
            formula = 'formula28';
```

```matlab
            char_den_gcs = ((q.*N_mat1_active).*((- H_surf.*K1 -
K1.*K2)./(H_surf.^2 + H_surf.*K1 + K1.*K2)))+((q.*N_mat2_active).*((H_surf.^2 +
H_surf.*K4)./(H_surf.^2 + H_surf.*K4 + K4.*K5)));
        end
        if (pK1 < 5.99 && pK2 < 5.99) && (pK4 < 5.99 && pK5 > 5.99)
            formula = 'formula29';
            char_den_gcs = ((q.*N_mat1_active).*((- H_surf.*K1 -
K1.*K2)./(H_surf.^2 + H_surf.*K1 + K1.*K2)))+((q.*N_mat2_active).*((H_surf.^2 -
K4.*K5)./(H_surf.^2 + H_surf.*K4 + K4.*K5)));
        end
        if (pK1 < 5.99 && pK2 < 5.99) && (pK4 < 5.99 && pK5 < 5.99)
            formula = 'formula30';
            char_den_gcs = ((q.*N_mat1_active).*((- H_surf.*K1 -
K1.*K2)./(H_surf.^2 + H_surf.*K1 + K1.*K2)))+((q.*N_mat2_active).*((- H_surf.*K4 -
K4.*K5)./(H_surf.^2 + H_surf.*K4 + K4.*K5)));
        end
        if (pK1 < 5.99 && pK2 > 5.99) && (pK4 > 5.99 && pK5 > 5.99)
            formula = 'formula31';
            char_den_gcs = ((q.*N_mat1_active).*((H_surf.^2 - K1.*K2)./(H_surf.^2 +
H_surf.*K1 + K1.*K2)))+((q.*N_mat2_active).*((H_surf.^2 + H_surf.*K4)./(H_surf.^2 +
H_surf.*K4 + K4.*K5)));
        end
        if (pK1 < 5.99 && pK2 > 5.99) && (pK4 < 5.99 && pK5 > 5.99)
            formula = 'formula32';
            char_den_gcs = ((q.*N_mat1_active).*((H_surf.^2 - K1.*K2)./(H_surf.^2 +
H_surf.*K1 + K1.*K2)))+((q.*N_mat2_active).*((H_surf.^2 - K4.*K5)./(H_surf.^2 +
H_surf.*K4 + K4.*K5)));
        end
        if (pK1 < 5.99 && pK2 > 5.99) && (pK4 < 5.99 && pK5 < 5.99)
            formula = 'formula33';
            char_den_gcs = ((q.*N_mat1_active).*((H_surf.^2 - K1.*K2)./(H_surf.^2 +
H_surf.*K1 + K1.*K2)))+((q.*N_mat2_active).*((- H_surf.*K4 - K4.*K5)./(H_surf.^2 +
H_surf.*K4 + K4.*K5)));
        end
    end
    if (pK2 == 0) && (pK5 ~= 0)
        if (pK1 > 5.99) && (pK4 > 5.99 && pK5 > 5.99)
            formula = 'formula34';
            char_den_gcs = ((q.*N_mat1_active).*((H_surf)./(H_surf +
K1)))+((q.*N_mat2_active).*((H_surf.^2 + H_surf.*K4)./(H_surf.^2 + H_surf.*K4 +
K4.*K5)));
        end
        if (pK1 > 5.99) && (pK4 < 5.99 && pK5 > 5.99)
            formula = 'formula35';
            char_den_gcs = ((q.*N_mat1_active).*((H_surf)./(H_surf +
K1)))+((q.*N_mat2_active).*((H_surf.^2 - K4.*K5)./(H_surf.^2 + H_surf.*K4 +
K4.*K5)));
        end
        if (pK1 > 5.99) && (pK4 < 5.99 && pK5 < 5.99)
```

```matlab
                formula = 'formula36';
                char_den_gcs = ((q.*N_mat1_active).*((H_surf)./(H_surf +
K1)))+((q.*N_mat2_active).*((- H_surf.*K4 - K4.*K5)./(H_surf.^2 + H_surf.*K4 +
K4.*K5)));
            end
            if (pK1 < 5.99) && (pK4 > 5.99 && pK5 > 5.99)
                formula = 'formula37';
                char_den_gcs = ((q.*N_mat1_active).*((-K1)./(H_surf +
K1)))+((q.*N_mat2_active).*((H_surf.^2 + H_surf.*K4)./(H_surf.^2 + H_surf.*K4 +
K4.*K5)));
            end
            if (pK1 < 5.99) && (pK4 < 5.99 && pK5 > 5.99)
                formula = 'formula38';
                char_den_gcs = ((q.*N_mat1_active).*((-K1)./(H_surf +
K1)))+((q.*N_mat2_active).*((H_surf.^2 - K4.*K5)./(H_surf.^2 + H_surf.*K4 +
K4.*K5)));
            end
            if (pK1 < 5.99) && (pK4 < 5.99 && pK5 < 5.99)
                formula = 'formula39';
                char_den_gcs = ((q.*N_mat1_active).*((-K1)./(H_surf +
K1)))+((q.*N_mat2_active).*((- H_surf.*K4 - K4.*K5)./(H_surf.^2 + H_surf.*K4 +
K4.*K5)));
            end
        end
        if (pK2 ~= 0) && (pK5 == 0)
            if (pK1 > 5.99 && pK2 > 5.99) && (pK4 > 5.99)
                formula = 'formula40';
                char_den_gcs = ((q.*N_mat1_active).*((H_surf.^2 +
H_surf.*K1)./(H_surf.^2 + H_surf.*K1 +
K1.*K2)))+((q.*N_mat2_active).*((H_surf)./(H_surf + K4)));
            end
            if (pK1 > 5.99 && pK2 > 5.99) && (pK4 < 5.99)
                formula = 'formula41';
                char_den_gcs = ((q.*N_mat1_active).*((H_surf.^2 +
H_surf.*K1)./(H_surf.^2 + H_surf.*K1 + K1.*K2)))+((q.*N_mat2_active).*((-
K4)./(H_surf + K4)));
            end
            if (pK1 < 5.99 && pK2 < 5.99) && (pK4 > 5.99)
                formula = 'formula42';
                char_den_gcs = ((q.*N_mat1_active).*((- H_surf.*K1 -
K1.*K2)./(H_surf.^2 + H_surf.*K1 +
K1.*K2)))+((q.*N_mat2_active).*((H_surf)./(H_surf + K4)));
            end
            if (pK1 < 5.99 && pK2 < 5.99) && (pK4 < 5.99)
                formula = 'formula43';
                char_den_gcs = ((q.*N_mat1_active).*((- H_surf.*K1 -
K1.*K2)./(H_surf.^2 + H_surf.*K1 + K1.*K2)))+((q.*N_mat2_active).*((-K4)./(H_surf +
K4)));
            end
```

```matlab
        if (pK1 < 5.99 && pK2 > 5.99) && (pK4 > 5.99)
            formula = 'formula44';
            char_den_gcs = ((q.*N_mat1_active).*((H_surf.^2 - K1.*K2)./(H_surf.^2 +
H_surf.*K1 + K1.*K2)))+((q.*N_mat2_active).*((H_surf)./(H_surf + K4)));
        end
        if (pK1 < 5.99 && pK2 > 5.99) && (pK4 < 5.99)
            formula = 'formula45';
            char_den_gcs = ((q.*N_mat1_active).*((H_surf.^2 - K1.*K2)./(H_surf.^2 +
H_surf.*K1 + K1.*K2)))+((q.*N_mat2_active).*((-K4)./(H_surf + K4)));
        end
    end
    if (pK2 == 0) && (pK5 == 0)
        if (pK1 > 5.99) && (pK4 > 5.99)
            formula = 'formula46';
            char_den_gcs = ((q.*N_mat1_active).*((H_surf)./(H_surf +
K1)))+((q.*N_mat2_active).*((H_surf)./(H_surf + K4)));
        end
        if (pK1 > 5.99) && (pK4 < 5.99)
            formula = 'formula47';
            char_den_gcs = ((q.*N_mat1_active).*((H_surf)./(H_surf +
K1)))+((q.*N_mat2_active).*((-K4)./(H_surf + K4)));
        end
        if (pK1 < 5.99) && (pK4 > 5.99)
            formula = 'formula48';
            char_den_gcs = ((q.*N_mat1_active).*((-K1)./(H_surf +
K1)))+((q.*N_mat2_active).*((H_surf)./(H_surf + K4)));
        end
        if (pK1 < 5.99) && (pK4 < 5.99)
            formula = 'formula49';
            char_den_gcs = ((q.*N_mat1_active).*((-K1)./(H_surf +
K1)))+((q.*N_mat2_active).*((-K4)./(H_surf + K4)));
        end
    end
end

if (pK2 == 0 && pK3 == 0) && (pK5 == 0 && pK6 == 0)
    if (pK1 < 5.99)
        formula = 'formula50';
        char_den_gcs = ((q.*N_mat1_active).*((-K1)./(H_surf + K1)));
    end
    if (pK1 > 5.99)
        formula = 'formula51';
        char_den_gcs = ((q.*N_mat1_active).*((H_surf)./(H_surf + K1)));
    end
end
end
```

D.7 Gouy-Chapman and Gouy-Chapman-Stern layer model

This function calculates the surface charge density by the Gouy-Chapman Stern layer model.

```matlab
function [pot_zeta, pot_surface] = pot_cal(pH_b)

global B Qo cstern toler numpHsteps pot_lower pot_higher_positive
pot_higher_negative pH_pzc;

pH_pzc = pHpzc; % use electric double layer parameter of corresponding
oxide/electrolyte

for i = 1:numpHsteps

        if pH_b(i) < pH_pzc

        pot_low(i) = pot_lower;
        pot_high(i) = pot_higher_positive;

        [f_low_int(i), f_low_edl(i)] = char_den(pH_b(i), pot_low(i));
        [f_high_int(i), f_high_edl(i)] = char_den(pH_b(i), pot_high(i));

            for n = 1:100
                if (f_high_edl(i)-f_high_int(i)) > 0
                    pot_high2(i)=0.5*(pot_low(i)+pot_high(i));
                    [fn_high_int(i,n), fn_high_edl(i,n)] = char_den(pH_b(i),
pot_high2(i));
                    if     (fn_high_edl(i,n)-fn_high_int(i,n)) > 0
                            pot_high(i)=pot_high2(i);
                            pot_high2(i)=0.5*(pot_low(i)+pot_high(i));
                    end
                    if     (fn_high_edl(i,n)-fn_high_int(i,n)) < 0
                            pot_low(i)=pot_high2(i);
                            pot_high2(i)=0.5*(pot_low(i)+pot_high(i));
                    end
                end
                err(i,n)=abs((pot_high(i)-pot_low(i))/pot_high(i));
                    if (err(i,n) < toler), break;
                    end
            end

    elseif pH_b(i) == pH_pzc
        pot_low = 0;

    else
        pot_low(i) = pot_lower;
        pot_high(i) = pot_higher_negative;

        [f_low_int(i), f_low_edl(i)] = char_den(pH_b(i), pot_low(i));
        [f_high_int(i), f_high_edl(i)] = char_den(pH_b(i), pot_high(i));

        for n = 1:100
```

```matlab
                if (f_high_edl(i)-f_high_int(i)) < 0
                    pot_high2(i)=0.5*(pot_low(i)+pot_high(i));
                    [fn_high_int(i,n), fn_high_edl(i,n)] = char_den(pH_b(i),
pot_high2(i));
                        if     (fn_high_edl(i,n)-fn_high_int(i,n)) < 0
                            pot_high(i)=pot_high2(i);
                            pot_high2(i)=0.5*(pot_low(i)+pot_high(i));
                        end
                        if     (fn_high_edl(i,n)-fn_high_int(i,n)) > 0
                            pot_low(i)=pot_high2(i);
                            pot_high2(i)=0.5*(pot_low(i)+pot_high(i));
                        end
                end
                err(i,n)=abs((pot_high(i)-pot_low(i))/pot_high(i));
                    if (err(i,n) < toler), break;
                    end
        end

        end

end

pot_zeta = pot_low;
pot_surface = ((((Qo*sinh(pot_zeta/(2*B)))/cstern) + pot_zeta));

end
```

D.8   Parameters function

```matlab
function [H_bulk, H_surf, pHS, beta, diffuseLayerCap, diffLayerCap, alpha,
totalCap, debyeLength, potVariation, nVariation, pVariation] = parameters(pH_B,
pot_Zeta, pot_Surface)

global q Ew Io Navo B Qo mol_per1 mol_length1 mol_per2 mol_length2 cstern zDistance
numpHsteps capBio;

zDistance = transpose(linspace(0,10e-9,numpHsteps));

pHB = (pH_B);
potZeta = (pot_Zeta);
potSurface = (pot_Surface);

[char_Den_GCS, char_Den_GC] = char_den(pHB, potZeta);

charDenGCS = (char_Den_GCS);
charDenGC = (char_Den_GC);

H_bulk = 10.^(-pHB);

H_surf = H_bulk.*exp(-potSurface./B);

pHS = pHB + (potSurface./(2.303*B));

beta = (-1./q)*gradient(charDenGCS, pHS);

diffuseLayerCap = (Qo./(2*B)*cosh(potZeta./(2*B)));

diffLayerCap = (diffuseLayerCap.*cstern)./(diffuseLayerCap+cstern);

alpha = (1./(((2.303*B*diffLayerCap)./(q*beta))+1));

capBio1 = mol_per1./mol_length1;
capBio2 = mol_per2./mol_length2;

if mol_per2 ==0
    capBio = capBio1;
else
    capBio = (capBio1.*capBio2)./(capBio1 + capBio2);
end

totalCap = diffLayerCap + capBio;

debyeLength = ((Ew*B)./(2*q*Io*Navo)).^0.5;

potVariation = (4*B).*atanh((exp(-zDistance./debyeLength)).*tanh(potZeta./(4*B)));

ni = (10^-3).*Navo.*Io;
```

```matlab
p_doping = (10^-3).*Navo.*(H_bulk); % Intrinsic Charge Carriers in Silicon

n_doping = (10^-3).*Navo.*((10.^-14./H_bulk)); % Intrinsic Charge Carriers in
Silicon

nb = ni + n_doping; % Bulk Concentration of Electrons

pb = ni + p_doping; % Bulk Concertation of Holes

nVariation = nb.*exp(potVariation/(B)); % Surface Concentration of Electrons

pVariation = pb.*exp(-potVariation/(B)); % Surface Concentration of Holes

end
```

Not enough input arguments.

Error in parameters (line 7)
pHB = (pH_B);

D.9 Device function

```matlab
function [depletionWidth, current] = device(potSurface, potSurfaceMax,
input_material, oxide_thickness, degraded_oxide_thickness, degradation, width,
height, length_channel, resistivity, depletion_width, voltage_DS)

global Eo q;

input = input_material;

database = readtable('amino.xlsx', 'ReadVariableNames', true);
check = strcmp(database.material, input);
rowNum = find(check==1);

permittivity = table2array(database(rowNum, 'permittivity'));

Er_Si = 11.68;
E_Si = Er_Si.*Eo;
Er_ox = permittivity;
E_ox = Er_ox.*Eo;
E_ox_degrad = E_ox.*degradation;
t_ox = oxide_thickness;
t_oxd = degraded_oxide_thickness;

if degradation == 0
    C_ox = (E_ox./t_ox);
else
    C_ox = (E_ox_degrad.*E_ox)./((E_ox.*t_oxd) + E_ox_degrad.*(t_ox - t_oxd));
end

w = width;
h = height;
l = length_channel;
rho = resistivity;
wd = depletion_width;
vds = voltage_DS;

Vgg = abs(potSurfaceMax);

Na = Vgg./(((q.*wd.^2)./(2*E_Si)) + ((q.*wd)./(C_ox)));
depletionWidth = -(E_Si./C_ox) + sqrt((E_Si./C_ox).^2 +
((2.*E_Si)./(q.*Na)).*(potSurface+Vgg));
Ids = (((w - 2.*depletionWidth).*h.*vds)./(rho.*l));
current = Ids*1e6;

end
```

D.10 Generate function

```matlab
global material1 material2 parent_folder project_dir;

projectdir = project_dir;
parentFolder = parent_folder;
folderName = material1;

folderPath = fullfile(projectdir, parentFolder, folderName);

mkdir( folderPath );

Alpha = transpose(alpha);
Beta = transpose(beta);
Charge_Density_GC = transpose(char_Den_GC);
Charge_Density_GCS = transpose(char_Den_GCS);
Current = transpose(current);
Depletion_Width = transpose(depletionWidth);
Difference_Layer_Cap = transpose(diffLayerCap);
Diffuse_Layer_Cap = transpose(diffuseLayerCap);
H_Bulk = transpose(H_bulk);
H_Surf = transpose(H_surf);
N_Variation = (nVariation);
PH_Bulk = transpose(pH_b);
PH_Surf = transpose(pHS);
Pot_Surface = transpose(pot_surface);
Pot_Zeta = transpose(pot_zeta);
Pot_Variation = (potVariation);
P_Variation = (pVariation);
Total_Cap = transpose(totalCap);
Z_Distance = (zDistance);

DPOTZETA_DPH = gradient(Pot_Zeta, PH_Bulk);
D2POTZETA_DPH2 = gradient(DPOTZETA_DPH);

DPOTSURFACE_DPH = gradient(Pot_Surface, PH_Bulk);
D2POTSURFACE_DPH2 = gradient(DPOTSURFACE_DPH);

writematrix(Alpha, fullfile(folderPath, 'Alpha.csv'));
writematrix(Beta, fullfile(folderPath, 'Beta.csv'));
writematrix(Charge_Density_GC, fullfile(folderPath, 'Charge_Density_GC.csv'));
writematrix(Charge_Density_GCS, fullfile(folderPath, 'Charge_Density_GCS.csv'));
writematrix(Current, fullfile(folderPath, 'Current.csv'));
writematrix(Depletion_Width, fullfile(folderPath, 'Depletion_Width.csv'));
writematrix(Difference_Layer_Cap, fullfile(folderPath,
'Difference_Layer_Cap.csv'));
writematrix(Diffuse_Layer_Cap, fullfile(folderPath, 'Diffuse_Layer_Cap.csv'));
writematrix(H_Bulk, fullfile(folderPath, 'H_Bulk.csv'));
writematrix(H_Surf, fullfile(folderPath, 'H_Surf.csv'));
writematrix(N_Variation, fullfile(folderPath, 'N_Variation.csv'));
```

```matlab
writematrix(PH_Bulk, fullfile(folderPath, 'PH_Bulk.csv'));
writematrix(PH_Surf, fullfile(folderPath, 'PH_Surf.csv'));
writematrix(Pot_Surface, fullfile(folderPath, 'Pot_Surface.csv'));
writematrix(Pot_Zeta, fullfile(folderPath, 'Pot_Zeta.csv'));
writematrix(Pot_Variation, fullfile(folderPath, 'Pot_Variation.csv'));
writematrix(P_Variation, fullfile(folderPath, 'P_Variation.csv'));
writematrix(Total_Cap, fullfile(folderPath, 'Total_Cap.csv'));
writematrix(Z_Distance, fullfile(folderPath, 'Z_Distance.csv'));

writematrix(DPOTZETA_DPH, fullfile(folderPath, 'DPOTZETA_DPH.csv'));
writematrix(D2POTZETA_DPH2, fullfile(folderPath, 'D2POTZETA_DPH2.csv'));
writematrix(DPOTSURFACE_DPH, fullfile(folderPath, 'DPOTSURFACE_DPH.csv'));
writematrix(D2POTSURFACE_DPH2, fullfile(folderPath, 'D2POTSURFACE_DPH2.csv'));
```

Appendix E

Synopsys Sentaurus TCAD code

E.1   3D device simulation code

```
;================================================================================
================================================================

;   In this Code you can vary *w_ch* (channel width), *g_ox* (gate oxide), *Y_fin* (height of fin) and
rest will be adjusted automatically accordingly

;================================================================================
================================================================


(sde:clear)


#box means buried oxide
(define X_box 10.1)
(define Y_box 0.6)
(define Z_box 1)


#Variables
(define w_ch 0.2)
(define g_ox 0.005)
(define Y_fin 2.6)


#Construced only one block of source,channel and drain as ch
#h is height
(define h_ch 2)


(define Z_fin 0.4)


#Source_ and_Drain_Oxide
(define X_sox 0.05)
(define X_dox 10.05)


(define Y_sdox 2.7)
```

#electro means Electrolyte

(define Y_electro 3.6)

;======================================
;   GEOMETRY DEFINITION
;======================================

#Dimensions as per paper by Pittino ONLY the z-direction dimension added by me

(define subcub (sdegeo:create-cuboid (position 0 0 0) (position X_box Y_box Z_box) "SiO2" "box_reg"))

(define subcub (sdegeo:create-cuboid (position 0 Y_box Z_fin) (position X_box Y_fin (+ Z_fin w_ch)) "Silicon" "fin_reg"))

;====================
;5nm thick GATE SiO2
;====================

#Dimensions as per paper by Pittino ONLY the z-direction dimension added by me

(define subcub (sdegeo:create-cuboid (position X_sox Y_box (- Z_fin g_ox)) (position X_dox (+ Y_fin g_ox) Z_fin) "SiO2" "SurfOx_reg"))

(define subcub (sdegeo:create-cuboid (position X_sox Y_fin Z_fin) (position X_dox (+ Y_fin g_ox) (+ Z_fin w_ch)) "SiO2" "SurfOx_reg"))

(define subcub (sdegeo:create-cuboid (position X_sox Y_box (+ Z_fin w_ch)) (position X_dox (+ Y_fin g_ox) (+ Z_fin w_ch g_ox)) "SiO2" "SurfOx_reg"))

;===
; 100nm (top) & 0.496 um (side) thick SOURCE and DRAIN SiO2
;===

#Dimensions as per paper by Pittino ONLY the z-direction dimension added by me

(define subcub (sdegeo:create-cuboid (position 0 Y_box 0) (position X_sox Y_sdox Z_fin) "SiO2" "SurfOx_reg"))

(define subcub (sdegeo:create-cuboid (position 0 Y_fin Z_fin) (position X_sox Y_sdox (+ Z_fin w_ch)) "SiO2" "SurfOx_reg"))

```
(define subcub (sdegeo:create-cuboid (position 0 Y_box (+ Z_fin w_ch)) (position X_sox Y_sdox
Z_box) "SiO2" "SurfOx_reg"))
```

#Dimensions as per paper by Pittino ONLY the z-direction dimension added by me

```
(define subcub (sdegeo:create-cuboid (position X_dox Y_box 0) (position X_box Y_sdox Z_fin) "SiO2"
"SurfOx_reg"))
```

```
(define subcub (sdegeo:create-cuboid (position X_dox Y_fin Z_fin) (position X_box Y_sdox (+ Z_fin
w_ch)) "SiO2" "SurfOx_reg"))
```

```
(define subcub (sdegeo:create-cuboid (position X_dox Y_box (+ Z_fin w_ch)) (position X_box Y_sdox
Z_box) "SiO2" "SurfOx_reg"))
```

```
;============================
;5um thick ELECTROLYTE HfO2
;============================
```

```
#(define subcub (sdegeo:create-cuboid (position X_sox Y_box 0) (position X_dox Y_electro (- Z_fin
g_ox)) "Electrolyte" "Elect_reg"))
```

```
#(define subcub (sdegeo:create-cuboid (position X_sox (+ Y_fin g_ox) (- Z_fin g_ox)) (position X_dox
Y_electro (+ Z_fin w_ch g_ox)) "Electrolyte" "Elect_reg"))
```

```
#(define subcub (sdegeo:create-cuboid (position X_sox Y_box (+ Z_fin w_ch g_ox)) (position X_dox
Y_electro Z_box) "Electrolyte" "Elect_reg"))
```

```
#(define subcub (sdegeo:create-cuboid (position 0 Y_sdox 0) (position X_sox Y_electro Z_box)
"Electrolyte" "Elect_reg"))
```

```
#(define subcub (sdegeo:create-cuboid (position X_dox Y_sdox 0) (position X_box Y_electro Z_box)
"Electrolyte" "Elect_reg"))
```

```
;=====================================
;   DOPING PROFILE
;=====================================
```

channel including source and drain p doped everywhere

```
(sdedr:define-constant-profile "Boron_BG_src" "BoronActiveConcentration" 1e17)
```

```
(sdedr:define-constant-profile-region "Boron_BG_PL_SRC" "Boron_BG_src" "fin_reg")
```

```
;========================================

;    CONTACTS DEFINITION

;========================================


#Source Contact

(sdegeo:set-contact (find-face-id (position 0 (+ Y_box (* 0.5 h_ch)) (* 0.5 Z_box))) "Source")


#Drain Contact

(sdegeo:set-contact (find-face-id (position X_box (+ Y_box (* 0.5 h_ch)) (* 0.5 Z_box))) "Drain")


#GATE CONTACT

;======
;TOP
;======


#Pittino paper on top of SiO2 layer

(sdegeo:set-contact-faces-by-polygon(list(list (position X_sox (+ Y_fin g_ox) (- Z_fin g_ox))(position
X_dox (+ Y_fin g_ox) (- Z_fin g_ox))(position X_dox (+ Y_fin g_ox) (+ Z_fin w_ch g_ox))(position X_sox
(+ Y_fin g_ox) (+ Z_fin w_ch g_ox))(position X_sox (+ Y_fin g_ox) (- Z_fin g_ox))))(list(gvector 0 0 -1))
"Gate")


;==============
;BACK
;==============


#Pittino paper on back of SiO2 layer

(sdegeo:set-contact-faces-by-polygon(list(list (position X_sox Y_box (+ Z_fin w_ch g_ox))(position
X_dox Y_box (+ Z_fin w_ch g_ox))(position X_dox (+ Y_fin g_ox) (+ Z_fin w_ch g_ox))(position X_sox
```

(+ Y_fin g_ox) (+ Z_fin w_ch g_ox))(position X_sox Y_box (+ Z_fin w_ch g_ox))))(list(gvector 0 0 -1)) "Gate")

;==========

;FRONT

;==========

#Pittino paper on front of SiO2 layer

(sdegeo:set-contact-faces-by-polygon(list(list (position X_sox Y_box (- Z_fin g_ox))(position X_dox Y_box (- Z_fin g_ox))(position X_dox (+ Y_fin g_ox) (- Z_fin g_ox))(position X_sox (+ Y_fin g_ox) (- Z_fin g_ox))(position X_sox Y_box (- Z_fin g_ox))))(list(gvector 0 0 -1)) "Gate")

;===========================

;ON THREE Sides for Electrolyte

;===========================

#(sdegeo:set-contact-faces-by-polygon(list(list (position 0 Y_electro 0)(position X_box Y_electro 0)(position X_box Y_electro Z_box)(position 0 Y_electro Z_box)(position 0 Y_electro 0)))(list(gvector 0 0 -1)) "Gate")

#(sdegeo:set-contact-faces-by-polygon(list(list (position 0 Y_electro 0)(position 0 Y_sdox 0)(position X_sox Y_sdox 0)(position X_sox Y_box 0)(position X_dox Y_box 0) (position X_dox Y_sdox 0) (position X_box Y_sdox 0) (position X_box Y_electro 0) (position 0 Y_electro 0)))(list(gvector 0 0 -1)) "Gate")

#(sdegeo:set-contact-faces-by-polygon(list(list (position 0 Y_electro Z_box)(position 0 Y_sdox Z_box)(position X_sox Y_sdox Z_box)(position X_sox Y_box Z_box)(position X_dox Y_box Z_box) (position X_dox Y_sdox Z_box) (position X_box Y_sdox Z_box) (position X_box Y_electro Z_box) (position 0 Y_electro Z_box)))(list(gvector 0 0 -1)) "Gate")

;=====================================

; MESHING STRATEGY

;=====================================

```
(sdedr:define-refinement-size "Si_Mesh" 0.1 0.1 0.1 0.01 0.01 0.01)

(sdedr:define-refinement-material "Si_Mesh_PL" "Si_Mesh" "Silicon" )

(sdedr:define-refinement-function "Si_Mesh_PL" "DopingConcentration" "MaxTransDiff" 2)


#(sdedr:define-refinement-size "Aluminum_Mesh" 0.01 0.01 0.01 0.001 0.001 0.001)

#(sdedr:define-refinement-material "Aluminum_Mesh_PL" "Aluminum_Mesh" "Aluminum" )

#(sdedr:define-refinement-function "Aluminum_Mesh_PL" "DopingConcentration" "MaxTransDiff"
2)


#(sdedr:define-refinement-size "SiO2_Mesh" 0.01 0.01 0.01 0.001 0.001 0.001)

#(sdedr:define-refinement-material "SiO2_Mesh_PL" "SiO2_Mesh" "SiO2" )

#(sdedr:define-refinement-function "SiO2_Mesh_PL" "DopingConcentration" "MaxTransDiff" 2)



##To create tdr file

##(sde:build-mesh "snmesh" "-a -c boxmethod" "n@node@")

(sde:build-mesh "n@node@")
```

```
#define _Vdd_    @Vdd@

#define _Vg_     @Vg@


File {
 * input files:
 Grid=  "n1_msh.tdr"
 Parameter=  "@parameter@"


 * output files:
 Plot=  "@tdrdat@"
 Current="@plot@"
 Output= "@log@"


}


Electrode {
 { Name= "Gate"    Voltage= 0.0 }
 { Name= "Source"   Voltage= 0.0 }
 { Name= "Drain"    Voltage= 0.0 }


}


Physics {
 Mobility( DopingDep HighFieldSat Enormal )
 EffectiveIntrinsicDensity( OldSlotboom )


}




Math {
```

-- Parallelization on multi-CPU machine --

  Number_Of_Threads=16   * change the number of threads to > 1 to make

                * parallelization possible. First ensure your machine

                * has shared-memory multi-CPU configuration.

-- Numeric/Solver Controls --

  Extrapolate   * switches on solution extrapolation along a bias ramp

  Derivatives   * considers mobility derivatives in Jacobian

  Iterations=10000   * maximum-allowed number of Newton iterations (3D)

  RelErrControl   * switches on the relative error control for solution

                * variables (on by default)

  Digits=5   * relative error control value. Iterations stop if

                * dx/x < 10^(-Digits)

  Method=ILS   * use the iterative linear solver with default parameter

  NotDamped=100   * number of Newton iterations over which the RHS-norm

                * is allowed to increase

  Transient=BE   * switches on BE transient method

}

Solve {

*- Buildup of initial solution:

  Coupled(Iterations=100){ Poisson }

  Coupled{ Poisson Electron Hole }

*- Bias drain to target bias

  Quasistationary(

    InitialStep=0.01 MinStep=1e-10 MaxStep=0.2

    Goal{ Name="Drain" Voltage= @Vdd@ }

  ){ Coupled{ Poisson Electron Hole } }

*- Gate voltage sweep

  Quasistationary(

```
    InitialStep=1e-3 MinStep=1e-15 MaxStep=0.05 Increment=1.41 Decrement=2.

    Goal{ Name="Gate" Voltage= @Vg@ }

  ){ Coupled{ Poisson Electron Hole } }

}


Plot{

 *--Density and Currents, etc

 eDensity hDensity

 TotalCurrent/Vector eCurrent/Vector hCurrent/Vector

 eMobility/Element hMobility/Element

 eVelocity hVelocity

 eQuasiFermi hQuasiFermi



 *--Fields and charges

 ElectricField/Vector Potential SpaceCharge


 *--Doping Profiles

 Doping DonorConcentration AcceptorConcentration


 *--Driving forces

 eGradQuasiFermi/Vector hGradQuasiFermi/Vector

 eEparallel hEparallel eENormal hENormal


 *--Band structure/Composition

 BandGap

 BandGapNarrowing

 Affinity

 ConductionBand ValenceBand

 eQuantumPotential hQuantumPotential
```

```
*--Visualizing Traps

eTrappedCharge

hTrappedCharge


}
```

E.2   Interface Trap Charges

```
;================================
;Made 2D Structure: proper meshing
;================================


#(sdegeo:create-rectangle (position 0 0 0) (position 0.004 0.05 0) "Anysemiconductor" "Elec_reg")
(sdegeo:create-rectangle (position 0 0 0) (position 0.004 0.05 0) "SiO2" "Elec_reg")


(sdegeo:create-rectangle (position 0.004 0 0) (position 0.006 0.05 0) "HfO2" "Ox_reg")


(sdegeo:create-rectangle (position 0.006 0 0) (position 0.016 0.05 0) "Silicon" "fin_reg")


(sdegeo:create-rectangle (position 0.016 0 0) (position 0.018 0.05 0) "HfO2" "Ox_reg")


#(sdegeo:create-rectangle (position 0.018 0 0) (position 0.022 0.05 0) "Anysemiconductor" "Elec_reg")
(sdegeo:create-rectangle (position 0.018 0 0) (position 0.022 0.05 0) "SiO2" "Elec_reg")


#Doping in Silicon region which is fin
(sdedr:define-constant-profile "Boron_BG_src" "BoronActiveConcentration" 1e17)
(sdedr:define-constant-profile-region "Boron_BG_PL_SRC" "Boron_BG_src" "fin_reg")


##Electrolyte doping:Considering with ntype doping of [OH-] ions


#(sdedr:define-constant-profile "Phosphorous_PH_elec" "PhosphorusActiveConcentration" 6.022e19)
#(sdedr:define-constant-profile-material "Phosphorous_PH_PL_elec" "Phosphorous_PH_elec" "Anysemiconductor")


;===============
;Put Gate Contact
;===============
(sdegeo:set-contact (find-edge-id (position 0.011 0.0 0)) "Drain")
```

```
(sdegeo:define-contact-set "Drain" 20 (color:rgb 0 1 1) "##")

(sdegeo:set-current-contact-set "Drain")


(sdegeo:define-contact-set "Source" 20 (color:rgb 0 1 1) "##")

(sdegeo:set-current-contact-set "Source")

(sdegeo:define-2d-contact (find-edge-id (position (* 0.022 0.5) 0.05 0)) "Source")



(sdegeo:set-contact (find-edge-id (position 0 0.022 0)) "Gate" "remove")

(sdegeo:define-contact-set "Gate" 20 (color:rgb 0 1 1) "##")

(sdegeo:set-current-contact-set "Gate")


(sdegeo:set-contact (find-edge-id (position 0.022 0.022 0)) "Gate" "remove")

(sdegeo:define-contact-set "Gate" 20 (color:rgb 0 1 1) "##")

(sdegeo:set-current-contact-set "Gate")



;=========

;Meshing

;=========


;=====================

;Both Interface Meshing

;=====================

(sdedr:define-refeval-window "RefEvalWin_1" "Rectangle" (position 0.002 0 0) (position 0.005 0.05
0))

(sdedr:define-refeval-window "RefEvalWin_2" "Rectangle" (position 0.017 0 0) (position 0.020 0.05
0))


#Half-nm

#(sdedr:define-refinement-size "RefDefnameI" 0.0005 0.001 0.000475 0.00095)

#One fourth-nm
```

#(sdedr:define-refinement-size "RefDefnameI" 0.00025 0.00025 0.00025 0.00025)

#One tenth-nm

(sdedr:define-refinement-size "RefDefnameI" 0.0001 0.0001 0.0001 0.0001)

(sdedr:define-refinement-placement "RefPlacename_1" "RefDefnameI" "RefEvalWin_1")

(sdedr:define-refinement-placement "RefPlacename_2" "RefDefnameI" "RefEvalWin_2")

;=====================

;Non-Interface Meshing

;=====================

(sdedr:define-refeval-window "RefEvalWin_3" "Rectangle" (position 0 0 0) (position 0.002 0.05 0))

(sdedr:define-refeval-window "RefEvalWin_4" "Rectangle" (position 0.005 0 0) (position 0.017 0.05 0))

(sdedr:define-refeval-window "RefEvalWin_5" "Rectangle" (position 0.020 0 0) (position 0.022 0.05 0))

#Half-nm

#(sdedr:define-refinement-size "RefDefnameNI" 0.0005 0.001 0.000425 0.00095)

#One fourth-nm

(sdedr:define-refinement-size "RefDefnameNI" 0.00025 0.00025 0.00025 0.00025)

#To activate other meshing-specific options such as refinement on doping gradients or interface refinements.

(sdedr:define-refinement-function "RefDef.Channel" "DopingConcentration" "MaxTransDiff" 2)

#(sdedr:define-refinement-function "RefDef.Channel" "MaxLenInt" "Anysemiconductor" "HfO2" 1e-5 1e-5)

(sdedr:define-refinement-function "RefDef.Channel" "MaxLenInt" "SiO2" "HfO2" 1e-5 1e-5)

(sdedr:define-refinement-placement "RefPlacename_3" "RefDefnameNI" "RefEvalWin_3")

(sdedr:define-refinement-placement "RefPlacename_4" "RefDefnameNI" "RefEvalWin_4")

(sdedr:define-refinement-placement "RefPlacename_5" "RefDefnameNI" "RefEvalWin_5")

```
(sde:build-mesh "n@node@")
```

===

SDEVICE CODE

===

```
#define _Vdd_    @Vdd@
#define _Vg_     @Vg@


File {
 * input files:
 Grid=   "n1_msh.tdr"
 Parameter=   "models.par"

 * output files:
 Plot=  "@tdrdat@"
 Current="@plot@"
 Output= "@log@"

}


Electrode {
 { Name= "Gate"     Voltage= 0.0 Material="Aluminum"}
 { Name= "Source"    Voltage= 0.0 }
 { Name= "Drain"    Voltage= 0.0 }
}


Physics {
 Mobility( DopingDep HighFieldSat Enormal )
 EffectiveIntrinsicDensity( OldSlotboom )
 #Recombination( SRH Auger Avalanche )
```

```
}
```

-- Putting traps @t interface between electrolyte and oxide --

```
#Physics(MaterialInterface="HfO2/Anysemiconductor")
Physics(MaterialInterface="HfO2/SiO2")
{
Traps((FixedCharge Conc= @pol_charge@))
}
```

```
Math {
*-- Parallelization on multi-CPU machine --*
 Number_Of_Threads=16   * change the number of threads to > 1 to make
              * parallelization possible. First ensure your machine
              * has shared-memory multi-CPU configuration.
*-- Numeric/Solver Controls --*
 Extrapolate        * switches on solution extrapolation along a bias ramp
 Derivatives        * considers mobility derivatives in Jacobian
 Iterations=10000       * maximum-allowed number of Newton iterations (3D)
 RelErrControl       * switches on the relative error control for solution
             * variables (on by default)
 Digits=5          * relative error control value. Iterations stop if
             * dx/x < 10^(-Digits)
 Method=ILS        * use the iterative linear solver with default parameter
 NotDamped=100       * number of Newton iterations over which the RHS-norm
             * is allowed to increase
 Transient=BE       * switches on BE transient method
```

```
    #Iterations=100

    NotDamped=0

    #Traps(MaterialWiseAssembly)

    Traps(Damping=0)


}


#Math{-CheckUndefinedModels}


Solve {
*- Buildup of initial solution:
  Coupled(Iterations=100){ Poisson }
  Coupled{ Poisson Electron Hole }
  Coupled(
    LineSearchDamping=1e-4
    Iterations=500
  ) {Poisson eQuantumPotential}
*- Bias drain to target bias
  Quasistationary(
    InitialStep=0.01 MinStep=1e-15 MaxStep=0.2
    Goal{ Name="Drain" Voltage= @Vdd@ }
  ){ Coupled{ Poisson Electron Hole } }
*- Gate voltage sweep
  Quasistationary(
    InitialStep=1e-3 MinStep=1e-15 MaxStep=0.05 Increment=1.41 Decrement=2.
    Goal{ Name="Gate" Voltage= @Vg@ }
  ){ Coupled{ Poisson Electron Hole } }
}


Plot{
  *--Density and Currents, etc
```

eDensity hDensity

TotalCurrent/Vector eCurrent/Vector hCurrent/Vector

eMobility/Element hMobility/Element

eVelocity hVelocity

eQuasiFermi hQuasiFermi

*--Temperature

#eTemperature hTemperature Temperature

*--Fields and charges

ElectricField/Vector Potential SpaceCharge

*--Doping Profiles

Doping DonorConcentration AcceptorConcentration

*--Generation/Recombination

#SRH Band2Band Auger

#AvalancheGeneration eAvalancheGeneration hAvalancheGeneration

*--Driving forces

eGradQuasiFermi/Vector hGradQuasiFermi/Vector

eEparallel hEparallel eENormal hENormal

*--Band structure/Composition

BandGap

BandGapNarrowing

Affinity

ConductionBand ValenceBand

eQuantumPotential hQuantumPotential

*--Visualizing Traps

eTrappedCharge

hTrappedCharge

TotalTrapConcentration

}

E.3   Physical Model Interface

```
;===============================
;Made 2D Structure: proper meshing
;===============================


(sdegeo:create-rectangle (position 0 0 0) (position 0.004 0.08 0) "Anysemiconductor" "Elec_reg")


(sdegeo:create-rectangle (position 0.004 0 0) (position 0.0040664 0.08 0) "Anyinsulator"
"Stern_reg")


(sdegeo:create-rectangle (position 0.0040664 0 0) (position 0.0060664 0.08 0) "SiO2" "Ox_reg")


(sdegeo:create-rectangle (position 0.0060664 0 0) (position 0.0560664 0.08 0) "Silicon" "fin_reg")


(sdegeo:create-rectangle (position 0.0560664 0 0) (position 0.0580664 0.08 0) "SiO2" "Ox_reg")


(sdegeo:create-rectangle (position 0.0580664 0 0) (position 0.0581328 0.08 0) "Anyinsulator"
"Stern_reg")


(sdegeo:create-rectangle (position 0.0581328 0 0) (position 0.0621328 0.08 0) "Anysemiconductor"
"Elec_reg")


#Doping in Silicon region which is fin
(sdedr:define-constant-profile "Boron_BG_src" "BoronActiveConcentration" 1e17)
(sdedr:define-constant-profile-region "Boron_BG_PL_SRC" "Boron_BG_src" "fin_reg")


##Electrolyte doping:Considering with ntype doping of [H+] ions pH=14


#(sdedr:define-constant-profile "Boron_PH_elec" "BoronActiveConcentration" 6.022e6)
#(sdedr:define-constant-profile-material "Boron_PH_PL_elec" "Boron_PH_elec"
"Anysemiconductor")


#(sdedr:define-constant-profile "Phosphorous_PH_elec" "PhosphorousActiveConcentration"
6.022e20)
```

```
#(sdedr:define-constant-profile-material "Phosphorous_PH_PL_elec" "Phosphorous_PH_elec"
"Anysemiconductor")




;===============
;Put Gate Contact
;===============
(sdegeo:set-contact (find-edge-id (position 0.0310664 0.0 0)) "Drain")
(sdegeo:define-contact-set "Drain" 20 (color:rgb 0 1 1) "##")
(sdegeo:set-current-contact-set "Drain")


(sdegeo:define-contact-set "Source" 20 (color:rgb 0 1 1) "##")
(sdegeo:set-current-contact-set "Source")
(sdegeo:define-2d-contact (find-edge-id (position (* 0.0621328 0.5) 0.08 0)) "Source")



(sdegeo:set-contact (find-edge-id (position 0 0.0621328 0)) "Gate" "remove")
(sdegeo:define-contact-set "Gate" 20 (color:rgb 0 1 1) "##")
(sdegeo:set-current-contact-set "Gate")


(sdegeo:set-contact (find-edge-id (position 0.0621328 0.0621328 0)) "Gate" "remove")
(sdegeo:define-contact-set "Gate" 20 (color:rgb 0 1 1) "##")
(sdegeo:set-current-contact-set "Gate")



;========
;Meshing
;========


;====================
;Both Interface Meshing--
```

```
;=====================



;===========================================
;Stern layer and stern layer interface meshing
;===========================================
(sdedr:define-refeval-window "RefEvalWin_2" "Rectangle" (position 0.003 0 0) (position 0.008 0.08
0))


#One fiveth-nm(5 lines)
(sdedr:define-refinement-size "RefDefname2" 0.0005 0.0005 0.0005 0.0005)
(sdedr:define-refinement-placement "RefPlacename_2" "RefDefname2" "RefEvalWin_2")



(sdedr:define-refeval-window "RefEvalWin_4" "Rectangle" (position 0.0546 0 0) (position 0.0596
0.08 0))


#Half nm(1/2 nm)
(sdedr:define-refinement-size "RefDefname4" 0.0005 0.0005 0.0005 0.0005)
(sdedr:define-refinement-placement "RefPlacename_4" "RefDefname4" "RefEvalWin_4")


;===========================================
;Non-Interface Meshing
;===========================================
(sdedr:define-refeval-window "RefEvalWin_1" "Rectangle" (position 0.0 0 0) (position 0.003 0.08 0))
(sdedr:define-refeval-window "RefEvalWin_3" "Rectangle" (position 0.008 0 0) (position 0.0546 0.08
0))
(sdedr:define-refeval-window "RefEvalWin_5" "Rectangle" (position 0.0596 0 0) (position 0.0621328
0.08 0))


#One nm (1nm)
(sdedr:define-refinement-size "RefDefname1" 0.001 0.001 0.001 0.001)
```

```
(sdedr:define-refinement-size "RefDefname3" 0.001 0.001 0.001 0.001)
(sdedr:define-refinement-size "RefDefname5" 0.001 0.001 0.001 0.001)



(sdedr:define-refinement-placement "RefPlacename_1" "RefDefname1" "RefEvalWin_1")
(sdedr:define-refinement-placement "RefPlacename_3" "RefDefname3" "RefEvalWin_3")
(sdedr:define-refinement-placement "RefPlacename_5" "RefDefname5" "RefEvalWin_5")



(sde:build-mesh "n@node@")
```

```
#define _Vdd_    @Vdd@
#define _Vg_     @Vg@



Device PMOS{
File {
 * input files:
 Grid = "n1_msh.tdr"
 Param = "models.par"


 * output files:
 Plot=  "@tdrdat@"
 Current="@plot@"



}


Electrode {
 { Name= "Gate"    Voltage= 0.0 Material="Aluminum"}
 { Name= "Source"   Voltage= 0.0 }
 { Name= "Drain"    Voltage= 0.0 }
}


Physics
{
        Temperature = 298
     AreaFactor = 1
}


Physics (material="Silicon")
{
```

```
        Mobility ( HighFieldSat)

        Fermi


}


Physics (MaterialInterface="Anyinsulator/Anysemiconductor")

{

  Traps((CBRate=("PMI_electron_traps",17) VBRate="PMI_prova_VB" Acceptor Conc=500e12)

        (VBRate=("PMI_hole_traps", 17) CBRate="PMI_prova_VB" Donor Conc=500e12)

   )

}



Plot{
 *--Density and Currents, etc
 eDensity hDensity
 TotalCurrent/Vector eCurrent/Vector hCurrent/Vector
 eMobility/Element hMobility/Element
 eVelocity hVelocity
 eQuasiFermi hQuasiFermi


 *--Temperature
 #eTemperature hTemperature Temperature


 *--Fields and charges
 ElectricField/Vector Potential SpaceCharge


 *--Doping Profiles
 Doping DonorConcentration AcceptorConcentration


 *--Generation/Recombination
```

```
    #SRH Band2Band Auger

    #AvalancheGeneration eAvalancheGeneration hAvalancheGeneration


    *--Driving forces

    eGradQuasiFermi/Vector hGradQuasiFermi/Vector

    eEparallel hEparallel eENormal hENormal


    *--Band structure/Composition

    BandGap

    BandGapNarrowing

    Affinity

    ConductionBand ValenceBand

    eQuantumPotential hQuantumPotential


    *--Visualizing Traps

    eTrappedCharge

    hTrappedCharge

    TotalTrapConcentration

    }
}



Math {
*-- Parallelization on multi-CPU machine --*

  Number_Of_Threads=20   * change the number of threads to > 1 to make

              * parallelization possible. First ensure your machine

              * has shared-memory multi-CPU configuration.
*-- Numeric/Solver Controls --*

  Extrapolate        * switches on solution extrapolation along a bias ramp

  Derivatives        * considers mobility derivatives in Jacobian

  Iterations=10000        * maximum-allowed number of Newton iterations (3D)
```

```
    RelErrControl        * switches on the relative error control for solution

              * variables (on by default)

    Digits=5          * relative error control value. Iterations stop if

            * dx/x < 10^(-Digits)

    Method=ILS         * use the iterative linear solver with default parameter

    NotDamped=100       * number of Newton iterations over which the RHS-norm

              * is allowed to increase

    Transient=BE        * switches on BE transient method



    NotDamped=0

    Traps(Damping=0)


}


File{

Output= "@log@"

ACExtract= "@acplot@"


PMIPath = "/opt/synopsys-2018/sentaurus/O_2018.06-SP1/tcad/O-2018.06-
SP1/lib/sdevice/src/pmi_sitebinding/"

}


System{

  PMOS trans (Drain=d Source=s Gate=g)

  Vsource_pset vd (d 0) {dc=0}

  Vsource_pset vs (s 0) {dc=0}

  Vsource_pset vg (g 0) {dc=0}

}


Solve {
```

```
*- Buildup of initial solution:

  Coupled(Iterations=100){ Poisson }

  Coupled{ Poisson Electron Hole }

  Coupled(

    LineSearchDamping=1e-4

    Iterations=500

  ) {Poisson eQuantumPotential}

*- Bias drain to target bias

  Quasistationary(

    InitialStep=0.01 MinStep=1e-9 MaxStep=0.2

    Goal{ Parameter=vd.dc Voltage= @Vdd@ }

  ){ Coupled{ Poisson Electron Hole } }

*- Gate voltage sweep

  Quasistationary(

    InitialStep=1e-3 MinStep=1e-15 MaxStep=0.05 Increment=1.41 Decrement=2.

    Goal{ Parameter=vg.dc Voltage= @Vg@ }

  )


*- AC Analysis

 {ACCoupled(

  StartFrequency=1e6 EndFrequency=1e6 NumberOfPoints=1 Decade

  Node(d s g)Exclude(vd vs vg)

  ACCompute (Time = (Range = (0 1)  Intervals = 30))

  ){Poisson Electron Hole}

  }


}
```

```
PMI_Electron_Traps.C

#include "PMI_electron_traps.h"


PMI_electron_traps::PMI_electron_traps(const PMI_Environment&
env):PMI_TrapCaptureEmission_Base (env){}


void PMI_electron_traps::compute (const Input& input, Output& output)

{

  output.capture = 0.000;

  output.emission = 1.2961*pow(10,-9);

}

extern "C" PMI_TrapCaptureEmission_Base * new_PMI_TrapCaptureEmission_Base(const
PMI_Environment& env, int id) {

        return new PMI_electron_traps(env);

}

PMI_Hole_Traps.C

#include "PMI_hole_traps.h"


PMI_hole_traps::PMI_hole_traps(const PMI_Environment& env):PMI_TrapCaptureEmission_Base
(env) {}


void PMI_hole_traps::compute (const Input& input, Output& output)

{


  output.capture = 2.9618*pow(10,-10);

  output.emission = 1*pow(10,-9);

}


extern "C" PMI_TrapCaptureEmission_Base * new_PMI_TrapCaptureEmission_Base(const
PMI_Environment& env, int id) {

        return new PMI_hole_traps(env);

}
```

Appendix F

Copyrights

Permissions Helpdesk <permissionshelpdesk@elsevier.com>

Wed 29/06/2022 15:24

To: Rakshita Pritam Singh Dhar (PGR) <r.dhar.1@research.gla.ac.uk>

Dear Dear Rakshita Dhar,

We hereby grant you permission to reprint the material below at no charge in your thesis subject to the following conditions:

1. If any part of the material to be used (for example, figures) has appeared in our publication with credit or acknowledgement to another source, permission must also be sought from that source. If such permission is not obtained then that material may not be included in your publication/copies.

2. Suitable acknowledgment to the source must be made, either as a footnote or in a reference list at the end of your publication, as follows:

"This article was published in Publication title, Vol number, Author(s), Title of article, Page Nos, Copyright Elsevier (or appropriate Society name) (Year)."

3. Your thesis may be submitted to your institution in either print or electronic form.

4. Reproduction of this material is confined to the purpose for which permission is hereby given.

5. This permission is granted for non-exclusive world English rights only. For other languages please reapply separately for each one required. Permission excludes use in an electronic form other than submission. Should you have a specific electronic project in mind please reapply for permission.

6. As long as the article is embedded in your thesis, you can post/share your thesis in the University repository.

7. Should your thesis be published commercially, please reapply for permission.

8. Posting of the full article/ chapter online is not permitted. You may post an abstract with a link to the Elsevier website [http://www.elsevier.com,]www.elsevier.com, or to the article on ScienceDirect if it is available on that platform.

Kind regards,

Roopa Lingayath
Senior Copyrights Coordinator
ELSEVIER | HCM - Health Content Management

Visit Elsevier Permissions

Figure F.1: Elsevier permission for using diagrams in thesis

Figure F.2: IEEE Xplore permission for using diagrams in thesis

Bibliography

[1] M. Harndahl, M. Rasmussen, G. Roder, I. Dalgaard Pedersen, M. Sørensen, M. Nielsen, and S. Buus, "Peptide-mhc class i stability is a better predictor than peptide affinity of ctl immunogenicity," *European journal of immunology*, vol. 42, no. 6, pp. 1405–1416, 2012.

[2] C. Bock, M. Coleman, B. Collins, J. Davis, G. Foulds, L. Gold, C. Greef, J. Heil, J. S. Heilig, B. Hicke *et al.*, "Photoaptamer arrays applied to multiplexed proteomic analysis," *Proteomics*, vol. 4, no. 3, pp. 609–618, 2004.

[3] M. Uttamchandani, J. Wang, and S. Q. Yao, "Protein and small molecule microarrays: powerful tools for high-throughput proteomics," *Molecular Biosystems*, vol. 2, no. 1, pp. 58–68, 2006.

[4] W. Kusnezow, A. Jacob, A. Walijew, F. Diehl, and J. D. Hoheisel, "Antibody microarrays: an evaluation of production parameters," *Proteomics*, vol. 3, no. 3, pp. 254–264, 2003.

[5] J. L. DeRisi, V. R. Iyer, and P. O. Brown, "Exploring the metabolic and genetic control of gene expression on a genomic scale," *Science*, vol. 278, no. 5338, pp. 680–686, 1997.

[6] G. MacBeath and S. L. Schreiber, "Printing proteins as microarrays for high-throughput function determination," *Science*, vol. 289, no. 5485, pp. 1760–1763, 2000.

[7] K.-L. Hsu, K. T. Pilobello, and L. K. Mahal, "Analyzing the dynamic bacterial glycome with a lectin microarray approach," *Nature chemical biology*, vol. 2, no. 3, pp. 153–157, 2006.

[8] M. C. Park, J. Y. Hur, H. S. Cho, S.-H. Park, and K. Y. Suh, "High-throughput single-cell quantification using simple microwell-based cell docking and programmable time-course live-cell imaging," *Lab on a Chip*, vol. 11, no. 1, pp. 79–86, 2011.

[9] A. Syahir, K. Usui, K.-y. Tomizaki, K. Kajikawa, and H. Mihara, "Label and label-free detection techniques for protein microarrays," *Microarrays*, vol. 4, no. 2, pp. 228–244, 2015.

[10] A. Poghossian, S. Ingebrandt, M. Abouzar, and M. J. Schöning, "Label-free detection of charged macromolecules by using a field-effect-based sensor platform: Experiments and

possible mechanisms of signal generation," *Applied physics A*, vol. 87, no. 3, pp. 517–524, 2007.

[11] G. Zheng, F. Patolsky, Y. Cui, W. U. Wang, and C. M. Lieber, "Multiplexed electrical detection of cancer markers with nanowire sensor arrays," *Nature biotechnology*, vol. 23, no. 10, pp. 1294–1301, 2005.

[12] B. M. Lowe, K. Sun, I. Zeimpekis, C.-K. Skylaris, and N. G. Green, "Field-effect sensors– from ph sensing to biosensing: sensitivity enhancement using streptavidin–biotin as a model system," *Analyst*, vol. 142, no. 22, pp. 4173–4200, 2017.

[13] M. Deen, M. Shinwari, J. Ranuárez, and D. Landheer, "Noise considerations in field-effect biosensors," *Journal of applied physics*, vol. 100, no. 7, p. 074703, 2006.

[14] M. Riordan and L. Hoddeson, "The origins of the pn junction," *Spectrum, IEEE*, vol. 34, pp. 46 – 51, 07 1997.

[15] J. M. Fiore, *Semiconductor Devices: Theory and Application*, 2021.

[16] T. Jenkins, "A brief history of... semiconductors," *Physics education*, vol. 40, no. 5, p. 430, 2005.

[17] "The nobel prize in physics 1956." 2022. [Online]. Available: Thu.9Jun2022.<https://www.nobelprize.org/prizes/physics/1956/summary/>

[18] K. K. Ng, *Complete guide to semiconductor devices*. Wiley Online Library, 2002.

[19] P. Bergveld, "Future applications of isfets," *Sensors and Actuators B: Chemical*, vol. 4, no. 1, pp. 125–133, 1991. [Online]. Available: https://www.sciencedirect.com/science/article/pii/092540059180187O

[20] J.-P. Colinge *et al.*, *FinFETs and other multi-gate transistors*. Springer, 2008, vol. 73.

[21] P. Nair and M. Alam, "Performance limits of nanobiosensors," *Applied physics letters*, vol. 88, no. 23, p. 233120, 2006.

[22] Y. Cui, Q. Wei, H. Park, and C. M. Lieber, "Nanowire nanosensors for highly sensitive and selective detection of biological and chemical species," *science*, vol. 293, no. 5533, pp. 1289–1292, 2001.

[23] C. Medina-Bailon, N. Kumar, R. P. S. Dhar, I. Todorova, D. Lenoble, V. P. Georgiev, and C. Pascual García, "Comprehensive analytical modelling of an absolute ph sensor," *Sensors*, vol. 21, no. 15, p. 5190, 2021.

[24] S. Sahay and M. J. Kumar, *Fundamentals of Junctionless Field [U+2010] Effect Transistors*, 2019, pp. 67–123.

[25] S. Rollo, D. Rani, R. Leturcq, W. Olthuis, and C. Pascual Garci´a, "High aspect ratio fin-ion sensitive field effect transistor: compromises toward better electrochemical biosensing," *Nano letters*, vol. 19, no. 5, pp. 2879–2887, 2019.

[26] F. W. Scheller, A. Yarman, T. Bachmann, T. Hirsch, S. Kubick, R. Renneberg, S. Schumacher, U. Wollenberger, C. Teller, and F. F. Bier, "Future of biosensors: a personal view," *Biosensors based on aptamers and enzymes*, pp. 1–28, 2013.

[27] A. Matsumoto and Y. Miyahara, "Current and emerging challenges of field effect transistor based bio-sensing," *Nanoscale*, vol. 5, no. 22, pp. 10 702–10 718, 2013.

[28] R. Van Hal, J. Eijkel, and P. Bergveld, "A general model to describe the electrostatic potential at electrolyte oxide interfaces," *Advances in colloid and interface science*, vol. 69, no. 1-3, pp. 31–62, 1996.

[29] B. Bhushan, K. Kwak, S. Gupta, and S. Lee, "Nanoscale adhesion, friction and wear studies of biomolecules on silane polymer-coated silica and alumina-based surfaces," *Journal of the Royal Society, Interface / the Royal Society*, vol. 6, pp. 719–33, 12 2008.

[30] S. Chen, J. G. Bomer, E. T. Carlen, and A. van den Berg, "Al2o3/silicon nanoisfet with near ideal nernstian response," *Nano Letters*, vol. 11, no. 6, pp. 2334–2341, 2011, pMID: 21526845. [Online]. Available: https://doi.org/10.1021/nl200623n

[31] S. Sørensen. In 1909 sørensen, a danish chemist, introduced the concept of ph as a convenient way of expressing acidity. [Online]. Available: https://sciencehistory.org/education/scientific-biographies/soren-sorensen/

[32] R. P. S. Dhar, N. Kumar, C. Medina-Bailon, C. P. García, and V. P. Georigiev, "Tcad simulations of high-aspect-ratio nano-biosensor for label-free sensing application," in *2021 Joint International EUROSOI Workshop and International Conference on Ultimate Integration on Silicon (EuroSOI-ULIS)*.   IEEE, 2021, pp. 1–4.

[33] B. A. . F. L. R.   New York: Wiley-Interscience., (2000).

[34] B. L. I. Delhi. Lecture 22: Electrical double layer (edl). Microfluidics Lectures (IIT Delhi). [Online]. Available: https://youtu.be/1gNeC4cT7P8

[35] M. Alam, "Principles of electronic nanobiosensors," *Nanohub web course*, 2013.

[36] S. Kim, D. W. Kwon, S. Kim, R. Lee, T.-H. Kim, H.-S. Mo, D. H. Kim, and B.-G. Park, "Analysis of current drift on p-channel ph-sensitive sinw isfet by

capacitance measurement," *Current Applied Physics*, vol. 18, pp. S68–S74, 2018, special issue on Recent Advances in Nanoscience and Nanotechnology. [Online]. Available: https://www.sciencedirect.com/science/article/pii/S1567173917303309

[37] C. Jakobson, M. Feinsod, and Y. Nemirovsky, "Low frequency noise and drift in ion sensitive field effect transistors," *Sensors and Actuators B: Chemical*, vol. 68, no. 1, pp. 134–139, 2000. [Online]. Available: https://www.sciencedirect.com/science/article/pii/S0925400500004731

[38] S. Jamasb, "Current-mode signal enhancement in the ion-selective field effect transistor (isfet) in the presence of drift and hysteresis," *IEEE Sensors Journal*, vol. 21, no. 4, pp. 4705–4712, 2021.

[39] M. Esashi and T. Matsuo, "Integrated micro multi ion sensor using field effect of semiconductor," *IEEE Transactions on Biomedical Engineering*, no. 2, pp. 184–192, 1978.

[40] T. Matsuo and M. Esashi, "Methods of isfet fabrication," *Sensors and Actuators*, vol. 1, pp. 77–96, 1981.

[41] L. Bousse and P. Bergveld, "The role of buried oh sites in the response mechanism of inorganic-gate ph-sensitive isfets," *Sensors and Actuators*, vol. 6, no. 1, pp. 65–78, 1984.

[42] R. P. Buck, "Kinetics and drift of gate voltages for electrolyte-bathed chemically sensitive semiconductor devices," *IEEE Transactions on Electron Devices*, vol. 29, no. 1, pp. 108–115, 1982.

[43] A. Elyasi, M. Fouladian, and S. Jamasb, "Counteracting threshold-voltage drift in ion-selective field effect transistors (isfets) using threshold-setting ion implantation," *IEEE Journal of the Electron Devices Society*, vol. 6, pp. 747–754, 2018.

[44] S. Böhm, B. Timmer, W. Olthuis, and P. Bergveld, "A closed-loop controlled electrochemically actuated micro-dosing system," *Journal of Micromechanics and Microengineering*, vol. 10, no. 4, p. 498, 2000.

[45] E. M. Briggs, S. Sandoval, A. Erten, Y. Takeshita, A. C. Kummel, and T. R. Martz, "Solid state sensor for simultaneous measurement of total alkalinity and ph of seawater," *ACS sensors*, vol. 2, no. 9, pp. 1302–1309, 2017.

[46] S. Sinha, N. Sahu, R. Bhardwaj, H. Ahuja, R. Sharma, R. Mukhiya, and C. Shekhar, "Modeling and simulation of temporal and temperature drift for the development of an accurate ISFET SPICE macromodel," *Journal of Computational Electronics*, vol. 19, no. 1, pp. 367–386, 2020, DOI: 10.1007/s10825-019-01425-0.

[47] R. Bhardwaj, S. Sinha, N. Sahu, S. Majumder, P. Narang, and R. Mukhiya, "Modeling and simulation of temperature drift for isfet-based ph sensor and its compensation through machine learning techniques," *International Journal of Circuit Theory and Applications*, vol. 47, no. 6, pp. 954–970, 2019. [Online]. Available: https://onlinelibrary.wiley.com/doi/abs/10.1002/cta.2618

[48] S. Jamasb, S. Collins, and R. L. Smith, "A physical model for drift in pH ISFETs," *Sensors and Actuators B: Chemical*, vol. 49, no. 1-2, pp. 146–155, 1998, DOI: 10.1016/S0925-4005(98)00040-9.

[49] D. G. Schlom, S. Guha, and S. Datta, "Gate oxides beyond sio2," *MRS Bulletin*, vol. 33, no. 11, pp. 1017–1025, Nov 2008. [Online]. Available: https://doi.org/10.1557/mrs2008.221

[50] S. Rollo, D. Rani, R. Leturcq, W. Olthuis, P. Garc, and C. Group, "A high aspect ratio Fin-Ion Sensitive Field Effect Transistor: compromises towards better electrochemical bio-sensing," *Nano Letters*, vol. 19, no. 5, pp. 2741–3386, 2019, DOI: 10.1021/acs.nanolett.8b04988.

[51] S. Rollo, D. Rani, W. Olthuis, and C. P. García, "High performance fin-fet electrochemical sensor with high-k dielectric materials," *Sensors and Actuators B: Chemical*, vol. 303, p. 127215, 2020.

[52] D. Rani, S. Rollo, W. Olthuis, S. Krishnamoorthy, and C. Pascual García, "Combining chemical functionalization and finfet geometry for field effect sensors as accessible technology to optimize ph sensing," *Chemosensors*, vol. 9, no. 2, p. 20, 2021.

[53] D. Dzombak and F. Morel, "Surface complexation modeling: Hydrous ferric oxide." (1990).

[54] D. Rani, S. Rollo, W. Olthuis, S. Krishnamoorthy, and C. Pascual García, "Combining chemical functionalization and finfet geometry for field effect sensors as accessible technology to optimize ph sensing," *Chemosensors*, vol. 9, no. 2, 2021. [Online]. Available: https://www.mdpi.com/2227-9040/9/2/20

[55] V. Vanova, K. Mitrevska, V. Milosavljevic, D. Hynek, L. Richtera, and V. Adam, "Peptide-based electrochemical biosensors utilized for protein detection," *Biosensors and Bioelectronics*, vol. 180, p. 113087, 2021. [Online]. Available: https://www.sciencedirect.com/science/article/pii/S095656632100124X

[56] J. Robertson, "High dielectric constant oxides," *The European Physical Journal-Applied Physics*, vol. 28, no. 3, pp. 265–291, 2004.

[57] P. Chalker, M. Werner, S. Romani, R. Potter, K. Black, H. Aspinall, A. Jones, C. Zhao, S. Taylor, and P. Heys, "Permittivity enhancement of hafnium dioxide high- films by cerium doping," *Applied Physics Letters*, vol. 93, 11 2008.

[58] "High aspect ratio fin-ion sensitive field effect transistor: Compromises toward better electrochemical biosensing." [Online]. Available: https://pubs.acs.org/doi/suppl/10.1021/acs.nanolett.8b04988/suppl_file/nl8b04988_si_001.pdf

[59] B. Midmore and R. Hunter, "The effect of electrolyte concentration and co-ion type on the -potential of polystyrene latices," *Journal of Colloid and Interface Science*, vol. 122, no. 2, pp. 521–529, 1988. [Online]. Available: https://www.sciencedirect.com/science/article/pii/0021979788903876

[60] R. Dhar, N. Kumar, C. P. Garcia, and V. Georgiev, "Deriving a novel methodology for nano-biofets and analyzing the effect of high-k oxides on the amino-acids sensing application," 2022.

[61] M. Kosmulski, "Attempt to determine pristine points of zero charge of nb2o5, ta2o5, and hfo2," *Langmuir*, vol. 13, no. 23, pp. 6315–6320, 1997.

[62] R. H. Yoon, T. Salman, and G. Donnay, "Predicting points of zero charge of oxides and hydroxides," *Journal of colloid and interface science*, vol. 70, no. 3, pp. 483–493, 1979.

[63] S. Rollo, D. Rani, W. Olthuis, and C. Pascual García, "High performance fin-fet electrochemical sensor with high-k dielectric materials," *Sensors and Actuators B: Chemical*, vol. 303, p. 127215, 2020. [Online]. Available: https://www.sciencedirect.com/science/article/pii/S0925400519314145

[64] R. Dhar, N. Kumar, C. P. Garcia, and V. Georgiev, "Assessing the effect of scaling high-aspect-ratio isfet with physical model interface for nano-biosensing application," *Solid-State Electronics*, p. 108374, 2022.

[65] S. D. U. Guide, "version q-2019; synopsys," *Inc.: Mountain View, CA, USA*, 2019.

[66] G. Betti Beneventi, "Technology computer aided design (tcad) laboratory, lecture 2, a simulation primer," 02 2015.

[67] B. J. Van Zeghbroeck, "Principles of semiconductor devices," 2011.

[68] R. Narang, M. Saxena, and M. Gupta, "Analytical model of ph sensing characteristics of junctionless silicon on insulator isfet," *IEEE Transactions on Electron Devices*, vol. 64, no. 4, pp. 1742–1750, 2017.

[69] I.-Y. Chung, H. Jang, J. Lee, H. Moon, S. M. Seo, and D. H. Kim, "Simulation study on discrete charge effects of sinw biosensors according to bound target position using a 3d tcad simulator," *Nanotechnology*, vol. 23, no. 6, p. 065202, 2012.

[70] S. Koneshan, J. C. Rasaiah, R. Lynden-Bell, and S. Lee, "Solvent structure, dynamics, and ion mobility in aqueous solutions at 25 c," *The Journal of Physical Chemistry B*, vol. 102, no. 21, pp. 4193–4204, 1998.

[71] A. Bandiziol, P. Palestri, F. Pittino, D. Esseni, and L. Selmi, "A tcad-based methodology to model the site-binding charge at isfet/electrolyte interfaces," *IEEE Transactions on Electron Devices*, vol. 62, no. 10, pp. 3379–3386, 2015.

[72] F. BRESCIA, J. ARENTS, H. MEISLICH, and A. TURK, "14 - ionic equilibrium calculations," in *Fundamentals of Chemistry: a Modern Introduction (Third Edition)*, third edition ed., F. BRESCIA, J. ARENTS, H. MEISLICH, and A. TURK, Eds.   Academic Press, 1975, pp. 265–296. [Online]. Available: https://www.sciencedirect.com/science/article/pii/B9780121323325500181

[73] S. Rollo, "A new design of an electrochemical (bio)sensor: High aspect ratio fin-fet," Ph.D. dissertation, University of Twente, Netherlands, Nov. 2019.

[74] A. J. Bard and L. R. Faulkner, *Electrochemical Methods: Fundamentals and Applications*, 2nd ed.   Wiley, 2001.

[75] K. J. Kuhn, "Considerations for ultimate cmos scaling," *IEEE transactions on Electron Devices*, vol. 59, no. 7, pp. 1813–1828, 2012.